UNIVERSITY OF CALIFORNIA

Los Angeles

Small Molecule Interactions in Organic and Perovskite Photovoltaics

A dissertation submitted in partial satisfaction of the

requirements for the degree

Doctor of Philosophy in Chemistry

by

Selbi Nuryyeva

2021

ABSTRACT OF THE DISSERTATION

Small Molecule Interactions in Organic and Perovskite Photovoltaics

by

Selbi Nuryyeva

Doctor of Philosophy in Chemistry

University of California, Los Angeles, 2021

Professor Kendall N. Houk, Chair

Organic and perovskite materials have shown a remarkable promise for solar cell manufacturing due to scalability, low cost and flexibility of the material compared to other solar panel technologies. The major challenge for organic and perovskite solar cell commercialization, however, is whether they can perform and last as long as silicon panels, which often depends on the molecular properties of materials. Hence, this dissertation focuses on understanding the crucial role and the effect that small molecules have on the efficiency and stability of organic and perovskite solar cells. Chapter 1 explores the *inter*- and *intra*molecular interactions of small molecules in organic solar cells. The electron-withdrawing character of functional groups and extension of conjugation strongly contributed to the performance of organic solar cells. Chapter 2 dives into radical formation in a novel small molecule hole-transport material for perovskite photovoltaics and its role in performance and stability of the device. In Chapter 3 and 4, recently

designed spirofluorene-based π···π-bonded organic framework and a spiroconjugated small molecule are introduced, both of which present remarkable transport properties in organic electronics. Chapter 5 and 6 examine the interactions between small molecules and perovskite quantum dots (QDs). First, a process that controls the density of small molecules on QD surface is developed, after which a small molecule is integrated onto the surface of QDs resulting in improved device performance. The focus then advances to the analysis of small molecule interactions with the thin-film perovskite. Chapter 7 demonstrates a kinetically-controlled and substrate-tolerant local epitaxial growth of formamidinium-based perovskite for thin-films using a cheap, versatile and simple method that improved stability and performance. Chapter 8 and 9 delve into passivation of perovskite defects using small molecules. Theophylline, a small molecule found in tea, emerged to be a strong candidate for silencing the most probable defects on perovskite surface due to its optimal configuration relative to the surface. It was also discovered that the passivation of perovskite surface defects with two small molecules can have synergistic effect on enhancing the performance of perovskite photovoltaics. In chapter 10, interactions in formation kinetics of mixed-halide perovskites are systematically investigated.

The dissertation of Selbi Nuryyeva is approved.

Yang Yang

Yves F. Rubin

Richard Kaner

Kendall N. Houk, Committee Chair

University of California, Los Angeles

2021

Table of Contents

List of Schemes ..... *viii*

List of Figures ..... *ix*

List of Tables ..... *xv*

Acknowledgments ..... *xvi*

Vita ..... *xxiii*

Chapter 1. Computational Study of the Intramolecular and Intermolecular Interactions in Small Molecule Acceptors for Organic Photovoltaics *1*

1.1. Background **1**

1.2. Methodology **2**

1.3. Results and Discussion **3**

1.3.1. Intramolecular interactions 3

1.3.2. Intermolecular interactions 8

1.4. References **10**

Chapter 2. Radical Formation in a Novel Hole-Transport Material for Perovskite Solar Cells *12*

2.1. Background **12**

2.2. Methodology **15**

2.2.1. Synthesis of Spiro-8Th by the Yang group 15

2.2.2. EPR characterization details 15

2.2.3. Computational details 16

2.3. Results and Discussion **16**

2.3.1. Transport properties of doped Spiro-8Th and its performance and stability in photovoltaics 16

2.3.2. Theoretical investigation of radical formation in doped Spiro-8Th 18

2.4. Conclusion **22**

2.5. References **23**

Chapter 3. Noncovalent π-stacked Robust Topological Organic Framework *26*

3.1. Background **26**

3.2. Methodology **28**

3.2.1. General procedure for synthesis of SFIC by Yang group 28

3.2.2. Computational details 28

3.3. Results and Discussion **30**

3.3.1. Synthetic approach and molecular assembly 30

3.3.2. Investigation of Sorption and Porosity of SFIC-πOF. 33

3.3.3. Single-Crystal Transistor Characterization of SFIC-πOF. 34

3.3.4. Mechanistic Studies of Transport: From a Computational Perspective. 36

3.4. Conclusion **39**

3.5. References **40**

Chapter 4. Chlorinated, Spiroconjugated, and Fused Extended Aromatics for Multifunctional Organic Electronics *44*

4.1. Background **44**

4.2. Methodology **46**

4.2.1. Synthetic Approach 46

4.2.1. Computational Details 48

4.3. Results and Discussion **49**

4.4. Conclusion **55**

4.5. References **56**

Chapter 5. Designing Surface Ligand Management for Stable $FAPbI_3$ Perovskite Quantum Dot-based Solar Cells *60*

5.1. Background **60**

5.2. Methodology **61**

5.2.1. Preparation of FA-oleate and Cs-oleate precursors 61

5.2.2. Synthesis of $FAPbI_3$ CQDs 62

5.2.3. Surface ligand management of $FAPbI_3$ CQDs in solution phase 62

5.2.4. Surface ligand management of $FAPbI_3$ CQDs in solid phase 63

5.2.5. Fabrication of photovoltaic devices with $FAPbI_3$ CQDs 64

5.3. Results and Discussion **65**

5.3.1. Morphological and structural properties of $FAPbI_3$ CQDs. 65

5.3.2. Motivation for and design of rational solvent treatment of $FAPbI_3$ CQDs. 66

5.3.3. Photovoltaic performance of surface-treated $FAPbI_3$ CQD-based devices. 72

5.3.4. Stability measurements of bulk $FAPbI_3$ and surface-treated $FAPbI_3$ CQD-based devices 74

5.4. Conclusion **75**

5.5. References **76**

Chapter 6. A Small-Molecule "Charge Driver" for Perovskite Quantum Dot Solar Cells with Efficiency Approaching 13% *80*

6.1. Background **80**

6.2. Methodology **82**

6.2.1. Synthesis and preparation of $FAPbI_3$ CQDs 82

6.2.2. Fabrication of $FAPbI_3$ CQD-based devices with ITIC 82

6.3. Results and Discussion **83**

6.4. Conclusion **89**

6.5. References **90**

Chapter 7. Solid-phase hetero epitaxial growth of α-phase formamidinium perovskite *93*

7.1. Background **93**

7.2. Methodology **95**

7.2.1. Preparation of perovskite precursor solution by Yang group 95

7.2.2. Fabrication of perovskite films by Yang group 95

7.2.3. DFT methods 96

7.3. Results and Discussion **97**

7.3.1. Phase conversion kinetics 97

7.3.2. Proof-of-concept devices 102
7.4. Conclusion 103
7.5. References 104
Chapter 8. Constructive molecular configurations for surface-defect passivation of perovskite photovoltaics 108
8.1. Background 108
8.2. Methodology 109
8.2.1. Computational methods 109
8.2.2. DFT characterization of surface defects and defect passivation 110
8.2.3. Device fabrication by the Yang group 111
8.3. Results and Discussion 112
8.4. Conclusion 122
8.5. References 123
Chapter 9. Electrostatic stabilization of the passivated wide-gap perovskite surface for stacked tandem photovoltaics 127
9.1. Background 127
9.2. Methodology 129
9.2.1. Computational methods 129
9.2.2. Device fabrication by the Yang group 132
9.3. Results and Discussion 133
9.3.1. Interaction of PEA and fluoride with the surface of perovskite 133
9.3.2. Properties of the material and thin film 136
9.3.3. Performance of semitransparent and tandem solar cells 139
9.4. Conclusion 142
9.5. References 143
Chapter 10. Investigation of Performance-Limiting Formation Kinetics in Mixed-Halide Perovskites 147
10.1. Background 147
10.2. Methodology 149
10.2.1. Computational methods 149
10.2.2. Preparation of perovskite precursors by the Yang group 152
10.2.3. Preparation of perovskite thin film and solar cells by the Yang group 153
10.3. Results and Discussion 153
10.3.1. In-situ photoluminescence studies performed by the Yang group 153
10.3.2. Absorption and crystallinity studies performed by the Yang group 156
10.3.3. Computational insights into formation mechanism 157
10.3.4. Solar-cell performance studies performed by the Yang group 160
10.3.5. Resulting overall model of the formation kinetics and defect physics 161
10.4. Conclusion 164
10.5. References 165

List of Schemes

Scheme 1.1. Library of chemical structures of linear small molecule acceptors with varying functional groups 7

Scheme 5.1. Schematic representation of device fabrication process (inset: photographs of CQDs film with the increasing number of layers) 63

Scheme 5.2. Strategy for designing rational solvent-treatment routes to manage surface ligands of $FAPbI_3$ CQDs 67

Scheme 6.1. $FAPbI_3$ CQD/ITIC film fabrication (inset: chemical structure of ITIC) 83

List of Figures

Figure 1.1. Chemical structures of small molecule acceptors synthesized by the Yang group. The ICT direction is modified depending on the functional group at the branch ends of small molecule acceptors. ICT stands for intramolecular charge transfer, A for acceptor and D for donor 3

Figure 1.2. Dihedral angle scans of C=C-C=C (highlighted in cyan color) in isolated functional groups. Dihedral angle scan between the functional group and the adjacent thiophene group in (A) TH-CHO, (B) TH-M, (C) TH-I and (D) TH-IC in its *E* and *Z* isomer forms. Inserts show chemical structures of isolated functional groups. Electronic energy differences between two lowest energy conformers, structures of which are on the graphs, are shown on top of the graphs 4

Figure 1.3. Optimized structures of D-M in ground and excited states. Bond lengths and three dihedral angles (blue, orange and green) in D-M in optimized ground state (black) and S_1 excited state (red). Units of bond lengths are in Angstroms 5

Figure 1.4. Absorption spectra of small molecule acceptors. (left) Experimental (in 1,1,2,2-tetrachloroethane) and (right) theoretical absorption spectra (in chloroform) of candidate small molecules D-CHO (black), D-M (red), D-I (blue), D-IC (pink) and D-H (orange).....6

Figure 1.5. Computed absorption spectra of additional small molecules. (left) Theoretical oscillators strengths (vertical solid lines) and absorption spectra (dotted line) of D-H (orange), D-vinyl (green) and D-vinyl-dialkynyl (purple) in chloroform; (right) table of calculated and experimental absorption values for all linear small molecules. Red and black arrows indicate the functional end groups that are similar in π-systems 7

Figure 1.6. Chemical structure (left) and crystal packing of m-ITIC-OR-4Cl (right) 8

Figure 1.7. Computed TD-DFT absorption spectra of monomer (blue) and dimer (black) of m-ITIC-OR-4Cl in gas phase. (A) Theoretical absorption (dotted lines) and oscillator strengths (vertical solid lines) with the wavelength of strongest ones indicated on top right corner and (B) corresponding energy levels of molecular frontier orbitals with arrows depicting the respective absorption of the strongest oscillator strengths 8

Figure 1.8. LUMO (top) and HOMO (bottom) orbitals of m-ITIC-OR-4Cl monomer (left) and dimer (right). Dimer has additional HOMO-1 and LUMO+1 orbitals that are degenerate to HOMO and LUMO orbitals. Green and blue colors indicate different phases of orbitals 9

Figure 2.1. Hole transport materials: (A) Spiro-OMeTAD, (B) Spiro-8Th, and (C) DPI-TPFB 13

Figure 2.2. Experimental EPR spectrum of Spiro-8Th measured at 298 K 13

Figure 2.3. Long-term thermal stability of PSC devices with DPI-TPFB-doped Spiro-8Th and Li-doped Spiro-OMeTAD under N_2 gas in glove box at 85 °C 18

Figure 2.4. Optimized structures of Spiro-8Th, TPFB and DPI in their singlet state using B3LYP method and LANL2DZ basis set for iodine and 6-31G(d) for all other atoms 19

Figure 2.5. Radical formation mechanism in doped Spiro-8Th. Electron transfer from tertiary amine of Spiro-8Th to DPI iodonium salt resulting in radical cation Spiro-8Th and iodyl radical DPI, which further decomposes into aryl radical and *p*-iodotoluene.....19

Figure 2.6. Energy levels of frontier orbitals of Spiro-8Th and DPI. HOMO-LUMO energies were computed using B3LYP method and LANL2DZ basis set for iodine and 6-31+G(d,p) for all other atoms. Dashed arrow indicates electron transfer from HOMO of Spiro-8Th to LUMO of DPI.....20

Figure 2.7. Spin density distribution in Spiro-8Th and the dopant salt computed with M06-2X method and LANL2DZ basis set for iodine and 6-31+G(d,p) for all other atoms. Spin density distribution in (A) Spiro-8Th radical cation, (B) DPI iodyl radical and (C) isopropylbenzene radical, a by-product of DPI iodyl radical decomposition. Top relative spin density values are also shown, with atoms of highest spin density values in bold. An inset in (B) depicts the spin density of H_2I that is used as a simplified model reference for DPI iodyl radical.....21

Figure 3.1. Synthetic route and crystal packing arrangement of SFIC. (A) Synthetic route with reaction conditions of (i) 3-(dicyanomethylidene)indan-1-one (IC, 12 equivalents) and pyridine (1 mL) in chloroform at 70 °C with yield of 90%. (B) The single-crystal X-ray molecular structure [top (Left) and side (Right) view] show a tetragonaldisphenoid motif. (C) The 2D crystal assembly along the ac plane via π···π interactions. The directions of up and down refer to the direction of the N atom. (D) The molecular packing arrangement of the 3D πOF structure is consists of 2D π···π (ac plane) interactions and 1D CH···π (b axis) interactions. dDP and dS represent packing and slippage distances between layers, respectively. The alkyl chains, cyano groups, and hydrogen and oxygen atoms are omitted for clarity 31

Figure 3.2. The interlayer CH···π interactions in πOF crystal along the b axis 32

Figure 3.3. Single-crystal transistor (OFET) characterization of πOF. (A) The OM image of πOF microplates [drop-casted in $CHCl_3$ (1 mg/mL)] self-assembled on SiO_2/Si. (B and C) CPOM images of the single-crystal microplates of πOF. (D) The SAED patterns and its corresponding TEM image. (E) One-dimensional out-of-plane XRD pattern of a single crystal data. (F) A transistor with four electrodes probing charge transport properties along different crystal planes. (G) The schematic diagram of πOF micro/nanocrystal transistor. (H) P-type and (I) N-type transfer characteristics of four OFET devices in different crystal planes.....34

Figure 3.4. Computational characterizations of hole/electron transport. (A) Crystal packing of πOF used in computations. Green spheres represent alkyl chains. (B) Computed binding energies (in electronvolts), hole transfer (J_h), and electron transfer (J_e) integrals (in millielectronvolts) (C) Direction-resolved hole and electron mobilities in ordered phase. (D) Atomistic morphology of the disordered phase. (E) Hole and electron transfer integral distributions in all transport directions. (F) Direction-resolved hole and electron mobilities in disordered phase.....37

Figure 3.5. Characterization of interactions in the computational model of πOF crystal structure. (A) Superposition of single SFIC molecule geometry obtained from X-ray measurements over the B3LYP/6-31G(d) gas-phase optimized one. (B) SFIC pair interactions present in the crystal structure and the respective B97D/6-31G(d,p)-calculated dimer binding

energies. (C) A diagram showing electric field variation for direction-resolved transport calculations. (D) MD-equilibrated atomistic morphologies of πOF along three packing directions. (E) Computed site-energy difference distributions for hole and electron transfers based on Thole model. (F) Connectivity graphs in πOF based on the strength of the hole (p) and electron (n) transfer integrals. Green dots represent site positions. For J>1 meV the bonds are in red and for 0.1 meV < J < 1 meV range, the bonds are in blue. Missing bonds are less than 0.1 meV. (left column) The connectivity along a single π···π plane, (right column) the connectivity for all directions 38

Figure 4.1. Synthetic route to SFIC-Cl. The reaction conditions were: i) Methyl 2-bromothiophene-3-carboxylate (4.5 equiv.), 2,2′,7,7′-tetrakis(pinacolatoboryl)-9,9′-spirobi[*9H*-fluorene] (1.0 equiv), $Pd(PPh_3)_4$ (0.3 equiv.), K_2CO_3 (2 m)/THF (1:2), 95 °C, 72 h. Yield: 80%. ii) 1-Bromo-4-hexylbenzene (22 equiv.), magnesium turnings (26.4 equiv.), THF, RT to 70 °C, 20 h. Yield: 85%. iii) Boron trifluoride diethyl etherate (diluted by chloroform), chloroform, 70 °C, 24 h. Yield: 75%. iv) DMF, $POCl_3$, 0 to 90 °C, 20 h. Yield: 70%. v) 2-(5,6-Dichloro-3-oxo-2,3-dihydro-1H-inden-1-ylidene) malononitrile (12 equiv.), pyridine (1 mL), chloroform, 70 °C, yield: 85% 47

Figure 4.2. Potential energy surface for rotation about the highlighted C-C-C-C dihedral in *E* and *Z*-TH-IC. Constrained optimization of E-isomer at 252° was unable to converge due to steric clashes between thiophene and cyano groups 48

Figure 4.3. Optimized structure of lowest energy conformer of MF-Ph and its frontier molecular orbitals.....49

Figure 4.4. Optimized structure of SFIC-Cl and its optical and electrochemical properties. A) DFT-optimized structure of the lowest energy conformer of SFIC-Cl (left: side view, right: top view). B) UV−vis absorption spectra of SFIC-Cl in solution ($CHCl_3$) and film. C) Cyclic voltammogram of SFIC-Cl film.....50

Figure 4.5. Frontier molecular orbitals (left) and depiction of the four lowest energy excited states (right) of SFIC-Cl.....52

Figure 4.6. Experimental absorption spectrums (black line) and calculated line spectrum (vertical orange lines) of SFIC-Cl in $CHCl_3$.....53

Figure 4.7. Electron density difference plots of degenerate excitations A of SFIC-Cl depicting electron density going from yellow to purple regions from different views (isodensity = 0.004) 54

Figure 5.1. Morphology and crystal structure of $FAPbI_3$ CQDs. Transmission electron microscopic image (A) and X-ray diffraction (XRD) patterns (B) of as-synthesized $FAPbI_3$ CQDs and bulk films. δ and * indicate hexagonal non-perovskite phase and PbI_2, respectively. 65

Figure 5.2. Size distribution of $FAPbI_3$ CQDs measured from Figure 5.1A 66

Figure 5.3. Gradual reduction in ligand density with surface treatment. (A) Nuclear magnetic resonance spectra of $FAPbI_3$ CQDs with increasing number of surface treatment cycles in solution, indicating a gradual decrease of the oleyl species (right) and schematic illustration of the ligand density control during solution-state surface treatment (left). Molecular structure of the oleyl species are shown as inset. Functional groups and corresponding signals are

highlighted with dashed yellow lines. (B) Fourier transform infrared spectra of $FAPbI_3$ CQDs before and after solid-state surface treatment (right) and a schematic illustration of the ligand density change and inter-dot coupling during the solid-state surface treatment (left). C-H modes associated with oleyl species are highlighted with dashed yellow lines 69

Figure 5.4. Photovoltaic performance of $FAPbI_3$ CQD devices with surface treatment. (A) Schematic of device structure and cross-sectional scanning electron microscopic image of the $FAPbI_3$ CQDs solar cell. (B) Current density-voltage (J-V) curves and (C) external quantum efficiency of the devices based on $FAPbI_3$ CQDs with increasing cycles of surface treatment....72

Figure 5.5. Stability of CQD and bulk FAPbI3 devices and under ambient and operational conditions. (A) Evolution of power-conversion efficiency (PCE) of photovoltaic devices based on bulk $FAPbI_3$ and $FAPbI_3$ CQDs stored under ambient condition without encapsulation. Inset shows photos of the device before and after exposure. (B) Change in PCE of the encapsulated device under continuous illumination (90 ± 5 mW/cm^2). The devices were maintained under open-circuit condition at room temperature (ca. 30°C ± 3°C). The error bars indicate standard deviation of the PCEs measured from 6 devices for each condition 75

Figure 6.1. Structure and performance of $FAPbI_3$ CQD-based photovoltaic devices. a) A cross-sectional SEM image of the device structure. b) J–V curves of the devices based on $FAPbI_3$ CQDs with and without ITIC.....85

Figure 6.2. Structural and photophysical properties of $FAPbI_3$ CQDs without and with ITIC. a) Transmission electron microscopy (TEM) image of as-synthesized $FAPbI_3$ CQDs. b) UV–visible absorption, c) steady-state photoluminescence (open circles indicate measured data while solid lines are fitted curves) and d) TRPL spectra of $FAPbI_3$ CQDs with (red) and without (black) ITIC 85

Figure 6.3. Energy levels and charge transfer in $FAPbI_3$ CQDs with ITIC. a) Ultraviolet photoelectron spectroscopy (UPS) determination of energy levels of fermi level and valence band maximum of $FAPbI_3$ CQDs. b) Schematic energy diagram showing charge transfer between $FAPbI_3$ CQDs and ITIC.....87

Figure 6.4. Performance comparison of selective vs even distribution of ITIC in $FAPbI_3$ CQD-based devices. Schematic diagrams of $FAPbI_3$ CQDs-based solar cell devices a) with and b) without the control of ITIC distribution. c) J-V curves of the corresponding devices with and without ITIC distribution control 88

Figure 7.1. Charge distribution determined by density functional theory (DFT) calculation. Schematics showing molecular structure structure of (a) phenethylammonium cation (PEA^+) and (b) 4-fluoro-phenethylammonium cation ($FPEA^+$). Charge distribution of the (c), (e) PEA^+ and (d), (f) $FPEA^+$ molecules. (c), (d) are top and (e), (f) are cross sectional views.....98

Figure 7.2. Phase conversion kinetics of formamidinium lead tri-iodide ($FAPbI_3$) perovskite with a hetero-interface at the grain boundaries and proof-of-concept devices. (a) Photographs of $FAPbI_3$ films on SnO_2-coated ITO substrates with different annealing times at 150 °C. Control: bare $FAPbI_3$, 1P: $FAPbI_3$ with 1.67 mol% PEA_2PbI_4, 3P: $FAPbI_3$ with 3.33 mol% PEA_2PbI_4, and 3F: $FAPbI_3$ with 3.33 mol% $FPEA_2PbI_4$. (b) Current density–voltage (J–V) of solar cell devices based on a bare $FAPbI_3$ film (control) and a $FAPbI_3$ film with NHE. Inset of (b) shows the steady-state power conversion efficiencies measured at maximum power points. (c) Voltage–radiance curves of the light emitting diode (LED) devices based on the

control and NHE films. Inset of (c) shows the electroluminescence spectra of the LED devices. (d) Device structure schematics and corresponding cross-sectional scanning electron microscopy image of the solar cell device based on the $FAPbI_3$ film with nano heteroepitaxy (NHE, with 3.33 mol% $FPEA_2PbI_4$) 99

Figure 7.3. Phase conversion energy barriers. (left) DFT-calculated free energy barriers (ΔG_cs) for phase conversion from cubic to hexagonal ($\alpha \rightarrow \delta$), from hexagonal to cubic ($\delta \rightarrow \alpha$), and formation enthalpy of the cubic phase (ΔH) with respect to that of the hexagonal phase. Dashed lines and solid lines indicate ΔG_c without and with strain, respectively. The interlayer spacing of the strain-free hexagonal phase, layered perovskite and cubic phase are indicated with gray colored dashed vertical lines (d-spacings of DFT optimized structures). (right) Schematic free energy diagrams for the hexagonal and cubic phased $FAPbI_3$ at different temperatures and strain condition. T is temperature and T_c is the temperature for phase conversion 101

Figure 8.1. Surface defect identification and constructive configuration of the C=O group in three different chemical environments. (A) Top view of the various types of surface defects. (B) Theoretical models of perovskite with molecular surface passivation of Pb_I antisite with theophylline, caffeine, and theobromine (C) J-V curves of perovskite solar cells with or without small molecules treatment under reverse scan direction 113

Figure 8.2. Interaction energies between the molecule and slab complex for the V_I case using DFT-D3 method.....114

Figure 8.3. Investigation of the interactions between surface defects and the small molecules. FTIR spectra of (A) pure theophylline and theophylline-PbI_2 films, (B) pure caffeine and caffeine-PbI_2 films, and (C) pure theobromine and theobromine-PbI_2 films with corresponding molecular models on the right.....119

Figure 8.4. Characterization of perovskite films and interfaces with theophylline treatment. (A) XPS data for Pb 4f 7/2 and Pb 4f 5/2 core-level spectra in perovskite films with or without theophylline treatment. (B) UPS spectra of perovskite films with or without theophylline treatment. (C) AFM and KPFM images of perovskite films with (right) or without (left) theophylline treatment. (D) Time-resolved PL spectra of perovskite films before and after depositing Spiro-OMeTAD without and with theophylline treatment. (E) Cross-section SEM images and the corresponding EBIC images and line profile of the perovskite solar cells with (right) or without (left) theophylline treatment.....120

Figure 9.1. Fermi level dependence of interaction energies. Neutral and charge defect cases are both considered 132

Figure 9.2. Top and side views of theoretical models used for V_I and Pb_I charged defects: interacting with bare PEA (a and b), PEA with fluoride presents nearby (c and d), and their corresponding interaction energies at the CBM. The Pb, I, FA, PEA and F atoms are as depicted at the bottom of the figure 134

Figure 9.3. Characterizations of the passivation agents and their interactions with perovskite thin films. (a) FTIR spectra of PEAI and F-treated PEAI in the range of bending (left) and stretching (right) mode of N-H group. (b) XPS data for Pb 4f 7/2 and Pb 4f 5/2 core level spectra from perovskite films with various treatments. (c) XPS data for I 3d 5/2 and I 3d 3/2 core level spectra from perovskite films with various treatments. (d) TRPL spectra of

perovskite films with or without treatments. (e) UPS spectra of perovskite films with or without treatments. (f) The energy levels of the perovskite surfaces with or without treatment derived from UPS measurements and the optical bandgap of the perovskite film 136

Figure 9.4. Device configuration of the semitransparent control and target perovskite cells.....139

Figure 9.5. Performance of the wide-bandgap and tandem perovskite cells. (a) J-V curves of the semitransparent perovskite cells with the targeted synergistic passivation treatment (target) and without any treatment (control). (b and c) J-V curves of the target semitransparent perovskite combined with the commercially available silicon (blue) and CIGS (green) solar cells. The semitransparent perovskite cells without splitting into mini cells were used as an optical filter to measure the filtered characteristics of the rear cells 140

Figure 10.1. In-situ photoluminescence measurements monitoring the formation kinetics of perovskite films. (A) Illustration of the in-situ PL measurement during spin-coating and annealing stage of perovskite formation. The contour plot of the captured PL spectra during the growth of (B) CsFAMAPb($I_{0.8}Br_{0.2}$)$_3$ and (C) CsFAMAPbI_3 films during spin-coating (left) and annealing (right). The extracted values of emission peak position (D), PL intensity (E), and FWHM (F) from the in-situ PL measurements.....154

Figure 10.2. Absorption and XRD patterns of perovskite thin films. (A) Absorption spectra of FAMACsPbX_3 films before(as-cast)/after fully annealed. (B) Photographs of the as-cast (top) and fully annealed (bottom) perovskite films with the stoichiometries of CsFAMAPb($I_{0.8}Br_{0.2}$)$_3$ (left) and CsFAMAPbI_3 (right). (C) The XRD patterns of the as-cast and fully annealed perovskite films 157

Figure 10.3. Computed interaction, formation and surface energies. (A) Interaction energy between DMSO and PbXX' molecule and formation energy of DMSO:PbXX' adduct phase. (B) The calculated results of surface energy difference in tri-iodide perovskites and tri-bromide perovskites with cations to be Cs, MA, or FA.....159

Figure 10.4. Optimized molecular structures and intermolecular interaction distances between coordinating solvent, DMSO, and PbXX' molecules.....159

Figure 10.6. Side (A) and top (B) views of the optimized supercell of DMSO:PbXX' adduct. X sites were assumed to be I in the structure.....160

Figure 10.7. J-V characteristics of perovskite solar cell devices based on CsFAMAPb($I_{0.8}Br_{0.2}$)$_3$ and CsFAMAPbI_3 161

Figure 10.8. A hypothetical physical model of formation kinetics in mixed-halide perovskite with high Br% (left) and their potential role with defect physics (right). Several but not all possible point defects were illustrated at the surface or in the bulk. For simplification purpose, only the halides were specified for Br as purple dots and I as yellow dots 162

Figure 10.9. Fermi energy (E_F) dependence of the defect formation energies: (left) FA vacancy and (right) FA interstitial point defects in FAPbI_3 (orange line), FAPb($I_{0.8}Br_{0.2}$)$_3$ (black line) and FAPbBr$_3$ (green line). E_F = 0 was set at valence band minimum 163

List of Tables

Table 2.1. Hole mobilities of doped Spiro-MeOTAD and Spiro-8Th 17

Table 2.2. Photovoltaic parameters of various doped HTMs in a perovskite solar cell.....17

Table 3.1. Field-effect electron (e) and hole (h) mobilities of four OFET devices with different crystal planes.....36

Table 4.1. Summary of optical and electronic properties of SFIC-Cl.....51

Table 5.1. Summary of solvents used for ligand treatment of $FAPbI_3$ CQDs. The polarity of mixed solvent was determined by the arithmetic average of solvent polarity adjusted according to the volume fraction of each solvent 68

Table 5.2. Photovoltaic parameters of $FAPbI_3$ CQD solar cells with different cycles of ligand treatment. Short-circuit current density (J_{SC}), open circuit voltage (V_{OC}), fill factor (FF), power conversion efficiency (PCE) 73

Table 8.1. ΔH_α, formation energies of neutral defects considered in this study 114

Table 8.2. Photovoltaic parameters of average and the best perovskite solar devices without and with various types of surface treatments 116

Table 9.1. The DFT relaxed crystal structures of the solid-state phases considered in chemical potential calculations 130

Table 9.2. Comparison of photovoltaic parameters of single- and multi-junction solar cells 142

Acknowledgments

First and foremost, I would like to express my sincere gratitude to my mentor, teacher and inspiration, Professor Ken Houk. He has gifted me the most creative and inspiring research experience of my academic journey. He patiently taught me the heavy theoretical background and critical thinking required for intelligent use of computational DFT tools, while wholeheartedly supporting my ambitious ventures into the experimental work of materials science and data engineering of our computational resources. As Professor Houk is a fascinating speaker and a farsighted wise leader as well, he unknowingly helped me develop multifaceted soft skills that resulted in our constructive and fruitful collaborations leading to numerous publications. Outside of lab work, he inspired me to become an avid feeder of hummingbirds, although not as successful as he is. I will forever be grateful to Professor Houk for his unyielding and continuous support and investment in me.

I am deeply grateful to my co-advisor, Professor Yang Yang, for taking a chance and offering me an opportunity to experience the experimental part of the photovoltaics. He has encouraged and inspired me to think outside the box, while providing me all the necessary tools and skills to achieve and succeed in execution of these creative and beautiful ideas. He also ensured that I had proper training and warm support within our group. Hence, I would like to sincerely thank Jingjing Xue, Tianyi Huang, Shaun Tan, Dr. Dong Meng, Rui Wang, Yepin Zhao, Dr. Jin-Wook Lee, Oliver Lin, Dr. Pei Cheng, Dr. Lei Meng and Sheng-Yung Chang. Late evenings in the lab synthesizing awe-inspiring quantum dots, long nights into writing exciting research proposals in the quickest time, interesting and funny conversations during lunches and dinners in dining halls and getting introduced to authentic Chinese and Korean cuisines with the Yang group members would always be my fond memories of Engineering V and CNSI.

Much of my success in periodic calculations is because of Professor Ilhan Yavuz. His deep intelligence and unceasing curiosity are mesmerizing to say the least. My heartfelt thanks to Professor Yavuz for walking me through the theoretical and computational parts of materials research, for welcoming me in Turkey with open arms and training me for mobility calculations, and for always being available and eager to help with any challenges I faced with my computations. Additionally, I would like to extend my gratitude to his group members, Caner Değer, Gülsevim Aydın and Olkan Koçak for their tight collaboration and cordial companionship.

I would also like to thank my committee members, Professor Yves Rubin and Professor Richard Kaner for continuously offering insightful feedback, guidance and career advice throughout my academic journey at UCLA. Their wisdom, constructive criticism and thought-provoking questions spurred me to broaden and deepen my understanding and mastery of my research field.

Thank you to my fellow Houkie group members, Dr. Janice Lin, Dr. Yike Zou, Dr. Xiaosong Xue, Dr. Katherine Bay, Dr. Jacob Sanders, Cooper Jamieson, Tyler Benton and Declan Evans who have trained me to become a better computational scientist, shared their expertise and projects with me and with whom we initiated the Tiptorials, where we shared our codes and skills.

To my parents, Jemal and Geldi: you have cheered and wholeheartedly supported my every decision and endeavor despite enduring the thousands of miles between us and silently having your own aspirations for me. There is no amount of gratitude that would be sufficient to express my appreciation of the upbringing, education and character that you have instilled in me. This dissertation is a reflection of your hard work. I would also like to profoundly thank my siblings, Ejegul and Batyr, for continuously motivating me to excel not only academically but also in my personal and professional life. You have been my rock and role models that I aspire to be today.

My dearest and most caring husband, Burhan Siddiqi, thank you for always being there for me throughout my both exciting and challenging times at UCLA with your daily check-ins and frequent trips across the US. Allah has truly blessed me with your unconditional love and patience, magnanimous support and unyielding partnership that I would forever be grateful for. I am a much better human today because of you.

The reason why I decided to pursue chemistry as my career is all because of my host parents, Todd and Susan Carlson. When I came to the US as an exchange student in 2008, my host father, Todd, who is also a university professor, turned my fear of chemistry into a deep fascination. My heartfelt thanks to Todd and Susan for inspiring me to pursue academic pathway and making my dreams of attending college and graduate school in the US come true.

My time at UCLA was a lot more fun, enjoyable and exciting because of the companionship of my closest friends. I would always be reminiscing about the countless boba teas with the kindest and wonderful of a human being Bryant Griffin, heartwarming conversations with inspiring Aygul Ovezliyeva while devouring Russian food. I will always think about the spiritually rewarding Ramadan celebrations with Amani Alsaied, and long hours of sweetest Zoom calls with Huda Alshaikh, Maral Amangurbanova and Sona Apbasova. I am sincerely thankful to you for generously lending me your ear and continuously lifting me up throughout the ups and downs of my academic and personal milestones. I would also like to extend my gratitude to my wonderful roommate, Ieva Liepuoniute, for always cheering me up, bouncing ideas and inspiring me to be a better researcher. I must express my sincere thanks to my dearest friends Nazik and Jemal Aytjanova, Vildan Embel, Armaghan Ahmed, Joe Mazzetti and Zach Hemminger, whose witty humor and fascinating intelligence has made my graduate school experience a lot more enjoyable.

I would like to express my genuine appreciation of Dr. Raffaella D'Auria and Dr. Weihong Yan for their unwavering assistance with Hoffman2 computing resources and GPU computing clusters. They have taught me to be a more conscious, efficient and educated user of high-performance computing resources. Last but not least, I would like to thank Annie Carpenter and Justyna Glodé from the Graduate Student Affairs Office of Chemistry Department for always ensuring our continual success in the program.

Chapter 1 describes *intra* and *inter*molecular interactions in various small molecule acceptors for organic solar cells from a computational perspective. This is a collaboration with the Yang group at UCLA. Dr. Dong Meng performed the experimental work, and I performed all DFT computations and analyses under the supervision of Prof. Ken Houk.

Chapter 2 describes the ongoing study of radical formation in the novel hole-transport material for perovskite photovoltaics. This is a joint collaboration with the Yang group at UCLA and Prof. Ilhan Yavuz's group at Marmara University. Dr. Dong Meng led the experimental work, and I performed all DFT calculations and analysis related to radical formation under the supervision of Prof. Ken Houk.

Chapter 3 is a modified version of the publication "Noncovalent π-stacked Robust Topological Organic Framework." Meng, D.; Yang, J. L.; Xiao, C.; Wang, R.; Xing, X.; Kocak, O.; Aydin, G.; Yavuz, I.; Nuryyeva, S.; Zhang, L.; Liu, G.; Li, Z.; Yuan, S.; Wang, Z.-K.; Wei, W.; Wang, Z.; Houk, K. N.; Yang, Y. *Proc. Natl. Acad. Sci.* **2020**, *117*, 20397. This is collaboration with the Yang group at UCLA and Prof. Ilhan Yavuz's group at Marmara University. Olkan Kocak, Gulsevim Aydin and I performed the DFT and mobility calculations under the supervision of Prof. Ilhan Yavuz and Prof. Kendall N. Houk.

Chapter 4 is a modified version of the publication "Chlorinated Spiroconjugated Fused Extended Aromatics for Multifunctional Organic Electronics." Meng, D.; Wang, R.; Lin, J. B.; Yang, J. L.; Nuryyeva, S.; Lin, Y.-C.; Yuan, S.; Wang, Z.-K.; Zhang, E.; Xiao, C.; Zhu, D.; Jiang, L.; Zhao, Y.; Li, Z.; Zhu, C.; Houk, K. N.; Yang, Y. *Adv. Mater.* **2021**, *33*, 2006120. This is a collaboration with the Yang group at UCLA. Dr. Janice Lin and I performed all DFT calculations under the supervision of Prof. Kendall N. Houk.

Chapter 5 is a modified version of the publication "Surface Ligand Management for Stable $FAPbI_3$ Perovskite Quantum Dot Solar Cells." Xue, J.; Lee, J.-W.; Dai, Z.; Wang, R.; Nuryyeva, S.; Liao, M. E.; Chang, S.-Y.; Meng, L.; Meng, D.; Sun, P.; Lin, O.; Goorsky, M. S., Yang, Y. *Joule* **2018**, *2*, 1866. I performed the thermodynamic analysis, and Jingjing Xue and I synthesized the colloidal quantum dots and carried out the device fabrication and characterization under supervision of Prof. Yang Yang.

Chapter 6 is a modified version of the publication "A Small-Molecule "Charge Driver" Enables Perovskite Quantum Dot Solar Cells with Efficiency Approaching 13%." Xue, J.; Wang, R.; Chen, L.; Nuryyeva, S.; Han, T.-H.; Huang, T.; Tan, S.; Zhu, J.; Wang, M.; Wang, Z.-K.; Zhang, C.; Lee, J.-W.; Yang, Y. *Adv. Mater.* **2019**, *31*, 1900111. I synthesized the colloidal quantum dots and performed the device fabrication and *J-V* characterization under supervision of Jingjing Xue and Prof. Yang Yang.

Chapter 7 is a modified version of the publication "Solid-Phase Hetero Epitaxial Growth of α-Phase Formamidinium Perovskite." Lee, J.-W.; Tan, S.; Han, T.-H.; Wang, R.; Zhang, L.; Park, C.; Yoon, M.; Choi, C.; Xu, M.; Liao, M. E.; Lee, S.-J.; Nuryyeva, S.; Zhu, C.; Huynh K.; Goorsky, M. S.; Huang, Y.; Pan, X.; Yang, Y. *Nat. Commun.* **2020**, *11*, 5514. I performed the DFT

calculations for charge distribution and relevant analysis, while the Yoon group performed the calculations for phase conversion energetics.

Chapter 8 is a modified version of the publication "Constructive Molecular Configurations for Surface-Defect Passivation of Perovskite Photovoltaics." Wang, R.; Xue, J.; Wang, K.-L.; Wang, Z.-K.; Luo, Y.; Fenning, D.; Xu, G.; Nuryyeva, S.; Huang, T.; Zhao, Y.; Yang, J. L.; Zhu, J.; Wang, M.; Tan, S.; Yavuz, I.; Houk, K. N.; Yang, Y. *Science* **2019**, *366*, 1509. This is collaboration with the Yang group at UCLA and Prof. Ilhan Yavuz's group at Marmara University. I performed the interaction energy and related calculations for small molecule-PbX_2 adducts under the supervision of Prof. Ilhan Yavuz and Prof. Kendall N. Houk.

Chapter 9 is a modified version of the manuscript "Surface passivation on wide-gap perovskite solar cell and the formation of stacked tandem structure with Si and CIGS PVs", which is undergoing submission. This is a joint collaboration with the Yang group at UCLA and Prof. Ilhan Yavuz's group at Marmara University. I performed all DFT computations under the supervision of Prof. Ilhan Yavuz and Prof. Kendall N. Houk.

Chapter 10 is a modified version of the manuscript "Unraveling the Surface States of Photovoltaic Perovskite Thin Film", which is undergoing submission. This is a joint collaboration with the Yang group at UCLA and Prof. Ilhan Yavuz's group at Marmara University. I performed the small molecule interaction energy and related calculations, and analysis under the supervision of Prof. Ilhan Yavuz and Prof. Kendall N. Houk.

I also would like to acknowledge and thank my funding sources. This work was supported by the UCLA, National Science Foundation (CHE-1764328), Saul Winstein Fellowship and Dissertation Year Fellowship. This dissertation used computational and storage services associated with the Hoffman2 Shared Cluster provided by UCLA Institute for Digital Research and

Education’s Research Technology Group and the Extreme Science and Engineering Discovery Environment (XSEDE)’s Comet supercomputer, which is supported by National Science Foundation (OCI-1053575).

Vita

Education

University of California, Los Angeles May, 2021
Ph.D. Candidate in Computational Materials Chemistry
GPA: 3.94

- Saul Winstein Fellowship
- Dissertation Year Fellowship
- Dr. Yuh Guo Pan Dissertation Award in Organic Chemistry

Dartmouth College August, 2017
M.Sc. in Chemistry

- Presidential Award
- NETA Scholars Award

New York University, Abu Dhabi May, 2015
B.Sc. in Chemistry
GPA: 3.69

- NYU Honors Scholar
- Founders Day Award

Teaching

Graduate Teaching Assistant at the University of California, Los Angeles 2017-2018

- CHEM 14A, CHEM14B, CHEM20A

Publications

1. Shumilov, K. D.; Mehmedovic, Z.; Ying, H.; Poths, P.; **Nuryyeva, S.**; Liepuoniute, I.; Jang, C.; Winardi, I.; Alexandrova, A. A. "Understanding Hardness of Doped $WB_{4.2}$" *J. Phys. Chem. C* **2021**, *125*, 9486.
2. Meng, D.; Wang, R.; Lin, J. B.; Yang, J. L.; **Nuryyeva, S.**; Lin, Y.-C.; Yuan, S.; Wang, Z.-K.; Zhang, E.; Xiao, C.; Zhu, D.; Jiang, L.; Zhao, Y.; Li, Z.; Zhu, C.; Houk, K. N.; Yang, Y. "Chlorinated Spiroconjugated Fused Extended Aromatics for Multifunctional Organic Electronics" *Adv. Mater.* **2021**, *33*, 2006120.
3. Hurlow, E. E.; Lin, J. B.; Dweck, M. J.; **Nuryyeva, S.**; Feng, Z.; Allred, T. K.; Houk, K. N.; Harran, P. G. "Photoarrangement of [8]-2,6-Pyridinophane *N*-Oxide" *J. Am. Chem. Soc.* **2020**, *142*, 20717.
4. Lee, J. W.; Tan, S.; Han, T.-H.; Wang, R.; Zhang, L.; Park, C.; Yoon, M.; Choi, C.; Xu, M.; Liao, M.; Lee, S.-J.; **Nuryyeva, S.**; Zhu, C.; Huynh, K.; Goorsky, M. S.; Huang, Y.; Pan, X.; Yang, Y. "Solid-phase Hetero Epitaxial Growth of a-phase Formamidinium Perovskite" *Nat. Commun.* **2020**, *11*, 5514.
5. Tan, S.; Yavuz, I.; Weber, M. H.; Huang, T.; Chen, C.-H.; Wang, R.; Wang, H.-C.; Ko, J. H.; **Nuryyeva, S.**; Xue, J.; Zhao, Y.; Wei, K.-H.; Lee, J.-W.; Yang, Y. "Shallow Iodine Defects Accelerate the Degradation of a-Phase Formamidinium Perovskite" *Joule*, **2020**, *4*, 2426.
6. Meng, D.; Yang, J. L.; Xiao, C.; Wang, R.; Xing, X.; Kocak, O.; Aydin, G.; Yavuz, I.; **Nuryyeva, S.**; Zhang, L.; Liu, G.; Li, Z.; Yuan, S.; Wang, Z.-K.; Wei, W.; Wang, Z.; Houk, K. N.; Yang, Y. "Noncovalent π-stacked Robust Topological Organic Framework" *Proc. Natl. Acad. Sci.* **2020**, *117*, 20397.

7. Li, H.; Liang, Y.-R.; Chen, S.-X.; Wang, W.-X.; Zou, Y.; **Nuryyeva, S**.; Houk, K. N.; Xiong, J.; Hu, J.-F. "Amentotaxins C-V, Structurally Diverse Diterpenoids from the Leaves and Twigs of the Vulnerable Conifer *Amentotaxus argotaenia* and Their Cytotoxic Effects" *J. Nat. Prod.* **2020**, *83*, 2129.
8. Tan, S.; Yavuz, I.; De Marco, N.; Huang, T.; Lee, S.-J.; Choi, C. S.; Wang, M.; **Nuryyeva, S.**; Wang, R.; Zhao, Y.; Wang, H.-C.; Han, T.-H.; Dunn, B.; Huang, Y.; Lee, J.-W.; Yang, Y. "Steric Impediment of Ion Migration Contributes to Improved Operational Stability of Perovskite Solar Cells" *Adv. Mater.* **2020**, *32*, 1906995.
9. Low, Z. J.; Ma, G.-L.; Tran, H. T.; Zou, Y.; Xiong, J.; Pang, L.; **Nuryyeva, S.;** Ye, H.; Hu, J.-F.; Houk, K.; Liang, Z.-X. "Sungeidines from a non-canonical enediyne biosynthetic pathway" *J. Am. Chem. Soc.* **2020**, *142*, 1674.
10. Wang, R.; Xue, J.; Wang, K.-L.; Wang, Z.-K.; Luo, Y.; Fenning, D.; Xu, G.; **Nuryyeva, S**.; Huang, T.; Zhao. Y.; Zhu, J.; Wang, M.; Tan, S.; Yavuz, I.; Houk, K. N.; Yang, Y. "Constructive Molecular Configuration in Surface Defect Passivation of Perovskite Photovoltaics" *Science*, **2019**, *366*, 1509.
11. Xue, J.; Wang, R.; Wang, K.; Wang, Z.-K.; Yavuz, I.; Wang, Y.; Yang, Y.; Gao, X.; Huang, T.; **Nuryyeva, S.**; Lee, J.-W.; Duan, Y.; Liao, L.-S.; Kaner, R.; Yang, Y. "Crystalline Liquid-like Behavior: Surface-Induced Secondary Grain Growth of Photovoltaic Perovskite Thin Film" *J. Am. Chem. Soc.*, **2019**, *141*, 13948.
12. Xue, J.; Wang, R.; Chen, L.; **Nuryyeva, S.**; Han, T.-H.; Huang, T.; Tan, S.; Zhu, J.; Wang, M.; Wang, Z.-K.; Zhang, C.; Lee, J.-W., Yang, Y. "A Small-Molecule "Charge Driver" Enables Perovskite Quantum Dot Solar Cells with Efficiency Approaching 13%." *Adv. Mater.* **2019**, 1900111.
13. Cheng, P.; Liu, Y.; Chang, S.-Y.; Li, T.; Sun, P.; Wang, R.; Cheng, H.-W.; Huang, T.; Meng, L.; **Nuryyeva, S.**; Zhu, C.; Wei, K.-H.; Sun, B.; Zhan, X.; Yang, Y. "Efficient Tandem Organic Photovoltaics with Tunable Rear Sub-cells" *Joule*, **2019**, *3*, 1.
14. Huang, W.; Chang, S.-Y.; Cheng, P.; Meng, D.; Zhu, B.; **Nuryyeva, S.**; Zhu, C.; Huo, L.; Wang, Z.; Wang, M.; Yang, Y. "High Efficiency Non-fullerene Organic Tandem Photovoltaics Based on Ternary Blend Subcells" *Nano Lett.* **2018**, *18*, 7977.
15. Xue, J.; Lee, J.-W.; Dai, Z.; Wang, R.; **Nuryyeva, S.**; Liao, M. E.; Chang, S.-Y.; Meng, L.; Meng, D.; Sun, P.; Lin, O.; Goorsky, M. S.; Yang, Y. "Surface Ligand Management for Stable $FAPbI_3$ Perovskite Quantum Dot Solar Cells" *Joule*, **2018**, *2*, 1866.
16. Tan, S.; Huang, T.; Yavuz, I.; Wang, R.; Yoon, T. W.; Xu, M.; Lee, D.-K.; Chen, C.-H.; Huynh, K.; **Nuryyeva, S.**; Zhao, Y.; Wang, H.-C.; Meng, D.; Xue, J.; Wei, K.-H.; Houk, K. N.; Song, Y. J.; Pan, X.; Park, N.-G.; Lee, J.-W.; Yang, Y. "Stability-Limiting Post Treatments of Halide Perovskites" *Nature* **2021**, *submitted*.
17. **Nuryyeva, S.;** Huang, T.; Tan, S.; Yavuz, I.; Babbe, F.; Abdelsamie, M.; Zhao, Y.; Weber, M. H.; Wang, R.; Houk, K. N.; Sutter-Fella, C. M.; Yang, Y. "Performance-Limiting Formation Kinetics in Mixed-Halide Perovskites" *Adv. Funct. Mat.* **2021**, *submitted*.
18. Huang, T.; Wang, R.; **Nuryyeva, S.**; Tan, S.; Xue, J.; Zhao, Y.; Wu, Q.; Cheng, P.; Meng, D.; Yavuz, I.; Houk, K. N.; Yang, Y. "Electrostatic Stabilization of the Passivated Wide-gap Perovskite Surface and the Formation of Stacked Tandem Structure with Si and CIGS PVs" *Sci. Adv.* **2021**, *submitted*.

Chapter 1. Computational Study of the *Intra*molecular and *Inter*molecular Interactions in Small Molecule Acceptors for Organic Photovoltaics

1.1. Background

Escalating demand for energy and global environmental concerns beg for a clean energy future. Solar energy is the most abundant, clean and inexhaustible renewable energy resource, the potential power of which is many times larger than the current rate of energy consumption. Solar cell technology is one of the finest ways to harness solar power.

As promising solar energy-harnessing technologies, organic photovoltaics (OPVs) have attracted considerable attention due to their advantages of scalability, flexibility and low cost.[1] Although the power conversion efficiency (PCE) of single-junction OPVs has reached 17.6%[2] in the last decade, in order to compete with silicon-based photovoltaics, a higher efficiency and longer stability in OPVs have to be realized. The photoactive active layer of OPVs commonly consists of the bulk-heterojunction (BHJ) architecture, where electron-acceptor and -donor are blended. The morphology of the active layer and the interface between both the donor and the acceptor play an important role in determining the stability and efficiency of the OPV.[3-5] Although both effective donor and effective acceptor components are key for high-performance OPVs, the donor components have received more attention over the past decade, most commonly using fullerene derivatives for the acceptor layer. However, the PCE of OPVs based on fullerenes is limited since fullerene derivatives suffer from weak absorption in the visible and NIR regions, limited tunability of their electron affinities, thermal and photochemical instability and onerous purification methods.

Designing a novel small molecule acceptor for BHJ cells is a complicated undertaking. A planar geometry with extended conjugation is typically beneficial for light absorption of the

molecule, but this can induce a strong aggregation that leads to excessively large domains with an inadequate interface between the donor and acceptor for efficient exciton dissociation. Therefore, a molecular design strategy, *e.g.*, reducing the coplanarity, is desirable to introduce enough miscibility and solubility to the molecule. However, reducing the coplanarity of the molecule is typically accompanied by a reduction of the charge carrier mobility. In addition to energetics and absorption, the essence of molecular design is to control judiciously the molecular geometry to balance exciton dissociation and charge carrier transport in a BHJ blend. Hence, this chapter focuses on the *intra*molecular and *inter*molecular interactions resulting from features of molecular structure, geometry and charge transfer in small molecule acceptors, which each directly influence the optical properties, molecular packing and morphology.

1.2. Methodology

Conformational search was performed using MMFF force field in Schrödinger's Maestro (version 11.2.014).[6] Each low energy conformer of up to 10 kcal/mol was first optimized at B3LYP/6-31G(d) in gas phase, after which top conformer of each small molecules was re-optimized at ωB97X-D/6-31+G(d,p) level in gas phase. Optimized structures were verified by frequency calculations as minima (zero imaginary frequencies) at the same level of theory. Dihedral angle scan was performed using the same method and basis set as re-optimization with 36 steps of 5º increments. Ground and first excited state optimizations were performed at ωB97X-D/6-31G(d,p) level in chloroform with integral equation formalism variant of polarizable continuum model (IEFPCM).

Using the optimized structures, theoretical absorption spectra were computed using TD-DFT at B3LYP/6-31+G(d,p) level in chloroform (IEFPCM) solved for 100 states. The spectra

were then generated based on rotatory strengths resulting from the TD-DFT calculation. HOMO-LUMO energies and plots were extracted from re-optimization calculation and visualized with GaussView 5.[7]

For the m-ITIC-OR-4Cl small molecule monomer and dimer, B3LYP/6-31G(d,p) method and basis set in gas phase was used for optimization, frequency, HOMO-LUMO and TD-DFT calculations. Optimized structures were verified by frequency calculations as minima (zero imaginary frequencies) at the same level of theory. In dimer optimization, the coordinates of all heavy atoms (except H) were frozen.

All DFT and TD-DFT computations were performed using Gaussian09.[8] All TD-DFT absorption spectra and oscillator strengths were plotted with Plot2 software (version 2.6.17).[9]

1.3. Results and Discussion

1.3.1. Intramolecular interactions

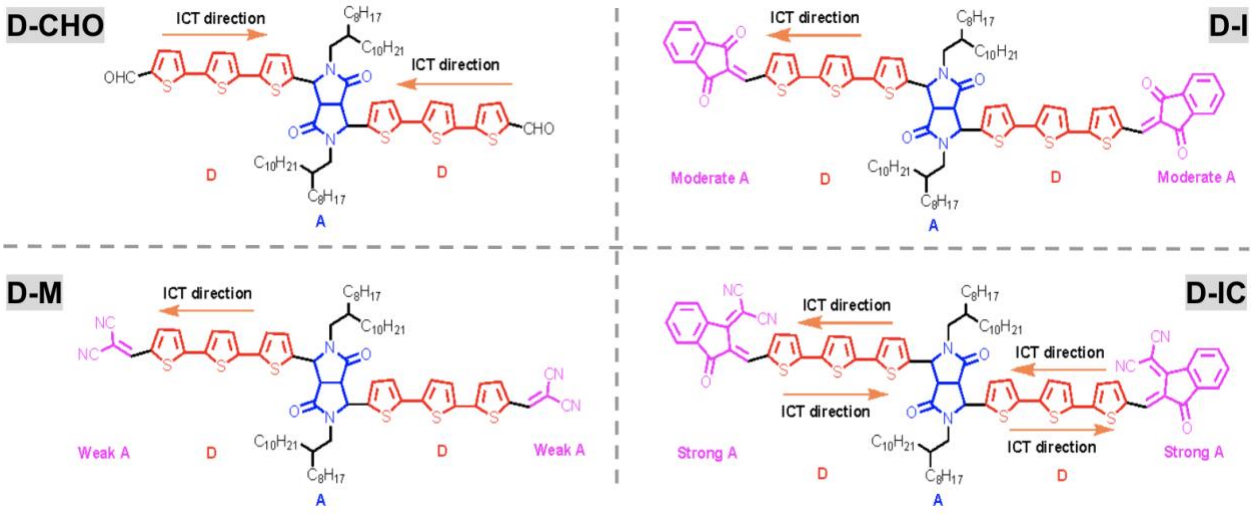

Figure 1.1. Chemical structures of small molecule acceptors synthesized by the Yang group. The ICT direction is modified depending on the functional group at the branch ends of small molecule acceptors. ICT stands for intramolecular charge transfer, A for acceptor and D for donor.

Recently, the Yang group has developed small molecule acceptors (Figure 1.1) featuring a linear geometry consisting of A-D-A-D-A (A - acceptor, D - donor) blocks. Diketopyrrolopyrrole is at the core functionalized at 3- and 6-positions with electron-donating thiophenes capped with end groups, resulting in greater planarity of the backbone and increased π-π interactions. Electron-accepting end groups were varied based on electron-withdrawing character (Figure 1.1) with a goal of modifying the strength and direction of the intramolecular charge transfer (ICT).

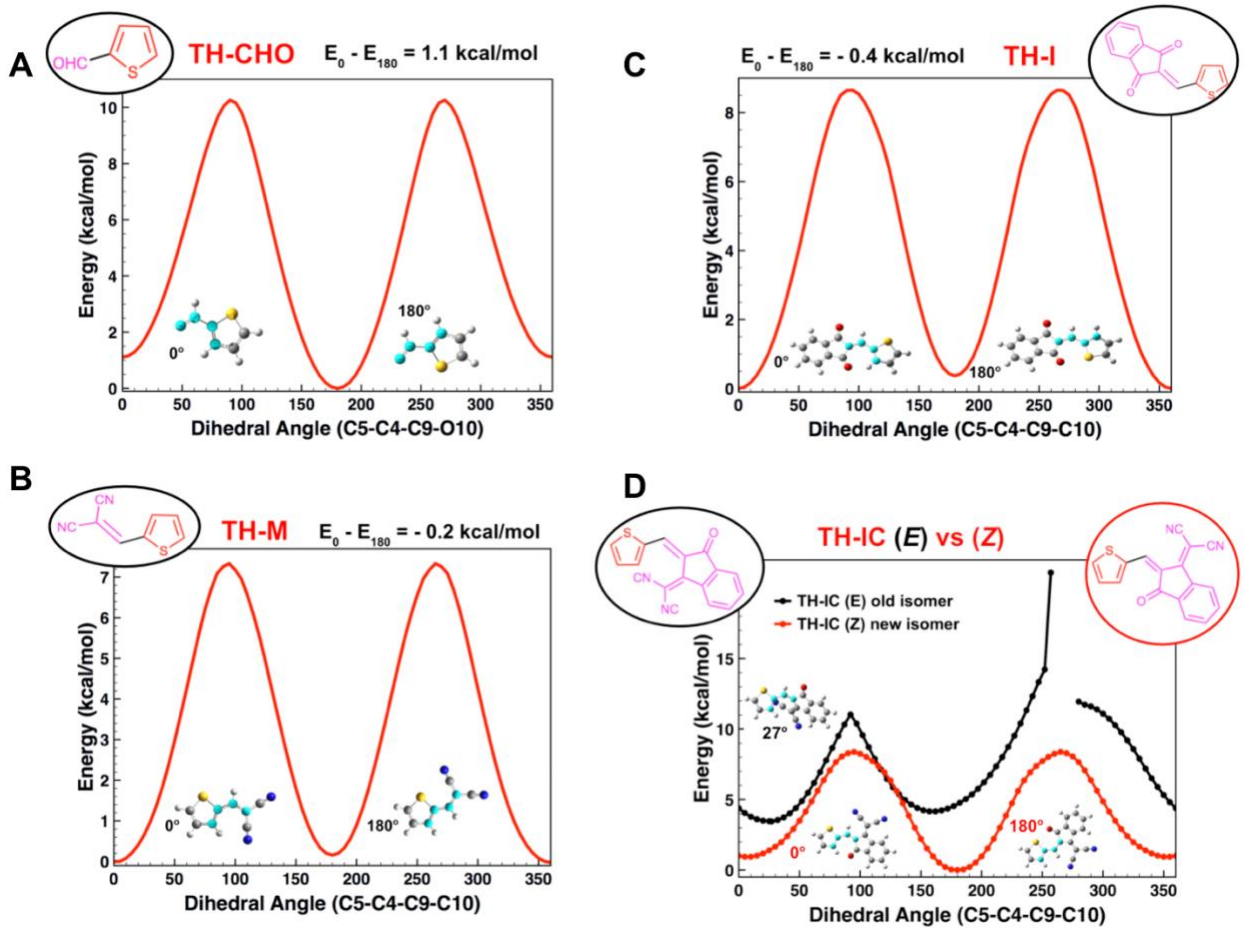

Figure 1.2. Dihedral angle scans of C=C-C=C (highlighted in cyan color) in isolated functional groups. Dihedral angle scan between the functional group and the adjacent thiophene group in (A) TH-CHO, (B) TH-M, (C) TH-I and (D) TH-IC in its *E* and *Z* isomer forms. Inserts show chemical structures of isolated functional groups. Electronic energy differences between two lowest energy conformers, structures of which are on the graphs, are shown on top of the graphs.

In order to elucidate the *intra*molecular interactions present in the proposed small molecule acceptor series, at first, a conformational search followed by lowest conformer optimization were performed on unsubstituted D-M (ie. dicyanoethylene end groups were replaced with hydrogens). Meanwhile, the ethylenemalononitrile unit attached to a thiophene, TH-M, was subjected to a dihedral angle scan analysis (Figure 1.2B) to determine the lowest energy dihedral angle between the thiophene plane and the ethylene unit. The ethylenemalononitrile unit was then adjusted at 0º dihedral angle to the adjacent thiophene group and attached to the lowest energy conformer of unsubstituted D-M. The conformational search on D-CHO, D-I and D-IC and dihedral angle scan analysis for corresponding isolated functional groups (TH-CHO, TH-I and TH-IC) were performed as well, as shown in Figures 1.2A, C and B, respectively. The dihedral angle in final structures was then similarly adjusted. Interestingly, TH-IC was found to be unstable in its *E* isomer form at 180º dihedral angle. As shown in Figure 1.2B, the structure is unable to converge between 250º and 280º due to steric repulsion between the thiophene and di-cyano functional groups. Hence, TH-IC was determined to adopt the *Z* isomer form and prefer it over *E* one by ~3.1 kcal/mol (when comparing the lowest energy conformers of each isomer on dihedral angle scan curve).

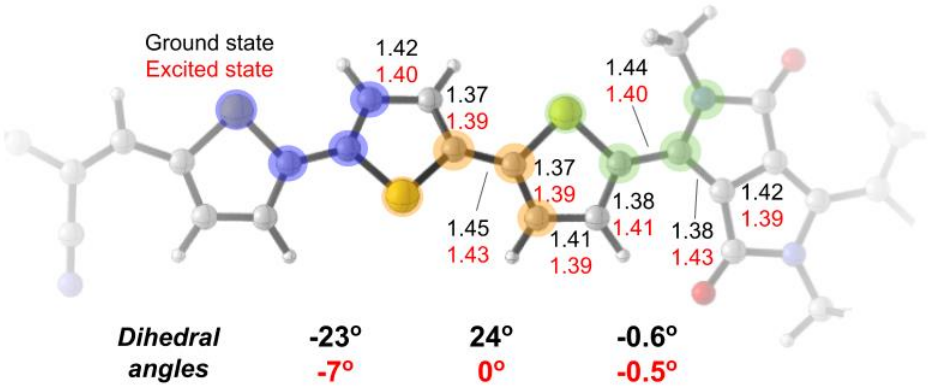

Figure 1.3. Optimized structures of D-M in ground and excited states. Bond lengths and three dihedral angles (blue, orange and green) in D-M in optimized ground state (black) and S_1 excited state (red). Units of bond lengths are in Angstroms.

In order to further characterize the ICT, the ground and S_1 excited states of D-M (Figure 1.3) were then optimized. We found that upon excitation, dihedral angles between thiophenes decrease and bond length alternation in the ground state decreases in the excited state. After successful ground state optimization, TD-DFT calculations on transition energies of D-M were computed and compared to experimental results (Figure 1.4) in order to investigate the trends in absorption maxima shifts across increasing electron-withdrawing nature of the functional end group.

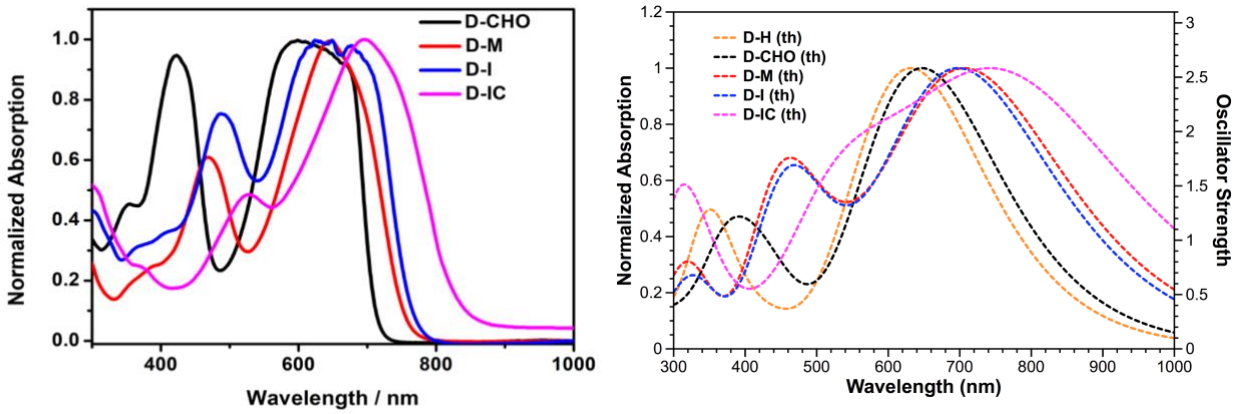

Figure 1.4. Absorption spectra of small molecule acceptors. (left) Experimental (in 1,1,2,2-tetrachloroethane) and (right) theoretical absorption spectra (in chloroform) of candidate small molecules D-CHO (black), D-M (red), D-I (blue), D-IC (pink) and D-H (orange).

Our TD-DFT absorption calculations are in good agreement with the experimental results. With increasing electron-withdrawing nature of the acceptor end groups, absorption red-shifts, both computationally and experimentally. We were also interested to find out if the red-shift was also due to extension of conjugation. Thus, we analyzed vinyl (D-vinyl) and vinyl-dialkynyl (D-vinyl-dialkynyl) end groups (see Scheme 1.1 for structures and Figure 1.5 for absorption spectra) due to their structural similarity to the aldehyde and ethylenemalononitrile functional groups, respectively. Our calculations revealed that the oscillator strength maximum for the aldehyde-functionalized small molecule (D-CHO) is almost the same as the one for the one functionalized

with vinyl (D-vinyl), while there is a 47 nm difference between D-vinyl-dialkynyl and D-M. This led us to conclude that, indeed, extension of conjugation red-shifts the absorption. However, the electron-withdrawing nature of the functional group is the one that plays a dominant role in red-shifting the absorption.

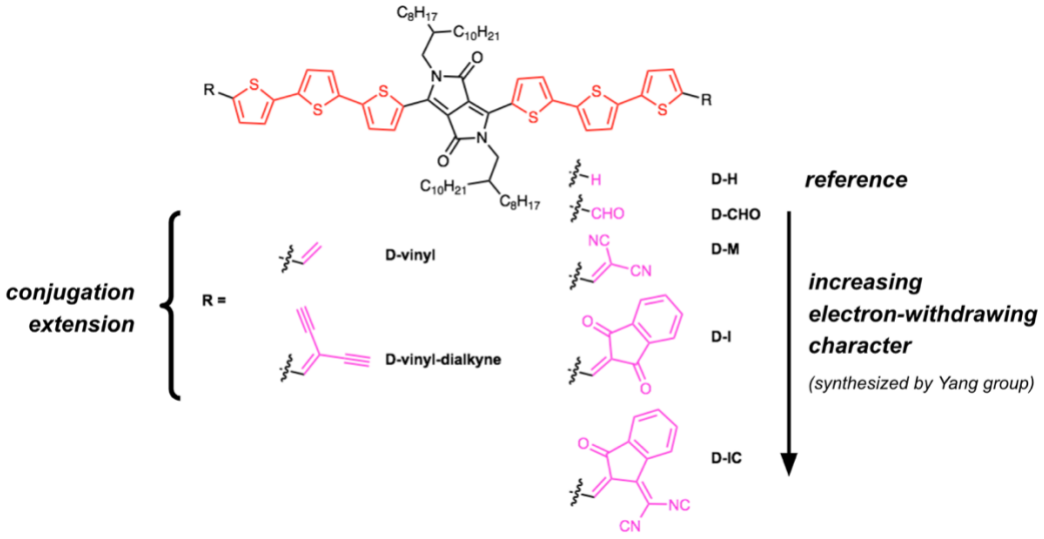

Scheme 1.1. Library of chemical structures of linear small molecule acceptors with varying functional groups.

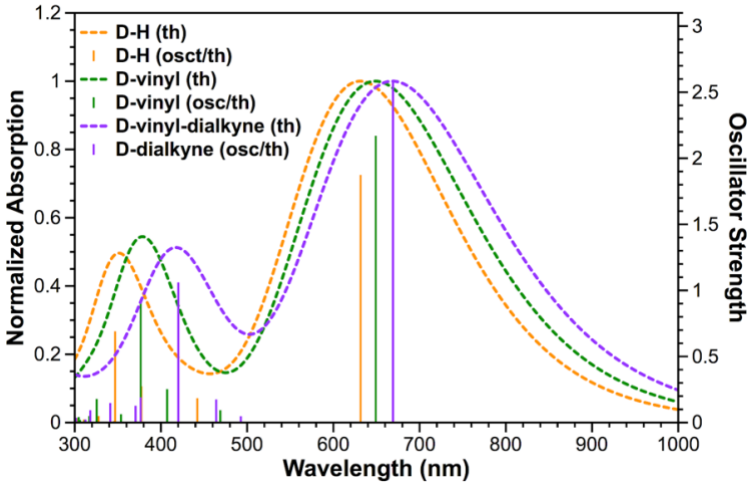

Func. group	Th. osc. str. max (nm)	Exp. λmax (nm)
H	632	
CHO	648	599
M	716	646
I	703	624
IC	785	691
vinyl	649	
dialkyne	669	

Figure 1.5. Computed absorption spectra of additional small molecules. (left) Theoretical oscillators strengths (vertical solid lines) and absorption spectra (dotted line) of D-H (orange), D-vinyl (green) and D-vinyl-dialkynyl (purple) in chloroform; (right) table of calculated and experimental absorption values for all linear small molecules. Red and black arrows indicate the functional end groups that are similar in π-systems.

1.3.2. Intermolecular interactions

In addition to diketopyrrolopyrrole-based small molecules discussed earlier, the Yang group has synthesized and successfully crystallized m-ITIC-OR-4Cl (Figure 1.6), a promising small molecule acceptor for OPVs. With a goal of assessing the *inter*molecular interactions (Figure 1.6), a TD-DFT analysis was performed on a monomer and dimer of m-ITIC-OR-4Cl, as shown in Figure 1.7.

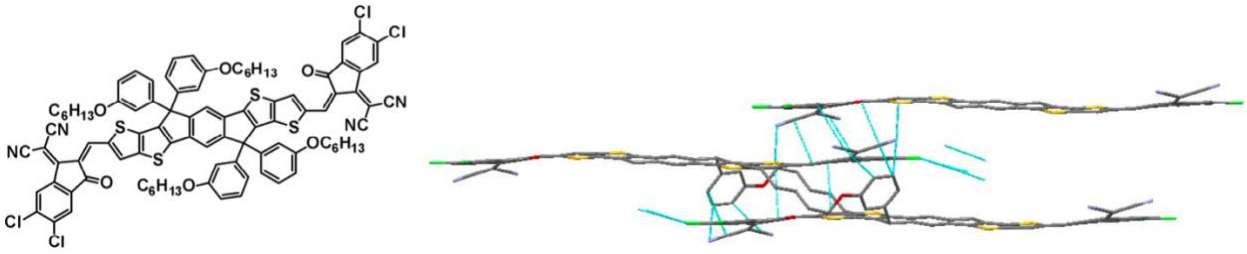

Figure 1.6. Chemical structure (left) and crystal packing of m-ITIC-OR-4Cl (right).

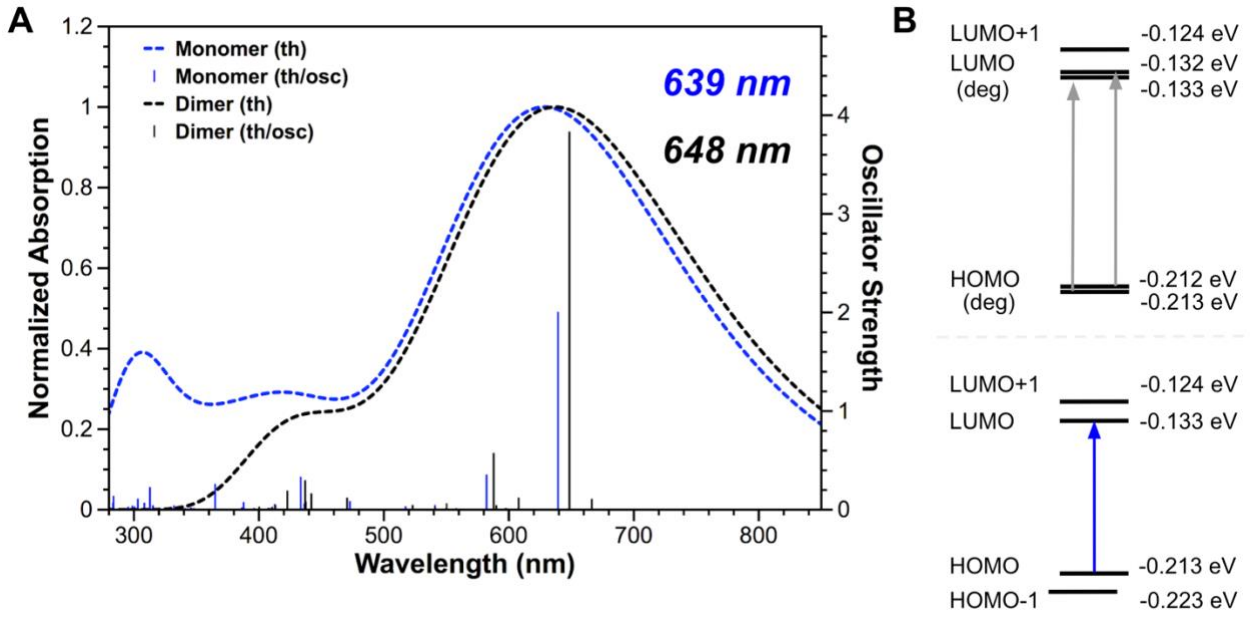

Figure 1.7. Computed TD-DFT absorption spectra of monomer (blue) and dimer (black) of m-ITIC-OR-4Cl in gas phase. (A) Theoretical absorption (dotted lines) and oscillator strengths (vertical solid lines) with the wavelength of strongest ones indicated on top right corner and (B) corresponding energy levels of molecular frontier orbitals with arrows depicting the respective absorption of the strongest oscillator strengths.

Figure 1.8 shows the computed HOMO and LUMO orbitals of m-ITIC-OR-4Cl monomer and dimer. In the monomer, we observed an even distribution of orbitals along the conjugated plane, whereas upon dimerization the HOMO shifts slightly toward the core of the molecule and the LUMO shifts significantly toward the ends of the molecule. There is also a slight red-shift in absorption maxima by 10 nm upon dimerization.

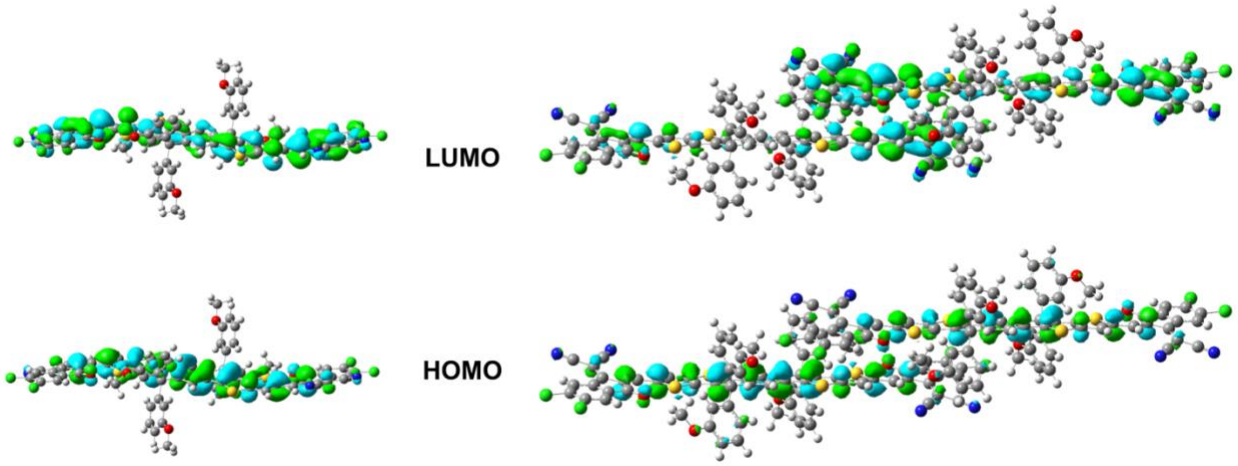

Figure 1.8. LUMO (top) and HOMO (bottom) orbitals of m-ITIC-OR-4Cl monomer (left) and dimer (right). Dimer has additional HOMO-1 and LUMO+1 orbitals that are degenerate to HOMO and LUMO orbitals. Green and blue colors indicate different phases of orbitals.

1.4. References

(1) Li, G.; Zhu, R.; Yang, Y. *Nat. Photonics* **2012**, *6*, 153–161.

(2) Liu, Q.; Jiang, Y.; Jin, K.; Qin, J.; Xu, J.; Li, W.; Xiong, J.; Liu, J.; Xiao, Z.; Sun, K.; Yang, S.; Zhang, X.; Ding, L. *Sci. Bull.* **2020**, *65*, 272–275.

(3) Ye, L.; Hu, H.; Ghasemi, M.; Wang, T.; Collins, B. A.; Kim, J.-H.; Jiang, K.; Carpenter, J. H.; Li, H.; Li, Z.; McAfee, T.; Zhao, J.; Chen, X.; Lai, J. L. Y.; Ma, T.; Brédas, J.-L.; Yan, H.; Ade, H. *Nat. Mater.* **2018**, *17*, 253–260.

(4) Ran, N. A.; Roland, S.; Love, J. A.; Savikhin, V.; Takacs, C. J.; Fu, Y.-T.; Li, H.; Coropceanu, V.; Liu, X.; Brédas, J.-L.; Bazan, G. C.; Toney, M. F.; Neher, D.; Nguyen, T.-Q. *Nat. Commun.* **2017**, *8*, 79.

(5) Kong, J.; Song, S.; Yoo, M.; Lee, G. Y.; Kwon, O.; Park, J. K.; Back, H.; Kim, G.; Lee, S. H.; Suh, H.; Lee, K. *Nat. Commun.* **2014**, *5*, 5688.

(6) *Schrödinger Release 2019-1:* Maestro, Schrödinger, LLC, New York, NY, **2019**.

(7) *GaussView*, Version 5, Dennington, R.; Keith, T. A.; Millam, J. M. Semichem Inc., Shawnee Mission, KS, **2008**.

(8) *Gaussian 09*, Revision D.01, Frisch, M. J.; Trucks, G. W.; Schlegel, H. B.; Scuseria, G. E.; Robb, M. A.; Cheeseman, J. R.; Scalmani, G.; Barone, V.; Mennucci, B.; Petersson, G. A.; Nakatsuji, H.; Caricato, M.; Li, X.; Hratchian, H. P.; Izmaylov, A. F.; Bloino, J.; Zheng, G.; Sonnenberg, J. L.; Hada, M.; Ehara, M.; Toyota, K.; Fukuda, R.; Hasegawa, J.; Ishida, M.; Nakajima, T.; Honda, Y.; Kitao, O.; Nakai, H.; Vreven, T.; Montgomery, J. A. Jr.; Peralta, J. E.; Ogliaro, F.; Bearpark, M.; Heyd, J. J.; Brothers, E.; Kudin, K. N.; Staroverov, V. N.; Keith, T.; Kobayashi, R.; Normand, J.; Raghavachari, K.; Rendell, A.; Burant, J. C.; Iyengar, S. S.; Tomasi, J.; Cossi, M.; Rega, N.; Millam, J. M.; Klene, M.; Knox, J. E.; Cross, J. B.;

Bakken, V.; Adamo, C.; Jaramillo, J.; Gomperts, R.; Stratmann, R. E.; Yazyev, O.; Austin, A. J.; Cammi, R.; Pomelli, C.; Ochterski, J. W.; Martin, R. L.; Morokuma, K.; Zakrzewski, V. G.; Voth, G. A.; Salvador, P.; Dannenberg, J. J.; Dapprich, S.; Daniels, A. D.; Farkas, O.; Foresman, J. B.; Ortiz, J. V.; Cioslowski, J.; Fox, D. J. *Gaussian, Inc*., Wallingford CT, **2013**.

(9) Wesemann, M. *Plot2* software available at: https://apps.micw.org/apps/plot2/, *Accessed on: April 25, 2021*.

Chapter 2. Radical Formation in a Novel Hole-Transport Material for Perovskite Solar Cells

2.1. Background

In recent years, the emergence and rapid advancement of perovskite solar cells (PSCs) and their power conversion efficiencies (PCE) have attracted global attention of photovoltaic research community and industry. In addition to photoelectric properties, PSCs boast facile processability, cost-effective fabrication and scalability.[1-4] Generally, PSCs consist of transparent top electrode, electron transport layer (ETL), perovskite active layer, hole transport layer (HTL) and bottom electrode. Carriers are created in the active layer after absorption of incident photons and travel through corresponding transport layer.

In order to achieve high performance in PSCs, a HTL material needs to have efficient hole transport properties.[5-6] One of the most commonly used HTLs in state-of-the-art PSCs is 2,2′,7,7′-tetrakis[N,N-di(4methoxyphenyl)amino]-9,9′-spirobiuorene, Spiro-MeOTAD (Figure 2.1A), due to its solution processability, amorphous nature, adequate energy level and high melting point.[7] The conductivity and hole mobility of Spiro-MeOTAD without dopants are very low (~10^{-5} S cm^{-2} and 10^{-4} cm^2 V^{-1} S^{-1}, respectively), which is destructive to performance of the PSC.[5,7] In order to improve the mobility of HTM and consequently the performance of PSC, Spiro-MeOTAD is often doped with *tert*-butylpyridine (*t*BP) and lithium bis(trifluoromethanesulfonyl)imide (Li-TFSI). *t*BP is known to prevent phase segregation of Spiro-OMeTAD, yielding a homogenous layer.[9] However, addition of these dopants was found to also induce slight degradation of perovskite active layer over time.[10] The dopants increase the hydrophilicity of the Spiro-MeOTAD, which in turn facilitates absorption and diffusion of external moieties into the perovskite layer. This process damages the perovskite layer, which has inherent ionic character,

leading to ultimate degradation of the entire solar cell device and threat to its long-term stability.[11-14] Beside the disadvantages of dopants, high cost, poor device stability and tedious synthesis process[12,15] overall still limit Spiro-MeOTAD's practical applications necessitating new alternative materials for hole transport layer.

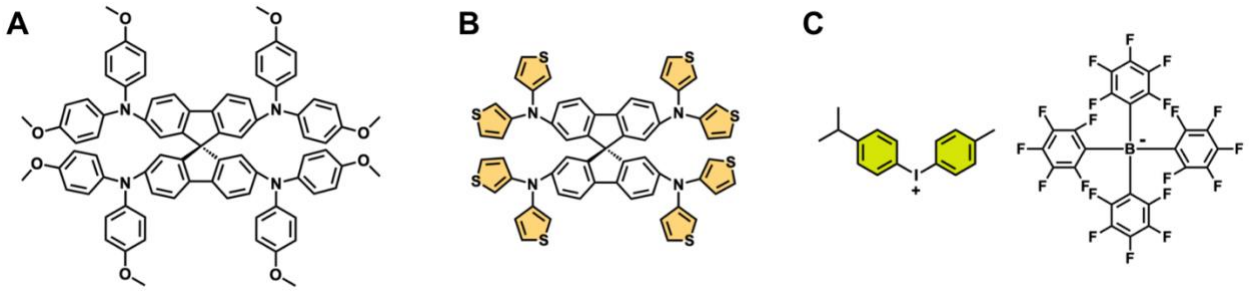

Figure 2.1. Hole transport materials: (A) Spiro-OMeTAD, (B) Spiro-8Th, and (C) DPI-TPFB.

Doped Spiro-8Th (Figure 2.1B), recently developed by the Yang group, is a promising HTM candidate for PSCs. The methoxyphenyl groups of Spiro-OMeTAD are substituted with thiophene in Spiro-8Th allowing for enhanced interaction with the perovskite surface and increased mobility overall. The 4-isopropyl-4′-methyldiphenyliodonium tetrakis-(pentafluoro-phenyl)-borate (DPI-TPFB) was used as an organic p-dopant, offering the benefit of increased stability over the inorganic lithium dopants.[6,16] DPI-TPFB is an ionic dopant consisting of iodonium-based cation (DPI) and boron-based anion (TPFB).

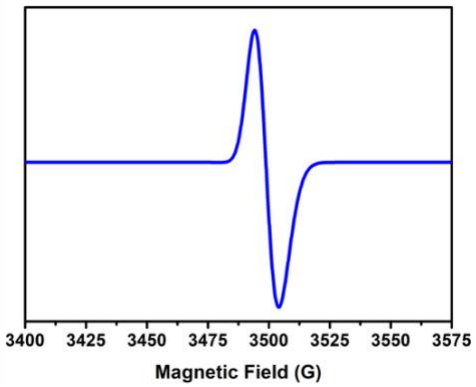

Figure 2.2. Experimental EPR spectrum of Spiro-8Th measured at 298 K.

During sample preparation, the Yang group has noticed a sudden color change of the DPI-TPFB solution in chlorobenzene from transparent to yellow to brown to a deep red color upon addition of it into the Spiro-8Th solution in chlorobenzene. This observation led to discovery of radical formation in the DPI-TPFB-doped Spiro-8Th, as was later confirmed by the electron paramagnetic resonance spectroscopy (EPR) measurement shown in Figure 2.2.

Occurrence of radicals in HTL of PSCs has been reported before. For example, PEDOT:PSS, an organic polymer used in HTL, was doped with dopamine semiquinone forming numerous radical cations in the backbone, which in turn resulted in better charge extraction from the perovskite layer into the HTL.[17] More notably, Sellinger *et al.* recently developed carbazole-based EH44/EH44-oz HTL, where EH44 is doped with its oxidized $TFSI^-$ salt, EH44-oz.[18,19] While EH44-based devices demonstrated noteworthy stability maintaining 94% of PCE over 1000 hours of continuous operation, the PCEs of these devices were generally lower than those of lithium-doped HTLs. Moreover, a significant degradation was observed at elevated temperatures possibly due to EH44's low glass transition temperature.[10,18] While radical formation and stabilization are often mentioned as a strong contributor towards enhanced stability in aforementioned studies, the insights into the mechanism of radical formation in HTL of PSCs are yet to be delineated.

We now report the design of a novel hole-transport material, Spiro-8Th, doped with organic ionic DPI-TPFB complex that generates radicals in the HTL leading to enhanced performance and stability over the commonly used Li-doped Spiro-OMeTAD. Computational studies further delineate the mechanism of radical formation in doped Spiro-8Th, where the electron is transferred from amine group of Spiro-8Th to iodonium of DPI dopant.

2.2. Methodology

2.2.1. Synthesis of Spiro-8Th by the Yang group

A mixture of 2,2′,7,7′-tetraamino-9,9′-spirobifluorene (500 mg, 1.33 mmol), NaO*t*-Bu (2.81 g, 29.2 mmol) and $Pd[P(t\text{-}Bu)_3]_2$ (136 mg, 0.27 mmol) was added to toluene (100 mL). 3-bromothiophene (2.6 mL, 26.6 mmol) was subsequently added and the resulting mixture was stirred at 100 °C for 48 h under argon atmosphere. Upon cooling to room temperature, H_2O (100 mL) was added to the mixture, followed by extraction with dichloromethane (3×150 mL). The organic phase was dried over $MgSO_4$ and concentrated under reduced pressure. The purification of the product was achieved through column chromatography (silica gel, 3:2, hexane/dichloromethane), yielding a faint yellow solid as the product (1.26 g, 92%), which was further dissolved in a small amount of dichloromethane and recrystallized in methanol.

2.2.2. EPR characterization details

EPR spectra were measured at room temperature on an EMXplus Bruker spectrometer equipped with an ER4119HS high sensitivity microwave resonator. The spectra were taken in two different configurations. In the first configuration, the samples were in the resonator, which was completely enclosed so that no visible light could reach the samples. In the second configuration, the top and front windows of the resonator were opened, and a small incandescent lamp (15 W) was placed close to the window, illuminating the sample with a visible light. Before taking the spectrum of a sample, the spectrum of the holding quartz tube was recorded to ensure that no signal is produced. The sample was placed in the quartz tube, which was then inserted in the center of the EPR resonator. Spectra were acquired using a sweep time of 30 s, sweep width of 200 G, center field of 3480 G, microwave power of 6.33 mW and modulation amplitude of 4.0 G.

2.2.3. Computational details

All singlet structures were pre-optimized with a very tight GFN2-xTB method using xTB program (version 6.2)[20-22] prior to conformational search. Conformational analysis of each structure was performed using metadynamic sampling in extended tight binding Conformer–Rotamer Ensemble Sampling Tool (xtb CREST) program package (version 6.2).[23-24] iMTD-GC workflow was used for conformational search algorithm with 6 kcal/mol energy and 0.5 Å RMSD thresholds at 298 K.

All density functional theory (DFT) calculations were performed using Gaussian16.[25] Geometry optimization and frequency calculations of all singlets and doublets were completed with B3LYP method and LANL2DZ basis set for iodine and 6-31G(d) for all other atoms in the gas phase. Optimized structures were verified by frequency calculations as minima (zero imaginary frequencies) and doublets were verified to be radicals based on total spin $<S^2>$ value. HOMO-LUMO energies were extracted from a single-point calculation using B3LYP method and LANL2DZ basis set for iodine and 6-31+G(d,p) for all other atoms and plotted with GaussView 6.0.16.[26] Similarly spin density distribution and values of each atom were computed with M06-2X method and LANL2DZ basis set for iodine and 6-31+G(d,p) for all other atoms and plotted with GaussView 6.0.16.

2.3. Results and Discussion

2.3.1. Transport properties of doped Spiro-8Th and its performance and stability in photovoltaics

The hole transporting ability of the hole transport materials was examined using space charge-limited-current (SCLC) method. Fitting the J-V curve of the hole-only devices

(ITO/Ag/hole transport material/Ag), the hole mobility of DPI-TPFB-doped Spiro-8th is determined to be 1.17×10^{-2} cm^2 V^{-1} s^{-1} (see Table 2.1), which is significantly higher than that of the Li-doped Spiro-OMeTAD (6.04×10^{-3} cm^2 V^{-1} s^{-1}).

Table 2.1. Hole mobilities of doped Spiro-MeOTAD and Spiro-8Th.

	Hole mobility μ_h (cm^2 V^{-1} s^{-1})
Li-doped Spiro-MeOTAD	6.04×10^{-3}
DPI-TPFB-doped Spiro-8Th	1.17×10^{-2}

We then fabricated the devices incorporated with either doped Spiro-8Th or doped Spiro-OMeTAD for HTL with SnO_2/$FAPbI_3$/DPI-TPFB-doped Spiro-8Th/Au architecture, the measured photovoltaic parameters of which are summarized in Table 2.2. Due to higher hole mobility and superior charge extraction capability, distinct improvements of open-circuit voltage (V_{oc}), short-circuit current (J_{sc}) and fill-factor (FF) can be observed in the device with Spiro-8Th used as the HTL compared with the Li-doped Spiro-OMeTAD. This led to enhanced PCE of 22.01%. Doping of Spiro-OMeTAD with DPI-TPFB, on the other hand, degraded the device performance to 15.19% most likely due to its lower mobility.

Table 2.2. Photovoltaic parameters of various doped HTMs in a perovskite solar cell.

	V_{oc} (V)	J_{sc} (mA/cm^2)	FF (%)	Eff (%)
Li-doped Spiro-MeOTAD	1.105	24.52	75.07	20.34
DPI-TPFB-doped Spiro-8Th	1.133	25.58	75.94	22.01
DPI-TPFB-doped Spiro-MeOTAD	1.051	23.17	62.38	15.19

We also monitored the long-term thermal and photo stability of devices with either doped Spiro-8Th or doped Spiro-OMeTAD as HTL. In addition to enhanced photovoltaic performance, devices with doped Spiro-8Th showed remarkable thermal stability at 85 °C under N_2 gas in glove box (see Figure 2.3) retaining >80% of its initial PCE for over 1000 h, while reference device with Spiro-OMeTAD completely degraded after 400 h. A similar behavior and trend were observed in photo-stability studies, where devices with doped Spiro-8Th as HTL maintained >75% of its PCE for over 1000 h, while doped Spiro-OMeTAD one underwent through complete degradation after 350 h.

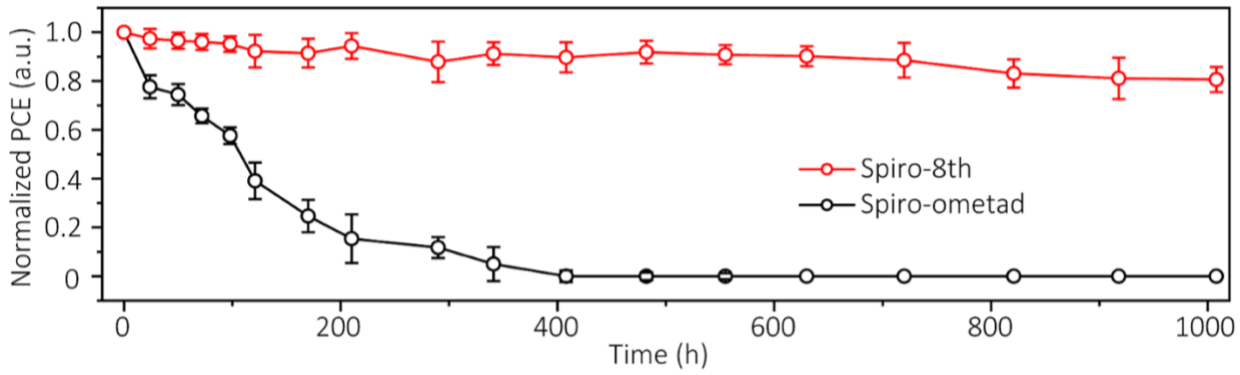

Figure 2.3. Long-term thermal stability of PSC devices with DPI-TPFB-doped Spiro-8Th and Li-doped Spiro-OMeTAD under N_2 gas in glove box at 85 °C.

2.3.2. Theoretical investigation of radical formation in doped Spiro-8Th

Spiro-8Th, TPFB and DPI were first optimized in their singlet state (Figure 2.4). The two planar branches of Spiro-8Th connected *via* a spiro atom adopt a 90° angle to each other, as it can be seen from the top view, while DPI shows a bent 102° bond angle between two branches connected *via* iodonium.

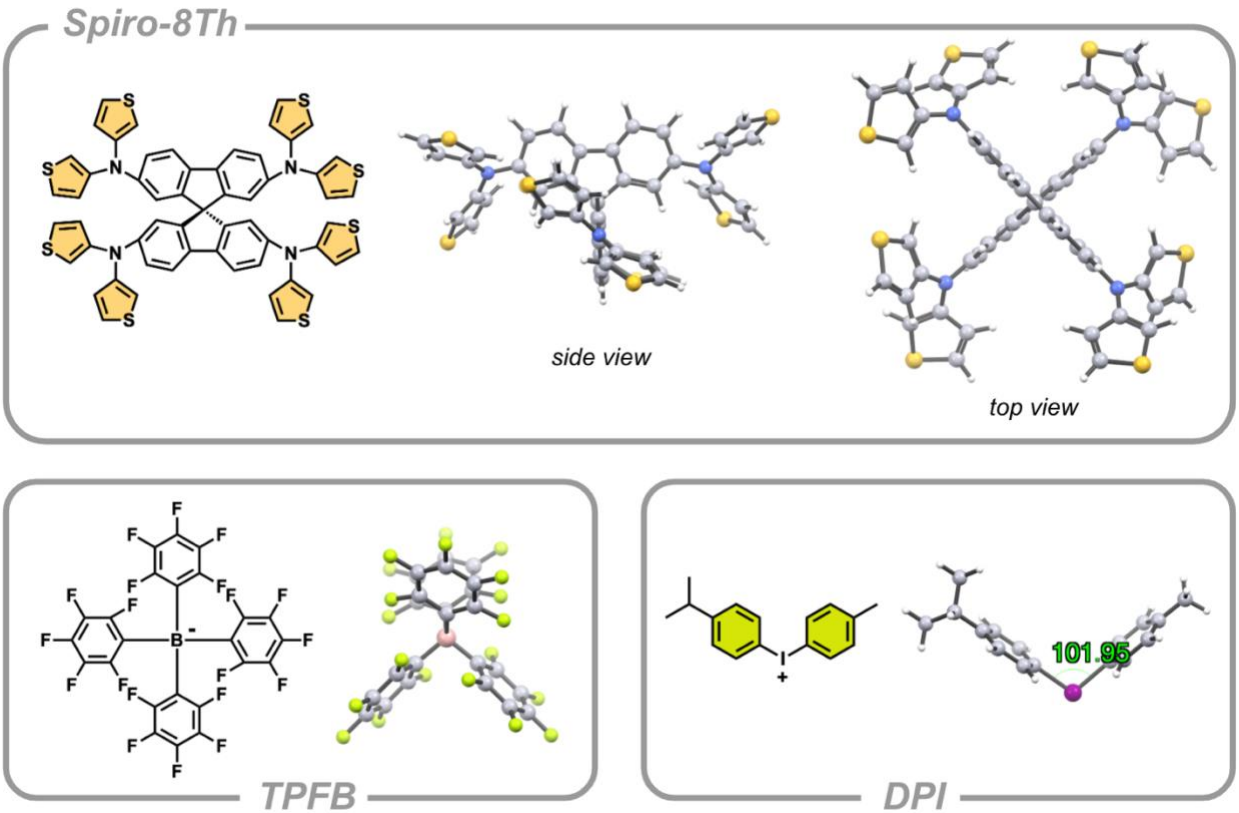

Figure 2.4. Optimized structures of Spiro-8Th, TPFB and DPI in their singlet state using B3LYP method and LANL2DZ basis set for iodine and 6-31G(d) for all other atoms.

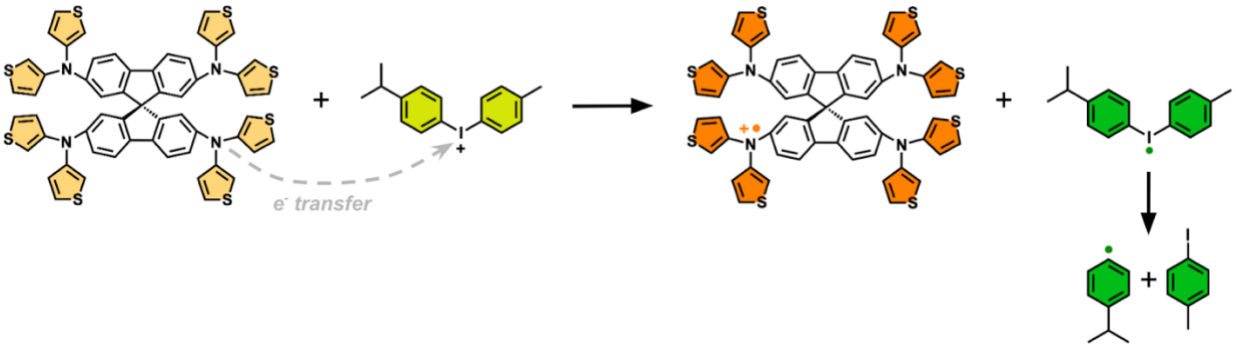

Figure 2.5. Radical formation mechanism in doped Spiro-8Th. Electron transfer from tertiary amine of Spiro-8Th to DPI iodonium salt resulting in radical cation Spiro-8Th and iodyl radical DPI, which further decomposes into aryl radical and *p*-iodotoluene.

We further hypothesized that the electron transfer happens from tertiary amine of Spiro-8Th to iodonium of DPI, as shown in Figure 2.5, resulting in oxidation of Spiro-8Th into radical

cation and reduction of DPI iodonium salt into the iodyl radical. However, upon optimization of DPI iodyl radical, we found that it was short-lived and decomposed further into aryl radical and *p*-iodotoluene. An overall electron transfer from Spiro-8Th to DPI and further decomposition of DPI iodyl radical was calculated to be thermodynamically highly favorable with electronic energy of -10.1 kcal/mol and Gibbs free energy of -23.6 kcal/mol using DFT. The electron transfer into iodonium and further decomposition behavior is not unseen in the literature. Strehmel *et al*, for example, reported a similar reactivity of iodonium salts as a result of a near-infrared initiated radical polymerization using a sensitizer.[27]

In order to further assess the feasibility of electron transfer, we computed the energy levels of frontier orbitals of Spiro-8Th and DPI iodonium salt (see Figure 2.6). The computed HOMO-LUMO energies of Spiro-8Th at -1.4 and -5.0 eV, respectively, compare well with experimental values of -2.8 and -5.2 eV, respectively. The HOMO energy level of Spiro-8Th is only slightly higher than the LUMO energy level of DPI, which facilitates the favorable electron transfer from Spiro-8Th to the iodonium salt.

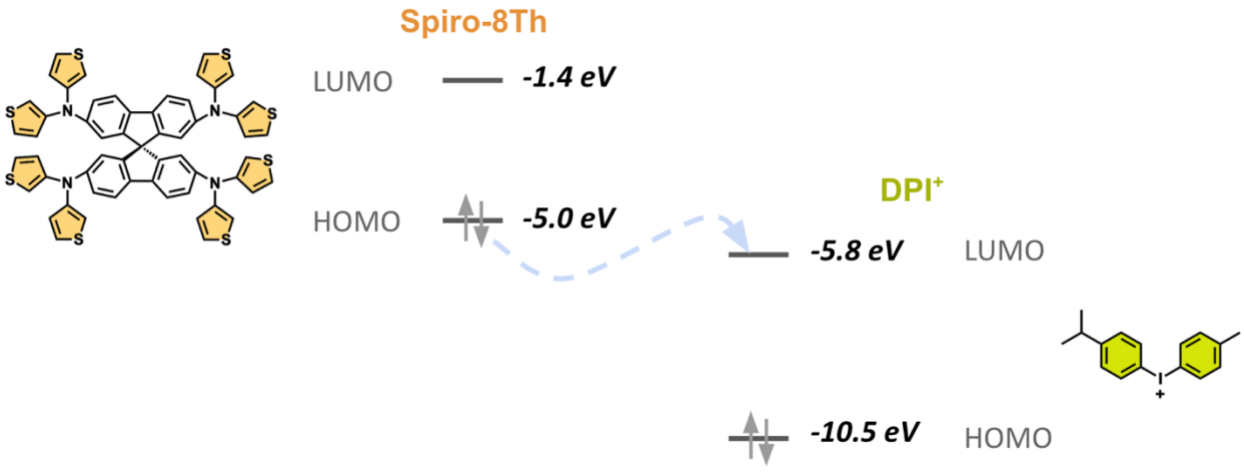

Figure 2.6. Energy levels of frontier orbitals of Spiro-8Th and DPI. HOMO-LUMO energies were computed using B3LYP method and LANL2DZ basis set for iodine and 6-31+G(d,p) for all other atoms. Dashed arrow indicates electron transfer from HOMO of Spiro-8Th to LUMO of DPI.

Spin density distribution of radical cation Spiro-8Th, DPI iodyl radical and isopropylbenzene radical, a by-product of iodyl radical decomposition, were computed as well and are shown in Figure 2.7. The highest spin density in Spiro-8Th radical cation is located on tertiary amine (Figure 2.7A), which indicates the most favorable atom for oxidation, and the density is delocalized throughout the linear branch *via* conjugation. The highest spin density on iodyl radical is found on the iodonium atom (Figure 2.7B) that is most likely to be reduced, with the radical delocalized over adjacent benzenes. An additional spin density analysis was performed on a simplified model of DPI, namely the iodyl radical (H_2I), which confirmed the electron transfer into the *d* orbital of DPI (insert of Figure 2.7B). Similarly, in isopropylbenzene radical (Figure 2.7C), the radical localizes on the unsaturated carbon in *para* position relative to the propyl group.

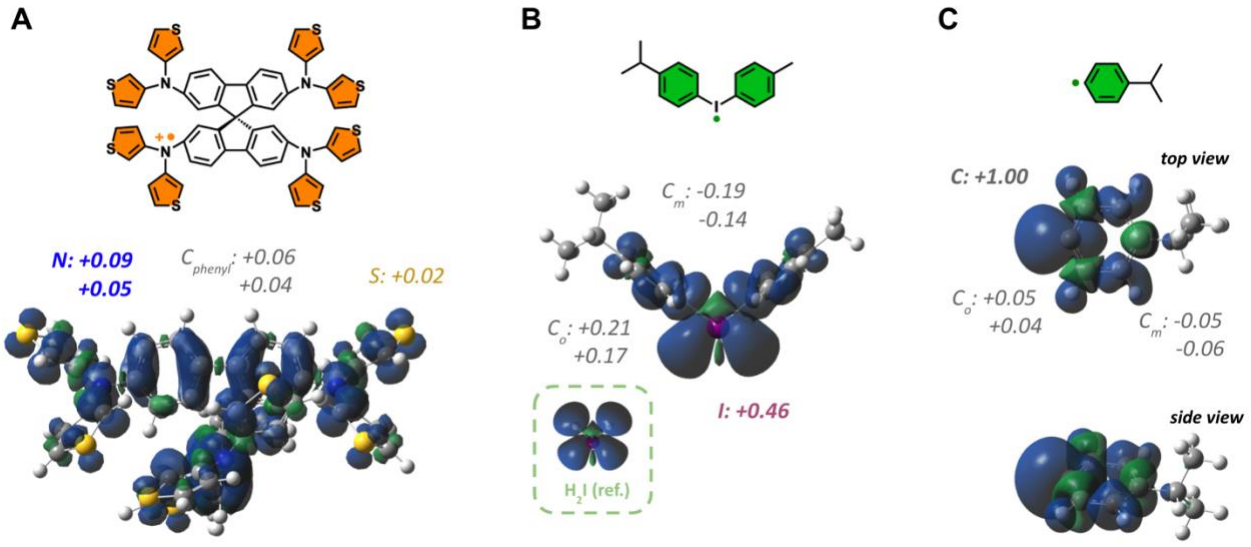

Figure 2.7. Spin density distribution in Spiro-8Th and the dopant salt computed with M06-2X method and LANL2DZ basis set for iodine and 6-31+G(d,p) for all other atoms. Spin density distribution in (A) Spiro-8Th radical cation, (B) DPI iodyl radical and (C) isopropylbenzene radical, a by-product of DPI iodyl radical decomposition. Top relative spin density values are also shown, with atoms of highest spin density values in bold. An inset in (B) depicts the spin density of H_2I that is used as a simplified model reference for DPI iodyl radical.

2.4. Conclusion

Low-cost novel DPI-TPFB-doped Spiro-8Th have been designed and fabricated into devices for significantly improving the hole mobility of HTL and enhancing the PSC's performance and stability. Devices with our Spiro-8Th formulation for HTL demonstrated increased PCE of 22.01% and long-term stability of retaining >80% of its initial PCE for over 1000 h. We speculate that the enhanced performance is due to formation of radicals as a result of doping with DPI-TPFB dopant, while the improved stability is because of organic nature of the dopant. Computational efforts reveal that the radical is formed as a result of electron transfer from the amine group of Spiro-8Th to iodonium of DPI cation, further causing the decomposition of DPI cation radical. These in-depth insights into the structure of effective hole-transport material and its dopant formulation inspired by the electron transfer and radical formation will guide pathways towards further improvement and commercialization of perovskite photovoltaics.

2.5. References

(1) Roy, P.; Kumar Sinha, N.; Tiwari, S.; Khare, A. *Sol. Energy* **2020**, *198*, 665–688.

(2) Li, N.; Niu, X.; Chen, Q.; Zhou, H. *Chem. Soc. Rev.* **2020**, *49*, 8235–8286.

(3) Rong, Y.; Hu, Y.; Mei, A.; Tan, H.; Saidaminov, M. I.; Seok, S. Il; McGehee, M. D.; Sargent, E. H.; Han, H. *Science* **2018**, *361*, eaat8235.

(4) Zhou, D.; Zhou, T.; Tian, Y.; Zhu, X.; Tu, Y. *J. Nanomater.* **2018**, *2018*, 8148072.

(5) Bakr, Z. H.; Wali, Q.; Fakharuddin, A.; Schmidt-Mende, L.; Brown, T. M.; Jose, R. *Nano Energy* **2017**, *34*, 271–305.

(6) Calió, L.; Kazim, S.; Grätzel, M.; Ahmad, S. *Angew. Chem. Int. Ed.* **2016**, *55*, 14522–14545.

(7) Hawash, Z.; Ono, L. K.; Qi, Y. *Adv. Mater. Interfaces* **2018**, *5*, 1700623.

(8) Leijtens, T.; Ding, I.-K.; Giovenzana, T.; Bloking, J. T.; McGehee, M. D.; Sellinger, A. *ACS Nano* **2012**, *6*, 1455–1462.

(9) Juarez-Perez, E. J.; Leyden, M. R.; Wang, S.; Ono, L. K.; Hawash, Z.; Qi, Y. *Chem. Mater.* **2016**, *28*, 5702–5709.

(10) Schloemer, T. H.; Christians, J. A.; Luther, J. M.; Sellinger, A. *Chem. Sci.* **2019**, *10*, 1904–1935.

(11) Tan, B.; Raga, S. R.; Chesman, A. S. R.; Fürer, S. O.; Zheng, F.; McMeekin, D. P.; Jiang, L.; Mao, W.; Lin, X.; Wen, X.; Lu, J.; Cheng, Y.-B.; Bach, U. *Adv. Energy Mater.* **2019**, *9*, 1901519.

(12) Rakstys, K.; Igci, C.; Nazeeruddin, M. K. *Chem. Sci.* **2019**, *10*, 6748–6769.

(13) Spalla, M.; Perrin, L.; Planes, E.; Matheron, M.; Berson, S.; Flandin, L. *ACS Appl. Energy Mater.* **2020**, *3*, 3282–3292.

(14) Yue, Y.; Salim, N.; Wu, Y.; Yang, X.; Islam, A.; Chen, W.; Liu, J.; Bi, E.; Xie, F.; Cai, M.; Han, L. *Adv. Mater.* **2016**, *28*, 10738–10743.

(15) Shi, Y.; Xue, Y.; Hou, K.; Meng, G.; Wang, K.; Chi, R.; Chen, F.; Ren, H.; Pang, M.; Hao, C. *RSC Adv.* **2016**, *6*, 96990–96996.

(16) Qin, P.; Tanaka, S.; Ito, S.; Tetreault, N.; Manabe, K.; Nishino, H.; Nazeeruddin, M. K.; Grätzel, M. *Nat. Commun.* **2014**, *5*, 3834.

(17) Xue, Q.; Liu, M.; Li, Z.; Yan, L.; Hu, Z.; Zhou, J.; Li, W.; Jiang, X.-F.; Xu, B.; Huang, F.; Li, Y.; Yip, H.-L.; Cao, Y. *Adv. Funct. Mater.* **2018**, *28*, 1707444.

(18) Christians, J. A.; Schulz, P.; Tinkham, J. S.; Schloemer, T. H.; Harvey, S. P.; Tremolet de Villers, B. J.; Sellinger, A.; Berry, J. J.; Luther, J. M. *Nat. Energy* **2018**, *3*, 68–74.

(19) Gao, L.; Schloemer, T. H.; Zhang, F.; Chen, X.; Xiao, C.; Zhu, K.; Sellinger, A. *ACS Appl. Energy Mater.* **2020**, *3*, 4492–4498.

(20) Grimme, S.; Bannwarth, C.; Shushkov, P. *J. Chem. Theory Comput.* **2017**, *13*, 1989–2009.

(21) Bannwarth, C.; Ehlert, S.; Grimme, S. *J. Chem. Theory Comput.* **2019**, *15*, 1652–1671.

(22) Pracht, P.; Caldeweyher, E.; Ehlert, S.; Grimme, S. *ChemRxiv*, **2019**.

(23) Grimme, S.; Bannwarth, C.; Dohm, S.; Hansen, A.; Pisarek, J.; Pracht, P.; Seibert, J.; Neese, F. *Angew. Chem. Int. Ed.* **2017**, *56*, 14763–14769.

(24) Grimme, S. *J. Chem. Theory Comput.* **2019**, *15*, 2847–2862.

(25) *Gaussian 16*, Revision A.03, Frisch, M. J.; Trucks, G. W.; Schlegel, H. B.; Scuseria, G. E.; Robb, M. A.; Cheeseman, J. R.; Scalmani, G.; Barone, V.; Petersson, G. A.; Nakatsuji, H.; Li, X.; Caricato, M.; Marenich, A. V.; Bloino, J.; Janesko, B. G.; Gomperts, R.; Mennucci, B.; Hratchian, H. P.; Ortiz, J. V.; Izmaylov, A. F.; Sonnenberg, J. L.; Williams-Young, D.; Ding, F.; Lipparini, F.; Egidi, F.; Goings, J.; Peng, B.; Petrone, A.; Henderson, T.;

Ranasinghe, D.; Zakrzewski, V. G.; Gao, J.; Rega, N.; Zheng, G.; Liang, W.; Hada, M.; Ehara, M.; Toyota, K.; Fukuda, R.; Hasegawa, J.; Ishida, M.; Nakajima, T.; Honda, Y.; Kitao, O.; Nakai, H.; Vreven, T.; Throssell, K.; Montgomery, J. A., Jr.; Peralta, J. E.; Ogliaro, F.; Bearpark, M. J.; Heyd, J. J.; Brothers, E. N.; Kudin, K. N.; Staroverov, V. N.; Keith, T. A.; Kobayashi, R.; Normand, J.; Raghavachari, K.; Rendell, A. P.; Burant, J. C.; Iyengar, S. S.; Tomasi, J.; Cossi, M.; Millam, J. M.; Klene, M.; Adamo, C.; Cammi, R.; Ochterski, J. W.; Martin, R. L.; Morokuma, K.; Farkas, O.; Foresman, J. B.; Fox, D. J. Gaussian, Inc., Wallingford CT, **2016**.

(26) *GaussView*, Version 6, Dennington, R.; Keith, T. A.; Millam, J. M. Semichem Inc., Shawnee Mission, KS, **2016**.

(27) Brömme, T.; Oprych, D.; Horst, J.; Pinto, P. S.; Strehmel, B. *RSC Adv.* **2015**, *5*, 69915–69924.

Chapter 3. Noncovalent π-stacked Robust Topological Organic Framework

3.1. Background

The emergence of organic semiconductors has sparked development of organic solar cells,[1-4] sensors,[5-7] flexible displays[8-10] and optical devices.[11-13] In addition to low cost, one of the most attractive properties of organic electronic materials is their adjustability via facile chemical modifications to different device requirements. Advanced experimental and computational tools have been developed to provide insights into organic semiconductors' structure–property relationship and consequently predict their electronic properties. However, for efficient charge transport in organic semiconductors, controlled large-scale assembly is one of the more critical aspects and is challenging to achieve. The rise of organic frameworks (OFs) has opened a path for determining and controlling the molecular assembly, especially in covalent OFs (COFs).[14-17] The final COF topology can now be ascertained based on the relative geometries of raw materials. However, insolubility of COF and poor electrical conductivity of covalent bonds still limit COFs practical applications in organic electronics. Moreover, the irreversibility of covalent bonds deprives COF of the likelihood for self-healing using simple methods.

It is well established that in a two-dimensional (2D) in-plane direction the transport along the π···π network is considered to be a key transport mechanism in organic semiconductors, which would lay the foundation for high-performance devices. Moreover, with a simple heat treatment the noncovalent π···π interaction is easily repairable due to its "soft" property. However, because of the intrinsic features of noncovalent π···π interactions (flexible, weak and poor directionality), direct construction of porous framework with a permanent porosity is difficult, as the structure will most probably collapse after solvent removal and decompose upon heating. Thus, pure intralayer noncovalent π···π interaction-constructed porous materials with an ordered structure kindle a

special interest. In this study, we accomplish to develop this material by increasing the π plane and enriching the effective overlapping area by intermolecular linking forces for a stable framework. Furthermore, the geometry of the middle core and the directional face-on packing of the end group yield a robust material with precise and predictable control.[18-23]

Here, we designed a three-dimensional (3D) organic framework, called πOF, based entirely on the noncovalent π···π interactions between SFIC molecules. This SFIC molecule consists of a biplanar conjugated cruciform-shaped spirobifluorene (SF) as the centroid core and 3-(dicyanomethylidene)indan-1-one (IC) as a multijoint fragment connecting adjacent molecules, which adopts a tetragonal-disphenoid-shaped molecular conformation and self-assembles into a 3D porous structure of πOF. In spite of the extremely labile noncovalent π···π interactions, πOF presented not only extremely high surface area (981.62 $m^2 \cdot g^{-1}$) and supramaximal micropore (1.69 nm) but also high thermal stability and recyclability, as shown by variable-temperature and recycling-test powder X-ray diffraction (PXRD) experiments. Additionally, following the heat treatment, πOF was able to self-heal and retrieve the parent porosity upon solvent annealing (methanol/chloroform) at room temperature. The activated powdered πOF demonstrated high N_2 and CO_2 adsorption capacity because of its pore-rich structure. πOF-based organic-field-effect transistor (OFET) also showed remarkable hole and electron transport abilities, which are ascribed to abundant π···π interactions in the structure. Theoretical computations suggest anisotropy in charge mobilities; π···π stacking consists of a strong transfer integral and both hole and electron mobilities are maximized in this transport direction.

3.2. Methodology

3.2.1. General procedure for synthesis of SFIC by Yang group

2-(3-oxo-2,3-dihydro-1H-inden-1-ylidene) malononitrile (112 mg, 0.575 mmol, 12 equivalents) and SF-CHO (100 mg, 0.048 mmol, 1 equivalent) were dissolved in $CHCl_3$ (35 mL), then pyridine (1 mL) was added under argon. The mixture was then refluxed for 18 h, cooled to room temperature, poured into CH_3OH (200 mL) and filtered. The crude product was purified with column chromatography using hexane/dichloromethane (1:1) as eluent to obtain pure SFIC as a black solid (120 mg, 90%).

3.2.2. Computational details

Atomistic morphologies and charge-transport in πOF are calculated using Molecular Dynamics (MD) and kinetic Monte Carlo (kMC) simulations, respectively. The supercell of SFIC was built from the duplications of the experimental unit-cell along a, b, c crystallographic directions. A supercell contained in total 576 SFIC molecules (217,152 atoms). For all MD simulations, AMBER software with GAFF force-fields for molecular mechanics parameters was employed. Partial atomic charges of πOF using RESP were obtained based on the Merz−Singh−Kollman (MSK) scheme from optimized geometries in the gas-phase using B3LYP/6-31G(d).[24] In the MD simulations, the supercell was first steadily heated from 0 K to 300 K in 2 ns, while the heavy-atom positions were restrained. The supercell was then relaxed for 2 ns at 300 K using a Langevin thermostat, after which a 2 ns equilibration run was performed with reduced restraint, with Berendsen barostat that maintained pressure at 1 atm.[25] In the end, all heavy-atom restraints were eliminated, and a final 20 ns production run was performed.

For charge-transport simulations, we used incoherent transport mechanism and computed hole and electron mobilities from the rate-based kinetic Monte Carlo simulations based on localized charge approximation. The electron ($A + A^- \rightarrow A^- + A$) and hole ($A + A^+ \rightarrow A^+ + A$) and transport rates were evaluated based on the non-adiabatic Marcus–Levich–Jortner (MLJ) expression including quantum-mechanical corrections:

$$k_{ij} = \frac{2\pi}{\hbar} J_{ij}^2 \frac{1}{\sqrt{4\pi\lambda_{\text{out}} k_B T}} \sum_v \exp[-S] \frac{S^v}{v!} \exp[-\frac{(\lambda_{\text{out}} + \Delta E_{ij} + v\hbar\omega)^2}{4\lambda_{\text{out}} k_B T}]$$

where J_{ij} is the transfer integral, S is the Huang-Rhys factor, $S = \lambda_i/\hbar\omega$ is the internal reorganization energy and $\hbar\omega$ is the mode frequency, λ_{out} is the external reorganization energy ($\lambda = \lambda_{in} + \lambda_{out}$), and $\Delta E_{ij} = E_i - E_j$ is site-energy difference. A value of 200 meV is used for both $\hbar\omega$ and λ_{out}.[26] The internal reorganization energies are calculated using: $\lambda_e = E^0(q^-) - E^0(q^0) + E^-(q^0) - E^-(q^-)$ *and* $\lambda_h = E^0(q^+) - E^0(q^0) + E^+(q^0) - E^+(q^+)$ at B3LYP/6-31G(d) level of theory. The internal reorganization energies of πOF were found to be 82 meV for both electron and hole transports, which yields a total 282 meV of reorganization energy. The binding energies of the π···π, x···x and CH···π dimers were calculated at B97D/6-31G(d,p) level of theory and using equation $E_{bind} = E_c - (E_a + E_b)$, where E_c is the energy of the complex, E_a and E_b are the corresponding monomers.

Transfer integrals for the crystal phases and disordered morphologies were evaluated using B3LYP/6-31G(d) of DFT and ZINDO methodology, respectively, and site-energies were calculated with Thole model, where RESP partial charges were calculated from MSK and atomic polarizabilities were reparametrized from B3LYP/6-31G(d) calculated molecular polarizabilities. kMC simulations were carried out for a single hole (or electron) carrier in an electric field ($\vec{E}$) in the equilibrated cell with periodic boundary conditions (resulting in a charge density of ~10^{23} m^{-3}). Electron and hole mobilities were computed from $\mu = \vec{v}.\hat{\epsilon}/E$. All DFT calculations were carried

out using Gaussian09[27] and all charge-transport calculations and simulations were performed using VOTCA package.[28]

3.3. Results and Discussion

3.3.1. Synthetic approach and molecular assembly

The target monomer SFIC was synthesized by the Yang group *via* Knoevenagel condensation between SF-CHO and 3-(dicyanomethylidene)indan-1-one (IC) in 90% yield (Figure 3.1A). The structure was confirmed with ^{1}H NMR, ^{13}C NMR, and high-resolution mass spectrometry (see ref. 29 for details). SFIC is soluble in common organic solvents such as chloroform, dichloromethane, chlorobenzene and ortho-dichlorobenzene at room temperature due to the cross-linked molecular scaffold and the branched alkyl chains. The thermal properties were assessed using thermal gravimetric analysis under nitrogen. SFIC exhibited high thermal stability with 5% weight loss at decomposition temperature of over 351 °C. From the edge of absorption spectra in the film, the optical bandgap was calculated to be 1.75 eV. The energy level and electrochemical bandgap were determined to be −5.77 eV for highest occupied molecular orbital (HOMO), −3.94 eV for lowest unoccupied molecular orbital (LUMO), and 1.83 eV for bandgap, based on the onset oxidation and reduction potentials and the difference of HOMO and LUMO, respectively (see ref. 29 for details). The narrow bandgap is ascribed to the strong electron withdrawing of end group IC lending the system ambipolar characteristics.

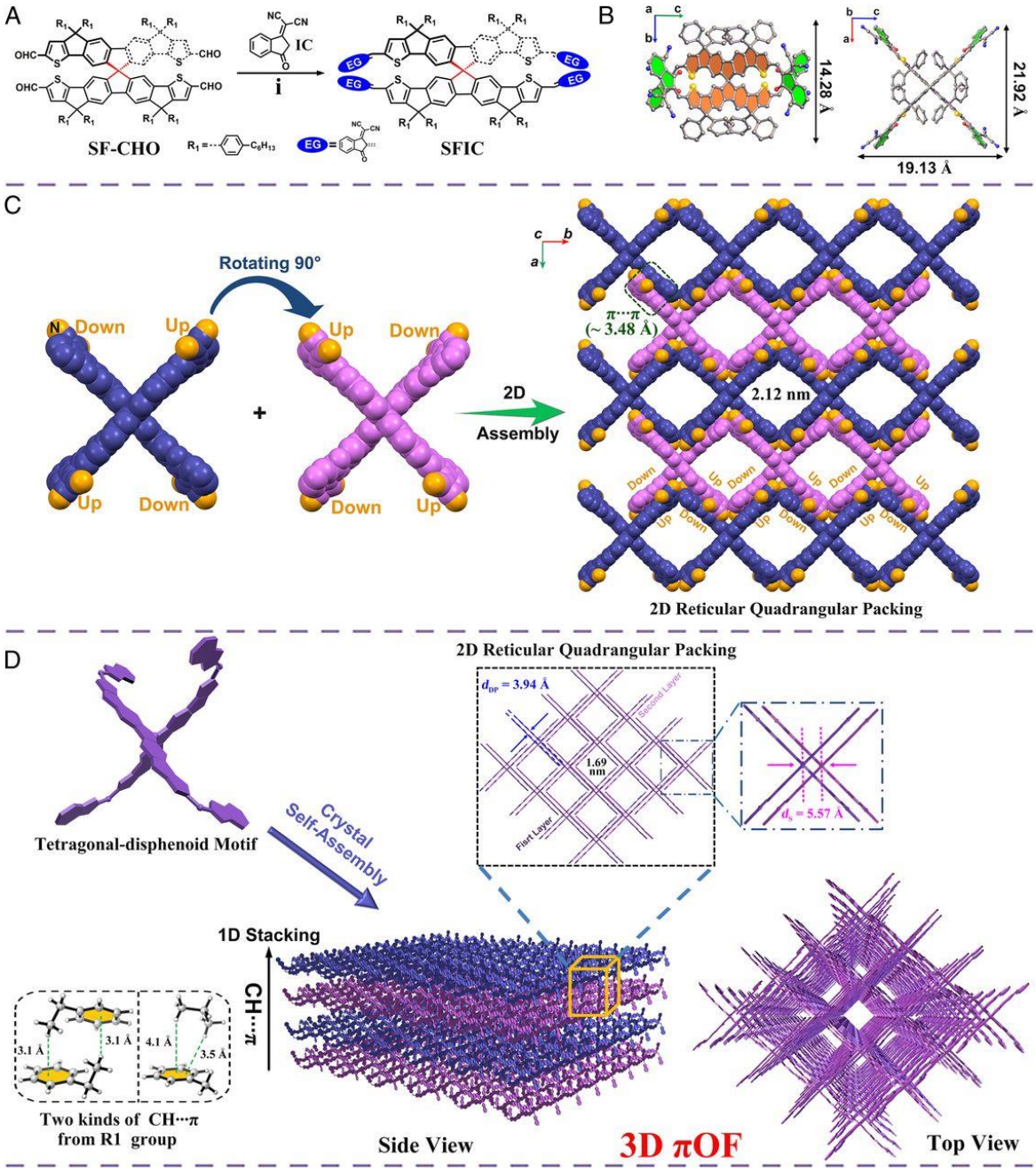

Figure 3.1. Synthetic route and crystal packing arrangement of SFIC. (A) Synthetic route with reaction conditions of (i) 3-(dicyanomethylidene)indan-1-one (IC, 12 equivalents) and pyridine (1 mL) in chloroform at 70 °C with yield of 90%. (B) The single-crystal X-ray molecular structure [top (Left) and side (Right) view] show a tetragonaldisphenoid motif. (C) The 2D crystal assembly along the ac plane via π···π interactions. The directions of up and down refer to the direction of the N atom. (D) The molecular packing arrangement of the 3D πOF structure is consists of 2D π···π (ac plane) interactions and 1D CH···π (b axis) interactions. dDP and dS represent packing and slippage distances between layers, respectively. The alkyl chains, cyano groups, and hydrogen and oxygen atoms are omitted for clarity.

The tetragonal-disphenoid molecular conformation of SFIC was determined with XRD analysis of single crystals obtained by slow vapor diffusion ($CHCl_3$/MeOH). The dimensions of SFIC conformer are ~19.13 Å in width, ~21.92 Å in length and ~14.28 Å in height (Figure 3.1B). Two IC groups of the same wing are noncoplanar with a dihedral angle of 28.07°. Each crisscrossed SFIC molecule is linked to four adjacent SFIC molecules (which are rotated 90° with respect to the centroid molecule) through four pairs of π···π interactions through antiparallel end groups (EGs) (Figure 3.1C). Such packing results in a 2D reticular quadrangular array which goes through perpendicular slipped one-dimensional (1D) stacking *via* two different types of CH···π interactions (Figure 3.1D and Figure 3.2) of hexylbenzene side chains forming a final 3D lamellar structure. The orientation of SFIC molecules of adjacent 2D layers were confirmed to be identical and to assemble into two repeating layers with a 3.94-Å-long unidirectional slippage (between two parallel wings, dsp) and 5.57-Å-long bidirectional slippage (between two central carbon atoms, ds) (Figure 3.1D). Closer inspection of the structure reveals that four distinct SFIC molecules of each layer form a dimetric micropore with a diameter of 2.12 nm (Figure 3.1C) across the layer and a lower diameter of 1.69 nm (Figure 3.1D) between two layers due to the slippage of adjacent layers.

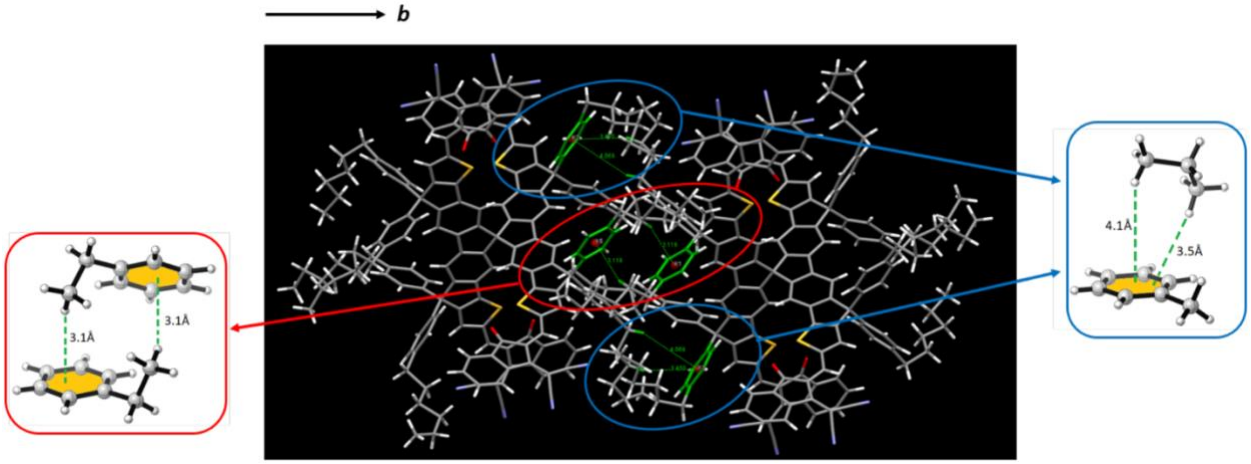

Figure 3.2. The interlayer CH···π interactions in πOF crystal along the b axis.

3.3.2. Investigation of Sorption and Porosity of SFIC-πOF.

The as-prepared πOF exhibited high CO_2 uptake capacity of 62.41 $cm^3 \cdot g^{-1}$ due to its highly porous structure and weak basicity of cyano group in SFIC (for further details on sorption properties of SFIC- πOF see ref. 30). The corresponding Brunauer–Emmett–Teller surface area of SFIC was determined to be over 981.62 $m^2 \cdot g^{-1}$ and pore volume of 0.44 $cm^3 \cdot g^{-1}$. The pore size distribution of πOF based on the nonlocal density functional theory (NLDFT) model exhibited a single peak at 1.69 nm, which is in agreement with the uniform dimetric pores of crystal packing structure. Porous material with supermicroporous range of 1 to 2 nm and higher surface area achieved in this work is a significant development that bridges the gap between mesoporous materials and microporous zeolites.

The porous crystals after activation, especially when guest-free, are less stable than other porous materials that are linked by metal coordination bonds or dynamic covalent bonds, while some hydrogen-bonded porous crystals are able to keep the native crystal framework after the guest molecules are removed. Few of the nonclassical hydrogen-bond-constructed (C-H···X) porous crystals could endure temperatures beyond 130 °C.[31,32] In comparison to conventional hydrogen bonds, and even the nonclassical ones, π···π interactions are far more labile. Surprisingly, our more-labile πOF-based on SFIC is considerably more thermally robust than the reported hydrogen-bonded frameworks, presenting no change up to 180 °C in variable-temperature PXRD patterns (see ref. 30). The structure of SFIC remained identical to that of the simulated one based on the single-crystal structure, with peaks at 2θ = 5.3°, 9.2°, and 11.5° assigned to (020), (031), and (400) lattice planes. Upon heating to 200 °C and beyond, a transition into a different crystalline phase is observed based on sudden change in the PXRD patterns.

3.3.3. Single-Crystal Transistor Characterization of SFIC-πOF.

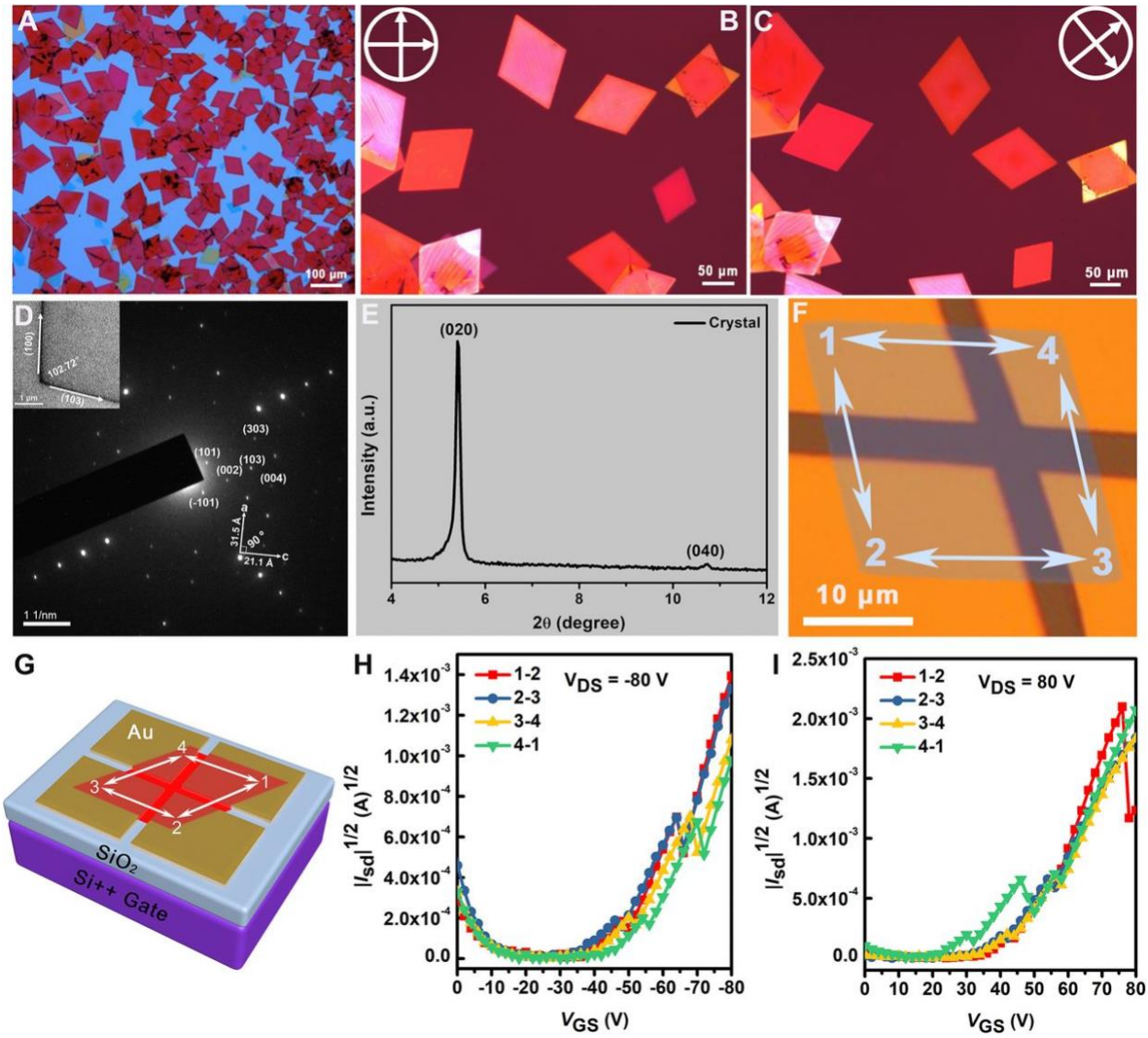

Figure 3.3. Single-crystal transistor (OFET) characterization of πOF. (A) The OM image of πOF microplates [drop-casted in $CHCl_3$ (1 mg/mL)] self-assembled on SiO_2/Si. (B and C) CPOM images of the single-crystal microplates of πOF. (D) The SAED patterns and its corresponding TEM image. (E) One-dimensional out-of-plane XRD pattern of a single crystal data. (F) A transistor with four electrodes probing charge transport properties along different crystal planes. (G) The schematic diagram of πOF micro/nanocrystal transistor. (H) P-type and (I) N-type transfer characteristics of four OFET devices in different crystal planes.

Due to its long-range π···π interactions, πOF presents an opportunity to expand the OF into organic electronics. Thus, we first prepared the single-crystal microplates of πOF by a typical drop-

casting method in $CHCl_3$ solution onto the SiO_2/Si substrates and measured the intrinsic charge transport properties of πOF. Optical microscope (OM) images and bright-field TEM images (top left inset) of the πOF microplates with a rhomboid shape and long-range regularity are shown in Figure 3.3A and D. In the cross-polarized optical microscopy (CPOM) images, the change in crystal intensities pinpoint to the single crystal nature of the microplates (Figure 3.3B and C). In Figure 3.3E, the out-of-plane XRD pattern with sharp and strong multiple Bragg diffractions indicate highly ordered lamellar structure and the high degree of crystallinity of πOF microplates. Based on the data from the single-crystal structure, the two strong diffraction peaks at $2\theta = 5.41°$ and 10.74° observed in the XRD analysis for the microplates (Figure 3.3E) could be attributed to (020) and (040) lattice planes, respectively. The out-of-plane XRD data together with SAED pattern (Figure 3.3D) and single-crystal XRD data (see ref. 30 for details) confirm that the πOF microplates are of the identical phase as in the previously obtained single crystals.

The field-effect transistor devices based on the rhomboid microcrystal of πOF were prepared with an "organic ribbon mask" technique with four electrodes and channels to analyze the directional charge transport properties (Figure 3.3F).[33] The transfer and output characteristics of four different crystal planes examined under ambient conditions are demonstrated in Figure 3.1H and I (see ref. 29 for more information) and the mobility data are outlines in Table 3.1. The OFET device based on πOF microplates exhibit ambipolar characteristics, a simultaneous existence of both hole (Figure 3.3H) and electron (Figure 3.3I) charge-carrier transport behavior. The same directional conducting channels, 1 ↔ 2 and 3 ↔ 4 or 2 ↔ 3 and 4 ↔ 1, present similar mobilities (in units of square centimeters per volt per second) [$\mu_{h(1-2)} = 0.0705$, $\mu_{e(1-2)} = 0.26$, $\mu_{h(3-4)} = 0.089$, $\mu_{e(3-4)} = 0.27$, or $\mu_{h(2-3)} = 0.0676$, $\mu_{e(2-3)} = 0.12$, $\mu_{h(4-1)} = 0.0495$, $\mu_{e(4-1)} = 0.13$] (see Table 3.1). Moreover, the channels of 1 ↔ 2 and 3 ↔ 4 show increased mobility over the 2 ↔ 3 and 4

↔ 1 channels. These results indicate that the reticular quadrangular lattice of πOF exhibits anisotropic properties, which are further explored using density functional theory (DFT) calculations.

Table 3.1. Field-effect electron (e) and hole (h) mobilities of four OFET devices with different crystal planes.

Device	W/L (μm)	μ^{max} (cm^2 V^{-1} s^{-1})	V_t /V	On/off Ratio
1-2	14.33/3.88	**7.05×10^{-2} (h)**	-45.72	3.63×10^{4}
		0.26 (e)	45.84	6.80×10^{5}
2-3	10.45/3.58	**6.76×10^{-2} (h)**	-43.28	3.05×10^{4}
		0.12 (e)	38.12	2.64×10^{5}
3-4	6.12/4.48	**8.90×10^{-2} (h)**	-42.98	2.50×10^{5}
		0.27 (e)	39.75	2.39×10^{5}
4-1	9.41/3.28	**4.95×10^{-2} (h)**	-47.67	6.71×10^{5}
		0.13 (e)	35.77	6.19×10^{4}

3.3.4. Mechanistic Studies of Transport: From a Computational Perspective.

We undertook extensive theoretical calculations to gather computational insights into the hole/electron transport behavior in πOF. We first concentrated on the packing along (100) and (103) planes, which correspond to the π···π and x···x interactions, respectively (Figure 3.4A and B). Based on the first-principles calculations (Figure 3.5), it was found that the dimer binding energies and transfer integrals of π···π interactions were considerably larger than those of x···x because of the relatively strong π···π binding. DFT calculated electron transfer integral (J_e) of π···π

in πOF is more than four times stronger than the hole transfer integral (J_h), while J_h was conversely stronger than J_e in x···x (Figure 3.4B). The intramolecular reorganization energies of hole (λ_h) and electron (λ_e) transfer were found to be identical (λ_h=λ_e=82 meV) (Figure 3.5B). Transport calculations implied that charge-carrier mobilities on the order of 1 cm^2/Vs can be accomplished in a defect-free πOF. Moreover, 1) $\mu_e > \mu_h$ over the π···π plane independent of the transport direction can be attributed to $J_e > J_h$ along π···π and 2) electron mobility along (100) is roughly two times larger than along (103) for both electron and hole mobilities, due to larger transfer integrals along π···π than those along x···x (Figure 3.5C). Both 1 and 2 are highly consistent with the OFET results shown in Figure 3.3.

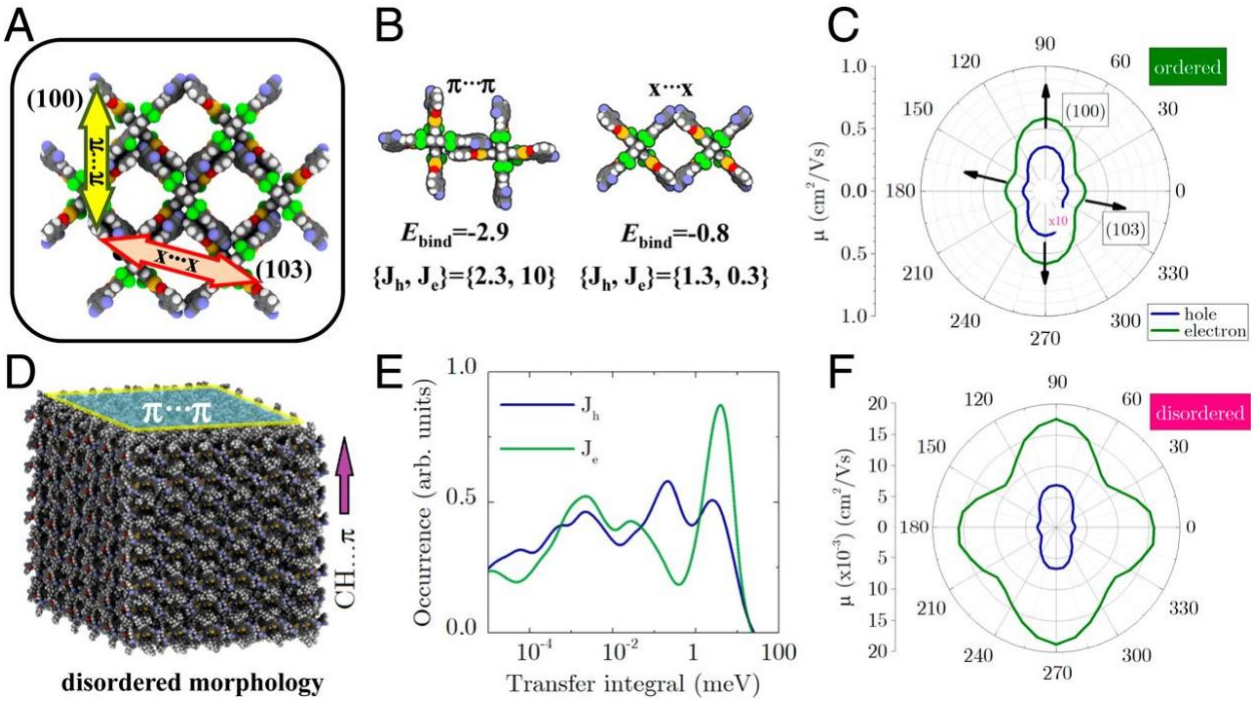

Figure 3.4. Computational characterizations of hole/electron transport. (A) Crystal packing of πOF used in computations. Green spheres represent alkyl chains. (B) Computed binding energies (in electronvolts), hole transfer (J_h), and electron transfer (J_e) integrals (in millielectronvolts) (C) Direction-resolved hole and electron mobilities in ordered phase. (D) Atomistic morphology of the disordered phase. (E) Hole and electron transfer integral distributions in all transport directions. (F) Direction-resolved hole and electron mobilities in disordered phase.

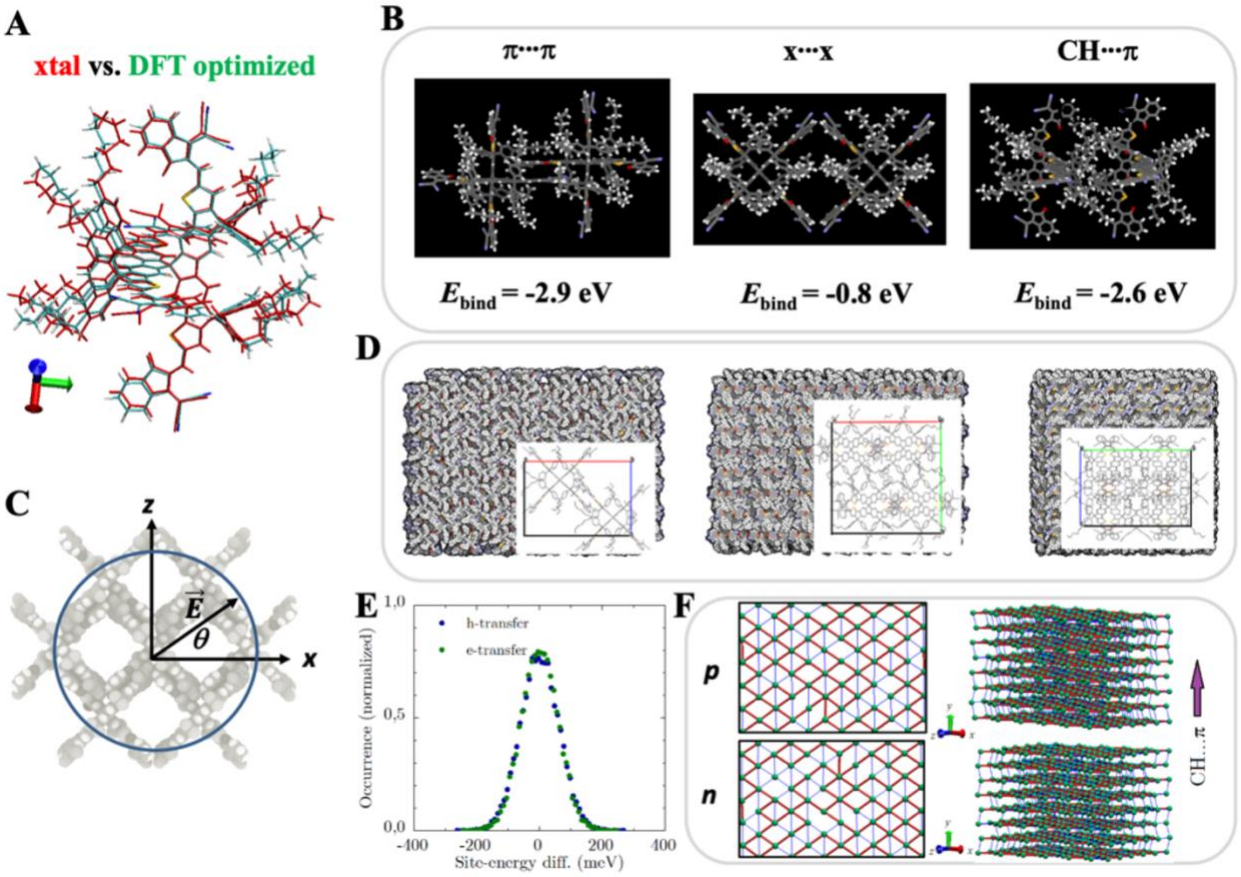

Figure 3.5. Characterization of interactions in the computational model of πOF crystal structure. (A) Superposition of single SFIC molecule geometry obtained from X-ray measurements over the B3LYP/6-31G(d) gas-phase optimized one. (B) SFIC pair interactions present in the crystal structure and the respective B97D/6-31G(d,p)-calculated dimer binding energies. (C) A diagram showing electric field variation for direction-resolved transport calculations. (D) MD-equilibrated atomistic morphologies of πOF along three packing directions. (E) Computed site-energy difference distributions for hole and electron transfers based on Thole model. (F) Connectivity graphs in πOF based on the strength of the hole (p) and electron (n) transfer integrals. Green dots represent site positions. For J>1 meV the bonds are in red and for 0.1 meV < J < 1 meV range, the bonds are in blue. Missing bonds are less than 0.1 meV. (left column) The connectivity along a single π···π plane, (right column) the connectivity for all directions.

Mobility calculations in the disordered phase (Figure 3.4D and Figure 3.5D) demonstrate that the charge transport in πOF is susceptible against structural fluctuations originating from the thermal effects, ascribed to decrease in both hole and electron mobilities relative to the crystal phase (Figure 3.4F), despite maintaining of directional mobility and $\mu_e > \mu_h$. On the other hand, the mobilities along CH···π are much lower because of missing π···π interactions. The site-energy

disorder of hole transport (Δ_h) and electron transport (Δ_e), stemming from local charge–phonon coupling, were discovered to be similar and 60 meV (i.e., $\Delta_h \sim \Delta_e = 60$ meV), as depicted in Figure 3.5E. The nonlocal electron–phonon coupling, on the other hand, were larger than nonlocal hole–phonon coupling (see also Figure 3.4E). Thus, computations indicate that the mobility and charge transport in πOF is primarily controlled by the intermolecular interactions, which highlights the significance of different interactions in the πOF.

3.4. Conclusion

In conclusion, we have designed a noncovalent π···π interaction-based organic framework (πOF). The 3D-ordered microporous structure that is linked via these kinds of weak interactions demonstrates not only the supramaximal micropore and extremely high surface area but also a superior stability and self-healing abilities. It also presents remarkable transport properties in an OFET device, exhibiting distinct advantage over traditional COFs. The πOF not only expands the concept of porous molecular frameworks but also offers a direction toward applications of porous materials in organic electronics. Our study sheds light on a generation of microporous materials-based organic electronics opening doors for strategic structural assembly for functionalities and an even better performance in the future.

3.5. References

(1) Meng, D.; Sun, D.; Zhong, C.; Liu, T.; Fan, B.; Huo, L.; Li, Y.; Jiang, W.; Choi, H.; Kim, T.; Kim, J. Y.; Sun, Y.; Wang, Z.; Heeger, A. J. *J. Am. Chem. Soc.* **2016**, *138*, 375–380.

(2) Meng, D.; Fu, H.; Xiao, C.; Meng, X.; Winands, T.; Ma, W.; Wei, W.; Fan, B.; Huo, L.; Doltsinis, N. L.; Li, Y.; Sun, Y.; Wang, Z. *J. Am. Chem. Soc.* **2016**, *138*, 10184–10190.

(3) Zhang, G.; Zhao, J.; Chow, P. C. Y.; Jiang, K.; Zhang, J.; Zhu, Z.; Zhang, J.; Huang, F.; Yan, H. *Chem. Rev.* **2018**, *118*, 3447–3507.

(4) Cheng, P.; Li, G.; Zhan, X.; Yang, Y. *Nat. Photonics* **2018**, *12*, 131–142.

(5) Briseno, A. L.; Mannsfeld, S. C. B.; Ling, M. M.; Liu, S.; Tseng, R. J.; Reese, C.; Roberts, M. E.; Yang, Y.; Wudl, F.; Bao, Z. *Nature* **2006**, *444*, 913–917.

(6) Thomas, S. W.; Joly, G. D.; Swager, T. M. *Chem. Rev.* **2007**, *107*, 1339–1386.

(7) Li, H.; Shi, Y.; Han, G.; Liu, J.; Zhang, J.; Li, C.; Liu, J.; Yi, Y.; Li, T.; Gao, X.; Di, C.; Huang, J.; Che, Y.; Wang, D.; Hu, W.; Liu, Y.; Jiang, L. *Angew. Chem. Int. Ed.* **2020**, *59*, 4380–4384.

(8) Wang, Y.; Sun, L.; Wang, C.; Yang, F.; Ren, X.; Zhang, X.; Dong, H.; Hu, W. *Chem. Soc. Rev.* **2019**, *48*, 1492–1530.

(9) Chen, X.; Rogers, J. A.; Lacour, S. P.; Hu, W.; Kim, D.-H. *Chem. Soc. Rev.* **2019**, *48*, 1431–1433.

(10) Kwon, S.; Hwang, Y. H.; Nam, M.; Chae, H.; Lee, H. S.; Jeon, Y.; Lee, S.; Kim, C. Y.; Choi, S.; Jeong, E. G.; Choi, K. C. *Adv. Mater.* **2020**, *32*, 1903488.

(11) Müllen, K.; Scherf, U. *Organic Light Emitting Devices: Synthesis, Properties and Applications*; John Wiley & Sons, 2006.

(12) Calik, M.; Auras, F.; Salonen, L. M.; Bader, K.; Grill, I.; Handloser, M.; Medina, D. D.; Dogru, M.; Löbermann, F.; Trauner, D.; Hartschuh, A.; Bein, T. *J. Am. Chem. Soc.* **2014**, *136*, 17802–17807.

(13) Jiang, J.; Zhao, Y.; Yaghi, O. M. *J. Am. Chem. Soc.* **2016**, *138*, 3255–3265.

(14) Côté, A. P.; Benin, A. I.; Ockwig, N. W.; O'Keeffe, M.; Matzger, A. J.; Yaghi, O. M. *Science* **2005**, *310*, 1166–1170.

(15) Huang, N.; Wang, P.; Jiang, D. *Nat. Rev. Mater.* **2016**, *1*, 16068.

(16) Deng, J.-H.; Luo, J.; Mao, Y.-L.; Lai, S.; Gong, Y.-N.; Zhong, D.-C.; Lu, T.-B. *Sci. Adv.* **2020**, *6*, eaax9976.

(17) Sozzani, P.; Comotti, A.; Bracco, S.; Simonutti, R. *Angew. Chem. Int. Ed.* **2004**, *43*, 2792–2797.

(18) Lyu, Y.-Y.; Kwak, J.; Jeon, W. S.; Byun, Y.; Lee, H. S.; Kim, D.; Lee, C.; Char, K. *Adv. Funct. Mater.* **2009**, *19*, 420–427.

(19) Qiu, N.; Yang, X.; Zhang, H.; Wan, X.; Li, C.; Liu, F.; Zhang, H.; Russell, T. P.; Chen, Y. *Chem. Mater.* **2016**, *28*, 6770–6778.

(20) Heredia, D.; Natera, J.; Gervaldo, M.; Otero, L.; Fungo, F.; Lin, C.-Y.; Wong, K.-T. *Org. Lett.* **2010**, *12*, 12–15.

(21) Han, G.; Guo, Y.; Ning, L.; Yi, Y. *Sol. RRL* **2019**, *3*, 1800251.

(22) Lin, Y.; Wang, J.; Zhang, Z.-G.; Bai, H.; Li, Y.; Zhu, D.; Zhan, X. *Adv. Mater.* **2015**, *27*, 1170–1174.

(23) Han, G.; Yi, Y.; Shuai, Z. *Adv. Energy Mater.* **2018**, *8*, 1702743.

(24) Case, D. A.; Darden, T. A.; Cheatham, T. A. III; Simmerling, C. L.; Wang, J.; Duke, R. E.; Luo, R.; Walker, R. C.; Zhang, W.; Merz, K. M.; Roberts, B.; Hayik, S.; Roitberg, A.; Seabra,

G.; Swails, J.; Götz, A. W.; Kolossváry, I.; Wong, K. F.; Paesani, F.; Vanicek, J.; Wolf, R. M.; Liu, J.; Wu, X.; Brozell, S. R.; Steinbrecher, T.; Gohlke, H.; Cai, Q.; Ye, X.; Wang, J.; Hsieh, M.-J.; Cui, G.; Roe, D. R.; Mathews, D. H.; Seetin, M. G.; Salomon-Ferrer, R.; Sagui, C.; Babin, V. Luchko, T.; Gusarov, S.; Kovalenko, A.; Kollman, P. A. *AMBER 12*, **2012**, University of California, San Francisco.

(25) Yavuz, I.; Martin, B. N.; Park, J.; Houk, K. N. *J. Am. Chem. Soc.* **2015**, *137*, 2856–2866 *and references therein*.

(26) Tsutsui, Y.; Schweicher, G.; Chattopadhyay, B.; Sakurai, T.; Arlin, J.-B.; Ruzié, C.; Aliev, A.; Ciesielski, A.; Colella, S.; Kennedy, A. R.; Lemaur, V.; Olivier, Y.; Hadji, R.; Sanguinet, L.; Castet, F.; Osella, S.; Dudenko, D.; Beljonne, D.; Cornil, J.; Samorì, P.; Seki, S.; Geerts, Y. H. *Adv. Mater.* **2016**, *28*, 7106–7114.

(27) *Gaussian 09*, Revision D.01, Frisch, M. J.; Trucks, G. W.; Schlegel, H. B.; Scuseria, G. E.; Robb, M. A.; Cheeseman, J. R.; Scalmani, G.; Barone, V.; Mennucci, B.; Petersson, G. A.; Nakatsuji, H.; Caricato, M.; Li, X.; Hratchian, H. P.; Izmaylov, A. F.; Bloino, J.; Zheng, G.; Sonnenberg, J. L.; Hada, M.; Ehara, M.; Toyota, K.; Fukuda, R.; Hasegawa, J.; Ishida, M.; Nakajima, T.; Honda, Y.; Kitao, O.; Nakai, H.; Vreven, T.; Montgomery, J. A. Jr.; Peralta, J. E.; Ogliaro, F.; Bearpark, M.; Heyd, J. J.; Brothers, E.; Kudin, K. N.; Staroverov, V. N.; Keith, T.; Kobayashi, R.; Normand, J.; Raghavachari, K.; Rendell, A.; Burant, J. C.; Iyengar, S. S.; Tomasi, J.; Cossi, M.; Rega, N.; Millam, J. M.; Klene, M.; Knox, J. E.; Cross, J. B.; Bakken, V.; Adamo, C.; Jaramillo, J.; Gomperts, R.; Stratmann, R. E.; Yazyev, O.; Austin, A. J.; Cammi, R.; Pomelli, C.; Ochterski, J. W.; Martin, R. L.; Morokuma, K.; Zakrzewski, V. G.; Voth, G. A.; Salvador, P.; Dannenberg, J. J.; Dapprich, S.; Daniels, A. D.; Farkas, O.; Foresman, J. B.; Ortiz, J. V.; Cioslowski, J.; Fox, D. J. *Gaussian, Inc*., Wallingford CT, **2013**.

(28) Rühle, V.; Lukyanov, A.; May, F.; Schrader, M.; Vehoff, T.; Kirkpatrick, J.; Baumeier, B.; Andrienko, D. *J. Chem. Theory Comput.* **2011**, *7*, 3335–3345.

(29) *Supporting Information Appendix of:* Meng, D.; Yang, J. L.; Xiao, C.; Wang, R.; Xing, X.; Kocak, O.; Aydin, G.; Yavuz, I.; Nuryyeva, S.; Zhang, L.; Liu, G.; Li, Z.; Yuan, S.; Wang, Z.-K.; Wei, W.; Wang, Z.; Houk, K. N.; Yang, Y. *Proc. Natl. Acad. Sci.* **2020**, *117*, 20397–20403.

(30) Meng, D.; Yang, J. L.; Xiao, C.; Wang, R.; Xing, X.; Kocak, O.; Aydin, G.; Yavuz, I.; Nuryyeva, S.; Zhang, L.; Liu, G.; Li, Z.; Yuan, S.; Wang, Z.-K.; Wei, W.; Wang, Z.; Houk, K. N.; Yang, Y. *Proc. Natl. Acad. Sci.* **2020**, *117*, 20397–20403.

(31) Bezzu, C. G.; Helliwell, M.; Warren, J. E.; Allan, D. R.; McKeown, N. B. *Science* **2010**, *327*, 1627–1630.

(32) Msayib, K. J.; Book, D.; Budd, P. M.; Chaukura, N.; Harris, K. D. M.; Helliwell, M.; Tedds, S.; Walton, A.; Warren, J. E.; Xu, M.; McKeown, N. B. *Angew. Chem. Int. Ed.* **2009**, *48*, 3273–3277.

(33) Jiang, L.; Gao, J.; Wang, E.; Li, H.; Wang, Z.; Hu, W.; Jiang, L. *Adv. Mater.* **2008**, *20*, 2735–2740.

Chapter 4. Chlorinated, Spiroconjugated, and Fused Extended Aromatics for Multifunctional Organic Electronics

4.1. Background

The advancements in organic semiconductors have sparked the development of flexible displays, organic light-emitting diodes, organic solar cells, organic field-effect transistors, and sensors. The properties of organic electronic materials could normally be adjusted rather easily via facile chemical modifications to accommodate the different device requirements.[1-3] In light of this, various hybrid devices have been developed for real-world applications. The preparation process of hybrid devices, however, usually involves vast variety of materials, which not only increases the cost but also makes the process more cumbersome. Thus, there emerges the need to explore multifunctional organic electronic materials to simplify the preparation process and reduce the cost.

Spiro-fused polycyclic aromatic compounds, with orthogonal π-subsystems linked by a sp3-hybridized spiro-atom, have been extensively explored as organic electronic materials due to rigid 3D orthogonal configuration, good processability, excellent thermal and optical stability, and exclusive spiroconjugation effects.[4-7] Spiroconjugation, first described by Simmons and Fukunaga in 1967, refers to the delocalization and bandgap alteration that occurs upon orbital interaction between the π systems of the two spiro-fused planar pieces.[8] The unique 3D rigid spiroconjugation architecture not only reduces intermolecular electronic coupling and in turn the charge recombination but also increases charge transport capability.[9] Notably, 9,9′-spirobifluorene, the most prominent class of spiroconjugated molecules, has served as a promising building block for the construction of functional materials in organic light-emitting diodes (OLEDs), organic field-effect transistors (OFETs), and organic photovoltaics (OPV).[10-18] Fused extended π-electron

systems are the crucial approach to improve mobility and tune the optoelectronic properties of functional materials for high performance optics and electronics. However, modification of 9,9′-spirobifluorene has mainly focused on the singly core-substitution at different reaction positions, and studies that explored extension of the spiro-π-systems via annulation, which could increase intermolecular π···π overlap area by expanded rigid spiroconjugation in the solid state, are rather limited.[19-28]

Halogenation has been an important chemical modification means applied in constructing various organic semiconductors such as fluorination and chlorination.[29,30] Compared to fluorination that has been well-studied, the chlorination strategy has not been extensively investigated as the larger atomic size of chlorine results in steric effects in conjugated backbones.[31] Nonetheless, a chlorination strategy is appealing due to its ease of synthesis, greater electron density capacity, and lower cost. Furthermore, in comparison with fluorine, chlorine is less electronegative (Pauling electronegativity F: 3.98, and Cl: 3.16) but is also an inferior π donor due to poor overlap of C2p and Cl3p orbitals. Bao *et al.* also suggested that the unoccupied 3d orbitals of the chlorine atom are able to better accommodate delocalized π-electrons.[32] Chlorine may increase the solubility of conjugated systems in common organic polar solvents, due to better polarizability of chlorine compared to fluorine.[33]

In view of the considerations discussed above, we designed a new molecule, namely SFIC-Cl, using a biplanar conjugated cruciform-shaped spirobifluorene (SF) as the centroid core and 2-(5,6-dichloro-3-oxo-2,3-dihydro-1H-inden-1-ylidene) malononitrile (2Cl-IC) as a multi-joint fragment connecting adjacent molecules. The two fluorene units of SF adopt an orthogonal configuration bearing a rigid 3D structure. Since thiophene has lower resonance energy and better mobility than benzene, thiophene units were introduced to effectively increase the spiro π-

conjugated plane of each fluorene unit of SF. The 2Cl-IC units were employed as end-groups (EG) due to their propensity to form directional face-on π···π interactions while serving as chromophores widely applied in electronic devices. Meanwhile, the introduction of Cl atom not only increases the solubility but also significantly lowers bandgap, an important property for electronic device applications. Based on the enhanced π-system, good solubility, and well-matched energy level with other components applied in devices, we integrated SFIC-Cl into OFET, OLED and OPV devices (see ref. 34 for details). SFIC-Cl showed remarkable electron transport abilities in OFET and retained efficient radiance in a near-infrared OLED emitting light at 700 nm. Furthermore, the intermolecular multi-dimensional connection enabled the fabrication of a single component large-area (2×2 cm^2) near-infrared OLED by spin-coating. SFIC-Cl-acceptor-based OPV also yielded an excellent power conversion efficiency of 10.16%, which is attributed to a well-matched lowest-energy unoccupied molecular orbital (LUMO) level with the polymer donor and good film morphology.

4.2. Methodology

4.2.1. Synthetic Approach

The synthetic route to SFIC-Cl performed by the Yang group is shown in Figure 4.1. Compound 1 was synthesized via four-fold Suzuki–Miyaura coupling reaction between 2-bromothiophene-3-carboxylate and 2,2′,7,7′-tetrakis(pinacolatoboryl)-9,9′-spirobi[9*H*-fluorene] using tetrakis(triphenylphosphine)-palladium(0) ($Pd(PPh_3)_4$) as catalyst and potassium carbonate (K_2CO_3) as base in 80% yield. Quadruple nucleophilic addition of freshly prepared 4-(2-ethylhexyl)phenyl magnesium bromide to the ester groups of compound 1 led to the formation of benzylic alcohol 2 which was subjected to intramolecular annulation through acid-mediated

Friedel–Crafts reaction to afford the fused double-heptacyclic arene 3. For the effective reaction, we used the organic acid boron trifluoride diethyl etherate and archived 75% high yield. Subsequent compound 4 was prepared by Vilsmeier–Haack reaction of 3 using phosphoryl chloride ($POCl_3$) and DMF (*N*,*N*-dimethylformamide). The target product SFIC-Cl was obtained via Knoevenagel condensation between compound 4 and 2-(5,6-dichloro-3-oxo-2,3-dihydro-1H-inden-1-ylidene) malononitrile in 85% excellent yield. All of these compounds were unambiguously characterized by ^{1}H NMR spectra, and ^{13}C NMR and high-resolution mass spectra were also performed for SFIC-Cl. SFIC-Cl is soluble in common organic solvents such as dichloromethane, chloroform, chlorobenzene, and *ortho*-dichlorobenzene (*o*-DCB) at room temperature due to the cross-linked molecular scaffold and the branched alkyl chains. The thermal properties were evaluated by thermal gravimetric analysis (TGA) performed under nitrogen. SFIC-Cl possesses excellent thermal stability with decomposition temperature of 5% weight loss over 335 °C (see ref. 35 for more information).

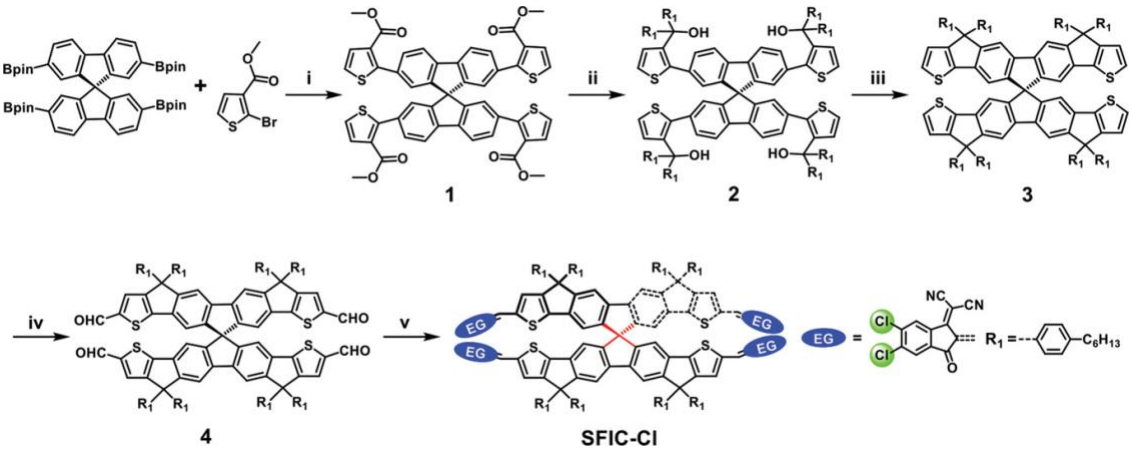

Figure 4.1. Synthetic route to SFIC-Cl. The reaction conditions were: i) Methyl 2-bromothiophene-3-carboxylate (4.5 equiv.), 2,2′,7,7′-tetrakis(pinacolatoboryl)-9,9′-spirobi[*9H*-fluorene] (1.0 equiv), $Pd(PPh_3)_4$ (0.3 equiv.), K_2CO_3 (2 m)/THF (1:2), 95 °C, 72 h. Yield: 80%. ii) 1-Bromo-4-hexylbenzene (22 equiv.), magnesium turnings (26.4 equiv.), THF, RT to 70 °C, 20 h. Yield: 85%. iii) Boron trifluoride diethyl etherate (diluted by chloroform), chloroform, 70 °C, 24 h. Yield: 75%. iv) DMF, $POCl_3$, 0 to 90 °C, 20 h. Yield: 70%. v) 2-(5,6-Dichloro-3-oxo-2,3-dihydro-1H-inden-1-ylidene) malononitrile (12 equiv.), pyridine (1 mL), chloroform, 70 °C, yield: 85%.

4.2.1. Computational Details

All DFT computations were performed with Gaussian 09.[36] To probe the conformational freedom of SFIC-Cl, dihedral scans of model system TH-IC were performed with ωB97XD/6-31+G(d,p) in 5 degree increments (see Figure 4.2). We found in a previous benchmarking study that ωB97X-D performs well for predicting torsional behavior of thiophene-based materials.[37]

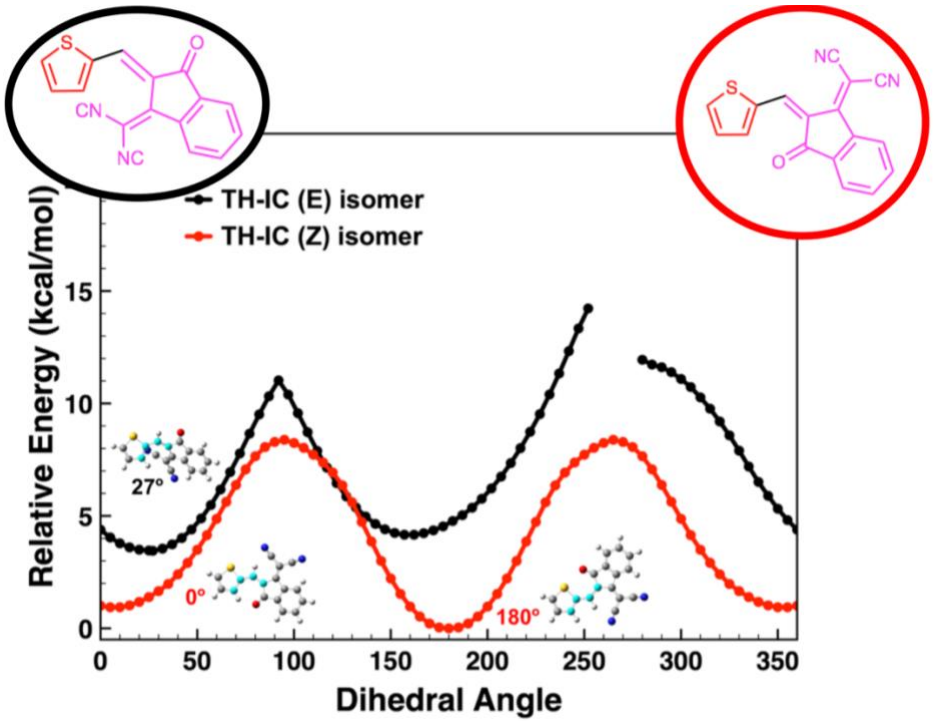

Figure 4.2. Potential energy surface for rotation about the highlighted C-C-C-C dihedral in *E* and *Z*-TH-IC. Constrained optimization of E-isomer at 252° was unable to converge due to steric clashes between thiophene and cyano groups.

All other ground state structures were optimized using B3LYP[38-41]/6-31G(d). This method was chosen over ωB97X-D due to the size of the full SFIC-Cl system to allow for computational efficiency. Vibrational analysis was used to confirm stationary points as minima (no imaginary frequencies). B3LYP/6-31G(d) was used for TD-DFT energy calculations with the polarizable continuum model PCM for solvation by chloroform.[42-45] In order to obtain absorption spectra for

each molecule, the lowest 100 excited electronic states were calculated based on the ground state geometry. The contributions described here have been normalized using a coefficient of ½√2. Electron difference density plots were obtained by subtracting the density of the ground state from the densities of the first and second excited states using the cubman program, as implemented in Gaussian.

The dihedral angle of interest is highlighted in cyan on the molecular models shown. Each structure shown represents a relative energy minimum or maximum. The *Z* isomer of TH-IC is overall lower in energy than its *E* form. Its energy is lowest when the C-C-C-C angle is at 180°, and the thiophene and the double bond of the 1-indenylidine group are coplanar with a stabilizing S-O interaction. This conformation was used in subsequent calculations of the MF-Ph and SFIC-Cl systems shown in Figure 4.3.

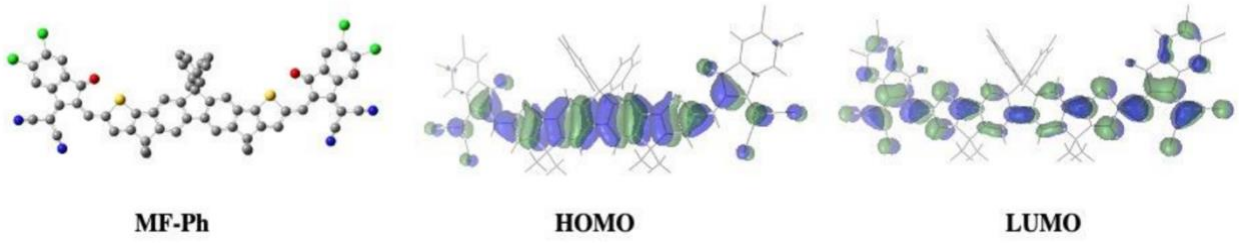

Figure 4.3. Optimized structure of lowest energy conformer of MF-Ph and its frontier molecular orbitals.

4.3. Results and Discussion

In order to fully characterize the structural properties of SFIC-Cl, we used density functional theory (DFT) calculations using B3LYP/6-31G(d) method and basis set. The DFT-optimized lowest energy conformer of SFIC-Cl is depicted in Figure 4.4A. This molecule has D2d symmetry, with the vinyl keto moieties appended at the end of each of its four hemispheres (Figure 4.2). The conformation about the rotatable bond is consistent with the potential energy surface of the same dimeric piece that was calculated, where the lowest energy conformer is coplanar. A top

view of the optimized structure shows that the two fluorenes are exactly orthogonal, with a 90° angle between the two planes.

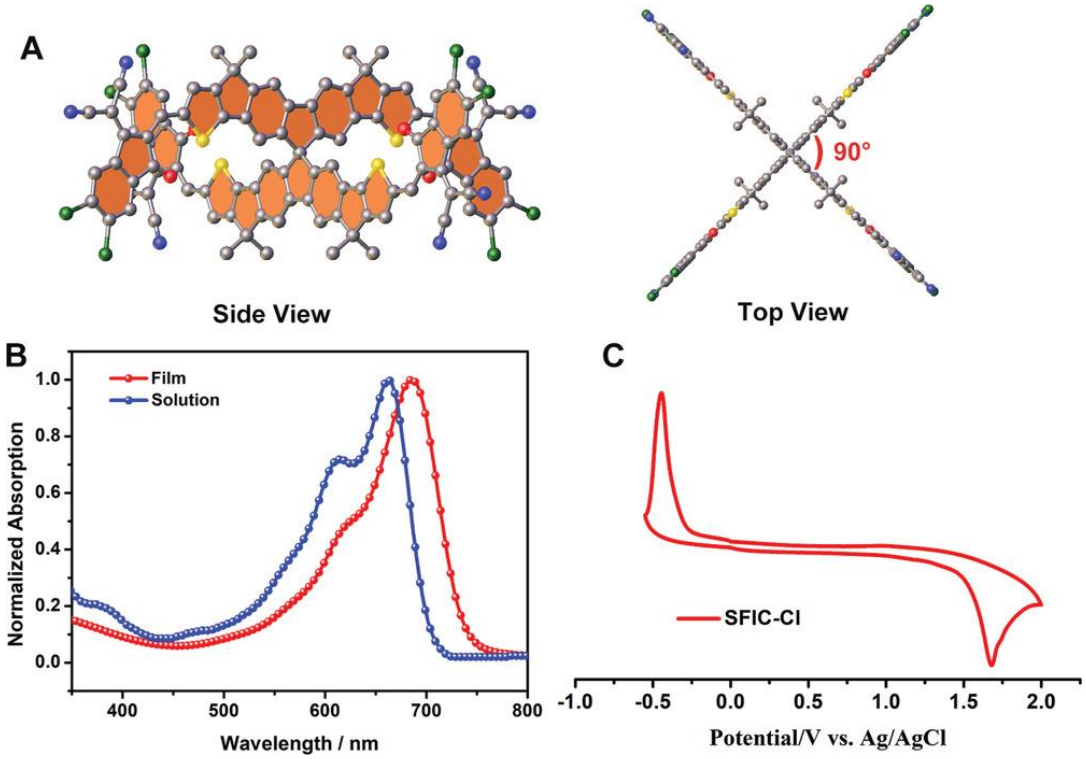

Figure 4.4. Optimized structure of SFIC-Cl and its optical and electrochemical properties. A) DFT-optimized structure of the lowest energy conformer of SFIC-Cl (left: side view, right: top view). B) UV−vis absorption spectra of SFIC-Cl in solution ($CHCl_3$) and film. C) Cyclic voltammogram of SFIC-Cl film.

The UV–vis spectrum of SFIC-Cl in chloroform and film are shown in Figure 4.4B. In dilute chloroform solution, SFIC-Cl displays a broad absorption in the wavelength range 500–700 nm with a maximum at 663 nm. Compared to the solution, the maximum of SFIC-Cl neat film is redshifted by approximately 23 nm, indicative of a better molecular packing model in solid states. The optical bandgap of SFIC-Cl predicted from the absorption onset is 1.68 eV. The energy level was investigated by electrochemical cyclic voltammetry (CV) shown in Figure 4.4C and Table 4.1. The highest-energy occupied molecular orbital (HOMO) and LUMO value are estimated to

be -5.85 eV and −4.07 eV from the onset oxidation and reduction potentials. The relatively low HOMO and LUMO energy levels are attributed to the electron-withdrawing nature of chlorine.

Table 4.1. Summary of optical and electronic properties of SFIC-Cl.

	$\lambda_{max\text{-}s}$ [a] [nm]	$\lambda_{max\text{-}f}$ [b] [nm]	$\lambda_{onset\text{-}s}$ [a] [nm]	$\lambda_{onset\text{-}f}$ [b] [nm]	E_{LUMO} [c] [eV]	E_{HOMO} [d] [eV]	$E_{g\text{-}E}$ [e] [eV]	$E_{g\text{-}opt\text{-}f}$ [f] [eV]
SFIC-Cl	663	686	701	738	-4.07	-5.85	1.78	1.68

[a] λ_{max} was measured in $CHCl_3$ solution. [b] λ_{max} was measured in film. [c] Estimated from the onset potential of the first reduction wave and calculated according to $E_{LUMO} = -(4.4 + E_{onset}^{re})$ eV. [d] Estimated from the onset potential of the first oxidation wave and calculated according to $E_{HOMO} = -(4.4 + E_{onset}^{ox})$ eV. [e] $E_{g\text{-}E}$ (eV) calculated according to $E_{g\text{-}E} = (E_{LUMO} - E_{HOMO})$ eV. [f] Obtained from the edge of the absorption spectra in film according to $E_g = (1240/\lambda_{onset})$.

To further characterize the spiroconjugation in the molecule, we visualized the frontier molecular orbitals (FMOs) of SFIC-Cl, which are shown in Figure 4.5. While the HOMO-1 is slightly lower in energy than the HOMO by 0.07 eV, the LUMO and LUMO+1 are exactly degenerate. The mixing of the HOMOs from the two halves of the molecule results from spiroconjugation, which derives from the S symmetry of the HOMOs of the halves, causing mixing.[5] The HOMO and HOMO-1 orbitals are localized in the central donor portion of the molecule (spiro-fluorene). By contrast, the LUMO fragments have a symmetry with respect to the C2 axis and do not mix. Moreover, the degenerate LUMOs are more concentrated on the chlorinated rings. The FMOs of SFIC-Cl are linear combinations of the FMOs of the monomeric systems MF-Ph, depicted in Figure 4.3.

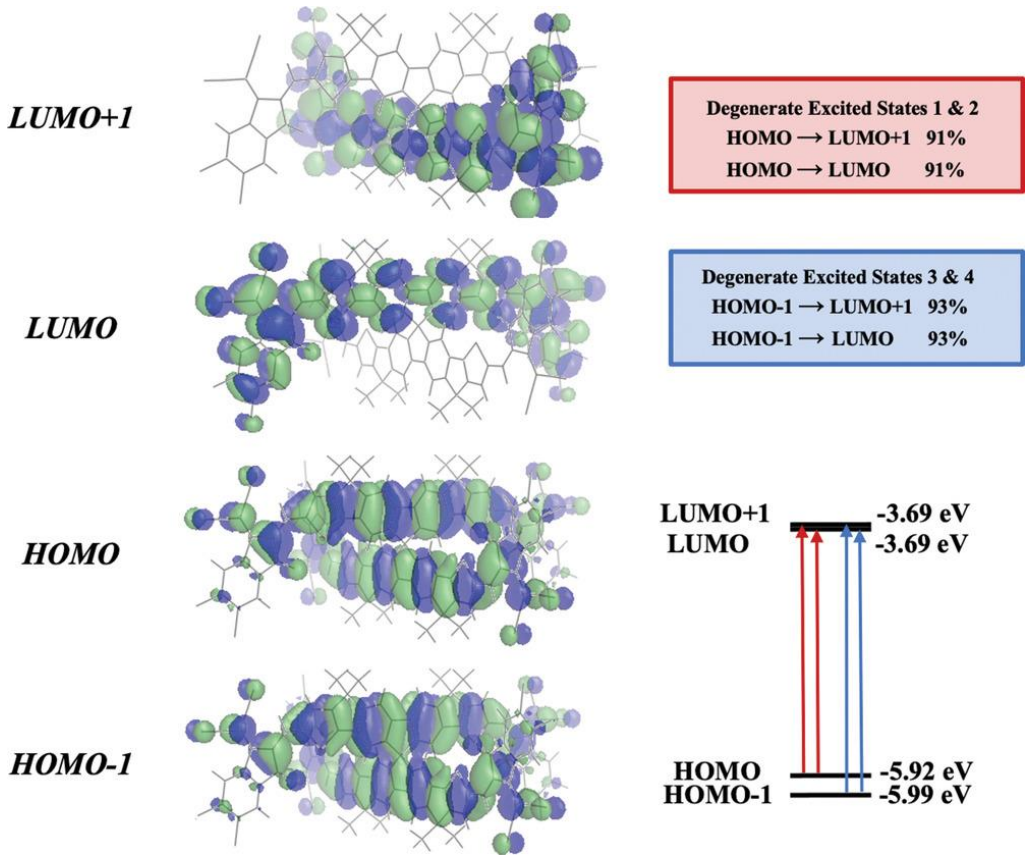

Figure 4.5. Frontier molecular orbitals (left) and depiction of the four lowest energy excited states (right) of SFIC-Cl.

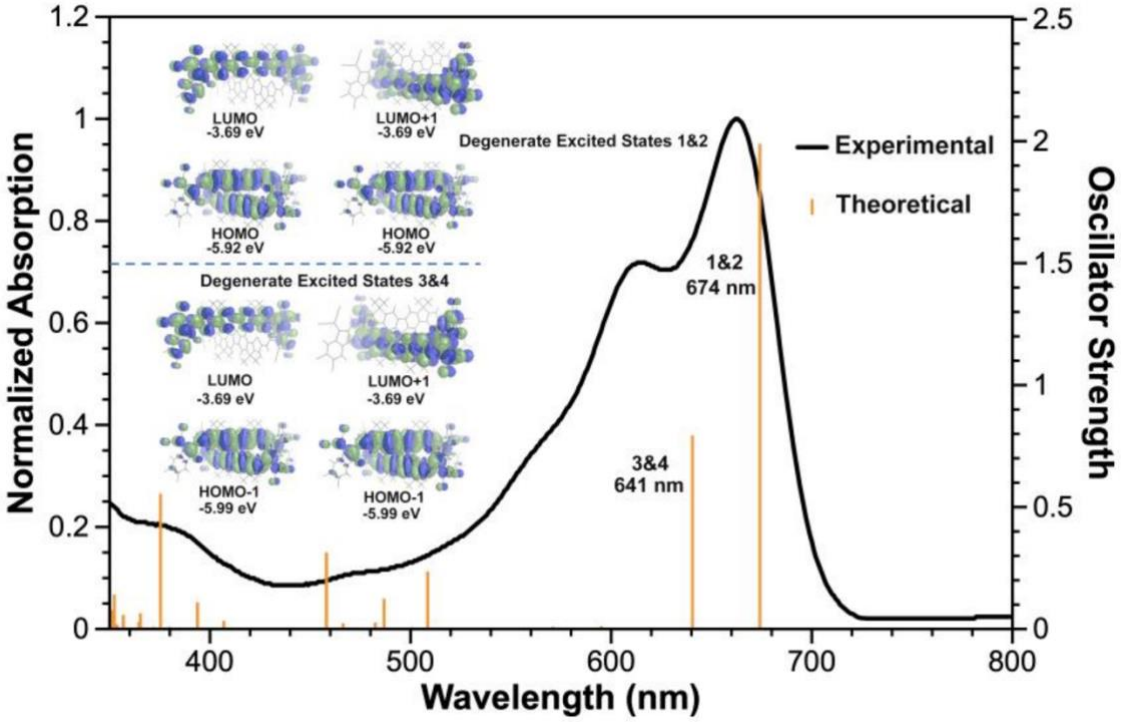

Figure 4.6. Experimental absorption spectrums (black line) and calculated line spectrum (vertical orange lines) of SFIC-Cl in $CHCl_3$.

To further investigate the behavior of the molecules upon excitation, we employed time-dependent DFT (TD-DFT) calculations using B3LYP/6-31G(d) with the polarizable continuum model for solvation by chloroform. The lowest 100 excited states were calculated in order to simulate the absorption profile of SFIC-Cl. The plots of experimental absorbance and calculated excited states are depicted in Figure 4.5 and Figure 4.6, which correspond well to each other. The lowest energy excited state, which gives rise to the transition with the highest oscillator strength, is similar in wavelength to experimental values. We further analyzed the excited states of SFIC-Cl. Two strong excitations are observed at 674 and 641 nm. Each of these consists of two degenerate excitations (Exc 1 and Exc 2). The first set of excitations occurs at 674 nm, with oscillator strengths of f = 1.99. The dominant transition in Exc 1 is the HOMO→LUMO transition (91%) while for Exc 2, HOMO→LUMO+1 is the dominant transition (91%). The second set of

excitations occurs at 641 nm, with oscillator strengths of f = 0.79, and the dominant transitions for Exc 1 and Exc 2 are HOMO-1→LUMO and HOMO-1→LUMO+1, which each comprising 93% orbital contribution.

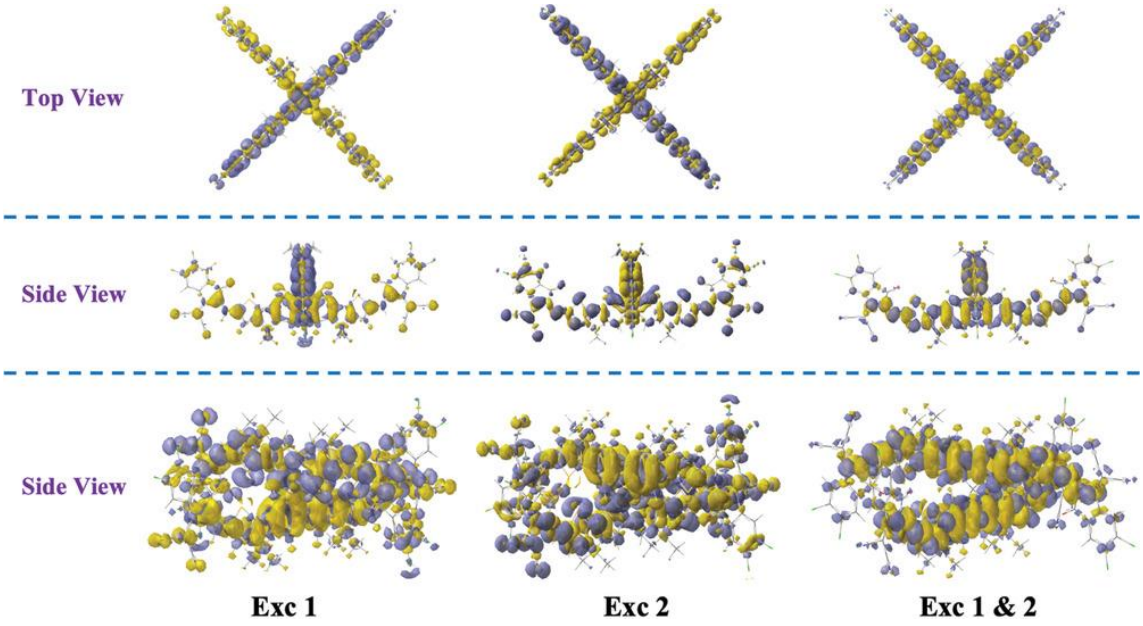

Figure 4.7. Electron density difference plots of degenerate excitations A of SFIC-Cl depicting electron density going from yellow to purple regions from different views (isodensity = 0.004).

In order to analyze the charge transfer character of these molecules, we plotted electron density differences that occur upon excitation. Recalling our earlier discussion, the transition to the lowest excited state of SFIC-Cl consists of two degenerate excitations. The electron density difference plots going from ground state to degenerate excited state 1 and degenerate excited state 2 are shown in the left and middle of Figure 4.7. The yellow regions represent areas of positive electron density, and the purple regions represent areas of negative electron density. For degenerate excitation 1, the electron density travels from the donor portion of the bottom half of the molecule (yellow) to the outer peripheral regions of the top half of the molecule (purple). The scenario is reversed in degenerate excitation 2. When these two dissimilar plots are added together, the

difference plot shows that charge transfer occurs simultaneously across the entire molecule and the two halves are symmetrical (Figure 4.7). The uniform and effective charge transfer offers SFIC-Cl good carrier-transport properties.

4.4. Conclusion

In summary, we have employed fused extended spiroconjugation and chlorination to devise a new molecule, SFIC-Cl. Theoretical calculations shows that spiroconjugation is effective and involves the HOMOs of each plane of the molecule. This offers excellent absorption, solubility, and energy levels owing to spiroconjugation and the chlorine atoms. Remarkable transport properties favoring applications in OFET, OPV, and OLED devices are also observed. These results demonstrate that chlorinated fused spiroconjugation provides new possibilities for development of high-performance organic semiconductors for hybrid organic electronic devices.

4.5. References

(1) Liu, Q.; Bottle, S. E.; Sonar, P. *Adv. Mater.* **2020**, *32*, 1903882.

(2) Surya, S. G.; Raval, H. N.; Ahmad, R.; Sonar, P.; Salama, K. N.; Rao, V. R. *TrAC Trends Anal. Chem.* **2019**, *111*, 27–36.

(3) Do, T.-T.; Chavhan, S.; Subbiah, J.; Ou, T.-H.; Manzhos, S.; Jones, D.; Bell, J. M.; Jou, J.-H.; Sonar, P. *New J. Chem.* **2019**, *43*, 9243–9254.

(4) Saragi, T. P. I.; Spehr, T.; Siebert, A.; Fuhrmann-Lieker, T.; Salbeck, J. *Chem. Rev.* **2007**, *107*, 1011–1065.

(5) Rios, R. *Chem. Soc. Rev.* **2012**, *41*, 1060–1074.

(6) Zhang, J.; Ugrinov, A.; Zhang, Y.; Zhao, P. *Angew. Chem. Int. Ed.* **2014**, *53*, 8437–8440.

(7) Zhang, Y.; Wei, J.; Chi, Y.; Zhang, X.; Zhang, W.-X.; Xi, Z. *J. Am. Chem. Soc.* **2017**, *139*, 5039–5042.

(8) Simmons, H. E.; Fukunaga, T. *J. Am. Chem. Soc.* **1967**, *89*, 5208–5215.

(9) Govindan, V.; Yang, K.-C.; Fu, Y.-S.; Wu, C.-G. *New J. Chem.* **2018**, *42*, 7332–7339.

(10) Romain, M.; Thiery, S.; Shirinskaya, A.; Declairieux, C.; Tondelier, D.; Geffroy, B.; Jeannin, O.; Rault-Berthelot, J.; Métivier, R.; Poriel, C. *Angew. Chem. Int. Ed.* **2015**, *54*, 1176–1180.

(11) Tao, Y.; Yang, C.; Qin, J. *Chem. Soc. Rev.* **2011**, *40*, 2943–2970.

(12) Lai, M.-Y.; Chen, C.-H.; Huang, W.-S.; Lin, J. T.; Ke, T.-H.; Chen, L.-Y.; Tsai, M.-H.; Wu, C.-C. *Angew. Chem. Int. Ed.* **2008**, *47*, 581–585.

(13) Thiery, S.; Tondelier, D.; Geffroy, B.; Jacques, E.; Robin, M.; Métivier, R.; Jeannin, O.; Rault-Berthelot, J.; Poriel, C. *Org. Lett.* **2015**, *17*, 4682–4685.

(14) Nguyen, W. H.; Bailie, C. D.; Unger, E. L.; McGehee, M. D. *J. Am. Chem. Soc.* **2014**, *136*, 10996–11001.

(15) Wu, X.-F.; Fu, W.-F.; Xu, Z.; Shi, M.; Liu, F.; Chen, H.-Z.; Wan, J.-H.; Russell, T. P. *Adv. Funct. Mater.* **2015**, *25*, 5954–5966.

(16) Wu, Y.; Zhang, J.; Fei, Z.; Bo, Z. *J. Am. Chem. Soc.* **2008**, *130*, 7192–7193.

(17) Saragi, T. P. I.; Fuhrmann-Lieker, T.; Salbeck, J. *Adv. Funct. Mater.* **2006**, *16*, 966–974.

(18) Nakagawa, T.; Ku, S.-Y.; Wong, K.-T.; Adachi, C. *Chem. Commun.* **2012**, *48*, 9580–9582.

(19) Luo, J.; Zhou, Y.; Niu, Z.-Q.; Zhou, Q.-F.; Ma, Y.; Pei, J. *J. Am. Chem. Soc.* **2007**, *129*, 11314–11315.

(20) Romain, M.; Tondelier, D.; Vanel, J.-C.; Geffroy, B.; Jeannin, O.; Rault-Berthelot, J.; Métivier, R.; Poriel, C. *Angew. Chem. Int. Ed.* **2013**, *52*, 14147–14151.

(21) Bach, U.; Lupo, D.; Comte, P.; Moser, J. E.; Weissörtel, F.; Salbeck, J.; Spreitzer, H.; Grätzel, M. *Nature* **1998**, *395*, 583–585.

(22) Feng, J.; Fu, L.; Geng, H.; Jiang, W.; Wang, Z. *Chem. Commun.* **2020**, *56*, 912–915.

(23) Hu, Y.; Wang, D.; Baumgarten, M.; Schollmeyer, D.; Müllen, K.; Narita, A. *Chem. Commun.* **2018**, *54*, 13575–13578.

(24) Jeon, N. J.; Lee, H. G.; Kim, Y. C.; Seo, J.; Noh, J. H.; Lee, J.; Seok, S. II. *J. Am. Chem. Soc.* **2014**, *136*, 7837–7840.

(25) Fournier, J.-H.; Maris, T.; Wuest, J. D. *J. Org. Chem.* **2004**, *69*, 1762–1775.

(26) Song, K. C.; Singh, R.; Lee, J.; Sin, D. H.; Lee, H.; Cho, K. *J. Mater. Chem. C* **2016**, *4*, 10610–10615.

(27) Rao, M. R.; Desmecht, A.; Perepichka, D. F. *Chem. – A Eur. J.* **2015**, *21*, 6193–6201.

(28) Poriel, C.; Barrière, F.; Thirion, D.; Rault-Berthelot, J. *Chem. – A Eur. J.* **2009**, *15*, 13304–13307.

(29) Facchetti, A.; Yoon, M.-H.; Stern, C. L.; Katz, H. E.; Marks, T. J. *Angew. Chem. Int. Ed.* **2003**, *42*, 3900–3903.

(30) Facchetti, A.; Mushrush, M.; Katz, H. E.; Marks, T. J. *Adv. Mater.* **2003**, *15*, 33–38.

(31) Park, J.-J.; Kim, Y.-A.; Lee, S.-H.; Kim, J.; Kim, Y.; Lim, D.-H.; Kim, D.-Y. *ACS Appl. Polym. Mater.* **2019**, *1*, 27–35.

(32) Tang, M. L.; Oh, J. H.; Reichardt, A. D.; Bao, Z. *J. Am. Chem. Soc.* **2009**, *131*, 3733–3740.

(33) Oh, J. H.; Suraru, S.; Lee, W.-Y.; Könemann, M.; Höffken, H. W.; Röger, C.; Schmidt, R.; Chung, Y.; Chen, W.-C.; Würthner, F.; Bao, Z. *Adv. Funct. Mater.* **2010**, *20*, 2148–2156.

(34) Meng, D.; Wang, R.; Lin, J. B.; Yang, J. L.; Nuryyeva, S.; Lin, Y.-C.; Yuan, S.; Wang, Z.-K.; Zhang, E.; Xiao, C.; Zhu, D.; Jiang, L.; Zhao, Y.; Li, Z.; Zhu, C.; Houk, K. N.; Yang, Y. *Adv. Mater.* **2021**, *33*, 2006120.

(35) *Supporting Information of:* Meng, D.; Wang, R.; Lin, J. B.; Yang, J. L.; Nuryyeva, S.; Lin, Y.-C.; Yuan, S.; Wang, Z.-K.; Zhang, E.; Xiao, C.; Zhu, D.; Jiang, L.; Zhao, Y.; Li, Z.; Zhu, C.; Houk, K. N.; Yang, Y. *Adv. Mater.* **2021**, *33*, 2006120.

(36) *Gaussian 09*, Revision D.01, Frisch, M. J.; Trucks, G. W.; Schlegel, H. B.; Scuseria, G. E.; Robb, M. A.; Cheeseman, J. R.; Scalmani, G.; Barone, V.; Mennucci, B.; Petersson, G. A.; Nakatsuji, H.; Caricato, M.; Li, X.; Hratchian, H. P.; Izmaylov, A. F.; Bloino, J.; Zheng, G.; Sonnenberg, J. L.; Hada, M.; Ehara, M.; Toyota, K.; Fukuda, R.; Hasegawa, J.; Ishida, M.; Nakajima, T.; Honda, Y.; Kitao, O.; Nakai, H.; Vreven, T.; Montgomery, J. A. Jr.; Peralta, J. E.; Ogliaro, F.; Bearpark, M.; Heyd, J. J.; Brothers, E.; Kudin, K. N.; Staroverov, V. N.; Keith, T.; Kobayashi, R.; Normand, J.; Raghavachari, K.; Rendell, A.; Burant, J. C.; Iyengar, S. S.; Tomasi, J.; Cossi, M.; Rega, N.; Millam, J. M.; Klene, M.; Knox, J. E.; Cross, J. B.; Bakken, V.; Adamo, C.; Jaramillo, J.; Gomperts, R.; Stratmann, R. E.; Yazyev, O.; Austin,

A. J.; Cammi, R.; Pomelli, C.; Ochterski, J. W.; Martin, R. L.; Morokuma, K.; Zakrzewski, V. G.; Voth, G. A.; Salvador, P.; Dannenberg, J. J.; Dapprich, S.; Daniels, A. D.; Farkas, O.; Foresman, J. B.; Ortiz, J. V.; Cioslowski, J.; Fox, D. J. *Gaussian, Inc*., Wallingford CT, **2013**.

(37) Lin, J. B.; Jin, Y.; Lopez, S. A.; Druckerman, N.; Wheeler, S. E.; Houk, K. N. *J. Chem. Theory Comput.* **2017**, *13*, 5624–5638.

(38) Becke, A. D. *J. Chem. Phys.* **1993**, *98*, 5648–5652.

(39) Lee, C.; Yang, W.; Parr, R. G. *Phys. Rev. B* **1988**, *37*, 785–789.

(40) Stephens, P. J.; Devlin, F. J.; Chabalowski, C. F.; Frisch, M. J. *J. Phys. Chem.* **1994**, *98*, 11623–11627.

(41) Vosko, S. H.; Wilk, L.; Nusair, M. *Can. J. Phys.* **1980**, *58*, 1200–1211.

(42) Kim, S.; Lee, J. K.; Kang, S. O.; Ko, J.; Yum, J.-H.; Fantacci, S.; De Angelis, F.; Di Censo, D.; Nazeeruddin, M. K.; Grätzel, M. *J. Am. Chem. Soc.* **2006**, *128*, 16701–16707.

(43) Abbotto, A.; Barolo, C.; Bellotto, L.; Angelis, F. De; Grätzel, M.; Manfredi, N.; Marinzi, C.; Fantacci, S.; Yum, J.-H.; Nazeeruddin, M. K. *Chem. Commun.* **2008**, *42*, 5318–5320.

(44) Salassa, L.; Garino, C.; Salassa, G.; Gobetto, R.; Nervi, C. *J. Am. Chem. Soc.* **2008**, *130*, 9590–9597.

(45) Fan, W.; Tan, D.; Deng, W.-Q. *ChemPhysChem* **2012**, *13*, 2051–2060.

Chapter 5. Designing Surface Ligand Management for Stable $FAPbI_3$ Perovskite Quantum Dot-based Solar Cells

5.1. Background

Semiconductor colloidal quantum dots (CQDs) have emerged as promising materials for next-generation photovoltaic devices owing to their unique features, such as low-temperature processability, tunable absorption, ability to design flexible devices, and multiple exciton generation.[1-4] A variety of semiconductor CQDs have been studied, such as PbS, PbSe, CdS, CdSe, and CdTe, with power-conversion efficiencies (PCEs) exceeding 10% achieved through development of surface chemistry.[4-8] Recently, a new class of halide perovskite CQDs have been added to the pool of semiconductor CQDs[9-11] and have shown great promise when incorporated into photovoltaic devices, breaking the record PCE of CQD photovoltaics.[12] The halide perovskite materials generally have an ABX_3 structure, where A is a monovalent organic cation or an alkali metal cation, B is a divalent cation (e.g., Pb^{2+}, Sn^{2+}) and X is a halide anion (e.g., Cl^-, Br^-, I^-). These materials exhibit a unique combination of high absorption coefficients, long carrier diffusion lengths and small exciton binding energy, making perovskite CQDs competitive with conventional chalcogenide CQDs for efficient photovoltaic devices.[13-16] Furthermore, it has been demonstrated that the enhanced contribution of surface energy in CQDs can stabilize the desirable cubic $CsPbI_3$ perovskite phase, which is thermodynamically unfavorable in bulk form at low temperature. This provides a new strategy of improving the stability of perovskite solar cells.[9]

The ionic bonding character of the halide perovskite materials makes them sensitive to polar solvents, resulting in accelerated degradation of perovskite CQDs upon exposure to such solvents.[17-19] This has posed the difficulty in dealing with the long organic ligands on the surface of as-synthesized perovskite CQDs, which are detrimental to carrier transport in CQD solar cells.

Furthermore, the relatively weaker bonding of the organic cations with inorganic cages (PbI_6 octahedra) in organic-inorganic hybrid perovskite CQDs compared with their inorganic counterparts[20-22] causes them to be even more vulnerable to polar solvents, posing greater challenges to effective treatment of the ligands. Hence, only few studies on perovskite CQD solar cells have been reported so far, with photoactive materials limited to cesium-containing inorganic perovskite CQDs.[9-12,23] However, the cesium-containing perovskite materials have a relatively larger bandgap (1.73 eV for $CsPbI_3$) and shorter carrier lifetime compared with their organic-inorganic hybrid counterparts, which limit further enhancement of PCE.[24,25] In this regard, formamidium lead triiodide ($FAPbI_3$) has the most desirable bandgap (ca. 1.5 eV) among the Pb-based perovskite materials.[26] Furthermore, the faster formation of large polaron in the organic-inorganic hybrid perovskite than in its inorganic counterparts would make $FAPbI_3$ CQD more desirable than $CsPbI_3$ CQD in terms of charge-transporting properties.[22]

Here, we introduce efficient strategies for managing the surface ligands on $FAPbI_3$ perovskite CQDs. Rational design of post-synthetic processes enabled effective control of ligand density. Because of the well-designed ligand control, $FAPbI_3$ CQDs solar cell with an initial PCE of 8.38% was demonstrated for the first time without device optimization. Furthermore, despite poor phase stability of bulk $FAPbI_3$,[27] the $FAPbI_3$ CQDs and devices showed superior ambient and operational stability over bulk $FAPbI_3$ films and devices.

5.2. Methodology

5.2.1. Preparation of FA-oleate and Cs-oleate precursors

0.521 g of formamidine acetate, 16 mL of octadecene (ODE) and 8 mL of oleic acid (OA) were added to a round-bottom flask and degassed under vacuum for 10 min at room temperature.

The mixture was then heated to 130 °C under N_2 gas until all FA-acetate reacted with OA, yielding a clear solution of FA-oleate. The solution was then put under vacuum for 30 min at 45 °C. For the preparation of Cs-oleate precursor, 0.077 g of Cs_2CO_3, 308 μL of OA and 7.7 mL of ODE were added to a round-bottom flask and dried under vacuum for 1 h at 120 °C, and then heated to 150 °C under N_2 gas resulting in a clear solution of Cs-oleate. Both, FA-oleate and Cs-oleate precursors needed to be preheated to 100 °C before use.

5.2.2. Synthesis of $FAPbI_3$ CQDs

For the synthesis of $FAPbI_3$ CQDs, 0.860 g of PbI_2 and 50 mL of ODE were added to a 3-neck flask and degassed under vacuum for 1 h at 120 °C. 5 mL of dried oleylamine (OLA) and 10 mL of dried OA (dried under vacuum at 120 °C for 1 h) were injected at 120 °C under N_2. After complete dissolution of PbI_2, the solution was cooled to 80 °C before swift injection of FA-acetate precursor. The mixture was then quickly cooled in an ice bath. For the synthesis of $CsPbI_3$ CQDs, 1 g of PbI_2 and 50 mL of ODE were loaded into a 3-neck flask and degassed under vacuum for 1 h at 120 °C. 5 mL of dried OLA and 5 of mL dried OA (dried under vacuum at 120 °C for 1 h) were injected under N_2, after which the temperature was elevated to 150 °C allowing for the complete dissolution of PbI_2. The solution was heated to 170 °C before swift injection of Cs-oleate precursor. After around 5 s stirring, the mixture was cooled down in an ice bath.

5.2.3. Surface ligand management of $FAPbI_3$ CQDs in solution phase

In the first cycle of ligand treatment, 2-pentanol was added to the $FAPbI_3$ CQDs solution (1:1 v:v ratio). After slight shaking, the $FAPbI_3$ CQDs were separated by centrifugation at 8000 rpm for 5 min. The supernatant was discarded and the $FAPbI_3$ CQDs could be collected by

redispersion in a nonpolar solvent for further characterization or device fabrication. In the second cycle of ligand treatment, mixed ACN/toluene (1:4 v:v ratio) solvent was added to induce $FAPbI_3$ CQDs flocculation. The $FAPbI_3$ CQDs were then separated by centrifugation at 8000 rpm for 2 min. The supernatant was discarded and the $FAPbI_3$ CQDs were re-dispersed in hexane, yielding $FAPbI_3$ CQDs with reduced ligand density. The solution was centrifuged at 4000 rpm for 5 min to remove the excess salts and aggregated $FAPbI_3$ nanoparticles. After storage at 4 °C for 24 h, the CQDs solution was centrifuged at 4000 rpm for 5 min to remove the solidified excess oleyl species and ODE.

5.2.4. Surface ligand management of $FAPbI_3$ CQDs in solid phase

The CQDs solution was concentrated to around 30 mg/mL in octane for solid-state ligand treatment. As shown in Scheme 5.1, the CQDs were spin casted on a substrate at 2000 rpm for 30 s, after which the CQDs film was rinsed twice by dropping EtOAc onto it while the substrate was spinning. This procedure was repeated multiple times to build a 150-200 nm-thick film of CQDs with minimized ligand density.

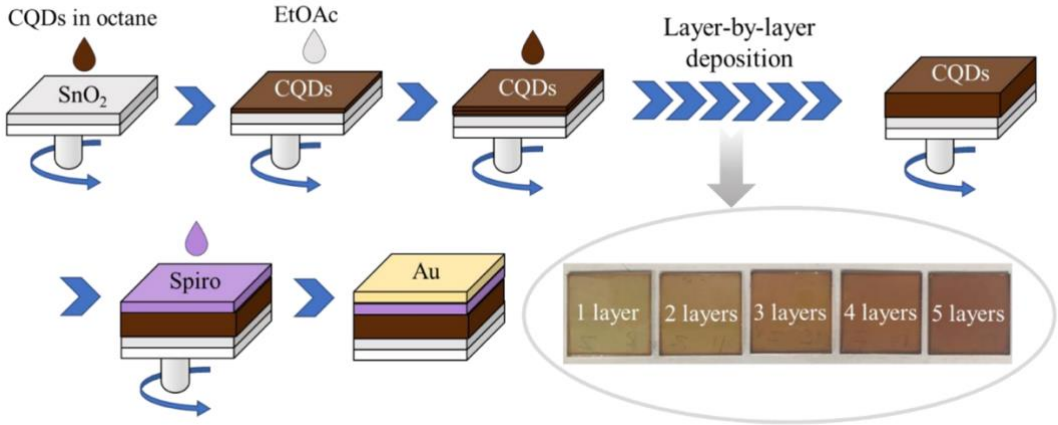

Scheme 5.1. Schematic representation of device fabrication process (inset: photographs of CQDs film with the increasing number of layers).

5.2.5. Fabrication of photovoltaic devices with $FAPbI_3$ CQDs

Glass/indium doped tin oxide (ITO) substrates were cleaned with successive sonication in detergent, deionized (DI) water, acetone and 2-propanol each for 15 min, respectively. The cleaned substrates were further treated in ultraviolet-ozone chamber for 30 min to remove the organic residual and enhance the wettability. Before use, the SnO_2 nanoparticle colloidal precursor solution was diluted with H_2O to 1.5%. Final solution was spin-coated onto glass/ITO substrates at 3000 rpm for 30 s, and then baked on a hot plate in ambient air at 150 °C for 30 min. For devices based on CQDs with only 1-cycle or 2-cycle ligand treatment, the CQDs solution obtained was concentrated in octane (to around 30 mg/mL) and spin-coated on the substrates at 2000 rpm for 30 s, which was repeated multiple times to build a 150-200 nm-thick film of CQDs (Scheme 5.1). For devices based on CQDs with full steps of ligand treatment, the CQDs were deposited on the substrate using the procedure described above. The bulk $FAPbI_3$ films were fabricated using the adduct method with modifications.[28]

The adduct solution was prepared by dissolving equimolar amount of $HC(NH_2)_2I$ (FAI), PbI_2 and N-Methyl-2-pyrrolidone (NMP) in N,N-dimethylformamide (DMF). Typically, 172 mg of FAI, 461 mg of PbI_2 and 99 mg of NMP were dissolved in 600 mg of DMF. The perovskite solution was spin-coated on SnO_2-coated ITO glass at 4000 rpm for 20 s, to which 0.15 mL of diethyl ether was dropped after 10 s. The resulting adduct film was annealed at 100 ^oC for 1 min, followed by 150 ^oC for 10 min. The spiro-MeOTAD solution was prepared by dissolving 85.8 mg of spiro-MeOTAD in 1 mL of chlorobenzene, which was doped with 33.8 μl of 4-tert-butylpyridine and 19.3 μl of Li-TFSI (520 mg/mL in acetonitrile) solution. The spiro-MeOTAD solution was spin-coated on the perovskite layer at 3000 rpm for 20 s by dropping 17 μl of the solution on the

spinning substrate (Scheme 5.1). On top of the spiro-MeOTAD layer, ca. 100 nm-thick gold layer was thermally evaporated at 0.5 Å/s to be used as an electrode.

5.3. Results and Discussion

5.3.1. Morphological and structural properties of $FAPbI_3$ CQDs.

$FAPbI_3$ CQDs were synthesized via a modified hot-injection method,[29] yielding a nearly cubic-shaped ensemble with an average size of 17.7±2.5 nm (Figures 5.1A and 5.2). The synthesized $FAPbI_3$ CQDs were confirmed to be cubic perovskite phase with no secondary phase from X-ray diffraction (XRD) measurement (Figure 5.1B).[30] For comparison, the XRD pattern of the bulk $FAPbI_3$ film was compared whereby hexagonal non-perovskite phase (δ phase) was observed.[28]

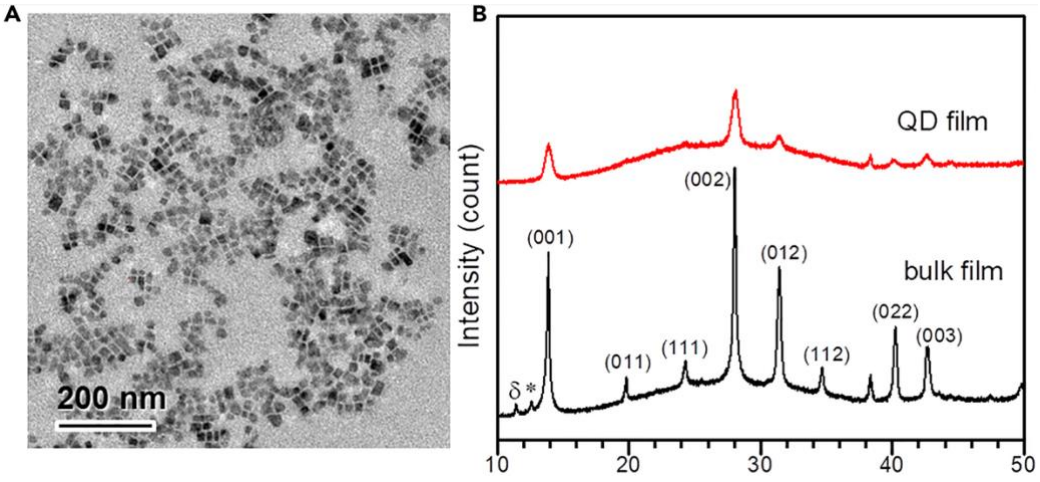

Figure 5.1. Morphology and crystal structure of $FAPbI_3$ CQDs. Transmission electron microscopic image (A) and X-ray diffraction (XRD) patterns (B) of as-synthesized $FAPbI_3$ CQDs and bulk films. δ and * indicate hexagonal non-perovskite phase and PbI_2, respectively.

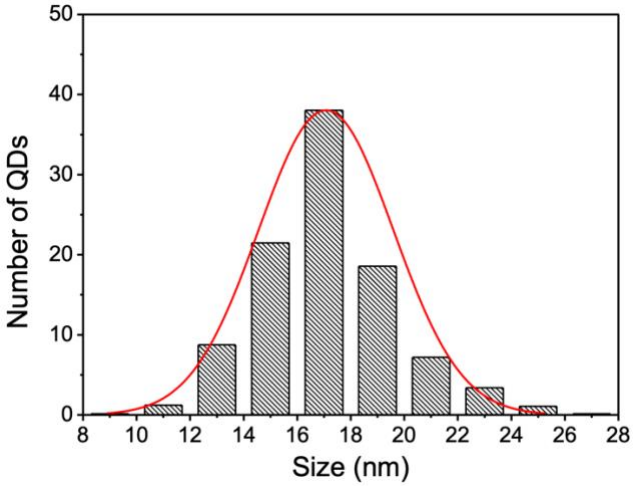

Figure 5.2. Size distribution of $FAPbI_3$ CQDs measured from Figure 5.1A.

5.3.2. Motivation for and design of rational solvent treatment of $FAPbI_3$ CQDs.

The as-synthesized $FAPbI_3$ CQDs were capped with oleic acid and oleylamine, which act as surface ligands that are necessary to maintain good dispersion. However, these long insulating ligands are detrimental to efficient charge-carrier transport because they introduce large potential barriers that prevent electrical coupling between the CQDs.[31] Therefore, dealing with the surface ligands become the prerequisite to constructing efficient photovoltaic devices based on perovskite CQDs. Upon synthesis, the surface of perovskite CQDs is reported to be terminated by oleylammonium halide and oleylammonium carboxylates, which are ionically bonded to the perovskite surface.[32] Such ionic nature of the ligand binding causes ligands to be highly loose and easy to completely desorb once attacked by any polar solvents. Hence, this results in difficulty to retain the colloidal integrity during the surface treatment.[17,33] Also, the ionic binding character of the perovskite lattice as well as the organic component FA^+ make it more challenging to retain perovskite structural integrity in highly polar solvents because of its weaker bonding with surrounding PbI_6 cages than inorganic counterparts, evidenced by relatively poor thermal stability and higher degree of rotational motion.[17] Furthermore, relatively poor phase stability of $FAPbI_3$

compared with other organic-inorganic hybrid perovskites, as observed in their bulk form, would require more delicate post-synthetic processes. As a result, no traditional surface treatment technique can be applied because they involve highly polar solvents such as methanol and acetone. These factors motivated us to design a customized surface treatment for $FAPbI_3$ perovskite CQDs.[34,35]

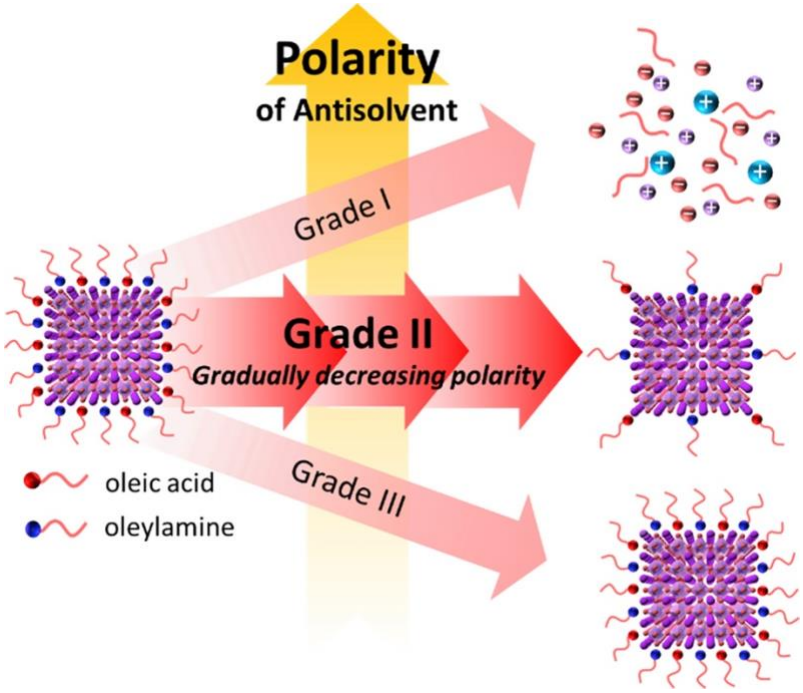

Scheme 5.2. Strategy for designing rational solvent-treatment routes to manage surface ligands of $FAPbI_3$ CQDs.

To design a rational surface treatment process, we classified the solvents into three grades by their polarity (Scheme 5.2). The highly polar solvents bearing the strongest dipoles fall under the "grade I" category, where ionic bonds in $FAPbI_3$ can be completely destroyed (Scheme 5.2). At the other end, solvents with too low polarity (grade III) will not be able to break the bond between the ligand and $FAPbI_3$.[34] To effectively handle the surface ligands without destroying CQDs, proper antisolvents with moderate polarity (grade II) should be employed. A series of

commonly used solvents with different polarity were tested (listed in Table 5.1). As a result, water, methanol, ethanol and isopropanol were classified as grade I solvents that would cause immediate degradation of $FAPbI_3$ CQDs once added; chlorobenzene, toluene, octane, and hexane were classified as grade III solvents that are not able to remove the ligands. By avoiding grade I and grade III solvents, a novel surface treatment method was successfully developed such that the ligand density was sequentially decreased in solution and in the solid phase while maintaining the integrity of $FAPbI_3$ CQDs. This was achieved by employing a set of grade II solvents with gradually reduced polarity in the surface treatment cycle.

Table 5.1. Summary of solvents used for ligand treatment of $FAPbI_3$ CQDs.[36] The polarity of mixed solvent was determined by the arithmetic average of solvent polarity adjusted according to the volume fraction of each solvent.[37]

'Grade I' solvent				
Name	Water	Methanol	Ethanol	Isopropanol
Relative polarity index	1.000	0.762	0.654	0.546
'Grade II' solvent				
Name	t-butanol	2-pentanol	ACN/toluene (v:v 2:3)	EtOAc
Relative polarity index	0.506	0.488	0.243	0.228
'Grade III' solvent				
Name	CB	Toluene	Octane	Hexane
Relative polarity index	0.188	0.099	0.012	0.009

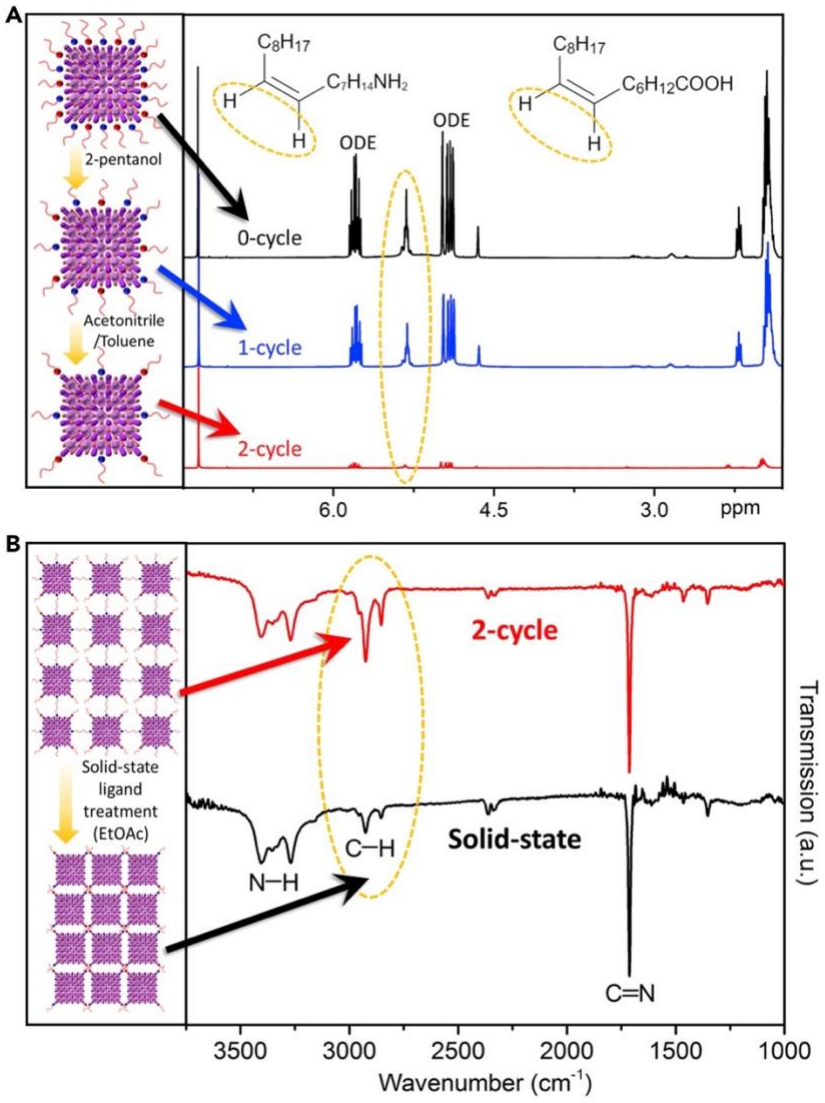

Figure 5.3. Gradual reduction in ligand density with surface treatment. (A) Nuclear magnetic resonance spectra of $FAPbI_3$ CQDs with increasing number of surface treatment cycles in solution, indicating a gradual decrease of the oleyl species (right) and schematic illustration of the ligand density control during solution-state surface treatment (left). Molecular structure of the oleyl species are shown as inset. Functional groups and corresponding signals are highlighted with dashed yellow lines. (B) Fourier transform infrared spectra of $FAPbI_3$ CQDs before and after solid-state surface treatment (right) and a schematic illustration of the ligand density change and inter-dot coupling during the solid-state surface treatment (left). C-H modes associated with oleyl species are highlighted with dashed yellow lines.

Our surface treatment process consists of three cycles. As shown in Figure 5.3A (left), the first two cycles of surface treatment processes are in solution phase. In the first cycle, 2-pentanol was used as an antisolvent. Compared with commonly used antisolvents such as methanol, ethanol,

and propanol, 2-pentanol has a relatively longer alkyl chain with stronger electron-donating effect that can reduce the dipole of C-O bond and, thus, the polarity of the solvent.[36] Additionally, 2-pentanol is a protic solvent, which can assist in keeping FA^+ protonated in $FAPbI_3$ CQDs so as to maintain the ionic lattice structure of perovskite. t-Butanol was also tested and was found to induce flocculation of $FAPbI_3$ CQDs without destroying them.

However, the long-term stability of these CQDs was found to be poor, undergoing degradation within 12 hr. Since the polarity indices of t-butanol and 2-pentanol are similar, we further consider dimensions of component compatibility using the Hansen model.[38] If the Hansen distance between PbI_2 (one of the precursors of perovskite) and a chosen antisolvent is small, this indicates that such an antisolvent will easily dissolve PbI_2 and thus, cause the degradation of perovskite lattice. In the case of 2-pentanol and t-butanol, the Hansen parameters are as follows: $\delta_D = 15.8$, $\delta_P = 5.7$, $\delta_H = 14.5$ for t-butanol; and $\delta_D = 15.6$, $\delta_P = 6.4$, $\delta_H = 13.3$ for 2-pentanol; where δ_D, δ_P and δ_H are dispersion, polar and hydrogen-bonding parameters, respectively. Since Hansen parameters of lead salts are unknown, we made an assumption, as suggested in the literature, that their position on the three-dimensional Hansen graph is somewhere between the positions of dimethylformamide and dimethyl sulfoxide because both these solvents dissolve PbI_2 very well.[39,40] In this case, t-butanol shows shorter distance to the assumed Hansen parameters of PbI_2, indicating a stronger interaction of the t-butanol with PbI_2 than that of the 2-pentanol, which might lead to a faster degradation of perovskite lattice. As the dispersion and polar components of the two solvents are similar, the stronger hydrogen bonding between t-butanol and lead salts might play a more important role. Interestingly, the $FAPbI_3$ CQDs are destroyed if 2-pentanol is used again in the second cycle of surface treatment. This might be due to the lower ligand density on the surface of $FAPbI_3$ CQDs, which exposes more of the perovskite ionic lattice to the antisolvent.

Hence, the CQDs cannot further "tolerate" the polarity of 2-pentanol. To maintain the integrity of perovskite CQDs in the second cycle of surface treatment, a different grade II antisolvent with slightly lower polarity should be used. Mixed solvent of acetonitrile/toluene is well known for its adjustable polarity by varying the volume ratio of acetonitrile and toluene. By rational control of its polarity, acetonitrile/toluene (Table 5.1) was used in the second cycle of surface treatment to further decrease the ligand density on the surface of $FAPbI_3$ CQDs. The gradual reduction of the surface ligand density was monitored by nuclear magnetic resonance (NMR). As shown in Figure 5.3A, the total concentration of oleyl species (determined by the resonance of hydrogen atoms on a double bond) gradually reduced with increasing cycles of surface treatment. After the first cycle of surface treatment, strong resonance signals from octadecene and oleyl species (at around 5.3 ppm)[41] were still detected; while after the second cycle of surface treatment these signals became negligible, indicating an effective removal of ligands from the surface.

After two cycles of surface treatment in solution phase the majority of excess ligands were removed, while a small amount of ligands remained to maintain the colloidal integrity of $FAPbI_3$ CQDs. To further decrease the ligand density and thus, improve the inter-dot coupling without losing colloidal integrity of $FAPbI_3$ CQDs,[31] we carried out one more step of surface treatment during the film-formation process (Figure 5.3B, left). However, 2-pentanol and the mixed solvent of acetonitrile/toluene used in the first two cycles of surface treatment were not applicable in this step, as upon addition of them on the CQDs film the CQDs underwent immediate degradation. This is because after two cycles of ligand density reduction, $FAPbI_3$ CQDs were more exposed and, hence, more sensitive to the polarity of both the 2-pentanol and acetonitrile/toluene mixed solvent. Therefore, in the solid-state surface treatment process (third cycle), ethyl acetate (EtOAc) with a lower polarity (Table 5.1) was employed to rinse the $FAPbI_3$ CQD film. Additionally, the

shorter exposure time to antisolvent in solid-state than in solution-state surface treatment further minimizes the loss of CQD integrity. Fourier transform infrared spectra in Figure 5.3B (right) confirmed the decreased amount of the ligands in CQDs film with exposure to EtOAc. The signal intensity of C-H modes around 3,000 cm^{-1} reduced, which partially belongs to the oleyl species.[9]

5.3.3. Photovoltaic performance of surface-treated $FAPbI_3$ CQD-based devices.

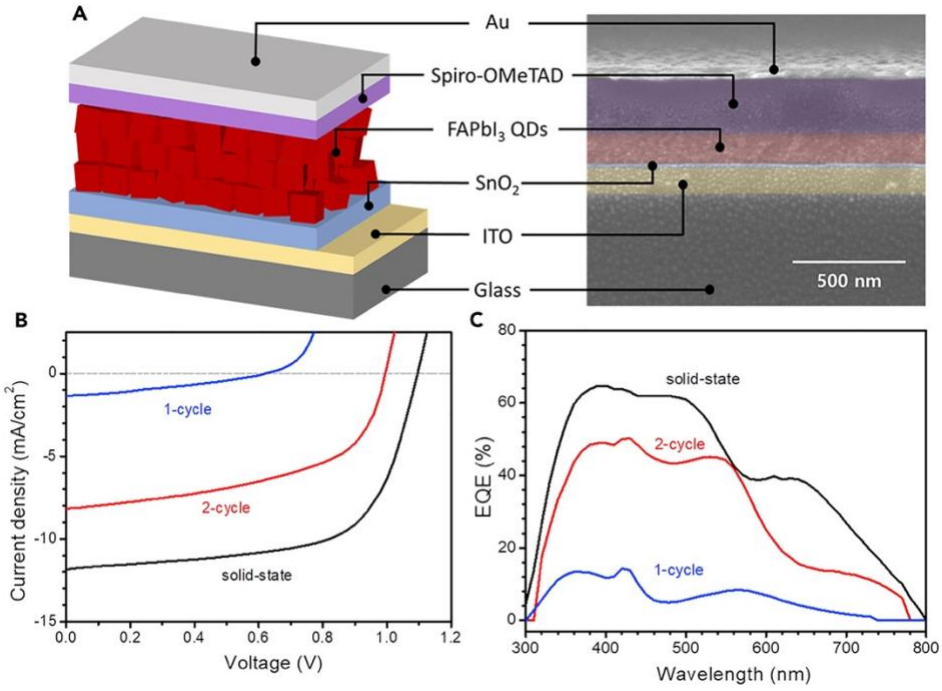

Figure 5.4. Photovoltaic performance of $FAPbI_3$ CQD devices with surface treatment. (A) Schematic of device structure and cross-sectional scanning electron microscopic image of the $FAPbI_3$ CQDs solar cell. (B) Current density-voltage (J-V) curves and (C) external quantum efficiency of the devices based on $FAPbI_3$ CQDs with increasing cycles of surface treatment.

Photovoltaic devices were fabricated with the $FAPbI_3$ CQDs as a photoactive material via layer-by-layer deposition at room temperature (Scheme 5.1). A schematic of the device structure along with the corresponding scanning electron microscopic cross-section image of the device is shown in Figure 5.4A. To correlate the ligand density on CQDs to the photovoltaic properties of resulting devices, we fabricated the devices based on $FAPbI_3$ CQDs with different cycles of surface

treatment. The corresponding current density-voltage (J-V) curves are shown in Figure 5.4B, where a gradual improvement in open-circuit voltage (V_{OC}), short-circuit current (J_{SC}), fill factor (FF) and consequently, the PCE was demonstrated with each step of the surface treatment process.

Table 5.2. Photovoltaic parameters of $FAPbI_3$ CQD solar cells with different cycles of ligand treatment. Short-circuit current density (J_{SC}), open circuit voltage (V_{OC}), fill factor (FF), power conversion efficiency (PCE).

Ligand treatment cycle	J_{SC} (mA/cm^2)	V_{OC} (V)	FF	PCE (%)
1-cycle	1.35	0.62	0.324	0.27
2-cycle	8.17	0.99	0.531	4.31
Solid state	11.84	1.10	0.644	8.38

The photovoltaic parameters are summarized in Table 5.2. The forward scan J-V curve of the device after a series of the surface treatments showed a high V_{OC} of 1.10 V, J_{SC} of 11.83 mA/cm^2 and FF of 64.42%, yielding a PCE of 8.38%. It is worth noting that the V_{OC} of the CQD device is relatively higher than that of the devices based on conventional chalcogenide CQDs.[4,8] This might be attributed to the relatively higher defect tolerance of perovskite materials, which make a large portion of the surface states in CQD film less detrimental to carrier transport and the resulting photovoltaic performance. As shown in Figure 5.4C, the devices showed an external quantum efficiency (EQE) onset at around 800 nm, which correlates with the onset of absorption. The EQE onset of the devices incorporating 1- and 2-cycle-treated films shows a slight blue shift compared with the one using the QD film post solid-state surface treatment. Considering that the absorption onset has hardly changed upon different surface treatment cycles (see ref. 42), the EQE of the devices at longer wavelength region might be below the resolution of our measurement setup due to poor charge-collection efficiency. The EQE of devices progressively increased with increasing numbers of ligand treatment cycles. This signifies a gradual improvement in dot-to-dot

coupling as a result of decreasing ligand density and, therefore, better charge collection from the CQD film.[31] This proof-of-concept device without further optimization of the structure or process parameters suggests that $FAPbI_3$ CQDs have high potential in achieving highly efficient CQD solar cells.

5.3.4. Stability measurements of bulk $FAPbI_3$ and surface-treated $FAPbI_3$ CQD-based devices

Finally, we evaluated the stability of the devices under ambient and operational conditions, as shown in Figures 5.5A and B. Under ambient conditions, the $FAPbI_3$ CQD device showed excellent stability without any degradation in PCE for 60 days. In the case of the $FAPbI_3$ bulk film-based device, however, the PCE significantly degraded to 29.5% of the initial PCE, which is likely due to the conversion of α phase to δ phase under ambient conditions. Due to phase transition, the color of the device was completely bleached after 60 days, while that of the CQD device remained unchanged (inset of Figure 5.5A). Light stability of the devices was further explored by exposing the encapsulated devices to continuous illumination (90 ± 5 mW/cm^2). Devices were encapsulated under nitrogen atmosphere and exposed under open-circuit condition, of which stabilized power output was periodically measured under 1-sun illumination (Figure 5.5B). The bulk $FAPbI_3$ device showed a rapid initial decay followed by a slower decay with almost linear profile, which is in agreement with the previous report.[43] Upon exposure for 226 hr, the PCEs of the devices were degraded to 69.1% of the initial PCEs. Surprisingly, the CQD devices showed only marginal degradation (1.1% of the initial PCE) after 226 hr of the exposure. The superior light stability of the CQD devices over bulk devices offers a possible approach to enhancing the operational stability of the perovskite solar cells using a QD approach.

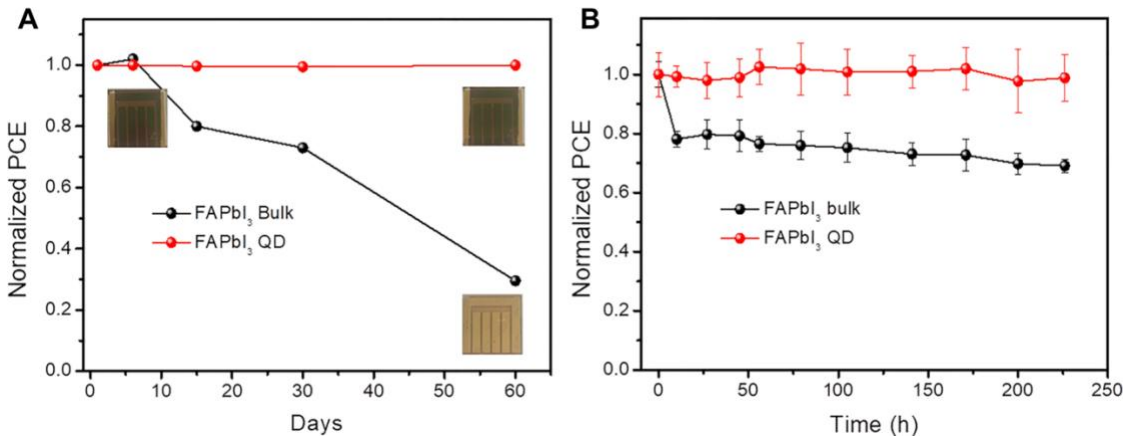

Figure 5.5. Stability of CQD and bulk $FAPbI_3$ devices and under ambient and operational conditions. (A) Evolution of power-conversion efficiency (PCE) of photovoltaic devices based on bulk $FAPbI_3$ and $FAPbI_3$ CQDs stored under ambient condition without encapsulation. Inset shows photos of the device before and after exposure. (B) Change in PCE of the encapsulated device under continuous illumination (90 ± 5 mW/cm^2). The devices were maintained under open-circuit condition at room temperature (ca. 30°C ± 3°C). The error bars indicate standard deviation of the PCEs measured from 6 devices for each condition.

5.4. Conclusion

In summary, the first $FAPbI_3$ CQD-based photovoltaic device has been achieved by effective control of surface ligand density using a rationally designed surface treatment process. A series of "grade II" solvents (with moderate polarity that can effectively reduce the ligand density, while maintaining the integrity of perovskite CQDs) with gradually reducing polarity were utilized in the process. Our proof-of-concept device showed a promising PCE exceeding 8% with a broad spectral response up to a near-infrared region. It is worth noting that the $FAPbI_3$ CQD films and devices have shown superior ambient and operational stability over their bulk form. We believe that our strategy to regulate the ligand density on the surface of hybrid perovskites will provide an effective methodological basis for achieving highly efficient and stable perovskite CQD optoelectronic devices.

5.5. References

(1) Kagan, C. R.; Lifshitz, E.; Sargent, E. H.; Talapin, D. V. *Science* **2016**, *353*, aac5523.

(2) McDonald, S. A.; Konstantatos, G.; Zhang, S.; Cyr, P. W.; Klem, E. J. D.; Levina, L.; Sargent, E. H. *Nat. Mater.* **2005**, *4*, 138–142.

(3) Nozik, A. J.; Beard, M. C.; Luther, J. M.; Law, M.; Ellingson, R. J.; Johnson, J. C. *Chem. Rev.* **2010**, *110*, 6873–6890.

(4) Carey, G. H.; Abdelhady, A. L.; Ning, Z.; Thon, S. M.; Bakr, O. M.; Sargent, E. H. *Chem. Rev.* **2015**, *115*, 12732–12763.

(5) Brown, P. R.; Kim, D.; Lunt, R. R.; Zhao, N.; Bawendi, M. G.; Grossman, J. C.; Bulović, V. *ACS Nano* **2014**, *8*, 5863–5872.

(6) Ning, Z.; Voznyy, O.; Pan, J.; Hoogland, S.; Adinolfi, V.; Xu, J.; Li, M.; Kirmani, A. R.; Sun, J.-P.; Minor, J.; Kemp, K. W.; Dong, H.; Rollny, L.; Labelle, A.; Carey, G.; Sutherland, B.; Hill, I.; Amassian, A.; Liu, H.; Tang, J.; Bakr, O. M.; Sargent, E. H. *Nat. Mater.* **2014**, *13*, 822–828.

(7) Tang, J.; Kemp, K. W.; Hoogland, S.; Jeong, K. S.; Liu, H.; Levina, L.; Furukawa, M.; Wang, X.; Debnath, R.; Cha, D.; Chou, K. W.; Fischer, A.; Amassian, A.; Asbury, J. B.; Sargent, E. H. *Nat. Mater.* **2011**, *10*, 765–771.

(8) Liu, H.; Li, T.; Han, W.-Y.; Chen, Q.; Huang, S.-Z.; Ming, E.-Y.; Sun, Q. *Front. Eng. Manage.* **2016**, *3*, 258–263.

(9) Swarnkar, A.; Marshall, A. R.; Sanehira, E. M.; Chernomordik, B. D.; Moore, D. T.; Christians, J. A.; Chakrabarti, T.; Luther, J. M. *Science* **2016**, *354*, 92–95.

(10) Liu, F.; Ding, C.; Zhang, Y.; Ripolles, T. S.; Kamisaka, T.; Toyoda, T.; Hayase, S.; Minemoto, T.; Yoshino, K.; Dai, S.; Yanagida, M.; Noguchi, H.; Shen, Q. *J. Am. Chem. Soc.* **2017**, *139*, 16708–16719.

(11) Hoffman, J. B.; Zaiats, G.; Wappes, I.; Kamat, P. V. *Chem. Mater.* **2017**, *29*, 9767–9774.

(12) Sanehira, E. M.; Marshall, A. R.; Christians, J. A.; Harvey, S. P.; Ciesielski, P. N.; Wheeler, L. M.; Schulz, P.; Lin, L. Y.; Beard, M. C.; Luther, J. M. *Sci. Adv.* **2017**, *3*, eaao4204.

(13) Yin, W.-J.; Yang, J.-H.; Kang, J.; Yan, Y.; Wei, S.-H. *J. Mater. Chem. A* **2015**, *3*, 8926–8942.

(14) Wehrenfennig, C.; Eperon, G. E.; Johnston, M. B.; Snaith, H. J.; Herz, L. M. *Adv. Mater.* **2014**, *26*, 1584–1589.

(15) Yin, W.-J.; Shi, T.; Yan, Y. *Adv. Mater.* **2014**, *26*, 4653–4658.

(16) Kovalenko, M. V; Protesescu, L.; Bodnarchuk, M. I. *Science* **2017**, *358*, 745–750.

(17) Akkerman, Q. A.; Rainò, G.; Kovalenko, M. V; Manna, L. *Nat. Mater.* **2018**, *17*, 394–405.

(18) Tong, Y.; Ehrat, F.; Vanderlinden, W.; Cardenas-Daw, C.; Stolarczyk, J. K.; Polavarapu, L.; Urban, A. S. *ACS Nano* **2016**, *10*, 10936–10944.

(19) Zhang, F.; Huang, S.; Wang, P.; Chen, X.; Zhao, S.; Dong, Y.; Zhong, H. *Chem. Mater.* **2017**, *29*, 3793–3799.

(20) Kulbak, M.; Gupta, S.; Kedem, N.; Levine, I.; Bendikov, T.; Hodes, G.; Cahen, D. *J. Phys. Chem. Lett.* **2016**, *7*, 167–172.

(21) Lee, J.-W.; Kim, D.-H.; Kim, H.-S.; Seo, S.-W.; Cho, S. M.; Park, N.-G. *Adv. Energy Mater.* **2015**, *5*, 1501310.

(22) Zhu, H.; Miyata, K.; Fu, Y.; Wang, J.; Joshi, P. P.; Niesner, D.; Williams, K. W.; Jin, S.; Zhu, X.-Y. *Science* **2016**, *353*, 1409–1413.

(23) Bian, H.; Bai, D.; Jin, Z.; Wang, K.; Liang, L.; Wang, H.; Zhang, J.; Wang, Q.; Liu, S. (F.). *Joule* **2018**, *2*, 1500–1510.

(24) Eperon, G. E.; Paternò, G. M.; Sutton, R. J.; Zampetti, A.; Haghighirad, A. A.; Cacialli, F.; Snaith, H. J. *J. Mater. Chem. A* **2015**, *3*, 19688–19695.

(25) Eperon, G. E.; Stranks, S. D.; Menelaou, C.; Johnston, M. B.; Herz, L. M.; Snaith, H. J. *Energy Environ. Sci.* **2014**, *7*, 982–988.

(26) Lee, J.-W.; Seol, D.-J.; Cho, A.-N.; Park, N.-G. *Adv. Mater.* **2014**, *26*, 4991–4998.

(27) Jeon, N. J.; Noh, J. H.; Yang, W. S.; Kim, Y. C.; Ryu, S.; Seo, J.; Seok, S. II. *Nature* **2015**, *517*, 476–480.

(28) Lee, J.-W.; Dai, Z.; Lee, C.; Lee, H. M.; Han, T.-H.; De Marco, N.; Lin, O.; Choi, C. S.; Dunn, B.; Koh, J.; Di Carlo, D.; Ko, J. H.; Maynard, H. D.; Yang, Y. *J. Am. Chem. Soc.* **2018**, *140*, 6317–6324.

(29) Protesescu, L.; Yakunin, S.; Kumar, S.; Bär, J.; Bertolotti, F.; Masciocchi, N.; Guagliardi, A.; Grotevent, M.; Shorubalko, I.; Bodnarchuk, M. I.; Shih, C.-J.; Kovalenko, M. V. *ACS Nano* **2017**, *11*, 3119–3134.

(30) Imran, M.; Caligiuri, V.; Wang, M.; Goldoni, L.; Prato, M.; Krahne, R.; De Trizio, L.; Manna, L. *J. Am. Chem. Soc.* **2018**, *140*, 2656–2664.

(31) Kagan, C. R.; Murray, C. B. *Nat. Nanotechnol.* **2015**, *10*, 1013–1026.

(32) De Roo, J.; Ibáñez, M.; Geiregat, P.; Nedelcu, G.; Walravens, W.; Maes, J.; Martins, J. C.; Van Driessche, I.; Kovalenko, M. V; Hens, Z. *ACS Nano* **2016**, *10*, 2071–2081.

(33) Anderson, N. C.; Hendricks, M. P.; Choi, J. J.; Owen, J. S. *J. Am. Chem. Soc.* **2013**, *135*, 18536–18548.

(34) Boles, M. A.; Ling, D.; Hyeon, T.; Talapin, D. V. *Nat. Mater.* **2016**, *15*, 141–153.

(35) Bekenstein, Y.; Koscher, B. A.; Eaton, S. W.; Yang, P.; Alivisatos, A. P. *J. Am. Chem. Soc.* **2015**, *137*, 16008–16011.

(36) Reichardt, C.; Welton, T. *Solvents and Solvent Effects in Organic Chemistry*; John Wiley & Sons, 2011.

(37) Cazes, J. *Encyclopedia of Chromatography*; CRC press, 2009.

(38) Hansen, C. M. *Hansen Solubility Parameters: A User's Handbook*; CRC press, 2007.

(39) Wang, J.; Di Giacomo, F.; Brüls, J.; Gorter, H.; Katsouras, I.; Groen, P.; Janssen, R. A. J.; Andriessen, R.; Galagan, Y. *Sol. RRL* **2017**, *1*, 1700091.

(40) Gardner, K. L.; Tait, J. G.; Merckx, T.; Qiu, W.; Paetzold, U. W.; Kootstra, L.; Jaysankar, M.; Gehlhaar, R.; Cheyns, D.; Heremans, P.; Poortmans, J. *Adv. Energy Mater.* **2016**, *6*, 1600386.

(41) Li, J.; Xu, L.; Wang, T.; Song, J.; Chen, J.; Xue, J.; Dong, Y.; Cai, B.; Shan, Q.; Han, B.; Zeng, H. *Adv. Mater.* **2017**, *29*, 1603885.

(42) *Supplemental Information of:* Xue, J.; Lee, J.-W.; Dai, Z.; Wang, R.; Nuryyeva, S.; Liao, M. E.; Chang, S.-Y.; Meng, L.; Meng, D.; Sun, P.; Lin, O.; Goorsky, M. S.; Yang, Y. *Joule* **2018**, *2*, 1866–1878.

(43) Domanski, K.; Roose, B.; Matsui, T.; Saliba, M.; Turren-Cruz, S.-H.; Correa-Baena, J.-P.; Carmona, C. R.; Richardson, G.; Foster, J. M.; De Angelis, F.; Ball, J. M.; Petrozza, A.; Mine, N.; Nazeeruddin, M. K.; Tress, W.; Grätzel, M.; Steiner, U.; Hagfeldt, A.; Abate, A. *Energy Environ. Sci.* **2017**, *10*, 604–613.

Chapter 6. A Small-Molecule "Charge Driver" for Perovskite Quantum Dot Solar Cells with Efficiency Approaching 13%

6.1. Background

Colloidal quantum dots (CQDs) have attracted significant attention for photovoltaic application in recent decades due to their unique properties. Not only their immense tunability in bandgap, electronic states, and surface chemistry enable them to be good candidates for new generation solar cells,[1-4] but also the multiple exciton generation phenomenon, specific to CQDs, opens an avenue to make full utilization of solar radiation.[5-7] Recently, halide perovskite CQDs have emerged as a new class of CQDs for photovoltaics, offering compelling combination of the advantages of traditional CQDs and exceptional properties of halide perovskite materials, such as the desirable bandgap, high absorption coefficient, and defect tolerance.[8-10] Furthermore, the perovskite CQDs, such as $CsPbI_3$ and formamidinium lead iodide ($FAPbI_3$), were reported to show superior phase stability over their bulk form owing to the size-induced lattice strain and enhanced contribution from the surface energy.[11,12] Accordingly, the CQD solar cells based on the perovskite material have demonstrated a great potential with a record power conversion efficiency (PCE) as high as 13% along with excellent operational stability.[12,13]

Although perovskite materials display superior optoelectronic properties to the conventional semiconductors, the low charge carrier separation efficiency, which is one of the critical obstacles toward higher performance of traditional CQD devices, still remains in the perovskite CQD solar cells.[14] While exciton binding energies (E_b) of bulk perovskite materials were measured to be as low as few millielectronvolts, facilitating spontaneous generation of free carriers at room temperature,[15] the E_b of the perovskite CQD was estimated to be significantly higher (up to ten times) than that of the bulk counterparts.[9,16] As a result, the photogenerated charge

carriers in the CQD films are subjected to be lost through recombination before being extracted to selective contact layers.[17] Therefore, promoting effective charge separation to reduce recombination becomes a crucial factor for boosting the PCE of the perovskite CQD solar cells.

In order to facilitate such charge separation process and thus reduce the charge recombination in conventional CQD solar cells, a lot of efforts have been developed, such as core–shell structural design, surface ligand modification, and device structure engineering.[18-23] These available strategies employed in the traditional CQDs devices, however, are still not compatible with perovskite CQD system owing to their vulnerable structural stability as well as absence of well-established synthetic routes.[3,8] For example, in contrast to various colloidal structures in chalcogenide quantum dots like type-II core–shell CdS/CdSe[24] and CdTe/CdSe[25] enabling spatial charge separation, no synthetic route has been developed yet for core–shell structured perovskite CQDs yet. Moreover, different from the versatile organic and inorganic surface functionalization of metal chalcogenide CQDs, the employed ligands in perovskite CQDs are limited to long-alkyl-chain acids and amines and hence, restrict the opportunity to tailor the electronic properties of CQDs via fine tuning of surface states as commonly achieved in traditional CQDs.[2,4,26,27] Therefore, we were motivated to develop a new strategy for facilitating efficient charge carrier collection in perovskite CQD solar cells. Here, we developed a facile strategy that takes advantage of conjugated small molecules and perovskite CQD heterointerface and, as a result, provides an additional driving force for effective charge separation in $FAPbI_3$ perovskite CQD solar cells. The champion CQD solar cell with a small molecule acting as a "charge driver" showed a promising PCE of 12.7%, the highest efficiency reported for $FAPbI_3$-CQD-based photovoltaics, demonstrating a great potential of this strategy for enhancing the efficiency of perovskite CQD solar cells.

6.2. Methodology

6.2.1. Synthesis and preparation of $FAPbI_3$ CQDs

$FAPbI_3$ CQDs were synthesized as reported with modifications.[12] Briefly, 0.28 g of formamidine acetate, 8.3 mL of octadecene (ODE) and 4.1 mL of oleic acid (OA) were added to a round-bottom flask and degassed under vacuum for 20 min at room temperature. The mixture was then heated up under inert gas until yielding a clear solution. The solution was then put under vacuum for 10 min at 50 °C. FA-oleate precursors needed to be preheated to 100 °C before use. 0.430 g of PbI_2 and 25 mL of ODE were added to another 2-neck flask and degassed under vacuum for 1 h at 120 °C. 2.5 mL of pre-dried oleylamine (OLA) and 5 mL of pre-dried OA were injected at 120 °C under inert gas. After around 30 min, the solution was cooled to 80 °C. FA-acetate precursor was then swiftly injected into PbI_2 precursor under stirring. After around 15 s, the mixture was cooled in an ice bath. $FAPbI_3$ CQDs were separated from crude solution by centrifugation at 9500 rpm for 10 min. The supernatant was discarded and the $FAPbI_3$ CQDs were collected by redispersion in toluene. The CQDs were then washed twice with toluene/acetonitrile mixture (with a molar ratio of 4:1 and 5:1, respectively). Finally, the washed CQDs were dispersed in hexane and centrifuged at 4000 rpm for 2 min to remove the excess salts and aggregated $FAPbI_3$ nanoparticles. Before device fabrication, CQDs solution was concentrated to around 35 $mg \cdot mL^{-1}$ in octane.

6.2.2. Fabrication of $FAPbI_3$ CQD-based devices with ITIC

Glass/indium doped tin oxide (ITO) substrates were cleaned with successive sonication in detergent, deionized (DI) water, acetone and 2-propanol each for 15 min, respectively. The cleaned substrates were further treated in ultraviolet-ozone chamber for 30 min to remove the organic

residual and enhance the wettability. The SnO_2 colloidal precursor was diluted by H_2O to 1.5% before use. Then, the diluted solution was spin-coated onto glass/ITO substrates at 3000 rpm for 30 s, and baked on a hot plate in ambient air at 160 °C for 30 min. The CQDs solution obtained was spin-coated on the substrates at 2000 rpm for 30 s and rinsed with pure EtOAc, or ITIC-saturated EtOAc solution. The ITIC-saturated EtOAc solution was prepared by dissolving excess ITIC into MeOAc and stirred vigorously under room temperature. The dispersion solution was filtered before use. The steps of spin-coating above were repeated multiple times to build a 200-300 nm thick film of CQDs. The spiro-MeOTAD solution was prepared by dissolving 85.8 mg of spiro-MeOTAD in 1 mL of chlorobenzene, which was doped with 33.8 µL of 4-tert-butylpyridine and 19.3 µL of Li-TFSI (520 $mg \cdot mL^{-1}$ in acetonitrile) solution. The spiro-MeOTAD solution was spin-coated on the perovskite layer at 3000 rpm for 20 s by dropping 17 µL of the solution on the spinning substrate. On top of the spiro-MeOTAD layer, ≈100 nm thick silver layer was thermally evaporated at 0.5 $Å \cdot s^{-1}$ to be used as an electrode.

6.3. Results and Discussion

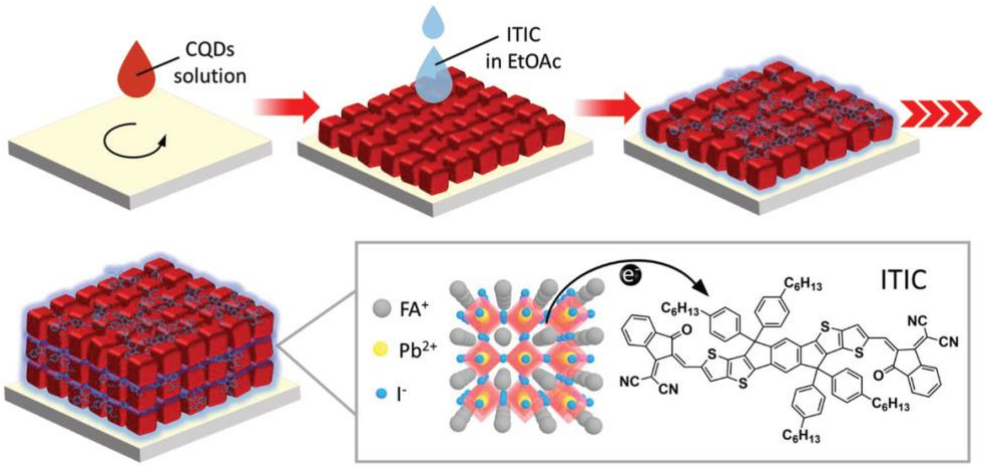

Scheme 6.1. $FAPbI_3$ CQD/ITIC film fabrication (inset: chemical structure of ITIC).

FAPbI$_3$-CQD-based photovoltaic devices were fabricated using a layer-by-layer deposition method as previously reported.[12] Ethyl acetate (EtOAc) was employed as an antisolvent to remove the ligands on the surface of CQDs during the solid-state film treatment. A conjugated small molecule 2,2′-[[6,6,12,12-tetrakis(4-hexylphenyl)-6,12-dihydrodithieno[2,3-d:2′,3′-d′]-s-indaceno[1,2-b:5,6-b′]dithiophene-2,8-diyl]bis[methylidyne(3-oxo-1H-indene-2,1(3H)-diylidene)]]bis[propanedinitrile] (ITIC), chemical structure of which is shown in the inset of Scheme 6.1, was introduced into EtOAc that was used to rinse the CQD film (illustrated in Scheme 6.1). While EtOAc removed the excess ligands of perovskite CQDs, ITIC in EtOAc remained in the CQD film forming a heterostructure. Based on this strategy, photovoltaic devices were fabricated with a structure of ITO/SnO$_2$/CQDs/Spiro-OMeTAD/Ag, cross-sectional scanning electron microscopy (SEM) image of which is shown in Figure 6.1a. A dense and uniform CQD film with a thickness of ~300 nm was clearly observed. Current density–voltage (J–V) curves of the CQDs devices without and with introduction of ITIC were compared in Figure 6.1b. The best device without ITIC showed a PCE of 10.4% with an open-circuit voltage (V_{OC}) of 1.03 V, short-circuit current density (J_{SC}) of 14.3 mA·cm^{-2}, and fill factor (FF) of 70.9% (Figure 6.1b). Upon incorporation of the ITIC, the device PCE increased to 12.7% with V_{OC} of 1.10 V, J_{SC} of 15.4 mA·cm^{-2}, and FF of 74.8%, indicating a large improvement in device performance with ITIC.

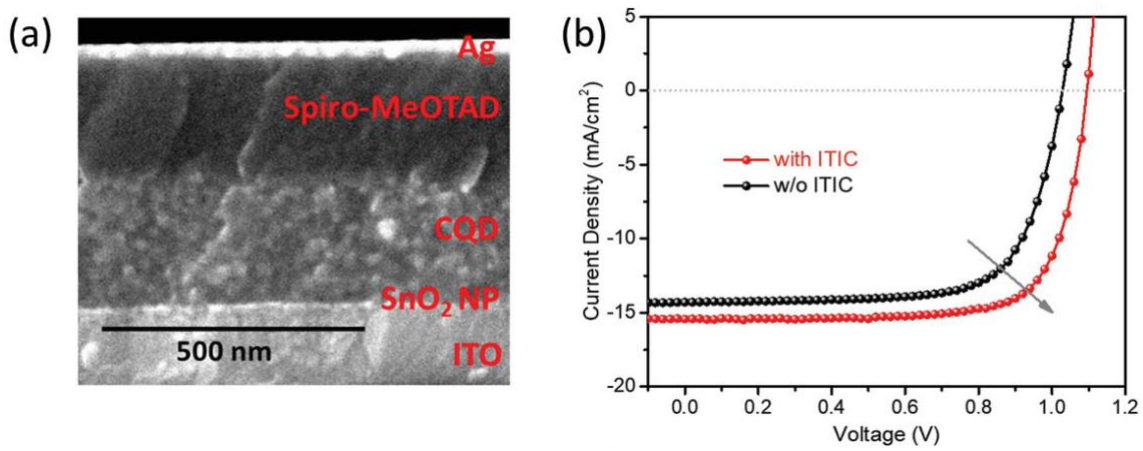

Figure 6.1. Structure and performance of $FAPbI_3$ CQD-based photovoltaic devices. a) A cross-sectional SEM image of the device structure. b) J–V curves of the devices based on $FAPbI_3$ CQDs with and without ITIC.

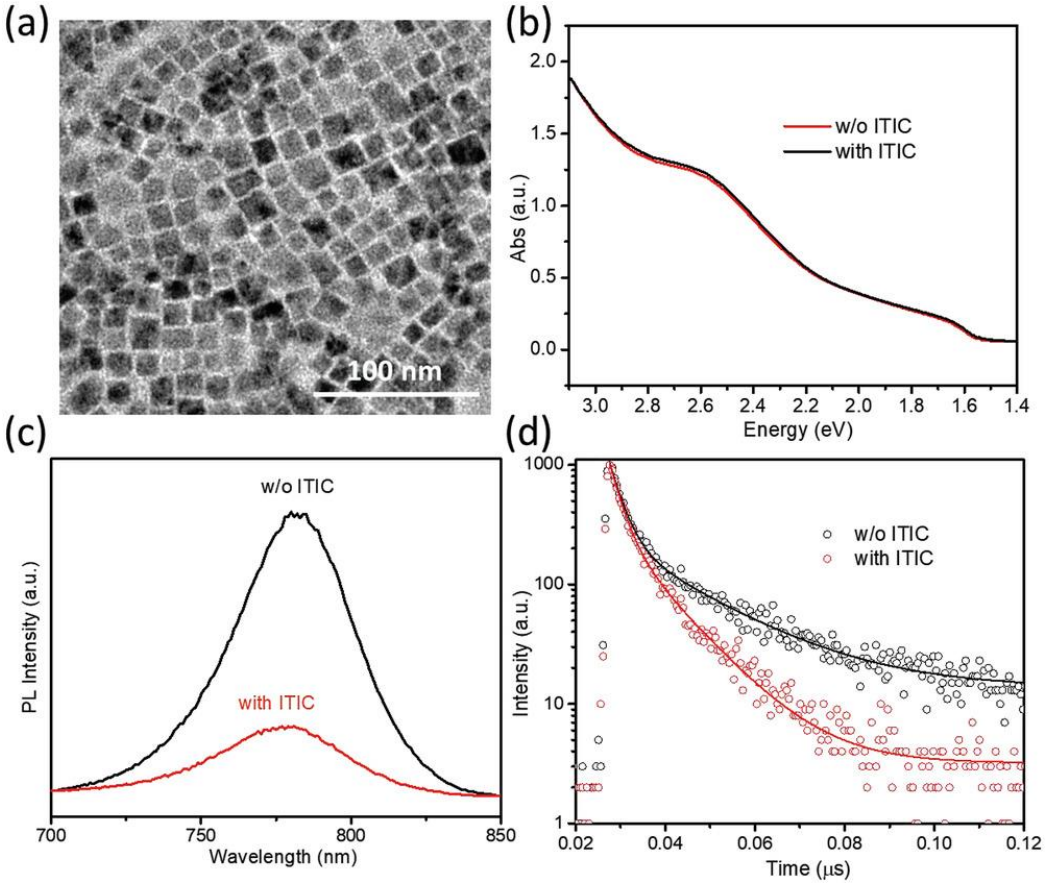

Figure 6.2. Structural and photophysical properties of $FAPbI_3$ CQDs without and with ITIC. a) Transmission electron microscopy (TEM) image of as-synthesized $FAPbI_3$ CQDs. b) UV–visible absorption, c) steady-state photoluminescence (open circles indicate measured data while solid lines are fitted curves) and d) TRPL spectra of $FAPbI_3$ CQDs with (red) and without (black) ITIC.

Figure 6.2a shows the transmission electron microscopy (TEM) image of the as-synthesized $FAPbI_3$ CQDs using a modified hot-injection method previously reported.[12] The CQDs were nearly monodispersed with an average size of 14 nm. High-resolution transmission electron microscopy (HRTEM) shows the cubic structure of the as-synthesized CQDs and X-ray diffraction (XRD) measurement of $FAPbI_3$ CQDs films with and without ITIC confirmed the cubic phase of the film in both cases (see ref. 28 for more details). The as-fabricated films exhibited a superior phase stability compared with their bulk counterparts due to the surface effects in CQDs.[11,13,29] Over a course of 5 days under ambient condition, the perovskite CQD film maintained its cubic phase, showing almost identical absorption spectrum before and after storage. In contrast, perovskite bulk film underwent an almost complete phase transformation to a "yellow" phase, showing a substantial decrease in absorption over visible wavelength region (see ref. 28 for more details). UV–vis absorption spectrum of $FAPbI_3$ CQDs film incorporated with ITIC was almost identical to that of pure $FAPbI_3$ CQDs film, suggesting that ITIC had negligible effect on the total absorbance of the film (Figure 6.2b). Thus, we speculated that the large improvement of device performance is related to a reduced charge recombination and/or enhanced charge collection efficiency instead of light harvesting.

To understand the carrier dynamics and ascertain the role of ITIC, photophysical properties of CQDs films were further investigated. As shown in Figure 6.2c, CQDs film with ITIC showed strong steady state photoluminescence (PL) quenching compared with the reference sample. Correspondingly, the time-resolved photoluminescence (TRPL) decay profile of $FAPbI_3$ CQDs with ITIC exhibited nearly biexponential decay characteristics with much shorter relaxation time of 2.5 ns (Figure 6.2d) than that of the bare $FAPbI_3$ CQDs (17.2 ns). The significantly quenched PL intensity and faster PL decay profile indicated the electron transfer from $FAPbI_3$ CQDs to ITIC

which is commonly known as an acceptor in organic photovoltaic (OPV) devices.[27,30] We posit that ITIC played a crucial role in charge carrier dynamics of CQDs film enhancing charge separation and reducing the charge recombination rate.[31,32]

The charge transfer dynamics in $FAPbI_3$ CQDs/ITIC system were further studied by measuring the broadband femtosecond time-resolved transient absorption (TA) spectra (see ref. 33 for more details). The dynamics observed in $FAPbI_3$ CQDs with ITIC were attributed to a charge-transfer state which generally features long lifetime.[34] Using ultraviolet photoelectron spectroscopy (UPS) measurement (Figure 6.3a), the conduction band edge of $FAPbI_3$ CQD was determined to be -3.78 eV relative to vacuum level, which was shallower than that of ITIC (-3.83 eV versus vacuum level), which further confirmed the electron transfer from CQD to ITIC (Figure 6.3b).[30,32]

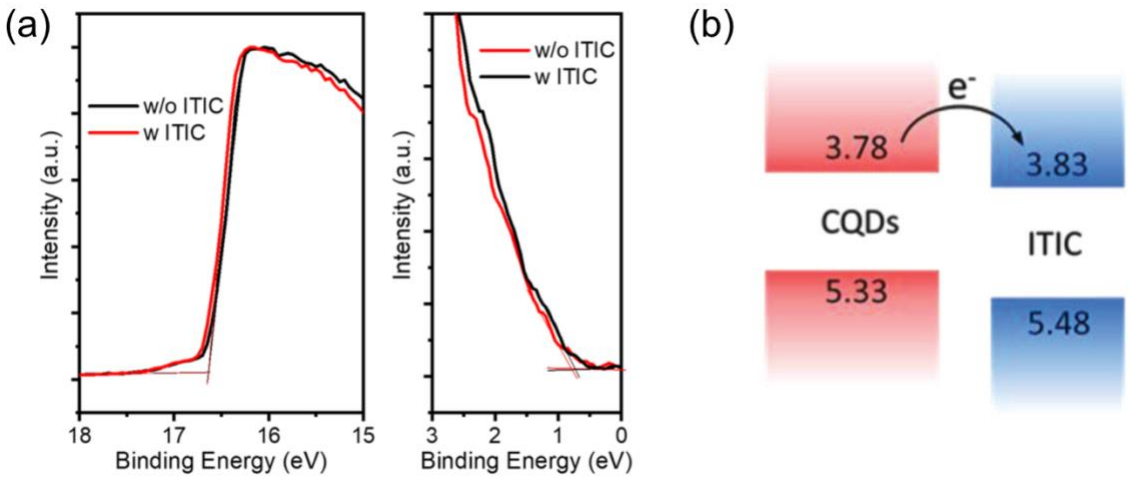

Figure 6.3. Energy levels and charge transfer in $FAPbI_3$ CQDs with ITIC. a) Ultraviolet photoelectron spectroscopy (UPS) determination of energy levels of fermi level and valence band maximum of $FAPbI_3$ CQDs. b) Schematic energy diagram showing charge transfer between $FAPbI_3$ CQDs and ITIC.

It is worth mentioning that our device configuration was carefully designed to maximize the function of ITIC in charge dynamics. Taking advantage of the layer-by-layer deposition

process of CQD film, the distribution of ITIC in CQD film could be easily controlled, where ITIC was selectively incorporated into the part of CQD layers in the vicinity of the electron transporting layer (Figure 6.4a) rather than in the entire CQD layers (Figure 6.4b). For the device configuration where ITIC was added to all of the CQD layers, due to the direct contact of n-type ITIC with the p-type hole transporting layer, carriers extracted toward spiro-MeOTAD were more likely to recombine with electrons transferred to the ITIC, resulting in a much lower Voc of 1.0 V, Jsc of 13.2 $mA \cdot cm^{-2}$, FF of 71.8%, and PCE of 9.5% (Figure 6.4c, Supporting Information).[30,35] In contrast, with a controlled configuration shown in Figure 6.4a, ITIC was not distributed in the top layers that were close to hole transporting layer. Therefore, unfavorable contact between the spiro-MeOTAD and ITIC and thus, carrier recombination could be strategically avoided, resulting in a much better device performance. This also provides another indication of the role of ITIC as a "charge driver" enabling the charge transfer from CQD to ITIC.

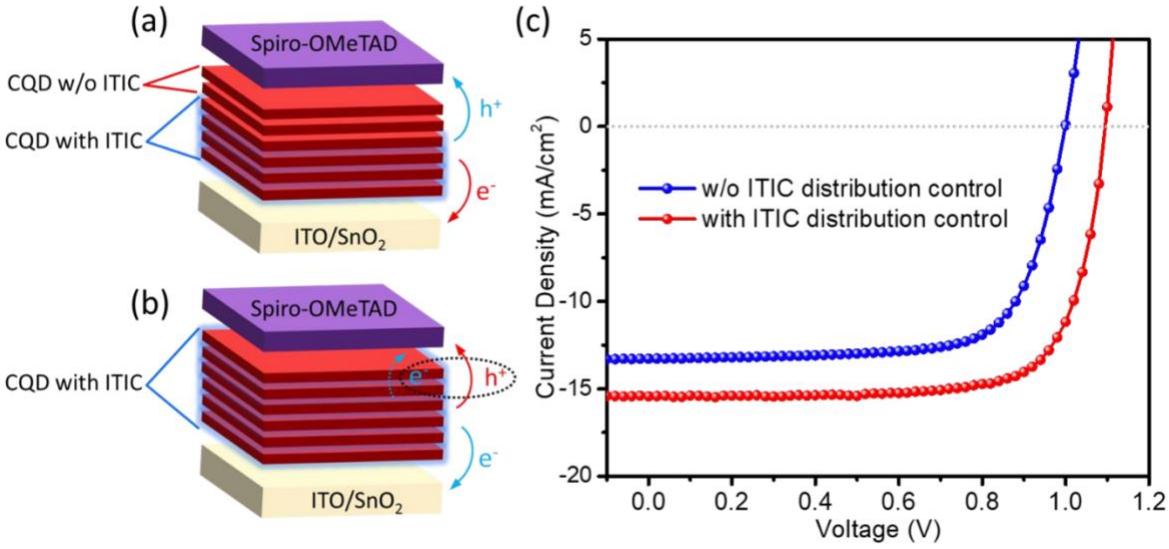

Figure 6.4. Performance comparison of selective *vs* even distribution of ITIC in $FAPbI_3$ CQD-based devices. Schematic diagrams of $FAPbI_3$ CQDs-based solar cell devices a) with and b) without the control of ITIC distribution. c) J-V curves of the corresponding devices with and without ITIC distribution control.

6.4. Conclusion

In conclusion, we have developed an effective strategy using a conjugated small molecule ITIC serving as a "charge driver" designed to enhance the charge separation and as a result, improve the carrier dynamics and boost the device performance in $FAPbI_3$ CQDs solar cells. The ITIC was introduced into the $FAPbI_3$ CQDs film simultaneously while removing the original insulating surface ligands of the $FAPbI_3$ CQD. Taking advantage of the layer-by-layer deposition techniques in CQD photovoltaics fabrication, the distribution of ITIC in CQD film was strategically controlled to boost the device efficiency up to 12.7%. Photophysical studies unraveled that the formation of ITIC/$FAPbI_3$ CQD heterointerface induce an effective charge transfer from the CQDs to ITIC, which in turn facilitated the charge separation, and thus reduced the carrier recombination and improved the carrier collection efficiency. Our results have provided a new route to improve the performance of perovskite CQD photovoltaic devices and shed light on the development of other CQD-based electronic devices.

6.5. References

(1) Carey, G. H.; Abdelhady, A. L.; Ning, Z.; Thon, S. M.; Bakr, O. M.; Sargent, E. H. *Chem. Rev.* **2015**, *115*, 12732–12763.

(2) Sun, B.; Voznyy, O.; Tan, H.; Stadler, P.; Liu, M.; Walters, G.; Proppe, A. H.; Liu, M.; Fan, J.; Zhuang, T.; Li, J.; Wei, M.; Xu, J.; Kim, Y.; Hoogland, S.; Sargent, E. H. *Adv. Mater.* **2017**, *29*, 1700749.

(3) Kagan, C. R.; Lifshitz, E.; Sargent, E. H.; Talapin, D. V. *Science* **2016**, *353*, aac5523.

(4) Wang, Y.; Lu, K.; Han, L.; Liu, Z.; Shi, G.; Fang, H.; Chen, S.; Wu, T.; Yang, F.; Gu, M.; Zhou, S.; Ling, X.; Tang, X.; Zheng, J.; Loi, M. A.; Ma, W. *Adv. Mater.* **2018**, *30*, 1704871.

(5) Semonin, O. E.; Luther, J. M.; Choi, S.; Chen, H.-Y.; Gao, J.; Nozik, A. J.; Beard, M. C. *Science* **2011**, *334*, 1530–1533.

(6) Beard, M. C. *J. Phys. Chem. Lett.* **2011**, *2*, 1282–1288.

(7) Yan, Y.; Crisp, R. W.; Gu, J.; Chernomordik, B. D.; Pach, G. F.; Marshall, A. R.; Turner, J. A.; Beard, M. C. *Nat. Energy* **2017**, *2*, 17052.

(8) Akkerman, Q. A.; Rainò, G.; Kovalenko, M. V; Manna, L. *Nat. Mater.* **2018**, *17*, 394–405.

(9) Kovalenko, M. V; Protesescu, L.; Bodnarchuk, M. I. *Science* **2017**, *358*, 745–750.

(10) Bian, H.; Bai, D.; Jin, Z.; Wang, K.; Liang, L.; Wang, H.; Zhang, J.; Wang, Q.; Liu, S. (F.). *Joule* **2018**, *2*, 1500–1510.

(11) Swarnkar, A.; Marshall, A. R.; Sanehira, E. M.; Chernomordik, B. D.; Moore, D. T.; Christians, J. A.; Chakrabarti, T.; Luther, J. M. *Science* **2016**, *354*, 92–95.

(12) Xue, J.; Lee, J.-W.; Dai, Z.; Wang, R.; Nuryyeva, S.; Liao, M. E.; Chang, S.-Y.; Meng, L.; Meng, D.; Sun, P.; Lin, O.; Goorsky, M. S.; Yang, Y. *Joule* **2018**, *2*, 1866–1878.

(13) Sanehira, E. M.; Marshall, A. R.; Christians, J. A.; Harvey, S. P.; Ciesielski, P. N.; Wheeler, L. M.; Schulz, P.; Lin, L. Y.; Beard, M. C.; Luther, J. M. *Sci. Adv.* **2017**, *3*, eaao4204.

(14) Xing, G.; Mathews, N.; Sun, S.; Lim, S. S.; Lam, Y. M.; Grätzel, M.; Mhaisalkar, S.; Sum, T. C. *Science* **2013**, *342*, 344–347.

(15) Miyata, A.; Mitioglu, A.; Plochocka, P.; Portugall, O.; Wang, J. T.-W.; Stranks, S. D.; Snaith, H. J.; Nicholas, R. J. *Nat. Phys.* **2015**, *11*, 582–587.

(16) Woo, H. C.; Choi, J. W.; Shin, J.; Chin, S.-H.; Ann, M. H.; Lee, C.-L. *Phys. Chem. Lett.* **2018**, *9*, 4066–4074.

(17) Faist, M. A.; Shoaee, S.; Tuladhar, S.; Dibb, G. F. A.; Foster, S.; Gong, W.; Kirchartz, T.; Bradley, D. D. C.; Durrant, J. R.; Nelson, J. *Adv. Energy Mater.* **2013**, *3*, 744–752.

(18) Yang, Z.; Fan, J. Z.; Proppe, A. H.; De Arquer, F. P. G.; Rossouw, D.; Voznyy, O.; Lan, X.; Liu, M.; Walters, G.; Quintero-Bermudez, R. *Nat. Commun.* **2017**, *8*, 1–9.

(19) Sun, Z.; Sitbon, G.; Pons, T.; Bakulin, A. A.; Chen, Z. *Sci. Rep.* **2015**, *5*, 1–11.

(20) Balazs, D. M.; Loi, M. A. *Adv. Mater.* **2018**, *30*, 1800082.

(21) Aqoma, H.; Al Mubarok, M.; Hadmojo, W. T.; Lee, E.-H.; Kim, T.-W.; Ahn, T. K.; Oh, S.-H.; Jang, S.-Y. *Adv. Mater.* **2017**, *29*, 1605756.

(22) Zhang, Y.; Ding, C.; Wu, G.; Nakazawa, N.; Chang, J.; Ogomi, Y.; Toyoda, T.; Hayase, S.; Katayama, K.; Shen, Q. *J. Phys. Chem. C* **2016**, *120*, 28509–28518.

(23) Brown, P. R.; Kim, D.; Lunt, R. R.; Zhao, N.; Bawendi, M. G.; Grossman, J. C.; Bulović, V. *ACS Nano* **2014**, *8*, 5863–5872.

(24) Santra, P. K.; Kamat, P. V. *J. Am. Chem. Soc.* **2012**, *134*, 2508–2511.

(25) Wang, J.; Mora-Seró, I.; Pan, Z.; Zhao, K.; Zhang, H.; Feng, Y.; Yang, G.; Zhong, X.; Bisquert, J. *J. Am. Chem. Soc.* **2013**, *135*, 15913–15922.

(26) Kagan, C. R.; Murray, C. B. *Nat. Nanotechnol.* **2015**, *10*, 1013–1026.

(27) Liu, M.; Voznyy, O.; Sabatini, R.; García de Arquer, F. P.; Munir, R.; Balawi, A. H.; Lan, X.; Fan, F.; Walters, G.; Kirmani, A. R.; Hoogland, S.; Laquai, F.; Amassian, A.; Sargent, E. H. *Nat. Mater.* **2017**, *16*, 258–263.

(28) *Supporting Information of:* Xue, J.; Wang, R.; Chen, L.; Nuryyeva, S.; Han, T.-H.; Huang, T.; Tan, S.; Zhu, J.; Wang, M.; Wang, Z.-K.; Zhang, C.; Lee, J.-W.; Yang, Y. *Adv. Mater.* **2019**, *31*, 1900111.

(29) Wheeler, L. M.; Sanehira, E. M.; Marshall, A. R.; Schulz, P.; Suri, M.; Anderson, N. C.; Christians, J. A.; Nordlund, D.; Sokaras, D.; Kroll, T.; Harvey, S. P.; Berry, J. J.; Lin, L. Y.; Luther, J. M. *J. Am. Chem. Soc.* **2018**, *140*, 10504–10513.

(30) Lin, Y.; Wang, J.; Zhang, Z.-G.; Bai, H.; Li, Y.; Zhu, D.; Zhan, X. *Adv. Mater.* **2015**, *27*, 1170–1174.

(31) Wu, Y.; Yang, X.; Chen, W.; Yue, Y.; Cai, M.; Xie, F.; Bi, E.; Islam, A.; Han, L. *Nat. Energy* **2016**, *1*, 16148.

(32) Niu, T.; Lu, J.; Munir, R.; Li, J.; Barrit, D.; Zhang, X.; Hu, H.; Yang, Z.; Amassian, A.; Zhao, K.; Liu, S. (F.). *Adv. Mater.* **2018**, *30*, 1706576.

(33) Xue, J.; Wang, R.; Chen, L.; Nuryyeva, S.; Han, T.-H.; Huang, T.; Tan, S.; Zhu, J.; Wang, M.; Wang, Z.-K.; Zhang, C.; Lee, J.-W.; Yang, Y. *Adv. Mater.* **2019**, *31*, 1900111.

(34) Liu, J.; Chen, S.; Qian, D.; Gautam, B.; Yang, G.; Zhao, J.; Bergqvist, J.; Zhang, F.; Ma, W.; Ade, H.; Inganäs, O.; Gundogdu, K.; Gao, F.; Yan, H. *Nat. Energy* **2016**, *1*, 16089.

(35) Cheng, P.; Wang, R.; Zhu, J.; Huang, W.; Chang, S.-Y.; Meng, L.; Sun, P.; Cheng, H.-W.; Qin, M.; Zhu, C.; Zhan, X.; Yang, Y. *Adv. Mater.* **2018**, *30*, 1705243.

Chapter 7. Solid-phase hetero epitaxial growth of α-phase formamidinium perovskite

7.1. Background

Epitaxial growth is one of the most powerful ways to fabricate semiconducting thin films with low defect density and a desired orientation.[1] The technique has been widely adopted to form semiconducting thin films for optoelectronic applications for which the defect density should be minimized to promote carrier transport and thus device performance. Highly crystalline semiconducting films including silicon, gallium nitride, gallium arsenide and two-dimensional materials have been successfully grown via epitaxial growth to be used in solar cells, light-emitting diodes (LEDs) and memory devices.[2-6] However, conventional epitaxy requires a compatible single crystalline substrate and the growth process is performed in extremely controlled environments such as ultra-high vacuum and temperature. Often, the grown materials should be transferred from the templating substrate onto a desired substrate for device fabrication by delicate lift-off processes. These limit not only the price competitiveness and scalability, but also versatility of the process for various materials and devices.

For instance, the epitaxial growth of metal halide perovskite thin films for used in devices has not yet been achievable because of (i) the absence of compatible substrates to template the growth of the perovskite film, and (ii) the difficulty of inducing controlled nucleation and growth at the surface of a templating substrate. For the former, typical transparent oxide substrates and other charge transporting bottom contact layers used for devices cannot direct the growth of the perovskite film. Single crystalline chunks of halide perovskites and epitaxially grown thin films on single crystal substrate have been demonstrated,[7-11] but thickness-controlled layer transfer of the grown materials onto a desired substrate has not been successful. For the latter, inherently fast reaction kinetics during the typical solution process causes numerous nuclei to form in the bulk

solution, resulting in the growth of randomly oriented fine grains with a high density of defects. In light of these limitations, huge research efforts have been devoted to control the nucleation and growth kinetics,[12,13] but accurate control over the kinetics in solution medium is still challenging.

Recently, strategies to incorporate layered perovskites into 3D perovskites have been extensively studied. Owing to their enhanced stability relative to 3D perovskites and favorable band alignment, layered perovskites effectively passivate the grain boundaries and surface of 3D perovskites, resulting in enhanced performance and stability of the perovskite solar cells and LEDs.[14-17] We present here a route to induce kinetic-controlled epitaxial crystal growth of formamidinium lead tri-iodide ($FAPbI_3$) perovskite thin films by using layered perovskite templates. The local epitaxial growth of the $FAPbI_3$ perovskite crystal was observed during its solid-state phase transformation from the hexagonal non-perovskite $FAPbI_3$ when it is heterostructured with layered perovskite, whereby the growth kinetics was dependent on strain energy originating from the hetero-interface. Our first-principles calculations revealed a mechanism to engineer the conversion energy barrier between the cubic and hexagonal phases by a synergistic effect between strain and entropy. The slow heteroepitaxy enabled the growth of tenfold enlarged $FAPbI_3$ perovskite crystals with a reduced defect density and strong preferred orientation. This nano-heteroepitaxy (NHE) is applicable to various substrates used for devices. The proof-of-concept solar cell and LED devices based on NHE–$FAPbI_3$ showed efficiencies and stabilities superior to those of devices fabricated without NHE.

7.2. Methodology

7.2.1. Preparation of perovskite precursor solution by Yang group

A precursor solution for bare $FAPbI_3$ (control) film was prepared by dissolving equimolar amount of $HC(NH_2)_2I$ (FAI), PbI_2 and N-methyl-2-pyrrolidone (NMP) in N,N-Dimethylformamide (DMF). In a typical process, 172 mg of FAI, 461 mg of PbI_2 and 99 mg of NMP were dissolved in 560 mg of DMF. For the films with layered perovskite, the corresponding $FAPbI_3$ precursors were replaced with the same molar amount of the precursors for the layered perovskite. Typically, the precursor solution for 1P film was prepared by dissolving 8.2 mg of phenethylammonium iodide (PEAI) 166 mg of FAI, 453 mg of PbI_2 and 97 mg of NMP in 560 mg of DMF. The precursor solution for 3P film was prepared by dissolving 16.4 mg of phenethylammonium iodide (PEAI), 161 mg of FAI, 446 mg of PbI_2 and 95.8 mg of NMP in 560 mg of DMF. The precursor solution for 3F film was prepared by dissolving 17.2 mg of 4-fluoro phenethylammonium iodide (FPEAI), 161 mg of FAI, 446 mg of PbI_2, and 95.8 mg of NMP in 560 mg of DMF.

7.2.2. Fabrication of perovskite films by Yang group

All the films were prepared inside a glove box filled with dry air (Dew point around −39 °C). The perovskite precursor solution was filtered with 0.2 μm pore sized PTFE syringe filter before use. The precursor solution was spin-coated at 4000 rpm for 20 s to which 0.15 mL of diethyl ether was dropped after 10 s. The resulting film was heat-treated at 150 °C for 20 min (the annealing time for bare $FAPbI_3$ film was 10 min due to thermal degradation with longer annealing time).

7.2.3. DFT methods

The DFT calculations for charge distribution were performed using Gaussian09 program package.[18] The geometry optimizations were carried out at the B3LYP-D3 level of theory with the 6–311++G(d,p) basis set in gas phase. The vibrational frequencies were computed at the same level to confirm that the optimized structures are at an energy minimum (zero imaginary frequencies). Electrostatic potentials on isosurfaces and atomic charges of all atoms were computed using B3LYP-D3 level of theory with 6–31G(d) basis set in gas phase according to Hirshfeld[19-21] population analysis. Dipole moments were computed using the same level of theory according to Merz–Singh–Kollman[22,23] scheme. Choice of schemes was based on preceding literature.[24,25] The diagrams were generated using GaussView 5.[26] For phase conversion energetics performed by the Yoon group, all the calculations are based on first-principles DFT using the Vienna ab initio simulation package[27] with the projector augmented wave method; a generalized gradient approximation in the form of Perdew–Burke–Ernzerhof functional for the exchange-correlation functional,[28,29] and an energy cutoff of 400 eV is employed for all the calculations. To consider the van der Waals interactions, the dispersion correction by using Grimme's DFT–D3 scheme is considered.[30] For the cubic $FAPbI_3$, a 4 × 4 × 4 Γ-centered Monkhorst–Pack sampling mesh is used to get the accurate lattice constants. For the hexagonal $FAPbI_3$ and the layered perovskite, the k-points sampling are 3 × 3 × 3 and 2 × 4 × 4. For surfaces, k-point mesh is taken to be 1 for the direction of the surface. The surfaces were modeled by a periodic slab consisting of at least five atomic layers, separated by at least 20 Å of vacuum in the surface normal direction. During our calculations, all atoms are fully relaxed until the residual forces on each atom are less than 0.02 eV/Å. The surface energy is defined as:

$$\gamma = \frac{1}{2A}(E_{slab} - n\mu_{mol} - m\mu_{Pb} - l\mu_{l}\ ,$$

where E_{slab} is the total energy of the slab model with two surfaces, A is the surface area per unit cell, and each quantities satisfy the relations, $\mu_{mol} + \mu_{Pb} + 3\mu_I = E_{cubic}$ for cubic phase and $\mu_{mol} + \mu_{Pb} + 3\mu_I = 1/2E_{hex}$ for hexagonal phase.

7.3. Results and Discussion

7.3.1. Phase conversion kinetics

$FAPbI_3$ crystallizes as its equilibrium hexagonal non-perovskite phase (yellow color, δ-phase) at room temperature, and is transformed into its cubic perovskite polymorph (black color, α-phase) upon annealing at 150 °C through a solid-state phase conversion process.[31,32] In polycrystalline films, grain boundaries are at a higher energy state due to the additional contribution of surface (or interfacial) energy. Consequently, the grain boundaries act as heterogeneous nucleation sites where phase transition is first triggered. We introduced a hetero-interface at the grain boundaries by incorporating small amounts of layered perovskites into the precursor solution.[14,15] We varied both the amount and type of the layered perovskite to observe the effects of the hetero-interface (hereafter we define, control: bare $FAPbI_3$, 1P: $FAPbI_3$ with 1.67 mol% of PEA_2PbI_4, where PEA stands for phenylethylammonium, 3P: $FAPbI_3$ with 3.33 mol% of PEA_2PbI_4, and 3F: $FAPbI_3$ with 3.33 mol% of $FPEA_2PbI_4$, where FPEA stands for 4-fluorophenethylammonium).

As shown in Figure 7.1, density functional theory (DFT) calculations were used to investigate the charge distributions in the PEA^+ and $FPEA^+$ cations to gain insights on the properties of the layered perovskites incorporated with the cations. Due to the strong electronegativity of fluorine, a strong localized negative charge of -0.072e was observed on the fluorine in the FPEA cation, which is relatively higher than the positive charges being delocalized

on the benzene ring in the PEA cation without the fluorine (0.042e and 0.035e). We speculate that this localized negative charge on the fluorine will disturb the assembly of the PbI_6-FPEA-FPEA-PbI_6 geometry when constructing the layered perovskite lattice due to the repulsive electrostatic force between the fluorines adjacent to each other in the two FPEA cations. Thus, the formation of the long-range ordered large crystals of layered $FPEA_2PbI_4$ perovskite will be less favorable than that for the layered PEA_2PbI_4 perovskite. Hence, we expect the hetero-interface area to increase in the order control < 1P < 3P < 3F.

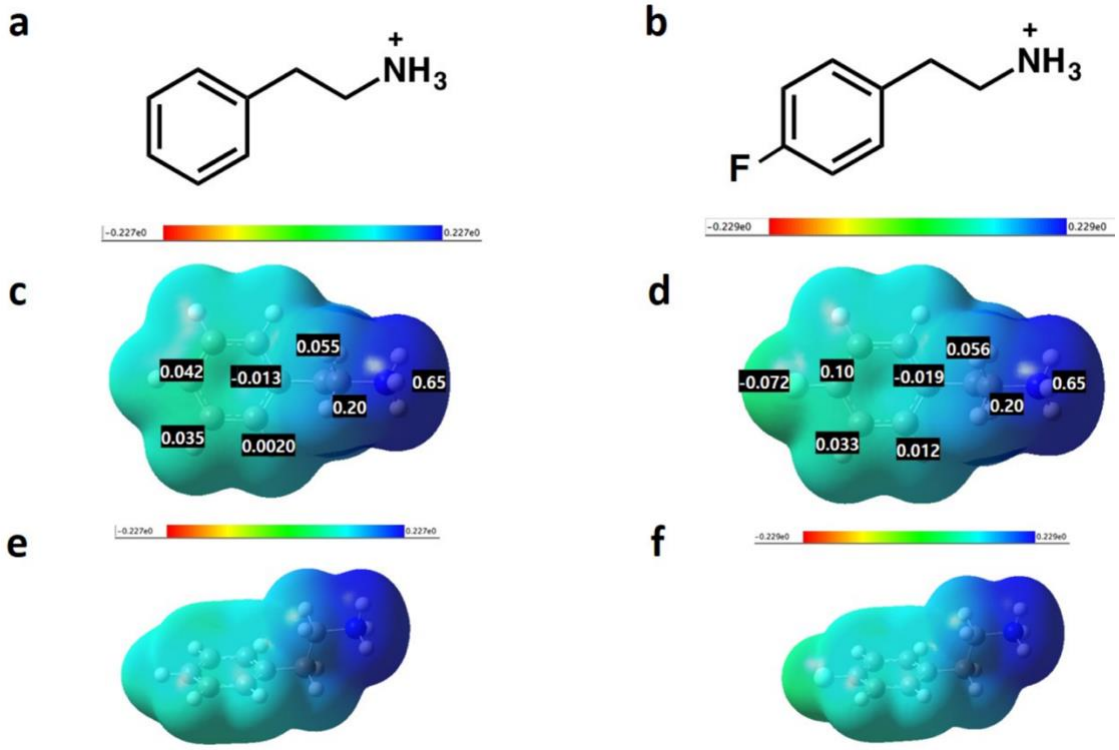

Figure 7.1. Charge distribution determined by density functional theory (DFT) calculation. Schematics showing molecular structure structure of (a) phenethylammonium cation (PEA^+) and (b) 4-fluoro-phenethylammonium cation ($FPEA^+$). Charge distribution of the (c), (e) PEA^+ and (d), (f) $FPEA^+$ molecules. (c), (d) are top and (e), (f) are cross sectional views.

The layered perovskite/$FAPbI_3$ hetero-structured films were formed by spin-coating the precursor solutions, and the photographs of the films as a function of annealing time are presented in Figure 7.2a. As-spun films were semitransparent yellowish irrespective of the added layered

perovskite, indicating the formation of the hexagonal δ-phase. Upon annealing at 150 °C, the color of the control film rapidly converted to black within a minute, whereas the color change was retarded with incorporation of the layered perovskites; 1P, 3P, and 3F took approximately 2, 6, and 8 min, respectively. The slower color change is indicative of a slower phase conversion process.

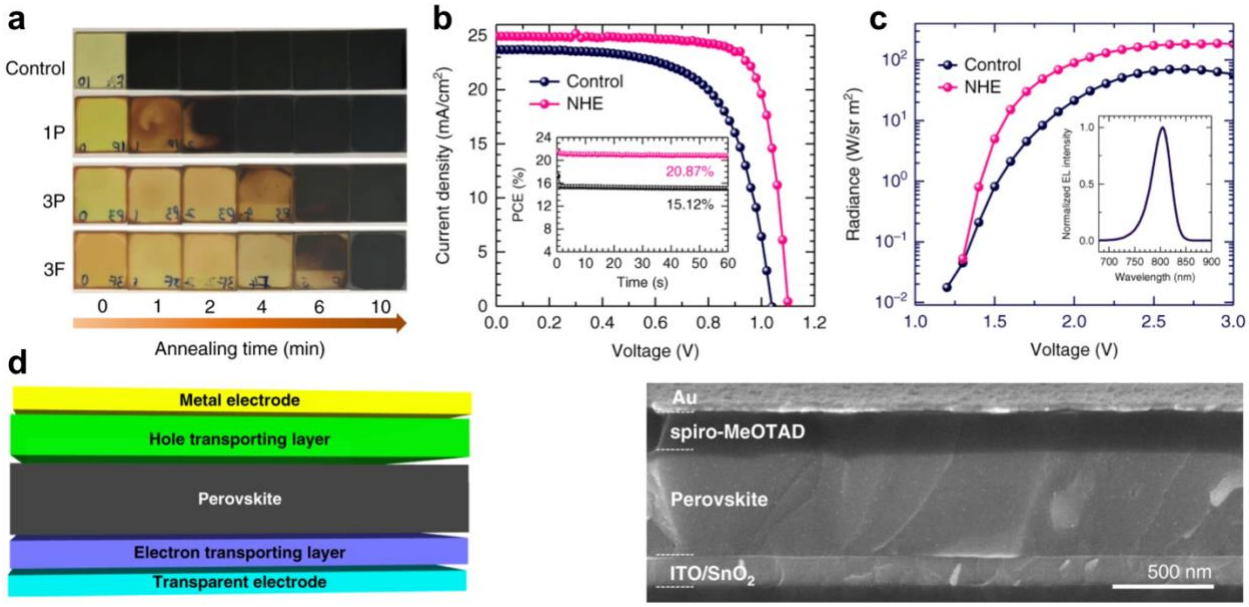

Figure 7.2. Phase conversion kinetics of formamidinium lead tri-iodide ($FAPbI_3$) perovskite with a hetero-interface at the grain boundaries and proof-of-concept devices. (a) Photographs of $FAPbI_3$ films on SnO_2-coated ITO substrates with different annealing times at 150 °C. Control: bare $FAPbI_3$, 1P: $FAPbI_3$ with 1.67 mol% PEA_2PbI_4, 3P: $FAPbI_3$ with 3.33 mol% PEA_2PbI_4, and 3F: $FAPbI_3$ with 3.33 mol% $FPEA_2PbI_4$. (b) Current density–voltage (J–V) of solar cell devices based on a bare $FAPbI_3$ film (control) and a $FAPbI_3$ film with NHE. Inset of (b) shows the steady-state power conversion efficiencies measured at maximum power points. (c) Voltage–radiance curves of the light emitting diode (LED) devices based on the control and NHE films. Inset of (c) shows the electroluminescence spectra of the LED devices. (d) Device structure schematics and corresponding cross-sectional scanning electron microscopy image of the solar cell device based on the $FAPbI_3$ film with nano heteroepitaxy (NHE, with 3.33 mol% $FPEA_2PbI_4$).

The phase conversion process was first monitored by in situ grazing incident wide angle X-ray scattering (GIWAXS) measurement of the corresponding films at 150 °C (under helium atmosphere on silicon substrates) (see ref. 33 for details). A clear delayed phase transformation

with incorporation of the layered perovskites from control, to 1P, to 3P, and to 3F was observed. The nucleation and/or growth rates of the cubic phase were significantly retarded by the incorporation of the layered perovskites. GIWAXS results also implied the presence of strained phases and a consequent change in energetics and kinetics of the phase conversion process. We speculated that the introduction of the hetero-interface between the $FAPbI_3$ and layered perovskites was probably associated with the observed strain and was responsible for retarding the phase conversion process.

To elucidate the origin of the different phase conversion kinetics, Yoon group performed first-principles density functional theory (DFT) calculations based on the observed strain and interfacial alignments as determined by the TEM studies (see ref. 34 for details). We initially postulated that two factors may have contributed to the change in phase conversion energetics: (i) strain itself which can be directly responsible for increasing the phase conversion nucleation barrier as is well-known from conventional nucleation theory,[35] and (ii) change in entropy induced by the presence of strain, which was previously reported to be a crucial factor affecting the energetics of $FAPbI_3$.[32] Firstly, to investigate the effect of strain, the energy barriers (ΔG_c) between the cubic and hexagonal phases with the lattice constants fixed to the given interlayer spacings are calculated as in Figure 7.3. Overall, the energy barrier increases when strain is applied to the transition state as expected from classical nucleation theory.[35] As the interlayer spacing decreases toward the 2D spacing, the compressive strain increases the cubic to hexagonal transformation barrier height by ~0.15 eV in comparison to the value for the fully relaxed lattice (blue arrows in Figure 7.3), which will be beneficial for the thermodynamic stability of the cubic phase at $T < Tc$ (Tc is the critical temperature for phase conversion), correlating with previous experimental observations.[9] In the case of the phase transition from the hexagonal to cubic phase ($\delta \rightarrow \alpha$), strain

seems to less affect the ΔG_c value. However, we found that the contribution of entropy becomes more dominant. The activated rotation of the FA molecule at elevated temperatures contributes to the entropy of the system, which is known to be more significant in isotropic cubic structures and thus stabilizes the cubic phase over the hexagonal phase at a finite temperature.[32] The differences in the Gibbs free energy between the two phases are about −0.27 eV at T = 300 K and −0.47 eV at T = 500 K. As the free energy linearly decreases with T for the cubic phase, the relative stability between the two phases inverted above T_c while its contribution is negligible for the hexagonal phase (third panel on the right of Figure 7.3).[32] On the other hand, the rotational entropy becomes a key contributor in stabilizing the strained hexagonal phase. Under the tensile strain, the interlayer spacing of the hexagonal phase increases significantly, and the activated isotropic rotation of the FA^+ cation also becomes accessible for the hexagonal phase. Consequently, the tensile strain applied to the hexagonal phase effectively increases the stability of the hexagonal phase at a finite temperature and contributes to slowing down the phase transformation process to the cubic phase (red arrow in the last panel in Figure 7.3).

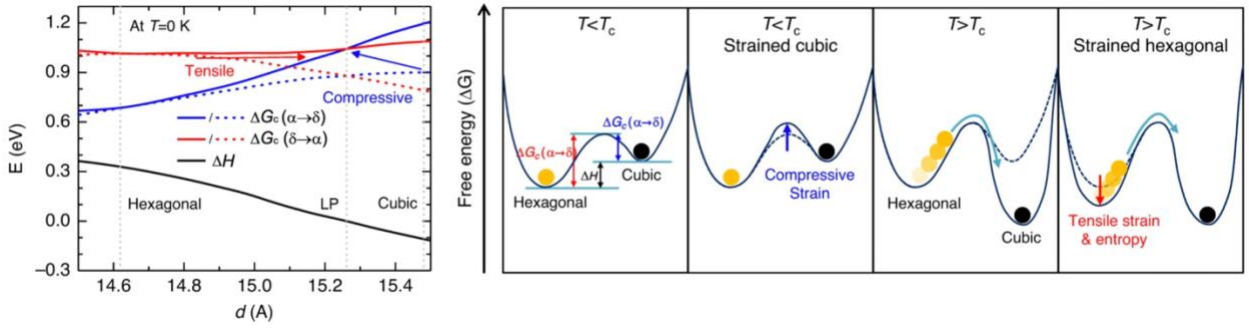

Figure 7.3. Phase conversion energy barriers. (left) DFT-calculated free energy barriers (ΔG_cs) for phase conversion from cubic to hexagonal ($\alpha \rightarrow \delta$), from hexagonal to cubic ($\delta \rightarrow \alpha$), and formation enthalpy of the cubic phase (ΔH) with respect to that of the hexagonal phase. Dashed lines and solid lines indicate ΔG_c without and with strain, respectively. The interlayer spacing of the strain-free hexagonal phase, layered perovskite and cubic phase are indicated with gray colored dashed vertical lines (d-spacings of DFT optimized structures). (right) Schematic free energy diagrams for the hexagonal and cubic phased $FAPbI_3$ at different temperatures and strain condition. T is temperature and T_c is the temperature for phase conversion.

7.3.2. Proof-of-concept devices

The Yang group fabricated proof-of-concept solar cell and LED devices to show the versatility of the high-quality NHE–$FAPbI_3$ films. Figure 7.2d shows schematics of the device structure and cross-sectional scanning electron microscopy images of the solar cell device based on the NHE film (3F film). The large and single-crystalline grains of the perovskite film perpendicular to the substrate is visible from the cross-sectional image. Current density–voltage (J–V) curves of the solar cell devices are shown in Figure 7.2b. The device based on the control film showed a short-circuit current density (J_{SC}) of 23.69 mA/cm^2, open-circuit voltage (V_{OC}) of 1.040 V, and fill factor (FF) of 0.649, corresponding to a power conversion efficiency (PCE) of 15.99%. Based on the NHE film, the PCE was significantly improved to 21.64% (35.3% improvement) with a J_{SC} of 24.93 mA/cm^2, VOC of 1.101 V, and FF of 0.788. The measured PCE is competitive relative to previously reported devices based on MA-free, or MA- and Br-free perovskite compositions (see ref. 34 for details).

The LED with the NHE film as the emitting layer (EML) also demonstrated largely improved electroluminescent characteristics compared to the control device (Figure 7.2c). The normalized electroluminescence spectra of the devices based on the control and NHE films were almost identical (inset of Figure 7.2c), whereas the NHE device showed much greater radiance over the whole operating voltage range. The maximum radiance of the device substantially increased from ~70.78 W sr^{-1}·m^{-2} for the control device to ~187.7 W sr^{-1}·m^{-2} by using the NHE EML (165.2% improvement). The lower current density of the 3F device than that of the control is due to more effective charge blocking within the NHE EML, enabled by the grain boundary layered perovskite formation (see ref. 34 for details). The considerable performance enhancements for both the solar cell and LED devices can be mainly attributed to enhanced crystallinity and thus

lower defect density of the perovskite films, resulting in the suppressed non-radiative recombination of the charge carriers. This might promote effective charge carrier collection and enhanced radiative recombination in the solar cells and LEDs, respectively. Also, the grain boundary layered perovskites forming a type-I band alignment would additionally help to repulse the photo-generated or injected charge carriers from the defective grain boundaries, which will be helpful for the performance of both solar cells and LEDs.

7.4. Conclusion

In this work, we demonstrated kinetic-controlled and substrate-tolerant local epitaxial growth of $FAPbI_3$ perovskite crystals. The layered perovskite-templated epitaxial crystal growth was induced during the solid-state phase transformation of hexagonal $FAPbI_3$ into its cubic perovskite polymorph. The phase conversion kinetics was retarded by the induced strain at the hetero-interface between the layered perovskites and $FAPbI_3$. Our first-principles calculations revealed that the hexagonal-to-cubic conversion energy barrier was controlled by a synergistic effect between the induced strain and entropy. The kinetic-controlled NHE facilitated the growth of 10-fold enlarged $FAPbI_3$ perovskite crystals with a reduced defect density and strong preferred orientation. Resultingly, our proof-of-concept solar cell and LED devices showed efficiencies and stabilities superior to the controls. We believe our approach will provide new insights to innovatively reduce the defect density in thin films of perovskites and other semiconducting materials using a simple, cheap and versatile method to further improve their stability and performance.

7.5. References

(1) Stringfellow, G. B. *Rep. Prog. Phys.* **1982**, *45*, 469.

(2) Meyerson, B. S. *Appl. Phys. Lett.* **1986**, *48*, 797–799.

(3) Waltereit, P.; Brandt, O.; Trampert, A.; Grahn, H. T.; Menniger, J.; Ramsteiner, M.; Reiche, M.; Ploog, K. H. *Nature* **2000**, *406*, 865–868.

(4) Yoon, J.; Jo, S.; Chun, I. S.; Jung, I.; Kim, H.-S.; Meitl, M.; Menard, E.; Li, X.; Coleman, J. J.; Paik, U. *Nature* **2010**, *465*, 329–333.

(5) Berger, C.; Song, Z.; Li, X.; Wu, X.; Brown, N.; Naud, C.; Mayou, D.; Li, T.; Hass, J.; Marchenkov, A. N. *Science* **2006**, *312*, 1191–1196.

(6) Shim, J.; Bae, S.-H.; Kong, W.; Lee, D.; Qiao, K.; Nezich, D.; Park, Y. J.; Zhao, R.; Sundaram, S.; Li, X. *Science* **2018**, *362*, 665–670.

(7) Walsh, A.; Scanlon, D. O.; Chen, S.; Gong, X. G.; Wei, S. *Angew. Chem. Int. Ed.* **2015**, *54*, 1791–1794.

(8) Kelso, M. V; Mahenderkar, N. K.; Chen, Q.; Tubbesing, J. Z.; Switzer, J. A. *Science* **2019**, *364*, 166–169.

(9) Chen, Y.; Lei, Y.; Li, Y.; Yu, Y.; Cai, J.; Chiu, M.-H.; Rao, R.; Gu, Y.; Wang, C.; Choi, W. *Nature* **2020**, *577*, 209–215.

(10) Jiang, J.; Sun, X.; Chen, X.; Wang, B.; Chen, Z.; Hu, Y.; Guo, Y.; Zhang, L.; Ma, Y.; Gao, L. *Nat. Commun.* **2019**, *10*, 1–12.

(11) Shi, E.; Yuan, B.; Shiring, S. B.; Gao, Y.; Guo, Y.; Su, C.; Lai, M.; Yang, P.; Kong, J.; Savoie, B. M. *Nature* **2020**, *580*, 614–620.

(12) Lee, J.-W.; Bae, S.-H.; Hsieh, Y.-T.; De Marco, N.; Wang, M.; Sun, P.; Yang, Y. *Chem* **2017**, *3*, 290–302.

(13) Im, J.-H.; Jang, I.-H.; Pellet, N.; Grätzel, M.; Park, N.-G. *Nat. Nanotechnol.* **2014**, *9*, 927–932.

(14) Lee, J.-W.; Dai, Z.; Han, T.-H.; Choi, C.; Chang, S.-Y.; Lee, S.-J.; De Marco, N.; Zhao, H.; Sun, P.; Huang, Y. *Nat. Commun.* **2018**, *9*, 1–10.

(15) Wang, Z.; Lin, Q.; Chmiel, F. P.; Sakai, N.; Herz, L. M.; Snaith, H. J. *Nat. Energy* **2017**, *2*, 1–10.

(16) Han, T.; Lee, J.; Choi, Y. J.; Choi, C.; Tan, S.; Lee, S.; Zhao, Y.; Huang, Y.; Kim, D.; Yang, Y. *Adv. Mater.* **2020**, *32*, 1905674.

(17) Min, H.; Kim, M.; Lee, S.-U.; Kim, H.; Kim, G.; Choi, K.; Lee, J. H.; Seok, S. II. *Science* **2019**, *366*, 749–753.

(18) *Gaussian 09*, Revision D.01, Frisch, M. J.; Trucks, G. W.; Schlegel, H. B.; Scuseria, G. E.; Robb, M. A.; Cheeseman, J. R.; Scalmani, G.; Barone, V.; Mennucci, B.; Petersson, G. A.; Nakatsuji, H.; Caricato, M.; Li, X.; Hratchian, H. P.; Izmaylov, A. F.; Bloino, J.; Zheng, G.; Sonnenberg, J. L.; Hada, M.; Ehara, M.; Toyota, K.; Fukuda, R.; Hasegawa, J.; Ishida, M.; Nakajima, T.; Honda, Y.; Kitao, O.; Nakai, H.; Vreven, T.; Montgomery, J. A. Jr.; Peralta, J. E.; Ogliaro, F.; Bearpark, M.; Heyd, J. J.; Brothers, E.; Kudin, K. N.; Staroverov, V. N.; Keith, T.; Kobayashi, R.; Normand, J.; Raghavachari, K.; Rendell, A.; Burant, J. C.; Iyengar, S. S.; Tomasi, J.; Cossi, M.; Rega, N.; Millam, J. M.; Klene, M.; Knox, J. E.; Cross, J. B.; Bakken, V.; Adamo, C.; Jaramillo, J.; Gomperts, R.; Stratmann, R. E.; Yazyev, O.; Austin, A. J.; Cammi, R.; Pomelli, C.; Ochterski, J. W.; Martin, R. L.; Morokuma, K.; Zakrzewski, V. G.; Voth, G. A.; Salvador, P.; Dannenberg, J. J.; Dapprich, S.; Daniels, A. D.; Farkas, O.; Foresman, J. B.; Ortiz, J. V.; Cioslowski, J.; Fox, D. J. *Gaussian, Inc*., Wallingford CT, **2013**.

(19) Hirshfeld, F. L. *Theor. Chim. Acta* **1977**, *44*, 129–138.

(20) Ritchie, J. P. *J. Am. Chem. Soc.* **1985**, *107*, 1829–1837.

(21) Ritchie, J. P.; Bachrach, S. M. *J. Comput. Chem.* **1987**, *8*, 499–509.

(22) Singh, U. C.; Kollman, P. A. *J. Comput. Chem.* **1984**, *5*, 129–145.

(23) Besler, B. H.; Merz Jr, K. M.; Kollman, P. A. *J. Comput. Chem.* **1990**, *11* (4), 431–439.

(24) Matczak, P. *Computation* **2016**, *4*, 3.

(25) Wiberg, K. B.; Rablen, P. R. *J. Org. Chem.* **2018**, *83*, 15463–15469.

(26) *GaussView*, Version 5, Dennington, R.; Keith, T. A.; Millam, J. M. Semichem Inc., Shawnee Mission, KS, **2008**.

(27) Kresse, G.; Furthmüller, J. *Phys. Rev. B* **1996**, *54*, 11169.

(28) Perdew, J. P.; Burke, K.; Ernzerhof, M. *Phys. Rev. Lett.* **1996**, *77*, 3865.

(29) Perdew, J. P.; Ruzsinszky, A.; Csonka, G. I.; Vydrov, O. A.; Scuseria, G. E.; Constantin, L. A.; Zhou, X.; Burke, K. *Phys. Rev. Lett.* **2008**, *100*, 136406.

(30) Grimme, S.; Antony, J.; Ehrlich, S.; Krieg, H. *J. Chem. Phys.* **2010**, *132*, 154104.

(31) Lee, J.-W.; Seol, D.-J.; Cho, A.-N.; Park, N.-G. *Adv. Mater.* **2014**, *26*, 4991–4998.

(32) Chen, T.; Foley, B. J.; Park, C.; Brown, C. M.; Harriger, L. W.; Lee, J.; Ruff, J.; Yoon, M.; Choi, J. J.; Lee, S.-H. *Sci. Adv.* **2016**, *2*, e1601650.

(33) Lee, J.-W.; Tan, S.; Han, T.-H.; Wang, R.; Zhang, L.; Park, C.; Yoon, M.; Choi, C.; Xu, M.; Liao, M. E.; Lee, S.-J.; Nuryyeva, S.; Zhu, C.; Huynh, K.; Goorsky, M. S.; Huang, Y.; Pan, X.; Yang, Y. *Nat. Commun.* **2020**, *11*, 5514.

(34) *Supplementary Information of:* Lee, J.-W.; Tan, S.; Han, T.-H.; Wang, R.; Zhang, L.; Park, C.; Yoon, M.; Choi, C.; Xu, M.; Liao, M. E.; Lee, S.-J.; Nuryyeva, S.; Zhu, C.; Huynh, K.; Goorsky, M. S.; Huang, Y.; Pan, X.; Yang, Y. *Nat. Commun.* **2020**, *11*, 5514.

(35) Porter, D. A.; Easterling, K. E. & Sherif, M. Y. *Phase Transformations in Metals and Alloys (Revised Reprint)*; CRC press, 1992.

Chapter 8. Constructive molecular configurations for surface-defect passivation of perovskite photovoltaics

8.1. Background

Defect passivation to reduce unproductive charge recombination is an effective strategy to increase the power conversion efficiency (PCE) of polycrystalline metal-halide perovskite thin-film photovoltaics (PVs).[1-6] The ionic nature of the perovskite lattice enables molecular passivation through coordinate binding based on Lewis acid-base chemistry.[7-10] While a variety of organic molecules containing functional groups that can interact with defects have been widely reported to enhance the PCE and stability of perovskite solar cells,[11-17] the mechanism of passivation is yet to be discovered. The tremendous versatility and tunability of organic molecular structures and lack of in-depth studies of the corresponding passivation mechanism pose a challenge to perovskite research community: the dire need for molecular design rules for effective passivation. For instance, molecules containing the carbonyl group, well-known as a Lewis base, have been extensively reported as effective passivation agents in perovskite.[11,14,15,17] However, while the rich chemistry in organic molecules enables the structure tunability, it also adds the complexity to exploring the most effective passivation molecules. This brings out the significance of investigating the chemical environment of the effective functional groups and its effect on defect passivation. The selection of molecules with optimal binding configurations for defect passivation would benefit from molecular design rules.

Herein, we demonstrate high efficiencies for $FA_xMA_{1-x}PbI_xBr_{3-x}$ (where FA is formamidinium and MA is methylammonium; x is 0.92 in the precursor) perovskite photovoltaic devices *via* rational design and comprehensive investigation of the chemical environment around active functional groups in defect passivation.

8.2. Methodology

8.2.1. Computational methods

The VASP code is employed to carry out all first-principles calculations.[18,19] A revised Perdew-Burke-Ernzerhof generalized gradient approximation (PBEsol)[20,21] was used for the exchange-correlation including a dispersion correction using Grimme's DFT-D3 scheme.[22,23] PBEsol functional has been introduced to improve the equilibrium properties of solids and surfaces.[24] Valence-core interactions were described by projector-augmented-wave (PAW) pseudopotentials.[25] Plane-wave expansions with kinetic energies up to 300 eV were chosen as the basis set for all geometry optimization calculations and then 500 eV were chosen for the single-point density-of-states (DOS) calculations based on these optimized geometries. Both atomic positions and cell dimensions were optimized using a conjugate gradient algorithm until all Hellman-Feynman forces are smaller than 0.02 eV/Å. All atomic positions are allowed to relax. 4x4x1-center k-point mesh was adopted for Brillouin-zone sampling for all cases. The surfaces were modeled by a slab consisting of 2x2 periodicity in the a-b plane and at least three atomic layers along the c axis, separated by 15-20 Å of vacuum in the surface normal direction.

All quantum chemical calculations were performed using Gaussian 16.1.[26] GaussView 6.0.16 was used to construct initial structures used in computations. For the initial structures, PbI_2 was positioned at various locations around the xanthine alkaloids and the geometry of each resulting PbI_2-small molecule geometry was optimized with the ωB97X-D density functional and the 6-311++G(2d,p) basis set for C, H, N and O atoms, and LANL2DZ basis set for Pb and I atoms. Optimized geometries were verified by frequency calculations as minima (zero imaginary frequencies) at the same level of theory as that used for geometry optimization. Interaction energies

were computed using the same level of theory as that for geometry optimization using the following equation:

$$\Delta E_{int} = E(PbI_2 \cdot small\ molecule) - [\ E(PbI_2) + E(small\ molecule)\ ].$$

Molecular structures were visualized and rendered using CYLview.[27]

8.2.2. DFT characterization of surface defects and defect passivation

PbI_2 terminated (001) slab of $FAPbI_3$ is considered for all point defect calculations. The starting structure parameters are taken from the experimental unit cell of the cubic phase.[28] We computationally described the defect formation based on the procedure by Yin et al.[29] We considered four different common perovskite intrinsic defects formed in bulk and/or surface:[30-32] lead anti-site (Pb_I), iodine vacancy (V_I), lead vacancy (V_{Pb}) and iodine anti-site (I_{Pb}) defects. The surface structures of the optimized defects are shown in Figure 8.1. For a defect *D* with a charge-state *q*, defect formation energies (DFE) over the slab surface are calculated from the following expression:

$$\Delta H_D(q) = E_D(q) - (E_{D=0} + n_I[\mu_I + E_{I_2}/2] + n_{Pb}[\mu_{Pb} + E_{Pb}]) + q(E_F + E_{VBM}) \quad \text{Eq. 1}$$

where $E_{D=0}$ is the total energy of the defect-free slab, μ_i are the chemical potentials E_{I_2} and E_{Pb} are corresponding electronic energies, n_i are the change in the number of atoms during the formation of the defect, E_F is the Fermi energy and E_{VBM} is the valence band maximum energy. The chemical potential, for the formation of $FAPbI_3$, should satisfy

$$\mu_{FA} + \mu_{Pb} + 3\mu_I = \Delta H(FAPbI_3) \quad \text{Eq. 2}$$

under thermodynamic equilibrium growth conditions, where $\Delta H(FAPbI_3)$ is the formation enthalpy of $FAPbI_3$. Also, within the equilibrium conditions of FAI and PbI_2, the equations below should be satisfied:

$$\mu_{FA} + \mu_I \leq \Delta H(FAI) \quad \text{Eq. 3}$$

$$\mu_{Pb} + 2\mu_I \leq \Delta H(PbI_2) \quad \text{Eq. 4}$$

When the Pb-rich is considered (depending on the fabrication and other conditions), where $\mu_{Pb} = 0$, then $\mu_I = \Delta H(PbI_2)/2$ and $\mu_{FA} = \Delta H(FAI)$ conditions can be met. Therefore, in the case of neutral defects and a Pb-rich condition Eq. 1 is simplified as:

$$\Delta H_D = E_D - (E_{D=0} + n_I[\Delta H(PbI_2) + E_{I_2}]/2 + n_{Pb}E_{Pb}) \quad \text{Eq. 5}$$

Thermodynamic charge transition levels, i.e., the Fermi level at which $\Delta H_D(q) = \Delta H_D(q')$ condition is satisfied, is calculated by

$$\epsilon(q/q') = [E_D(q) - E_D(q')]/(q - q') + E_{VBM} \quad \text{Eq. 6}$$

Finally, the interaction energy between the molecule and the slab with defect *D* is found from

$$E_{int} = E_{D,X} - (E_D + E_X) \quad \text{Eq. 7}$$

where, $E_{D,X}$ is the total energy of the slab+molecule complex (see Figure 8.1), E_D is the energy of the free slab and E_X is the gas phase energy of the molecule, i.e., $X =$ {Theophylline, Caffeine, Theobromine}.

8.2.3. Device fabrication by the Yang group

Perovskite solar cells were fabricated with the following structure: indium tin oxide (ITO)/SnO_2/$(FAPbI_3)_x(MAPbBr_3)_{1-x}$/Spiro-OMeTAD/Ag or Au. The ITO glass was precleaned in an ultrasonic bath of acetone and isopropanol and treated in ultraviolet ozone for 20 min. A thin layer (ca. 30 nm) of SnO_2 was spin-coated onto the ITO glass and baked at 180 °C for 60 min. SnO_2 was diluted in water (2 mg·mL^{-1}). After cooling to room temperature, the glass/ITO/SnO_2

substrates were transferred into a nitrogen glove box. The PbI_2 solution was prepared by dissolving 1.4 mM PbI_2 into 1 mL N, N-dimethylformamide/dimethyl sulfoxide mixed solvent (v/v 94/6). The FAI/MABr/MACl solution was prepared by dissolving 70 mg FAI, 4 mg MABr and 10 mg MACl into 1 mL isopropyl alcohol (IPA). The solutions should be stirring overnight before use. The PbI_2 solution was spincoated on the substrate at 1500 rpm for 30 s and annealed at 70 °C for 1 min. And the FAI/MABr/MACl solution was spin-coated on the substrate at 1800 rpm for 30 s, then the film was annealed outside the glove box at 150 °C for 10 min with 40% humidity. And then either the Theophylline/IPA:CB (CB stands for chlorobenzene; the volume ratio of IPA and CB is 1:1), Caffeine/IPA:CB or Theobromine/IPA:CB solution was drop-casted at 4000 rpm on the perovskite film. The film was dried at 100 °C for 30 s. The Spiro-OMeTAD solution [60mg Spiro-OMeTAD in 700 µL CB with 25.5 µL tBP, 15.5 µL Li-TFSI (520 mg/mL in ACN) and 12.5 µL FK209 (375 mg/mL in ACN)], or PTAA solution for stability test [40 mg/mL; in CB with 10% TPFB] was spun onto the perovskite film as a hole conductor. The devices were completed by evaporating the 100-nm gold or silver as a last lear in a vacuum chamber (base pressure, 5×10^{-4} Pa).

8.3. Results and Discussion

We demonstrate high efficiencies for $(FAPbI_3)_x(MAPbBr_3)_{1-x}$ perovskite photovoltaic (PV) devices through defect identification followed by rational design and comprehensive investigation of the chemical environment around the active functional group for defect passivation.[29] In high-quality perovskite polycrystalline thin films that have monolayered grains,[33-35] interior defects of perovskite are negligible compared to the surface defects. We used density-functional theory (DFT) calculations to compare the formation energies of selected native defects on the perovskite

surface. Particularly taken into consideration were Pb- and I-involving point defects, Pb vacancy (V_{Pb}), I vacancy (V_I) and Pb-I antisite (Pb_I and I_{Pb}, corresponding to I site substitution by Pb, and Pb site substitution by I, respectively) because the band edges of perovskite were reported to be composed of Pb and I orbitals.[36,37]

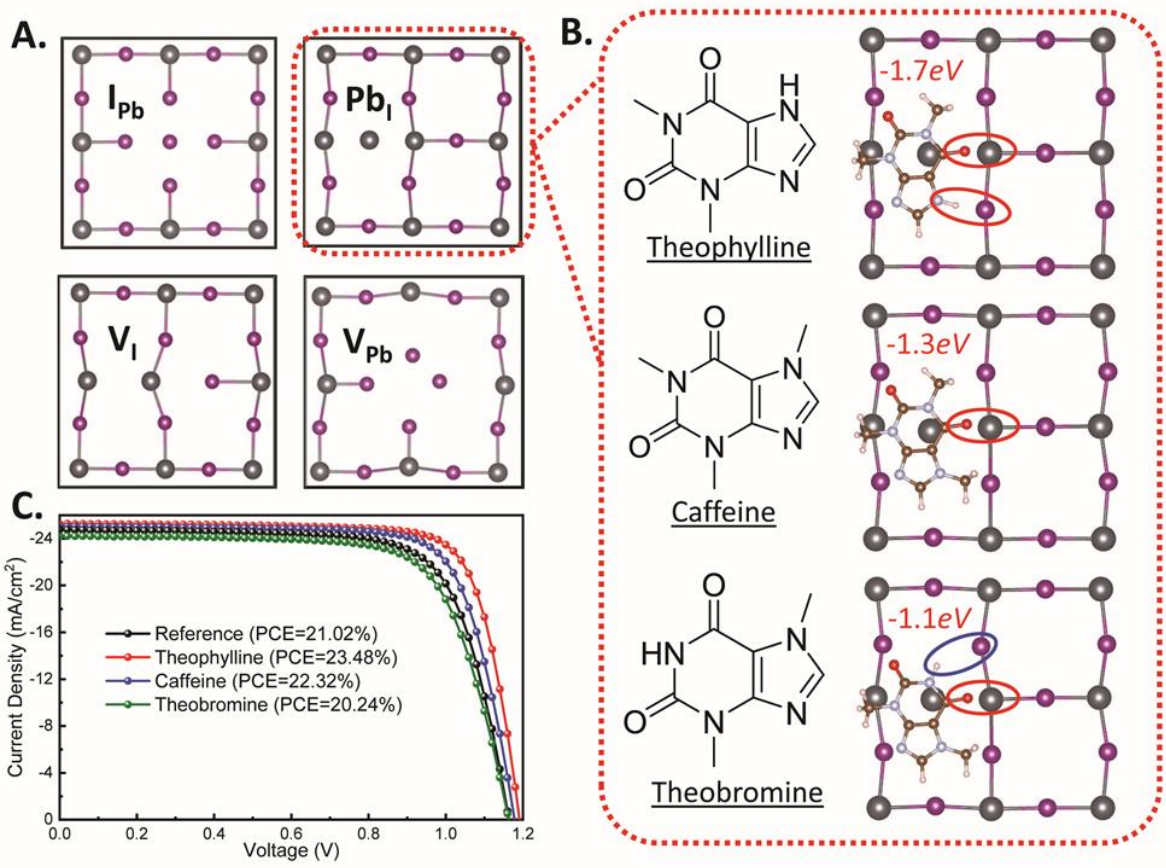

Figure 8.1. Surface defect identification and constructive configuration of the C=O group in three different chemical environments. (A) Top view of the various types of surface defects. (B) Theoretical models of perovskite with molecular surface passivation of Pb_I antisite with theophylline, caffeine, and theobromine (C) J-V curves of perovskite solar cells with or without small molecules treatment under reverse scan direction.

As confirmed by x-ray photoelectron spectroscopy (XPS), the surface of the as-fabricated perovskite thin film synthesized by a two-step method was Pb-rich (see ref. 38 for details), and we focused on the (100) surface with PbI_2 termination in a Pb-rich condition. The types of surface defects studied, and their corresponding top-layer view of atomic structures are shown in Figure

8.1A. Using the Dispersion Correction 3 (DFT-D3) method, we calculated the defect formation energies (DFEs) (Table 8.1) of V_{Pb}, V_I, Pb_I, and I_{Pb} on the surface to be 3.20, 0.51, 0.57 and 3.15 eV, respectively. Compared with the values reported in bulk perovskite, V_{Pb}, V_I and I_{Pb} defects show similar DFEs,[30] whereas the Pb_I antisite defect exhibited particularly lower formation energy than that in the bulk. Thus, the Pb_I antisite defect should form more readily and predominate on the surface. We did not consider V_I further despite its DFE being as low as that of Pb_I, because the interaction of molecules with the V_I turned out to be not energy favorable (Figure 8.2).

Table 8.1. ΔH_α, formation energies of neutral defects considered in this study.

Defect type	ΔH_α (eV) Surface	ΔH_α (eV) Bulk*
I_{Pb}	3.15	3.89
Pb_I	0.57	1.46
V_I	0.51	0.63
V_{Pb}	3.20	2.97

*from reference 12.

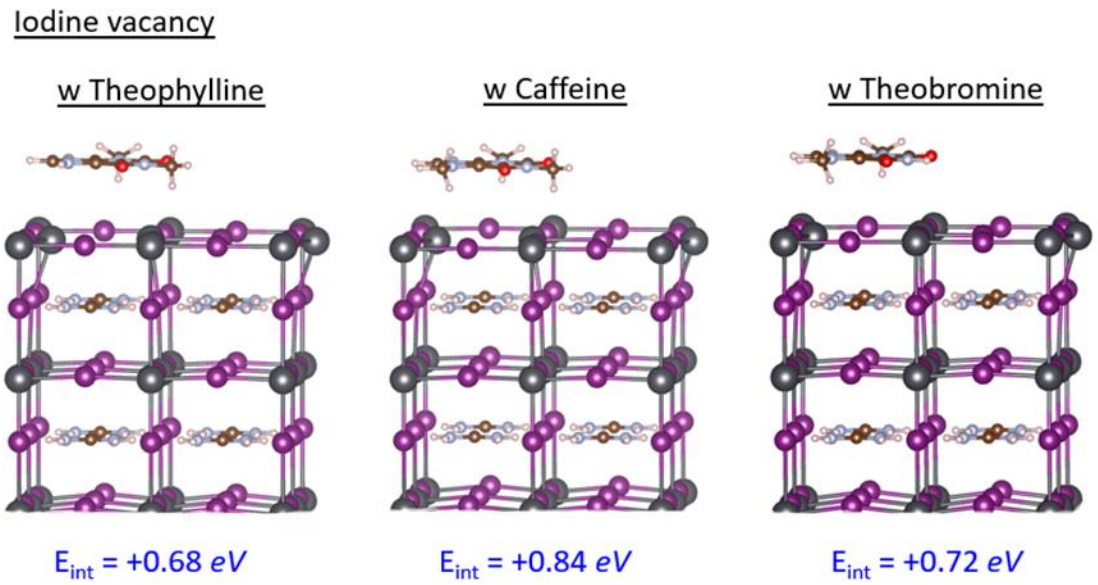

Figure 8.2. Interaction energies between the molecule and slab complex for the V_I case using DFT-D3 method.

Based on these results, we focused on the interaction between the surface Pb_I antisite defect and candidate molecules for defect passivation. A set of small molecules sharing the identical functional groups but with strategically varying chemical structure were investigated, namely theophylline, caffeine and theobromine, interacting with the defects (Figure 8.1B). These molecules are found in natural products (tea, coffee and chocolate, respectively) and are readily accessible. In these molecules, the conjugated structure as well as the dipoles induced by the hetero atoms tend to increase the intermolecular interaction. This renders them nonvolatile in nature, which is key to the investigation of their interactions with defects in perovskite and long-term stability of the devices. The xanthine core also helps maintain the coplanarity of the carbonyl group and the N–H. Unlike other small molecules with flexible alkyl chains, this rigidity allows us to define the configuration and distance between the carbonyl group and N–H when they are interacting with the defects, as a result of which the constructive molecular configuration for defect passivation can be unraveled.

We incorporated theophylline onto the surface of perovskite thin film using a post-treatment method, and a PCE enhancement from 21.02% to 23.48% was observed in the photovoltaic (PV) devices with ITO/SnO_2/perovskite/Spiro-OMeTAD/Ag structure under reverse scan direction (where ITO is indium tin oxide, SnO_2 is tin oxide and Spiro-OMeTAD is 2,2′7,7′-tetrakis-(*N*,*N*-di-p-methoxyphenyl amine)-9,9′-spirobifluorene). Current density-voltage (J-V) curves of the PV devices with and without theophylline treatment are compared in Figure 8.1C and Table 8.2. The control device showed an open circuit voltage (V_{OC}) of 1.164 V, a short circuit current (J_{SC}) of 24·78 $mA \cdot cm^{-2}$, a fill factor (FF) of 72.88%, whereas the target device showed a V_{OC} of 1.191 V, a J_{SC} of 25·24 $mA \cdot cm^{-2}$, a FF of 78.11%. The enhancement in the V_{OC} we attributed to the surface passivation by theophylline through the Lewis base-acid interaction

between C=O group and the antisite Pb. As shown in the surface structure model of perovskite with theophylline (Figure 8.1B), the C=O group on theophylline strongly interacted with the antisite Pb. The neighboring N-H on the imidazole ring also interacted with the I of PbI_6^{2-} octahedron through a hydrogen bond (H-bond), which strengthened the absorption of theophylline onto the Pb_I defect, resulting in an interaction energy (E_{int}, defined as $E_{molecule\text{-}perovskite}$ - $E_{perovskite}$ - $E_{molecule}$) as strong as -1.7 eV.

Table 8.2. Photovoltaic parameters of average and the best perovskite solar devices without and with various types of surface treatments.

Type of Treatment	V_{OC} (V)	J_{SC} (mA cm^{-2})	FF	PCE (%)	
				average	best
Ref	1.153±0.02	24.19±0.35	0.73±0.07	20.36±0.53	21.02
Theophylline	1.187±0.01	24.74±0.46	0.77±0.02	22.61±0.58	23.48
Caffeine	1.168±0.02	24.63±0.39	0.75±0.01	21.58±0.69	22.32
Theobromine	1.151±0.02	24.36±0.43	0.70±0.03	19.63±0.65	20.24

This observation suggested that the neighboring H-bond between the xanthine molecule and the PbI_6^{2-} octahedron can contribute to the defect passivation. A methyl group was added to the N on the imidazole ring of theophylline (resulting in caffeine) to eliminate the effect from H-bonding between the N-H and I, leaving just the interaction with surface Pb_I defects (Figure 8.1B). The missing H-bond between N-H and PbI_6^{2-} octahedron resulted in a weakened interaction and a less favorable E_{int} of -1.3 eV. Compared with the theophylline-treated device, a caffeine-treated perovskite PV device had a lower PCE of 22.32% along with a lower V_{OC} of 1.178 V, J_{SC} of 25.04 mA·cm^{-2} and FF of 75.76%.

When the N-H group was located next to the C=O group on the same six-membered ring, producing a shorter distance between the C=O and the N-H, in theobromine, the spatially effective interaction between the N-H and I was disabled as C=O was bound to antisite Pb, resulting in an even weaker interaction energy of -1.1 eV (Figure 8.1B). Although both C=O and N-H are both present on the molecule, the lack of appropriate coordination of I to the molecule led to a spatially destructive molecular configuration. The theobromine-treated devices showed a decrease in PCE to 20.24% with a lower V_{OC} of 1.163 V, J_{SC} of 24.27 $mA \cdot cm^{-2}$ and FF of 71.58% compared with the reference device. This result emphasizes the importance of the constructive configuration of N-H and C=O groups that enable the cooperative multisite interaction and synergistic passivation effect.

We studied the variation in the C=O and the PbI_2-terminated perovskite surface interaction with different molecular configurations using Fourier-transform infrared spectroscopy (FTIR). The C=O in pure theophylline showed a typical stretching vibration mode at 1660 cm^{-1} that it shifted to 1630 cm^{-1} upon binding to PbI_2 (Figure 8.3A). The downward shift of 30 cm^{-1} of the C=O stretching vibration frequency resulted from the electron delocalization in C=O when a Lewis base-acid adduct was formed, demonstrating a strong interaction between PbI_2 and C=O in theophylline. The atomic distance between the O in C=O and the Pb in PbI_2, on the basis of theoretical modeling was as low as 2.28 Å.

When the H atom was replaced by a methyl group on the N of imidazole to eliminate the effect of a H-bond, the vibration frequency of C=O in caffeine shifted only 10 cm^{-1} upon addition of PbI_2, indicating a weakened interaction between the C=O and PbI_2 (Figure 8.3B). The atomic distance between the corresponding O and Pb also increased to 2.32 Å. In the case of theobromine, when the N-H was in a closer position to C=O, the interaction between the molecule and PbI_2

became comparable to that in theophylline, as evidenced by the large shift of C=O stretching vibration frequency from 1655 to 1620 cm^{-1} and the short distance between O and Pb (Figure 8.3C). However, this strong interaction was enabled by the free rotation of PbI_2, which resulted in a different configuration than that in theophylline and caffeine. Hence, when the configuration of PbI_2 was fixed and had a 90° angle between Pb and I atom, like that on perovskite surface (the PbI_6^{2-} octahedron), the N-H was in a position that led to an unfavorable interaction with I. This configuration would either cause weakened interaction between the molecule and the perovskite surface or distorted PbI_6^{2-} octahedron, resulting in the ineffectiveness of defect passivation and perhaps causing even more defects through lattice distortion.

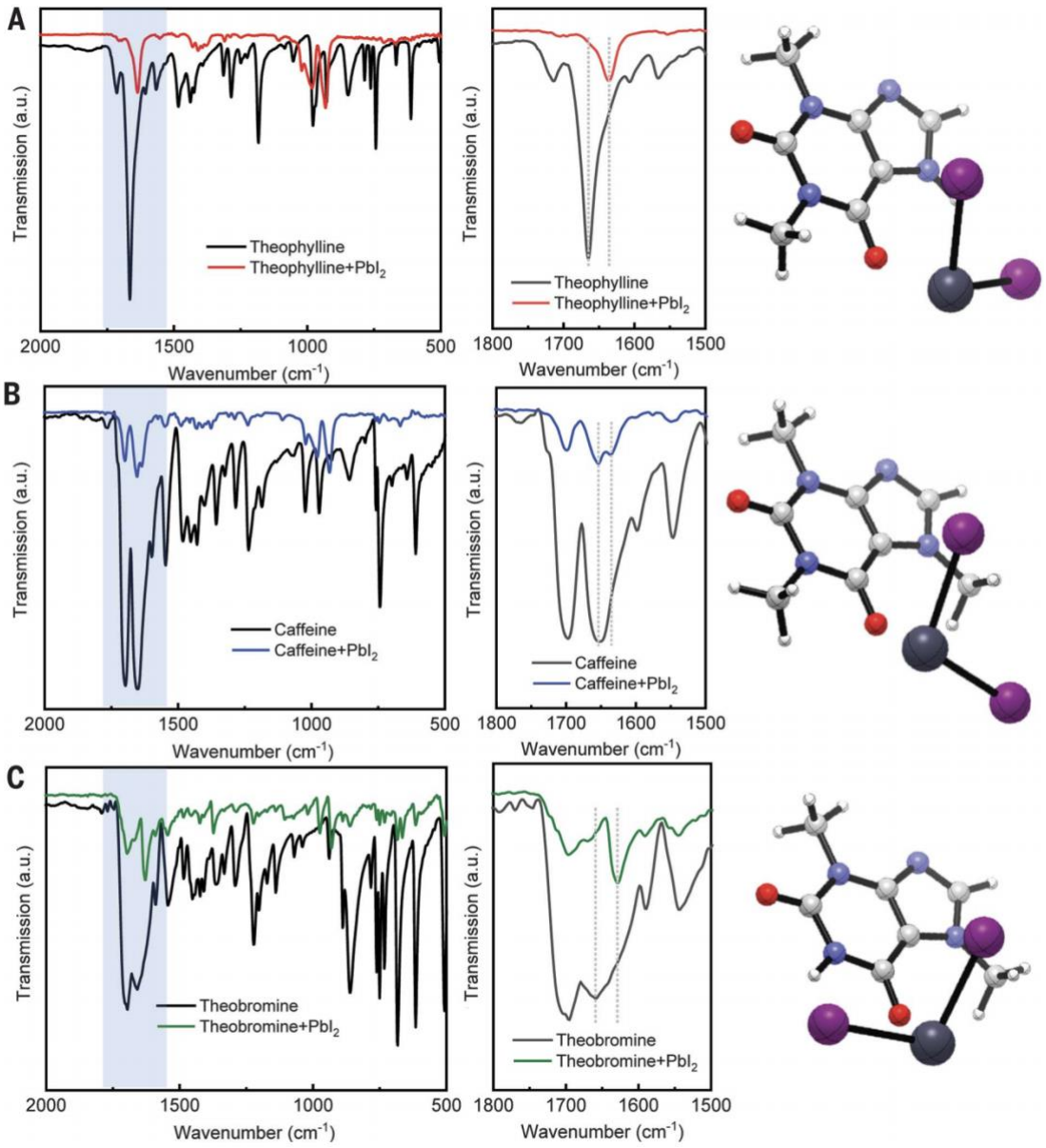

Figure 8.3. Investigation of the interactions between surface defects and the small molecules. FTIR spectra of (A) pure theophylline and theophylline-PbI_2 films, (B) pure caffeine and caffeine-PbI_2 films, and (C) pure theobromine and theobromine-PbI_2 films with corresponding molecular models on the right.

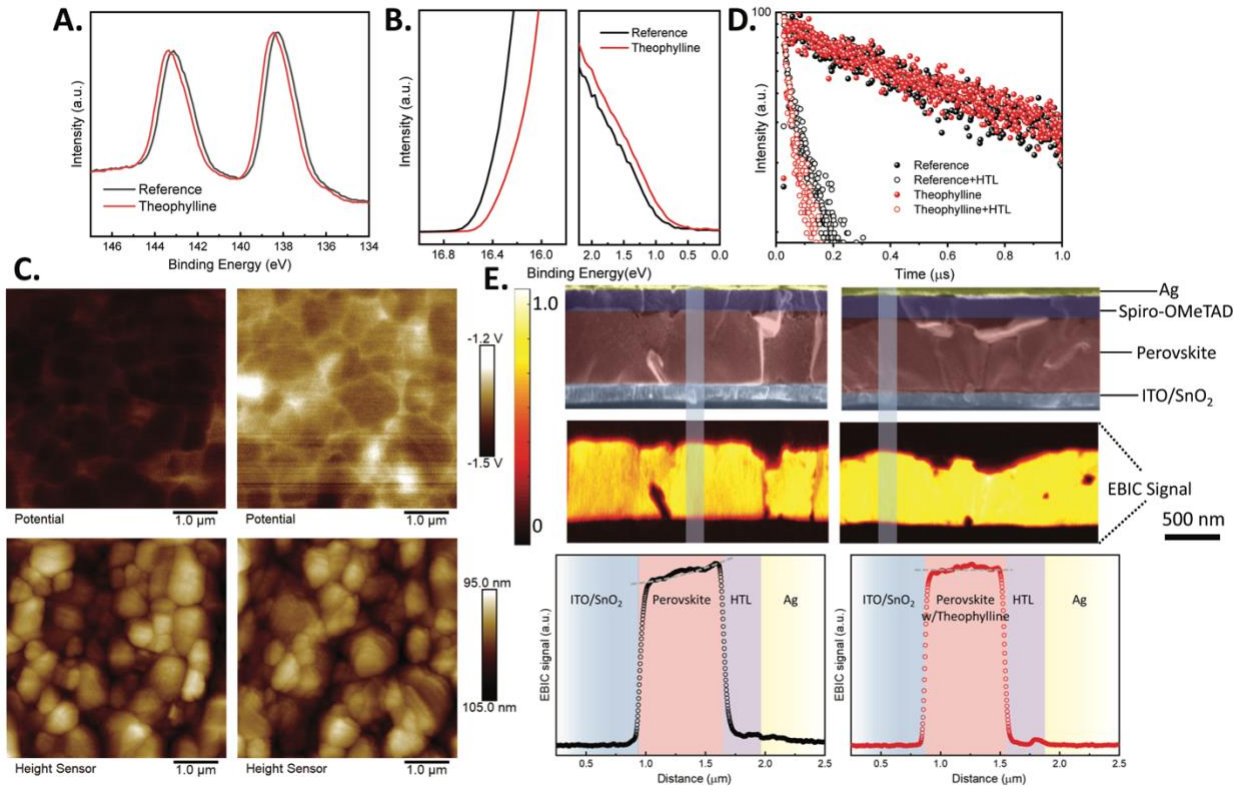

Figure 8.4. Characterization of perovskite films and interfaces with theophylline treatment. (A) XPS data for Pb 4f 7/2 and Pb 4f 5/2 core-level spectra in perovskite films with or without theophylline treatment. (B) UPS spectra of perovskite films with or without theophylline treatment. (C) AFM and KPFM images of perovskite films with (right) or without (left) theophylline treatment. (D) Time-resolved PL spectra of perovskite films before and after depositing Spiro-OMeTAD without and with theophylline treatment. (E) Cross-section SEM images and the corresponding EBIC images and line profile of the perovskite solar cells with (right) or without (left) theophylline treatment.

Further characterizations were performed to better understand the perovskite interface with theophylline. High-resolution XPS patterns of the Pb 4f for the theophylline-treated film showed two main peaks located at 138.48 and 143.38 eV, corresponding to the Pb 4f 7/2 and Pb 4f 5/2, respectively (Figure 8.4A), whereas the reference film showed two main peaks at 138.27 and 143.13 eV. The peaks from Pb 4f shifted to higher binding energies in the film with theophylline surface treatment, indicating the interaction between the theophylline and the Pb on perovskite surface. We used ultraviolet photoelectron spectroscopy (UPS) to measure the surface band

structure with and without the theophylline surface treatment. The work function was determined to be -4.77 eV and -4.96 eV with the valance band maximum of -5.66 and -5.73 eV for reference and theophylline, respectively (Figure 8.4B). This difference indicated a less n-type surface after theophylline treatment, which could improve the hole extraction in devices.

Atomic force microscopy (AFM) combined with Kelvin probe force microscopy (KPFM) was further applied to probe the effect of theophylline on the surface morphology and surface potential. The theophylline-treated surface exhibited a higher electronic chemical potential than that of reference film, while keeping the surface morphology unchanged (Figure 8.4C). The transient photoluminescence (PL) of the perovskite films with hole-transporting layer (HTL) was compared in Figure 8.4D to delineate the carrier dynamics of the devices. The perovskite film with theophylline treatment showed a slightly longer carrier lifetime than the reference film, whereas a faster decay profile was observed when adding the HTL on top of the perovskite film. This result demonstrated a better hole extraction with theophylline treatment,[34] most likely arising from lesser recombination sites at the interface and the slightly shallower work function of the perovskite film with theophylline.

The improved carrier dynamics originating from the effective surface passivation by theophylline was further characterized by cross-sectional electron-beam-induced current (EBIC) measurement. In EBIC measurement, the electron-beam excited carriers were collected based on the collection probability CP (x, L_d), where x is the distance between junction and incident beam position, and L_d is the diffusion length of the carriers. The device with theophylline treatment exhibited higher EBIC current compared to the reference device (Figure 8.4E). The average intensity extracted from these EBIC maps demonstrated a general increase in the EBIC signal after treated with theophylline (see ref. 38 for more details), indicating an enhanced carrier collection

efficiency.[39] Specifically, in Figure 8.4E, a representative EBIC line profile of the reference device showed a current decay from the HTL/perovskite to the SnO_2/perovskite interface. The decay indicates that carrier collection was limited by the hole-diffusion length as the beam position moved away from the HTL/perovskite interface. By contrast, the device with theophylline treatment displays minimal decay within the perovskite layer in the EBIC line profile. This difference suggests that a longer diffusion length of holes was present in theophylline-treated sample and balanced electron and hole charge transport and collection was achieved, which is likely the result of fewer surface recombination sites (Figure 8.4E).

8.4. Conclusion

In conclusion, we demonstrated the so far largely ignored chemical environment around the effective functional group for defect passivation in perovskite. The hydrogen bond formation between N-H and I was investigated to be in secondary assistance to the primary C=O binding with Pb and maximize the surface defect passivation in perovskite. This synergistic effect can be enabled only when the N-H and C=O are in a constructive configuration in the molecular structure: while the co-existence of C=O with a neighboring N-H is required, it is not sufficient; a constructive relative position is also a necessity. This provides new insights on the molecular design of effective defect passivation strategy for highly efficient and stable perovskite optoelectronics where non-radiative recombination must be mitigated.

8.5. References

(1) Tong, J.; Song, Z.; Kim, D. H.; Chen, X.; Chen, C.; Palmstrom, A. F.; Ndione, P. F.; Reese, M. O.; Dunfield, S. P.; Reid, O. G.; Liu, J.; Zhang, F.; Harvey, S. P.; Li, Z.; Christensen, S. T.; Teeter, G.; Zhao, D.; Al-Jassim, M. M.; van Hest, M. F. A. M.; Beard, M. C.; Shaheen, S. E.; Berry, J. J.; Yan, Y.; Zhu, K. *Science* **2019**, *364*, 475–479.

(2) Tan, H.; Jain, A.; Voznyy, O.; Lan, X.; De Arquer, F. P. G.; Fan, J. Z.; Quintero-Bermudez, R.; Yuan, M.; Zhang, B.; Zhao, Y. *Science* **2017**, *355*, 722–726.

(3) Zheng, X.; Chen, B.; Dai, J.; Fang, Y.; Bai, Y.; Lin, Y.; Wei, H.; Zeng, X. C.; Huang, J. *Nat. Energy* **2017**, *2*, 1–9.

(4) Yoo, J. J.; Wieghold, S.; Sponseller, M. C.; Chua, M. R.; Bertram, S. N.; Hartono, N. T. P.; Tresback, J. S.; Hansen, E. C.; Correa-Baena, J.-P.; Bulović, V. *Energy Environ. Sci.* **2019**, *12*, 2192–2199.

(5) Jiang, Q.; Zhao, Y.; Zhang, X.; Yang, X.; Chen, Y.; Chu, Z.; Ye, Q.; Li, X.; Yin, Z.; You, J. *Nat. Photonics* **2019**, *13*, 460–466.

(6) Li, N.; Tao, S.; Chen, Y.; Niu, X.; Onwudinanti, C. K.; Hu, C.; Qiu, Z.; Xu, Z.; Zheng, G.; Wang, L.; Zhang, Y.; Li, L.; Liu, H.; Lun, Y.; Hong, J.; Wang, X.; Liu, Y.; Xie, H.; Gao, Y.; Bai, Y.; Yang, S.; Brocks, G.; Chen, Q.; Zhou, H. *Nat. Energy* **2019**, *4*, 408–415.

(7) Manser, J. S.; Christians, J. A.; Kamat, P. V. *Chem. Rev.* **2016**, *116*, 12956–13008.

(8) Zhang, H.; Chen, H.; Stoumpos, C. C.; Ren, J.; Hou, Q.; Li, X.; Li, J.; He, H.; Lin, H.; Wang, J. *ACS Appl. Mater. Interfaces* **2018**, *10*, 42436–42443.

(9) Lee, J.-W.; Kim, H.-S.; Park, N.-G. *Acc. Chem. Res.* **2016**, *49*, 311–319.

(10) Zong, Y.; Zhou, Y.; Zhang, Y.; Li, Z.; Zhang, L.; Ju, M.-G.; Chen, M.; Pang, S.; Zeng, X. C.; Padture, N. P. *Chem* **2018**, *4*, 1404–1415.

(11) Bi, D.; Yi, C.; Luo, J.; Décoppet, J.-D.; Zhang, F.; Zakeeruddin, S. M.; Li, X.; Hagfeldt, A.; Grätzel, M. *Nat. Energy* **2016**, *1*, 16142.

(12) Chen, B.; Rudd, P. N.; Yang, S.; Yuan, Y.; Huang, J. *Chem. Soc. Rev.* **2019**, *48*, 3842–3867.

(13) Wu, T.; Wang, Y.; Li, X.; Wu, Y.; Meng, X.; Cui, D.; Yang, X.; Han, L. *Adv. Energy Mater.* **2019**, *9*, 1803766.

(14) Niu, T.; Lu, J.; Munir, R.; Li, J.; Barrit, D.; Zhang, X.; Hu, H.; Yang, Z.; Amassian, A.; Zhao, K.; Liu, S. (F.) *Adv. Mater.* **2018**, *30*, 1706576.

(15) Wang, R.; Xue, J.; Meng, L.; Lee, J.-W.; Zhao, Z.; Sun, P.; Cai, L.; Huang, T.; Wang, Z.; Wang, Z.-K.; Duan, Y.; Yang, J. L.; Tan, S.; Yuan, Y.; Huang, Y.; Yang, Y. *Joule* **2019**, *3*, 1464–1477.

(16) Xu, W.; Hu, Q.; Bai, S.; Bao, C.; Miao, Y.; Yuan, Z.; Borzda, T.; Barker, A. J.; Tyukalova, E.; Hu, Z.; Kawecki, M.; Wang, H.; Yan, Z.; Liu, X.; Shi, X.; Uvdal, K.; Fahlman, M.; Zhang, W.; Duchamp, M.; Liu, J.-M.; Petrozza, A.; Wang, J.; Liu, L.-M.; Huang, W.; Gao, F. *Nat. Photonics* **2019**, *13*, 418–424.

(17) Zhang, H.; Nazeeruddin, M. K.; Choy, W. C. H. *Adv. Mater.* **2019**, *31*, 1805702.

(18) Kresse, G.; Furthmüller, J. *Comput. Mater. Sci.* **1996**, *6*, 15–50.

(19) Kresse, G.; Furthmüller, J. *Phys. Rev. B* **1996**, *54*, 11169.

(20) Perdew, J. P.; Burke, K.; Ernzerhof, M. *Phys. Rev. Lett.* **1996**, *77*, 3865.

(21) Perdew, J. P.; Ruzsinszky, A.; Csonka, G. I.; Vydrov, O. A.; Scuseria, G. E.; Constantin, L. A.; Zhou, X.; Burke, K. *Phys. Rev. Lett.* **2008**, *100*, 136406.

(22) Grimme, S.; Antony, J.; Ehrlich, S.; Krieg, H. *J. Chem. Phys.* **2010**, *132*, 154104.

(23) Grimme, S. *J. Comput. Chem.* **2006**, *27*, 1787–1799.

(24) Blöchl, P. E. *Phys. Rev. B* **1994**, *50*, 17953.

(25) Csonka, G. I.; Perdew, J. P.; Ruzsinszky, A.; Philipsen, P. H. T.; Lebègue, S.; Paier, J.; Vydrov, O. A.; Ángyán, J. G. *Phys. Rev. B* **2009**, *79*, 155107.

(26) *Gaussian 16*, Revision A.03, Frisch, M. J.; Trucks, G. W.; Schlegel, H. B.; Scuseria, G. E.; Robb, M. A.; Cheeseman, J. R.; Scalmani, G.; Barone, V.; Petersson, G. A.; Nakatsuji, H.; Li, X.; Caricato, M.; Marenich, A. V.; Bloino, J.; Janesko, B. G.; Gomperts, R.; Mennucci, B.; Hratchian, H. P.; Ortiz, J. V.; Izmaylov, A. F.; Sonnenberg, J. L.; Williams-Young, D.; Ding, F.; Lipparini, F.; Egidi, F.; Goings, J.; Peng, B.; Petrone, A.; Henderson, T.; Ranasinghe, D.; Zakrzewski, V. G.; Gao, J.; Rega, N.; Zheng, G.; Liang, W.; Hada, M.; Ehara, M.; Toyota, K.; Fukuda, R.; Hasegawa, J.; Ishida, M.; Nakajima, T.; Honda, Y.; Kitao, O.; Nakai, H.; Vreven, T.; Throssell, K.; Montgomery, J. A., Jr.; Peralta, J. E.; Ogliaro, F.; Bearpark, M. J.; Heyd, J. J.; Brothers, E. N.; Kudin, K. N.; Staroverov, V. N.; Keith, T. A.; Kobayashi, R.; Normand, J.; Raghavachari, K.; Rendell, A. P.; Burant, J. C.; Iyengar, S. S.; Tomasi, J.; Cossi, M.; Millam, J. M.; Klene, M.; Adamo, C.; Cammi, R.; Ochterski, J. W.; Martin, R. L.; Morokuma, K.; Farkas, O.; Foresman, J. B.; Fox, D. J. Gaussian, Inc., Wallingford CT, **2016**.

(27) CYLview, 1.0b; Legault, C. Y., Université de Sherbrooke, 2009 (http://www.cylview.org)

(28) Weller, M. T.; Weber, O. J.; Frost, J. M.; Walsh, *J. Phys. Chem. Lett.* **2015**, *6*, 3209–3212.

(29) Yin, W.-J.; Shi, T.; Yan, Y. *Appl. Phys. Lett.* **2014**, *104*, 63903.

(30) Liu, N.; Yam, C. *Phys. Chem. Chem. Phys.* **2018**, *20*, 6800–6804.

(31) Ran, C.; Xu, J.; Gao, W.; Huang, C.; Dou, S. *Chem. Soc. Rev.* **2018**, *47*, 4581–4610.

(32) Uratani, H.; Yamashita, K. *J. Phys. Chem. Lett.* **2017**, *8*, 742–746.

(33) Yang, W. S.; Park, B.-W.; Jung, E. H.; Jeon, N. J.; Kim, Y. C.; Lee, D. U.; Shin, S. S.; Seo, J.; Kim, E. K.; Noh, J. H. *Science* **2017**, *356*, 1376–1379.

(34) Jeon, N. J.; Na, H.; Jung, E. H.; Yang, T.-Y.; Lee, Y. G.; Kim, G.; Shin, H.-W.; Seok, S. Il; Lee, J.; Seo, J. *Nat. Energy* **2018**, *3*, 682–689.

(35) Jung, E. H.; Jeon, N. J.; Park, E. Y.; Moon, C. S.; Shin, T. J.; Yang, T.-Y.; Noh, J. H.; Seo, J. *Nature* **2019**, *567*, 511–515.

(36) Green, M. A.; Ho-Baillie, A.; Snaith, H. J. *Nat. Photonics* **2014**, *8*, 506–514.

(37) Xiao, Z.; Song, Z.; Yan, Y. *Adv. Mater.* **2019**, *31*, 1803792.

(38) *Supplementary Materials of:* Wang, R.; Xue, J.; Wang, K.-L.; Wang, Z.-K.; Luo, Y.; Fenning, D.; Xu, G.; Nuryyeva, S.; Huang, T.; Zhao, Y.; Yang, J. L.; Zhu, J.; Wang, M.; Tan, S.; Yavuz, I.; Houk, K. N.; Yang, Y. *Science* **2019**, *366*, 1509–1513.

(39) Edri, E.; Kirmayer, S.; Mukhopadhyay, S.; Gartsman, K.; Hodes, G.; Cahen, D. *Nat. Commun.* **2014**, *5*, 1–8.

Chapter 9. Electrostatic stabilization of the passivated wide-gap perovskite surface for stacked tandem photovoltaics

9.1. Background

Multi-junction solar cells mitigate the unavoidable thermalization losses in traditional single-diode-based photovoltaics (PVs) that limit their maximum performance. By tailoring the solar spectrum harvesting by proper choice of absorbers with cascading band gaps,[1] multi-junction solar cells have the potential to overcome the single-junction Shockley-Queisser efficiency limit of 33.7%. Commercial multi-junction solar cells are limited to the costly III-V semiconductor-based technologies, but the emergence of solution-processable organic metal halide perovskites at the bandgap between 1.64-1.68 eV is sparking the development and hence, recent surge in multi-junction solar cells based on rear cells, such as Sn-Pb perovskite[2,3] or cost-friendly commercialized PVs such as silicon and $Cu(In,Ga)(S,Se)_2$.[4–9]

As an emerging PV technology, minimizing the V_{OC} deficiency and improving the efficiency of the perovskite front cell, subsequently, became the go-to option when pairing with matured commercial PV materials. Suppressing non-radiative recombination by defect passivation improves the splitting of the quasi-fermi level of perovskite, and eventually leads to higher power conversion efficiencies (PCEs) and good device stabilities.[10] By combining the experimental and computational methods, advancements on understanding their defect passivation strategies have been continuously evolving. For example, the iodine vacancy (V_I) defect in perovskites was revealed to be shallow in the forbidden band,[11] although some early reports claimed that successful passivation of it led to performance improvements.[12,13] Organic cations with ammonium ($-NH^{3+}$) functionality were mostly believed to passivate negatively charged defects *via* ionic bonding,[14,15] and a subgroup of this family such as butylammonium (BA^+), octylammonium (OA^+) and

phenylethylammonium (PEA^+) were reported to passivate perovskites by forming grain boundary/surface 2D structures.[16–18] On the other hand, You et. al. also stressed the effectiveness of phenylethylammonium iodide (PEAI) itself as a surface passivation agent without the formation of a 2D perovskite structure,[19] and the latest high-efficiency reports also used similar treatment without intentionally deriving 2D structures.[20,21] Our own recent discoveries by mixing PEAI and its derivatives with $FAPbI_3$ even proved that it could initiate a strain-controlled growth to kinetically slow down the perovskite growth rate to result in large crystal grains and suppressed defect densities.[22,23]

In this work, we focused on unravelling the long-debated mechanism behind this organic-ammonium salts family using its representative member, PEAI, and aiming at developing methodologies that magnifies its effect. By utilizing first-principles calculations, we observed a strong electrostatic stabilization via hydrogen bonding originating from PEAI's ammonium group, and cation-π interaction of the phenyl group of PEAI, based on which we designed a targeted synergistic strategy to rationally enhance these interactions. The strategy was realized on a wide-bandgap perovskite to dramatically minimize the front cell voltage loss and improve photovoltaic (PV) performance in a stacked tandem application. With the target front cell, the stacked tandem structure boosted c-Si and copper indium gallium selenide (CIGS) PVs with original efficiency of 18.0% and 20.2%, respectively, (both commercial PV products) to over 25%, and a theoretical efficiency of 28.1% if the record silicon cell was available. These improvements achieved by the stacked configuration (also known as 4-terminal configuration) provides a crucial step towards integration of perovskite PVs into the current PV market and lowering the levelized cost of energy (LCEO) without having to modify the current product line of commercial PV industries.[24]

9.2. Methodology

9.2.1. Computational methods

Density functional theory calculations were performed using Vienna ab-initio simulation package (VASP) code.[25] The revised Perdew-Burke-Ernzerhof generalized gradient approximation (PBEsol)[26,27] method was used for exchange-correlation functional including the dispersion corrections to the total energies using Grimme's DFT-D3 scheme.[28,29] The core-valence interactions were treated by the projected augmented wave (PAW) pseudopotentials.[30] Plane-wave energy cut-off was set to 400 eV and 4×4×1 Γ-centered k-point mesh was used for Brillouin-zone sampling. During the optimization, the positions of the atoms and the volume of the unit cell were allowed to relax using a conjugate gradient algorithm until all Hellman-Feynman forces on all atoms were less than 0.08 eV/Å with an energy convergence of 1×10^{-4} eV. The surfaces were modeled by a slab consisting of 2×2 periodicity in the a-b plane and four atomic layers along the c axis, separated by 11-18 Å of vacuum in the surface normal direction. The interaction energies are calculated using the following equation:

$$\Delta E_{int}^{q} = E_{comp.} - [E_{d}^{q} + \sum n_i \mu_i + \Delta q(\epsilon_F + E_{vbm})] \qquad \text{Eq. 1}$$

which includes possible "charged" defect and anion (cation) interactions. Here, $E_{comp.}$ is the energy of the slab complex, E_{d}^{q} is the energy of the defective "d" surface with charge-state "q". n_i is the number of the *i*th anion (cation) added to the surface and μ_i is the corresponding chemical potential. Δq is the number of charges exchanged (with fermi energy ϵ_F measured from E_{vbm}) exchanged between system and reservoir in order to form the charged defect. Here, the chemical potential can be explicitly written as $\mu_i = \mu_{0i} + \Delta\mu_i$, where $\Delta\mu_i$ is the shift in the chemical potential depending on the growth conditions and $\mu_{0i} = E(i)$ is the intrinsic chemical potential

(i.e., free of the growth conditions). We define fluoride (F) or PEA attachment to a neutral defect as:

$$\Delta E_{int}^{0} = E_{comp.} - [E_{d}^{0} + \mu_{x}] \qquad \text{Eq. 2}$$

where, $x = \{F, PEA\}$, and attachment of both F and PEA as:

$$\Delta E_{int}^{0} = E_{comp.} - [E_{d}^{0} + \mu_{PEA} + \mu_{F}] \, . \qquad \text{Eq. 3}$$

For the calculation of chemical potential of F and PEA, we used conditions that are more relevant to the systems we studied. First, to calculate the intrinsic chemical potential μ_{0F}, we used the reported orthorhombic crystal structure (see Table 9.1) and then relaxed it using DFT and for μ_{0PEA}, we manually constructed a unit-cell and similarly relaxed using DFT.

Table 9.1. The DFT relaxed crystal structures of the solid-state phases considered in chemical potential calculations.

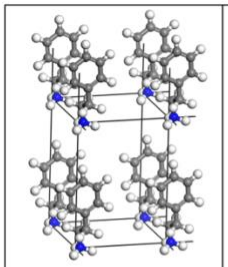	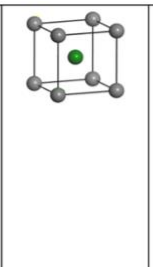	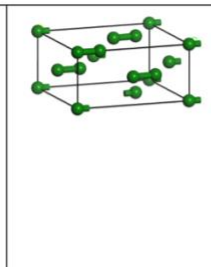	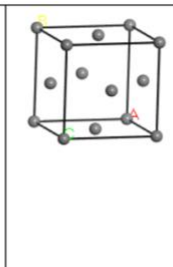	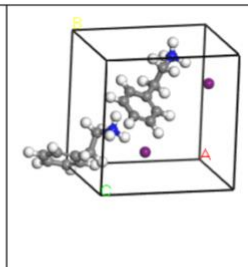	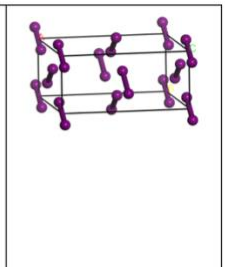
PEA	KF cubic	F_2 orthorombic	K cubic	PEAI	I_2 orthorombic

To calculate $\Delta\mu_F$ and $\Delta\mu_{PEA}$, as to be consistent with our experimental conditions, we considered that the former is the source of potassium fluoride (KF) and the latter is that of PEAI (I: iodide). Therefore, the following two relations should be satisfied:

$$\Delta\mu_K + \Delta\mu_F = \Delta H(KF) \qquad \text{Eq. 4}$$

$$\Delta\mu_{PEA} + \Delta\mu_I = \Delta H(PEAI) \, . \qquad \text{Eq. 5}$$

We also tested the formation energy of the reported KF_2 phase and found that KF is more stable by roughly 0.5 eV. Here, the formation enthalpy of cubic KF and PEAI crystals are calculated with respect to units of potassium (K), fluoride (F), PEA and iodide (I) in their crystal phases, as shown in Table 9.1. In our study, we manually constructed and tested different possible crystal structure cases for PEA and PEAI. The resulting optimized crystal structures were either unstable, less stable or the ammonium groups got deprotonated, except for the structures reported in Table 9.1. Hence, we used those structure for further calculations, while other crystal structure arrangements did not significantly differ energetically (~0.2 eV).

Our computational results showed that $\Delta H(KF) = -5.49\, eV$ and $\Delta H(PEAI) = -3.32\, eV$. Here, $\Delta H(KF)$ value we found computationally is reasonably close to the solid-state value (-5.89 eV) of KF reported in *NIST Webbook*. Next, in order to be consistent with experimental conditions in our study, we assumed an equipartition in the chemical potentials for both cases. Therefore, using Eq. (4)-(5) $\Delta\mu_F$ and $\Delta\mu_{PEA}$ were calculated to be -2.75 eV and -1.66 eV, respectively.

We found that the interaction energy of PEA attachment to neutral iodine-vacancy (V_I) is -1.07 eV and to neutral iodine-lead replacement (Pb_I) is -1.32 eV. Both F and PEA attachments to neutral V_I is -3.23 eV and to neutral Pb_I is -2.83 eV. We then calculated the ΔE_{int}^{q} in the case of charged defect cases (V_I^+ and Pb_I^+) and obtained the following plots for PEA, F and F/PEA attachments:

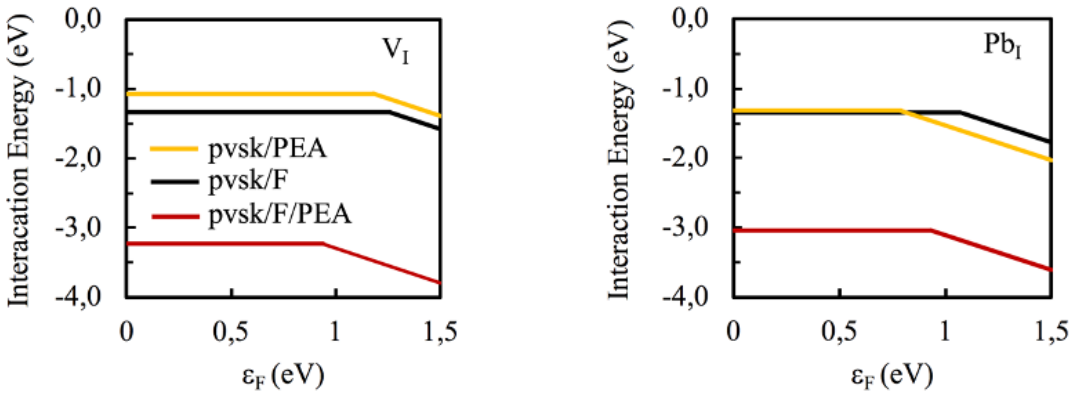

Figure 9.1. Fermi level dependence of interaction energies. Neutral and charge defect cases are both considered.

For each case, the stronger interaction energy between defects d^0, d^+ as a function of Fermi energy is shown. Thus, we found that for both V_I and Pb_I defects the fluoride binds relatively strongly, and attachment of PEA further increases interaction energy roughly by 2 eV. For low Fermi energy values (p-type region) F and PEA binds strongly to neutral defects, whereas they bind to positively charge defect more strongly in the high Fermi energy values (n-type region).

9.2.2. Device fabrication by the Yang group

Semitransparent perovskite solar cells were fabricated by spin-coating PTAA (3 mg·mL^{-1} in toluene) on the glass/ITO substrates at 4000 rpm for 60 s, followed with a 110 °C annealing for 10 min. 100 µL $Cs_{0.09}FA_{0.77}MA_{0.14}Pb(I_{0.84}Br_{0.16})_3$ solution (0.2% access PbI_2 was added to guarantee a Pb-rich perovskite surface) at the concentration of 1.8 M in *N*,*N*-dimethylformamide: dimethyl sulfoxide (DMF:DMSO) = 7:3 (volume ratio) was dripped onto the substrates for spin-coating of the perovskite layer at 3500 rpm. The total spinning time was 6 min, including the addition of 250 µL of ethyl acetate (EA) used as anti-solvent after 90 s of spinning. The flash color change from yellowish precursor wet-film to brown sol-gel state perovskite quasi-wet film was observed after dripping antisolvent, indicating an effective solvent removal and nucleation

triggered by EA. During the rest of the spinning period, the film further transformed, gradually, into a black perovskite-phase film corresponding to a slow crystal growth into a high-quality perovskite polycrystalline assisted by the abundant use of DMSO, which helped the mass transportation in the quasi-dry film. Please note that the 6 min spinning time is required to allow excess DMSO to slowly diffuse from the bulk of the micrometer-thick perovskite film to avoid pinholes generated upon annealing. The perovskite was then annealed at 100 °C for 4 min after preheating at 70 °C. For the F-treatment, KF was chosen as the F-source by thermal evaporation at a growth rate of ~0.1 Å/s for 7 seconds. PEAI treatment was carried out by spin-coating a 3 mg/mL PEAI in isopropyl alcohol (IPA) at 3000 rpm without thermal annealing. $PC_{61}BM$ (20 $mg \cdot mL^{-1}$ in CB, with 5 $mg \cdot mL^{-1}$ PMMA as additive) at 1400 rpm and ZnO nanoparticle ink (2.5 wt% in IPA, 3.2 cP) at 5000 rpm (one drop when spinning to avoid washing off the beneath $PC_{61}BM$ layer) was then subsequently deposited to form a compact electron transporting layers. The sample was then transferred to the in-house ULVAC RF sputter system to grow indium tin oxide (ITO) transparent electrode. 150 nm MgF_2 was eventually thermally evaporated on the home-sputtered ITO side as an anti-reflection coating. Opaque devices were finished with 180 nm of Ag electrode instead of ITO sputtering, using the same transporting layers.

9.3. Results and Discussion

9.3.1. Interaction of PEA and fluoride with the surface of perovskite

We firstly carried out Density Functional Theory (DFT) calculations to evaluate the interaction between PEA and the two most thermodynamically favorable surface defects based on our previous work on a Pb-rich perovskite surface, namely the iodine vacancy (V_I) and Pb-I antisite (Pb_I) defects.[31] Although it was determined that only Pb_I serves as a deep-level defect, passivation

of V_I has also been reported to enhance the stability of perovskite.[11,32,33] DFT calculations show a strong interaction of PEA with both charged defects at the perovskite surface at the conduction band minimum (CBM) with interaction energy of -1.7 eV with V_I and Pb_I, as shown in Figure 9.2a and b. All interaction energy calculations on neutral defects near valence band maximum (VBM) show a similar trend (see details in section 9.2.1). We observed favorable electrostatic stabilization and hydrogen-bonding between the ammonium group of PEA and the iodine on the perovskite surface with an average N-H···I bond length of as short as 2.5 Å. In the case of Pb_I defect, the phenyl group of PEA slightly tilts towards the interstitial Pb, engaging in a cation-π interaction further stabilizing the complex.

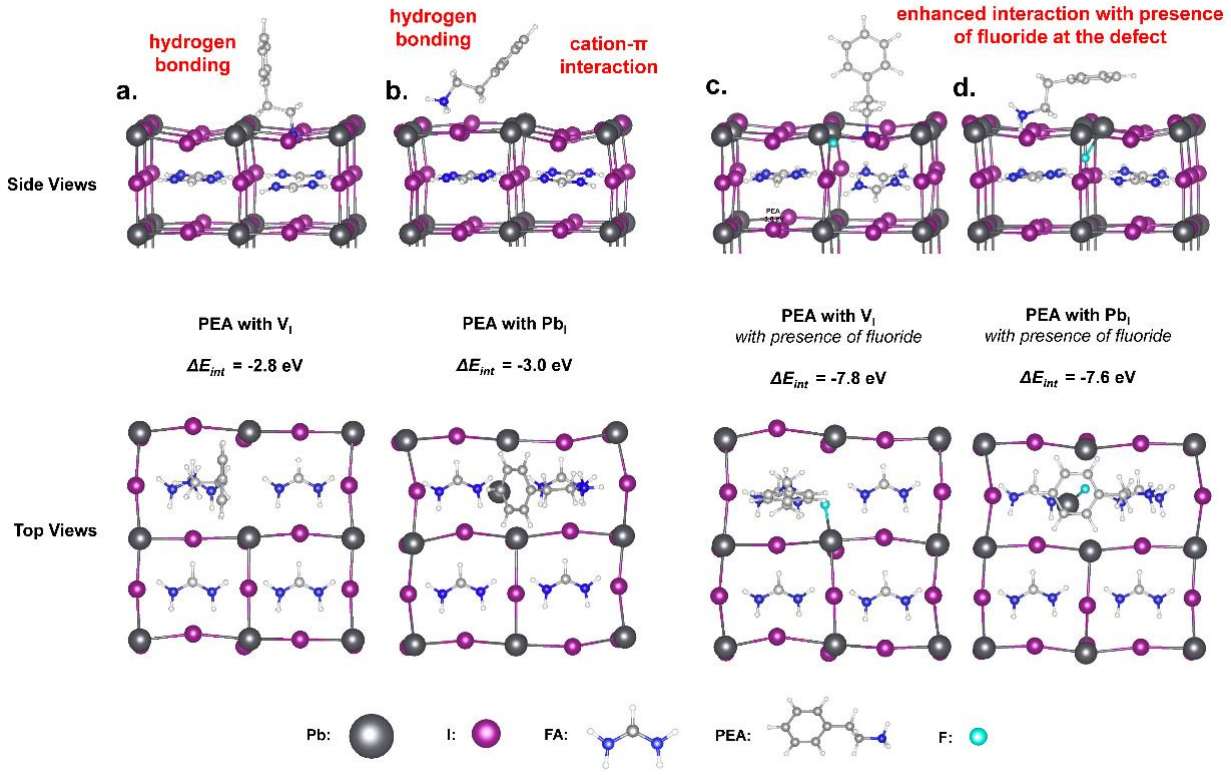

Figure 9.2. Top and side views of theoretical models used for V_I and Pb_I charged defects: interacting with bare PEA (a and b), PEA with fluoride presents nearby (c and d), and their corresponding interaction energies at the CBM. The Pb, I, FA, PEA and F atoms are as depicted at the bottom of the figure.

Given the strong proton-donating character of ammonium, we investigated the possibility of introducing a targeted fluoride (F^-) to rationally enhance the interaction between PEA and the surface defects. We found that the fluoride did prefer to occupy a thermodynamically stable site near both defects (as shown in Figure 9.2c and d). The interaction energy between PEA and both V_I and Pb_I charged defects at CBM increased to -3.8 eV and -3.6 eV, respectively, when the fluoride is present. Interestingly, we observed two different modes of synergy between PEA, the fluoride and the surface defects. Due to its smaller size compared to iodine, the fluoride, in the case of V_I, acts as an anchor that forms stronger electrostatic bonds with the ammonium group of PEA, which as a result strengthens the interaction of PEA with the defects on the surface of the perovskite. In the case of Pb_I, while the fluoride lodges itself between the antisite and native lead atoms, the phenyl group coordinates to the interstitial lead. This synergistic dynamic of fluoride and PEA in both Pb_I and V_I surface defects are hypothesized to play a significant role in increased interaction energies that could potentially lead to an even stronger passivating effect.

9.3.2. Properties of the material and thin film

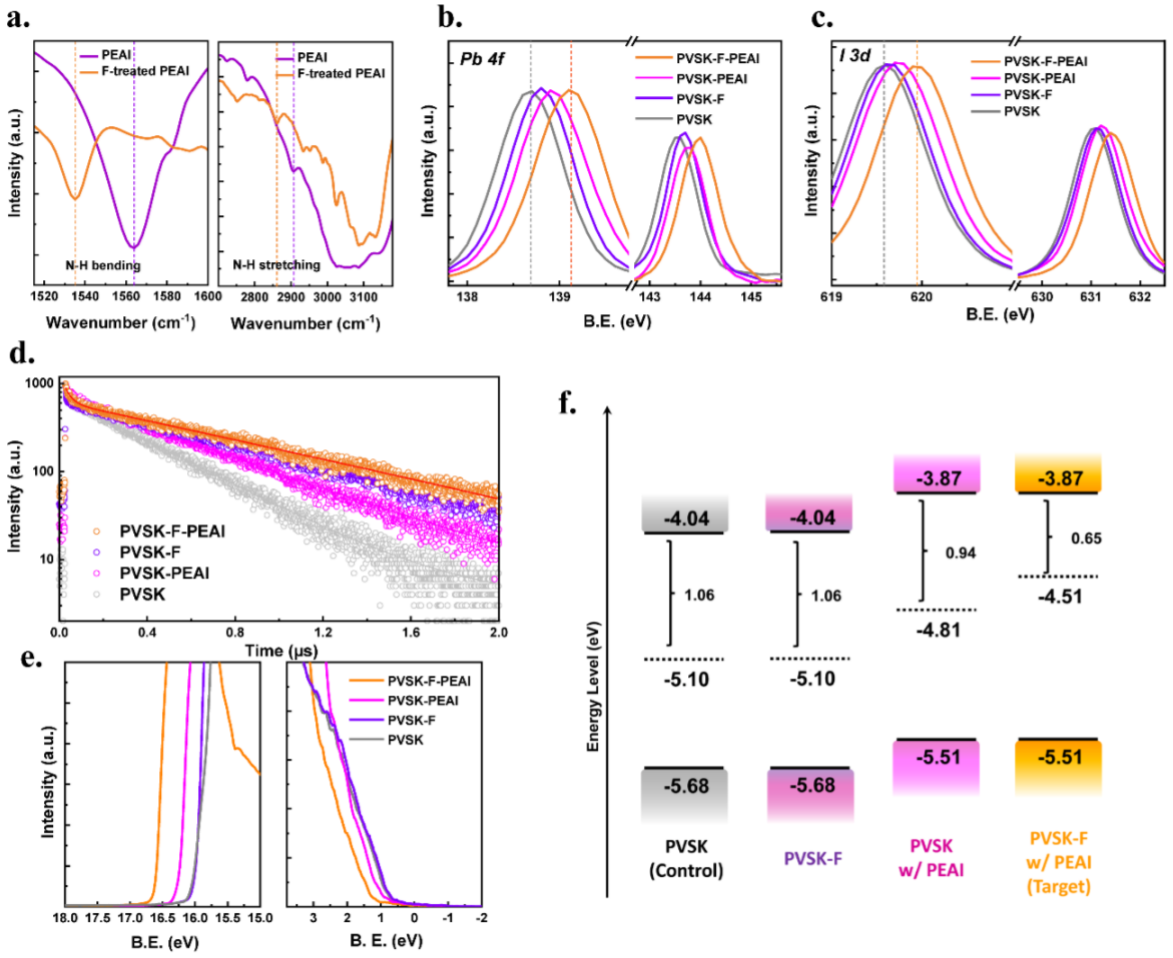

Figure 9.3. Characterizations of the passivation agents and their interactions with perovskite thin films. (a) FTIR spectra of PEAI and F-treated PEAI in the range of bending (left) and stretching (right) mode of N-H group. (b) XPS data for Pb 4f 7/2 and Pb 4f 5/2 core level spectra from perovskite films with various treatments. (c) XPS data for I 3d 5/2 and I 3d 3/2 core level spectra from perovskite films with various treatments. (d) TRPL spectra of perovskite films with or without treatments. (e) UPS spectra of perovskite films with or without treatments. (f) The energy levels of the perovskite surfaces with or without treatment derived from UPS measurements and the optical bandgap of the perovskite film.

To experimentally deliver our DFT results, the fluoride had to be deposited onto the perovskite surface in a way that preserves the pristine surface properties, such as defect types, defect densities, and atomic arrangements. Potassium fluoride (KF) cluster was thermally evaporated (less than 1 nm, denoted as the F treatment) onto the perovskite surface to satisfy these

requirements in supplying fluoride before PEAI treatment. We first investigated the fluoride-introduced F-PEAI interaction using Fourier-transform infrared spectroscopy (FTIR) without the perovskite. As shown in Figure 9.3a, an N-H bond stretching vibration was identified from the PEAI samples at 2910 cm^{-1}, while for the F-treated PEAI samples a downshift of ~50 cm^{-1} to 2860 cm^{-1} vibrational frequency was observed. Considering that the C-H and O-H vibrational frequencies also populate in this IR region, we also referred to the N-H bond bending mode of our PEAI samples found at 1564 cm^{-1}, which also downshifted to 1535 cm^{-1} after F treatment. These results indicated the presence of an electrostatic interaction between F and the ammonium group of PEA.

High-resolution X-ray photoelectron spectroscopy (XPS) measurements on perovskite films (with 0.2% excess PbI_2 to form a Pb-rich perovskite surface as the calculation assumed, details in Methods) without surface treatment showed that the characteristic Pb 4*f* peaks were located at 138.66 eV and 143.55 eV for Pb 4*f* 7/2 and Pb 4*f* 5/2, respectively. Surface treatment with only PEAI shifted the peaks to higher binding energies of 138.92 eV and 143.79 eV, respectively, while surface treatment with just F also shifted them to 138.80 eV and 143.69 eV, respectively. The targeted synergistic effect of F-PEAI treatment showed the strongest interaction with the Pb 4*f* orbitals, which consequently shifted the Pb 4*f* 7/2 peak to 139.13 eV and Pb 4*f* 5/2 peak to 144.00 eV. Similar shifting was also observed for the I 3*d* characteristic peak, where the targeted synergistic treatment with both F and PEAI showed the largest shifts to higher binding energies, similar to the Pb 4*f* orbitals.

Time-resolved photoluminescence (TRPL) of the perovskite films prepared on glass substrates without transporting layers were carried out (Figure 9.3d) to study the passivation effect. The fitted parameters show that the PEAI treatment (without thermal annealing) alone significantly

increases the carrier lifetime from $\tau_{average}$ = 291.6 ns (τ_1 = 2.5 ns, τ_2 = 336.6 ns) to $\tau_{average}$ = 371.4 ns (τ_1 = 34.4 ns, τ_2 = 482 ns), while treatment with just F enhanced the $\tau_{average}$ to 532.3 ns (τ_1 = 34.3 ns, τ_2 = 708.5 ns). Both surface treatments separately improved the carrier decay profile. This result again indicates that PEAI alone could passivate the perovskite surface without forming a 2D structure or interacting with negatively charged surface defect, since there was no annealing to surpass the formation barrier of 2D perovskite and the detrimental Pb_I defect was positively charged. However, with the F-PEAI treatment, the perovskite film showed the longest carrier lifetime of $\tau_{average}$ = 677.1 ns (τ_1 = 39.4 ns, τ_2 = 336.6 ns), indicating the most improved and superior charge recombination dynamics when the interaction between the perovskite surface defects and PEAI was enhanced with the F bridge. Together with our DFT studies regarding the most favorable occupancy location for F, it is highly possible that the synergistic effect was established by facilitating a stronger hydrogen bonding between the surface Pb_I defects and the ammonium group of PEA.

Ultraviolet photoelectron spectroscopy (UPS) was also carried out to study the surface band structure of the perovskite film with or without treatment (Figure 9.3e). We observed that neither the fermi-level nor the energy cutoff shifted after the F treatment alone, consistent with the fact that thermal deposition of F barely forms a continuous film on the perovskite surface. On the other hand, the surface energy band changed dramatically after PEAI or F-PEAI treatment as the fermi-energies shifted to higher levels, together with decreased electron affinities. By plotting the surface energy levels based on the UPS data (Figure 9.3f), the VBM for the PEAI-treated perovskite surface alone lifted from -5.68 eV to -5.51, while the fermi energy (E_f) shifted from -5.10 eV to -4.81 eV. Interestingly, the synergistic F-PEAI treatment did not affect the VBM level further, but E_f was upshifted to -4.51 eV. With the CBM calculated based on the optical bandgap

of our perovskite film, we unexpectedly found that the perovskite surface became more n-type after PEAI treatment, with the additional incorporation of F further amplifying this effect. We concluded that the target sample with F-PEAI treatment had the lowest electron affinity with the most n-type surface, which is rather preferential in the inverted perovskite solar cell device configuration[34] which adopts a semitransparent front cell in a tandem device.

9.3.3. Performance of semitransparent and tandem solar cells

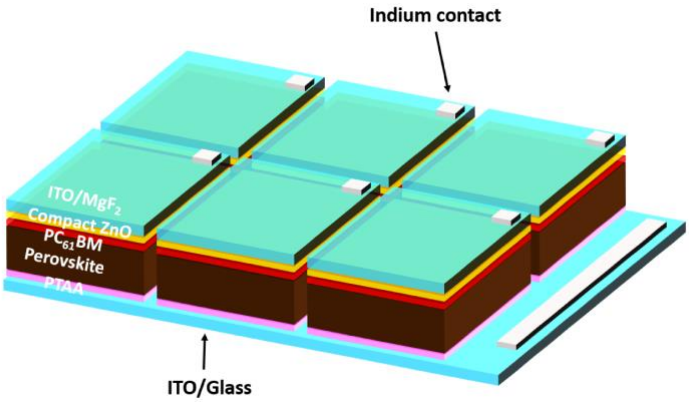

Figure 9.4. Device configuration of the semitransparent control and target perovskite cells.

Semitransparent perovskite solar cells were then fabricated, adopting an inverted device configuration shown in Figure 9.4. The *J-V* curves (illuminated from the home-deposited ITO/MgF_2 side), as well as the solar cell parameters of the control and the target devices are provided in Figure 9.5a. The champion target device demonstrated a PCE of 17.7% with a V_{OC} of 1.17 V and FF of 81%, an improvement from the 1.13 V and 75% of the control device as a result of the effective surface passivation of perovskite and improved energy level alignment between the perovskite and the ETL. We note that, to the best of our knowledge, this is one of the highest

V_{OC} reported for state-of-the-art semitransparent perovskite PVs, which are usually under inadequate light absorption near band edge, compared with opaque devices.

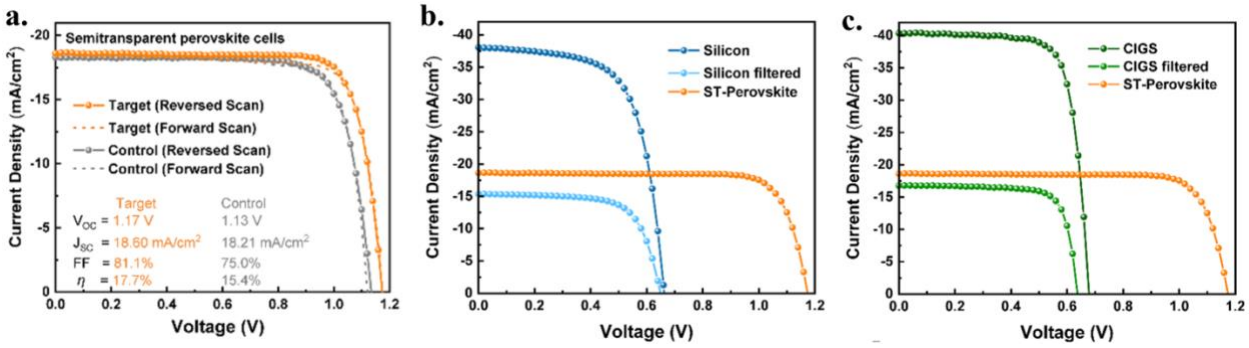

Figure 9.5. Performance of the wide-bandgap and tandem perovskite cells. (a) J-V curves of the semitransparent perovskite cells with the targeted synergistic passivation treatment (target) and without any treatment (control). (b and c) J-V curves of the target semitransparent perovskite combined with the commercially available silicon (blue) and CIGS (green) solar cells. The semitransparent perovskite cells without splitting into mini cells were used as an optical filter to measure the filtered characteristics of the rear cells.

To demonstrate that our semitransparent perovskite cells can be appropriately integrated with commercial PVs for multi-junction tandem applications, we first measured the ambient stability (room temperature, in dark) of the semitransparent perovskite cells. Compared with opaque perovskite solar cells with silver contacts, which quickly degrade in ~200 h, our semitransparent devices showed far superior ambient stability. Since the surface defects, which would have otherwise acted as degradation initiation points, have been effectively passivated, the semitransparent solar cells showed negligible efficiency loss after ~1000 h without further encapsulation. After the first 1128 h of ambient stability test, we carried out an operational stability test for the same batch of devices. With continuous illumination of one-sun, the devices still retained ~87% of the original performance after 500 h.

Lastly, we coupled our high-performance semitransparent target devices with silicon solar cells and CIGS solar cells provided by commercial PV companies Solargiga (China, original

efficiency 18.0% c-Si) and Solar Frontier (Japan, original efficiency 20.2%). A four-terminal configuration was adopted to simplify the coupling process and to verify the concept as previously reported for perovskite in tandem applications. The *J-V* curves are shown in Figure 9.5b with silicon and Figure 9.5c with CIGS. The power conversion efficiencies of the coupled devices were obtained by numerically adding up the efficiency of the target semitransparent perovskite front cell and the efficiencies of the rear cells (with the front cell as an optical filter). The photovoltaic parameters are summarized in Table 9.2. Due to the absorption and additional reflection of the front cell, the J_{SC} of the rear cells dropped from 38.6 mA/cm^2 to 15.5 mA/cm^2 for silicon, and from 40.3 mA/cm^2 to 16.8 mA/cm^2 for CIGS, respectively. The V_{OC} of the rear cells dropped likewise due to the lower light intensity reaching the rear cells. The FF of the silicon rear cell was improved since the initial shunting due to the poor device boundary conditions was mitigated in the tandem configuration, while the FF for the CIGS rear cell remained similar as the shunting was already good initially. Consequently, in the rare cell configuration, the silicon cells and CIGS cells had efficiencies of 7.4% and 8.1%, respectively. Thus, the overall efficiencies of four-terminal perovskite-silicon tandem cells reached 25.1% and perovskite-CIGS tandem cells reached 25.8%, even when both silicon and CIGS cells are commercial products with much lower original efficiencies compared with other reports.[7,35,36] We also show that if the semitransparent perovskite cells in this work are stacked with the record-performing rear cells reported,[37,38] the four-terminal solar cells could yield power conversion efficiencies of 28.1% and 27.5% for perovskite-silicon and perovskite-CIGS, respectively.

Table 9.2. Comparison of photovoltaic parameters of single- and multi-junction solar cells.

	V_{OC} (V)	J_{SC} (mA/cm^2)	$J_{SC,\,EQE}$ (mA/cm^2)	*FF* (%)	*Eff.* (%)
ST-Perovskite	1.17	18.6	18.5	81.1	17.7
Silicon	0.66	38.6	38.0	70.3	18.0
Silicon (filtered)	0.65	15.5	15.2	73.7	7.4
CIGS	0.69	40.3	39.8	74.8	20.2
CIGS (filtered)	0.64	16.8	16.7	75.4	8.1
Perovskite-Silicon	----------				25.1
Perovskite-CIGS	----------				25.8
Perovskite-Silicon *	**----------**				**28.1**
Perovskite-CIGS *	**----------**				**27.5**

* Data calculated by coupling our semitransparent perovskite cells with the record-performing silicon and CIGS as rear cells

9.4. Conclusion

In conclusion, we used theoretical analysis to unravel the interaction between perovskite surface defects and PEAI, a highly representative molecule in the organic-ammonium salts family is dominated by strong hydrogen bonding, electrostatic stabilization, and weak cation-π interaction, and thus developed an effective targeted synergistic approach that could enhance these effects. By this combination of theoretical and experimental study, we delivered high-performance semitransparent perovskite with a V_{OC} of 1.17 V for stacked tandem solar cells. The target cell was coupled with commercial silicon and CIGS solar cells with original efficiency of 18.0% and 20.2%, respectively, to prove that even with commercial products, the tandem solar cells can still reach efficiencies of over 25% using our strategy (28.1% if the record silicon cell was available).

9.5. References

(1) Leijtens, T.; Bush, K. A.; Prasanna, R.; McGehee, M. D. *Nat. Energy* **2018**, *3*, 828–838.

(2) Tong, J.; Song, Z.; Kim, D. H.; Chen, X.; Chen, C.; Palmstrom, A. F.; Ndione, P. F.; Reese, M. O.; Dunfield, S. P.; Reid, O. G.; Liu, J.; Zhang, F.; Harvey, S. P.; Li, Z.; Christensen, S. T.; Teeter, G.; Zhao, D.; Al-Jassim, M. M.; van Hest, M. F. A. M.; Beard, M. C.; Shaheen, S. E.; Berry, J. J.; Yan, Y.; Zhu, K. *Science* **2019**, *364*, 475–479.

(3) Xiao, K.; Lin, R.; Han, Q.; Hou, Y.; Qin, Z.; Nguyen, H. T.; Wen, J.; Wei, M.; Yeddu, V.; Saidaminov, M. I.; Gao, Y.; Luo, X.; Wang, Y.; Gao, H.; Zhang, C.; Xu, J.; Zhu, J.; Sargent, E. H.; Tan, H. *Nat. Energy* **2020**, *5*, 870–880.

(4) Kim, D.; Jung, H. J.; Park, I. J.; Larson, B. W.; Dunfield, S. P.; Xiao, C.; Kim, J.; Tong, J.; Boonmongkolras, P.; Ji, S. G.; Zhang, F.; Pae, S. R.; Kim, M.; Kang, S. B.; Dravid, V.; Berry, J. J.; Kim, J. Y.; Zhu, K.; Kim, D. H.; Shin, B. *Science* **2020**, *368*, 155–160.

(5) Hou, Y.; Aydin, E.; De Bastiani, M.; Xiao, C.; Isikgor, F. H.; Xue, D.-J.; Chen, B.; Chen, H.; Bahrami, B.; Chowdhury, A. H.; Johnston, A.; Baek, S.-W.; Huang, Z.; Wei, M.; Dong, Y.; Troughton, J.; Jalmood, R.; Mirabelli, A. J.; Allen, T. G.; Van Kerschaver, E.; Saidaminov, M. I.; Baran, D.; Qiao, Q.; Zhu, K.; De Wolf, S.; Sargent, E. H. *Science* **2020**, *367*, 1135–1140.

(6) Al-Ashouri, A.; Magomedov, A.; Roß, M.; Jošt, M.; Talaikis, M.; Chistiakova, G.; Bertram, T.; Márquez, J. A.; Köhnen, E.; Kasparavičius, E.; Levcenco, S.; Gil-Escrig, L.; Hages, C. J.; Schlatmann, R.; Rech, B.; Malinauskas, T.; Unold, T.; Kaufmann, C. A.; Korte, L.; Niaura, G.; Getautis, V.; Albrecht, S. *Energy Environ. Sci.* **2019**, *12*, 3356–3369.

(7) Kim, D. H.; Muzzillo, C. P.; Tong, J.; Palmstrom, A. F.; Larson, B. W.; Choi, C.; Harvey, S. P.; Glynn, S.; Whitaker, J. B.; Zhang, F.; Li, Z.; Lu, H.; van Hest, M. F. A. M.; Berry, J. J.; Mansfield, L. M.; Huang, Y.; Yan, Y.; Zhu, K. *Joule* **2019**, *3*, 1734–1745.

(8) Han, Q.; Hsieh, Y.-T.; Meng, L.; Wu, J.-L.; Sun, P.; Yao, E.-P.; Chang, S.-Y.; Bae, S.-H.; Kato, T.; Bermudez, V.; Yang, Y. *Science* **2018**, *361*, 904–908.

(9) Xu, J.; Boyd, C. C.; Yu, Z. J.; Palmstrom, A. F.; Witter, D. J.; Larson, B. W.; France, R. M.; Werner, J.; Harvey, S. P.; Wolf, E. J.; Weigand, W.; Manzoor, S.; van Hest, M. F. A. M.; Berry, J. J.; Luther, J. M.; Holman, Z. C.; McGehee, M. D. *Science* **2020**, *367*, 1097–1104.

(10) Stolterfoht, M.; Wolff, C. M.; Márquez, J. A.; Zhang, S.; Hages, C. J.; Rothhardt, D.; Albrecht, S.; Burn, P. L.; Meredith, P.; Unold, T.; Neher, D. *Nat. Energy* **2018**, *3*, 847–854.

(11) Liu, N.; Yam, C. *Phys. Chem. Chem. Phys.* **2018**, *20*, 6800–6804.

(12) Abdi-Jalebi, M.; Andaji-Garmaroudi, Z.; Cacovich, S.; Stavrakas, C.; Philippe, B.; Richter, J. M.; Alsari, M.; Booker, E. P.; Hutter, E. M.; Pearson, A. J.; Lilliu, S.; Savenije, T. J.; Rensmo, H.; Divitini, G.; Ducati, C.; Friend, R. H.; Stranks, S. D. *Nature* **2018**, *555*, 497–501.

(13) Son, D.-Y.; Lee, J.-W.; Choi, Y. J.; Jang, I.-H.; Lee, S.; Yoo, P. J.; Shin, H.; Ahn, N.; Choi, M.; Kim, D.; Park, N.-G. *Nat. Energy* **2016**, *1*, 16081.

(14) Han, T.-H.; Tan, S.; Xue, J.; Meng, L.; Lee, J.-W.; Yang, Y. *Adv. Mater.* **2019**, *31*, 1803515.

(15) Chen, B.; Rudd, P. N.; Yang, S.; Yuan, Y.; Huang, J. *Chem. Soc. Rev.* **2019**, *48*, 3842–3867.

(16) Zhou, L.; Lin, Z.; Ning, Z.; Li, T.; Guo, X.; Ma, J.; Su, J.; Zhang, C.; Zhang, J.; Liu, S.; Chang, J.; Hao, Y. *Sol. RRL* **2019**, *3*, 1900293.

(17) Jung, M.; Shin, T. J.; Seo, J.; Kim, G.; Seok, S. II. *Energy Environ. Sci.* **2018**, *11*, 2188–2197.

(18) Fu, W.; Liu, H.; Shi, X.; Zuo, L.; Li, X.; Jen, A. K.-Y. *Adv. Funct. Mater.* **2019**, *29*, 1900221.

(19) Jiang, Q.; Zhao, Y.; Zhang, X.; Yang, X.; Chen, Y.; Chu, Z.; Ye, Q.; Li, X.; Yin, Z.; You, J *Nat. Photonics* **2019**, *13*, 460–466.

(20) Kim, M.; Kim, G.-H.; Lee, T. K.; Choi, I. W.; Choi, H. W.; Jo, Y.; Yoon, Y. J.; Kim, J. W.; Lee, J.; Huh, D.; Lee, H.; Kwak, S. K.; Kim, J. Y.; Kim, D. S. *Joule* **2019**, *3*, 2179–2192.

(21) Kim, G.; Min, H.; Lee, K. S.; Lee, D. Y.; Yoon, S. M.; Seok, S. II. *Science* **2020**, *370*, 108–112.

(22) Lee, J.-W.; Dai, Z.; Han, T.-H.; Choi, C.; Chang, S.-Y.; Lee, S.-J.; De Marco, N.; Zhao, H.; Sun, P.; Huang, Y.; Yang, Y. *Nat. Commun.* **2018**, *9*, 3021.

(23) Han, T.-H.; Lee, J.-W.; Choi, Y. J.; Choi, C.; Tan, S.; Lee, S.-J.; Zhao, Y.; Huang, Y.; Kim, D.; Yang, Y. *Adv. Mater.* **2020**, *32*, 1905674.

(24) Rong, Y.; Hu, Y.; Mei, A.; Tan, H.; Saidaminov, M. I.; Seok, S. Il; McGehee, M. D.; Sargent, E. H.; Han, H. *Science* **2018**, *361*, eaat8235.

(25) Kresse, G.; Furthmüller, J. *Comput. Mater. Sci.* **1996**, *6*, 15–50.

(26) Perdew, J. P.; Burke, K.; Ernzerhof, M. *Phys. Rev. Lett.* **1996**, *77*, 3865.

(27) Perdew, J. P.; Ruzsinszky, A.; Csonka, G. I.; Vydrov, O. A.; Scuseria, G. E.; Constantin, L. A.; Zhou, X.; Burke, K. *Phys. Rev. Lett.* **2008**, *100*, 136406.

(28) Grimme, S.; Antony, J.; Ehrlich, S.; Krieg, H. *J. Chem. Phys.* **2010**, *132* (15), 154104.

(29) Grimme, S. *J. Comput. Chem.* **2006**, *27*, 1787–1799.

(30) Blöchl, P. E. *Phys. Rev. B* **1994**, *50* (24), 17953.

(31) Wang, R.; Xue, J.; Wang, K.-L.; Wang, Z.-K.; Luo, Y.; Fenning, D.; Xu, G.; Nuryyeva, S.; Huang, T.; Zhao, Y.; Yang, J. L.; Zhu, J.; Wang, M.; Tan, S.; Yavuz, I.; Houk, K. N.; Yang, Y. *Science* **2019**, *366*, 1509–1513.

(32) Saidaminov, M. I.; Kim, J.; Jain, A.; Quintero-Bermudez, R.; Tan, H.; Long, G.; Tan, F.; Johnston, A.; Zhao, Y.; Voznyy, O.; Sargent, E. H. *Nat. Energy* **2018**, *3*, 648–654.

(33) Li, N.; Tao, S.; Chen, Y.; Niu, X.; Onwudinanti, C. K.; Hu, C.; Qiu, Z.; Xu, Z.; Zheng, G.; Wang, L.; Zhang, Y.; Li, L.; Liu, H.; Lun, Y.; Hong, J.; Wang, X.; Liu, Y.; Xie, H.; Gao, Y.; Bai, Y.; Yang, S.; Brocks, G.; Chen, Q.; Zhou, H. *Nat. Energy* **2019**, *4*, 408–415.

(34) Luo, D.; Yang, W.; Wang, Z.; Sadhanala, A.; Hu, Q.; Su, R.; Shivanna, R.; Trindade, G. F.; Watts, J. F.; Xu, Z.; Liu, T.; Chen, K.; Ye, F.; Wu, P.; Zhao, L.; Wu, J.; Tu, Y.; Zhang, Y.; Yang, X.; Zhang, W.; Friend, R. H.; Gong, Q.; Snaith, H. J.; Zhu, R. *Science* **2018**, *360*, 1442–1446.

(35) Wang, Z.; Zhu, X.; Zuo, S.; Chen, M.; Zhang, C.; Wang, C.; Ren, X.; Yang, Z.; Liu, Z.; Xu, X.; Chang, Q.; Yang, S.; Meng, F.; Liu, Z.; Yuan, N.; Ding, J.; Liu, S. (Frank); Yang, D. *Adv. Funct. Mater.* **2020**, *30*, 1908298.

(36) Gharibzadeh, S.; Hossain, I. M.; Fassl, P.; Nejand, B. A.; Abzieher, T.; Schultes, M.; Ahlswede, E.; Jackson, P.; Powalla, M.; Schäfer, S.; Rienäcker, M.; Wietler, T.; Peibst, R.; Lemmer, U.; Richards, B. S.; Paetzold, U. W. *Adv. Funct. Mater.* **2020**, *30*, 1909919.

(37) Green, M. A.; Dunlop, E. D.; Levi, D. H.; Hohl-Ebinger, J.; Yoshita, M.; Ho-Baillie, A. W. Y. *Prog. Photovoltaics Res. Appl.* **2019**, *27*, 565–575.

(38) Yoshikawa, K.; Kawasaki, H.; Yoshida, W.; Irie, T.; Konishi, K.; Nakano, K.; Uto, T.; Adachi, D.; Kanematsu, M.; Uzu, H.; Yamamoto, K. *Nat. Energy* **2017**, *2*, 17032.

Chapter 10. Investigation of Performance-Limiting Formation Kinetics in Mixed-Halide Perovskites

10.1. Background

Metal halide perovskites with X-sites of iodine partially substituted with bromine have demonstrated a great potential for commercialization of the halide perovskite technology in tandem photovoltaics (PVs) where perovskite is integrated with conventional PV products such as Si and $CuInGaSe_2$.[1] By controlling the I/Br ratio, mixed-halide perovskite have shown suitable bandgap tunability that can achieve optical bandgap of 1.64-1.68 eV, which is usually considered as a wide-bandgap (WBG) perovskite that is ideal to serve as the front cell for two-junction tandem solar cells.[2] Using such mixed-halide perovskite, the perovskite-Si and perovskite-CIGS tandem cells have reached remarkable power conversion efficiencies (PCEs) of 29.52% and 24.2%, respectively.[3]

While the PV performance associated with mixed-halide perovskites is surging, $FAPbI_3$-based tri-iodide perovskite (E_g = 1.48 eV, $V_{OC,SQ}$ = 1.21 V) has recently reached notable PCEs close to 25% as single-junction with an eye-catching voltage deficiency as low as 0.30 V.[4] For WBG mixed-halide perovskites, even the champion single-junction cell reported in one of the best perovskite-Si tandems shows a 0.46 V voltage deficiency (E_g = 1.68 eV, $V_{OC,SQ}$ = 1.40 V), which was achieved using new hole-transporting materials with negligible energy offsets with the perovskite layer.[5] This is still considerably larger than that of the tri-iodide perovskite. Even though perovskites are reported to have good defect tolerance,[6,7] deep traps still do exist, especially at the surface region[8] that could lead to dramatic performance loss[9] and affect perovskite stability.[10] Moreover, the formation of defects were also reported to accelerate the halide-segregation process, which is deleterious for WBG perovskites.[11] Although in the early days, bromide was incorporated

to stabilize α-$FAPbI_3$ *via* addition of $MAPbBr_3$,[12,13] several A-site engineering strategies have been reported since then that stabilize the α-$FAPbI_3$ and achieve remarkable single-junction solar cells.[14-16] Due to these developments, the ultimate goal of developing WBG mixed-halide photovoltaic perovskites is gradually shifting towards using them in tandem applications as the front-cell to reduce total thermalization losses of the cell.[17] Understanding the large voltage deficiency compared with the tri-iodide perovskites and the potentially different defect nature in mixed-halide perovskites, thus become even more crucial.

The formation kinetics has been reported to significantly affect film quality, defect density and the device performance in halide perovskites. For example, the introduction of Lewis base adduct for $MAPbI_3$ that made the efficient $MAPbI_3$ solar cells highly reproducible in the early days of perovskite research, and the MACl-induced intermediate phase for $FAPbI_3$ finally delivered room-temperature α-phase that is stable and have exceptional photoconversion efficiencies (PCEs).[14,18] In terms of understanding the phase transition and the role of cations, in-situ wide-angle X-ray scattering (in-situ WAXS) has unveiled that mixed-halide perovskite nucleates into the 3C phase upon anti-solvent casting, coupled with simultaneous formation of several hexagonal phases (2H, 4H, and 6H phases).[19,20] Lu et al. reported that formulations with Cs^+ promoted early 3C phase formation, and effectively extended the process window,[20] which was later found to be essential to achieve homogeneous halide distribution and critical for highly efficient mixed-halide perovskite PVs by Fenning et al.[21] Although in-situ WAXS provides valuable first-hand evidence regarding the phase transitions tuned via cation-engineering, the evolution of halide dynamics during the growth does not necessarily involve phase transitions, nor dramatically affect the diffraction pattern. To the best of our knowledge, for WBG mixed-halide perovskites, most recent research has focused on understanding/preventing halide-segregation and improving interface

charge extraction.[5,22,23] However, the contrast in formation kinetics, defect physics, and consequently significant difference in voltage deficiencies between mixed-halide and tri-iodide perovskites is still not well understood.

In this work, we investigate the formation kinetics of mixed-halide perovskites are systematically investigated to understand their significant distinction from the tri-iodide perovskites: adding bromide will slow down the growth rate, introduce an excess growth stage during annealing to form the target stoichiometry from initially Br-rich crystal nuclei, and increase the defect densities in the film. A physical model was proposed that linked the formulation (amount of bromine used), formation kinetics and defect physics, thus, providing a unique perspective towards understanding the nature and performance-limiting factors of WBG mixed-halide perovskites in a holistic way.

10.2. Methodology

10.2.1. Computational methods

All quantum chemical calculations of interaction energies between DMSO and PbXX' were performed using Gaussian 16.1.[24] The initial structures used in computations were constructed using GaussView 6.0.16. PbXX' was positioned at various locations around the DMSO and the geometry of each resulting DMSO:PbXX' complex was optimized with the ωB97X-D density functional and the 6-31+G(d,p) basis set for C, H, O, S and Br atoms, and LANL2DZ basis set for Pb and I atoms. Optimized geometries were verified as minima (zero imaginary frequencies) by frequency calculations at the same level of theory. Molecular structures were visualized and rendered using Mercury 4.3.1 (Build 273956).[25-27] Interaction energies were computed using the same level of theory as well using the following equation:

$$\Delta E_{int} = E_{(DMSO:PbXX')} - [E_{DMSO} + E_{PbXX'}].$$

All first-principles calculations for bulk and slab systems are carried out using the VASP code.[28,29] A revised Perdew-Burke-Ernzerhof generalized gradient approximation (PBEsol)[30,31] was used for the exchange-correlation including a dispersion correction using Grimme's DFT-D3 scheme.[32,33] PBEsol functional has been introduced to improve the equilibrium properties of solids and surfaces.[34] Valence-core interactions were described by projector-augmented-wave (PAW) pseudopotentials.[35] Plane-wave expansions with kinetic energies up to 300 eV were chosen as the basis set for all geometry optimization and energy calculations. Both atomic positions and cell dimensions were optimized using a conjugate gradient algorithm until all Hellman-Feynman forces are smaller than 0.02 eV/Å. All atomic positions were allowed to relax. 4x4x4 and 4x4x1 Γ-center k-point mesh was adopted for Brillouin-zone sampling in bulk and surface calculations, respectively.

For formation energies of DMSO:PbXX' adduct crystals, we used the following expression:

$$\Delta H(DMSO:PbXX') = H(DMSO:PbXX') - [H(DMSO) + H(PbXX')],$$

where the first, second and third terms in the right-hand side are the energies of DMSO:PbXX', DMSO and PbXX', respectively. We considered XX'=I_2, IBr and Br_2 and used the monoclinic DMSO in all cases and the crystal structures of DMSO:PbXX' and PbXX' are based on orthorhombic DMSO:PbI_2 and hexagonal PbI_2 crystals, respectively.

For surface energy calculations, the 2x2xL surfaces were formed along (001) by periodic slabs including 9 to 11 atomic layers for a surface separated by 10-15 Å of vacuum. To characterize the formation and stability of the ABX_3 surfaces we use surface energies described as follows: we first calculate the cleavage energy of the clean surface

$$\sigma^{clv} = \frac{1}{2}[E_{slab}^{unrel} - NE_{bulk} + \sum_i n_i\mu_i] \qquad \text{Eq. 1}$$

where the first term is the energy of the unrelaxed slab, μ_i are the chemical potentials, n_i is the number of *i*th unit removed and $E_{bulk} = \mu_A + \mu_{Pb} + 3\mu_X$ is the energy *per* formula unit of the bulk perovskite. The relaxation energy is then calculated from

$$\sigma^{rl} = E_{slab}^{rel} - E_{slab}^{unrel} \qquad \text{Eq. 2}$$

where the first and second terms are the total energy of the relaxed and unrelaxed slabs, respectively. The surface energy is calculated by $\gamma = (\sigma^{clv} + \sigma^{rel})/A$, where *A* is the area of the surface. For the $APbX_3$ perovskite, A = FA, MA or Cs and X = Br or I were calculated independently. For this study, we considered PbX_2-terminated surfaces.

Formation energies of the defects in $FAPb(I_xBr_{1-x})_3$ in a charge-state q, is calculated from

$$\Delta H_d(q) = E_d(q) - E_{pr} + \Sigma_i n_i\mu_i' + q(E_F + E_{VBM}) \qquad \text{Eq. 3}$$

where $E_d(q)$ is the total energy of the system with defect, E_{pr} is the pristine system. $\mu_i' = \mu_{0i} + \mu_i$ is the chemical potential, which includes intrinsic μ_{0i} and growth-condition dependent term μ_i. n_i is the number of *i*th unit (i.e., atom or molecule) exchanged with the reservoir to form the defect. E_F is the Fermi energy and E_{VBM} is the energy at the valence-band maximum. Following Freysoldt's correction scheme,[36] the energy corrections arising from the spurious interactions due to the finite-size are included in equation (3).[37]

To determine the chemical potentials required for formation energy of a $FAPb(I_xBr_{1-x})_3$

$$\mu_{FA} + \mu_B + 3[x\mu_I + (1-x)\mu_{Br}] = \Delta H_1 \qquad \text{Eq. 4}$$

should be satisfied under thermodynamic equilibrium growth conditions, where ΔH_1 is the formation energy of $FAPb(I_xBr_{1-x})_3$.[38] In this study we considered x=1, 0.8 and 0. To avoid the formation of undesired phases

$$\mu_{FA} + \mu_{Br} < \Delta H(FABr), \quad \mu_{FA} + \mu_{Br} < \Delta H(FABr) \qquad \text{Eq. 5}$$

$$\mu_{Pb} + 2\mu_I < \Delta H(PbI_2), \;\; \mu_{Pb} + 2\mu_{Br} < \Delta H(PbBr_2) \qquad \text{Eq. 6}$$

conditions should also be satisfied where appropriate. The formation energies in the right hand sides of (5)-(6) are calculated from $\Delta H(FABr) = H(FABr) - [H(FA) + \frac{1}{2}H(Br_2)]$, $\Delta H(FAI) = H(FAI) - [H(FA) + \frac{1}{2}H(I_2)]$, $\Delta H(PbI_2) = H(PbI_2) - [H(Pb) + H(I_2)]$ and $\Delta H(PbBr_2) = H(PbBr) - [H(Pb) + H(Br_2)]$. Here, to calculate each energy term we used the respective structures; FABr and FAI in the rock-salt phases, PbI_2 and $PbBr_2$ in the hexagonal phases, FA in the bcc phase, Pb in the cubic phase and I_2 and Br_2 in the gas phase. We considered the Pb-rich growth conditions in all chemical potential calculations.

10.2.2. Preparation of perovskite precursors by the Yang group

FAMACs-Based Perovskites: 35.8 mg/mL CsI, 193 mg/mL FAI, 22.3 mg/mL MAI and 645 mg/mL PbI_2 were dissolved in a dimethylformamide/dimethylsufoxide (DMF:DMSO 80:20) solvent mix for the $FAMACsPbI_3$ precursor. For $FAMACsPb(I_{0.8}Br_{0.2})_3$ precursor, 35.8 mg/mL CsI, 169 mg/mL FAI, 516 mg/mL PbI_2, 31.4 mg/mL MABr and 103 mg/mL $PbBr_2$ were used. The final stoichiometries were $(CsPbI_3)_{0.1}(FAPbI_3)_{0.8}(MAPbI_3)_{0.1}$ and $(CsPbI_3)_{0.10}(FAPbI_3)_{0.7}(MAPbBr_3)_{0.2}$, respectively.

FACs-Based Perovskites: 71.7 mg/mL CsI, 193 mg/mL FAI and 645 mg/mL PbI_2 were dissolved in a DMF:DMSO (75:25) solvent mix for the $FACsPbI_3$ precursor. For $FACsPb(I_{0.83}Br_{0.17})_3$ precursor, 71.7 mg/mL CsI, 193 mg/mL FAI, 481 mg/mL PbI_2 and 116 mg/mL $PbBr_2$ were used. The final stoichiometries were $FA_{0.8}Cs_{0.2}PbI_3$ and $FA_{0.8}Cs_{0.2}Pb(I_{0.83}Br_{0.17})_3$, respectively. 30 mol% MACl were added to all perovskite precursors without further specification.

10.2.3. Preparation of perovskite thin film and solar cells by the Yang group

All processes were done in a N_2-filled glovebox if without further specification. For the 1-step FACs-perovskites and FAMACs-perovskites, the precursor solutions were casted to the substrate (either glass for in-situ PL or glass/ITO/SnO_2 for solar cells) and spin-coated at 3500 rpm. Chlorobenzene (CB) was casted to films at 45 s, after which it was spin-coated for another 60 s. After, the samples would be immediately transferred to a 65°C hot plate for a 5 min pre-annealing, and then transferred to a 150°C hot plate in ambient for 10 min full annealing.

For solar cells fabrication, SnO_2 layer was prepared by spin-coating a diluted SnO_2 colloidal solution on pre-cleaned glass/ITO substrates at 3000 rpm for 30s followed with 30 min ambient annealing at 150 °C. The perovskite layers were prepared on top of SnO_2 layer. For the best device performance, the passivation layer was done by spin-coating n-octylammonium iodide (10 mM in isopropyl alcohol) at 5000 rpm followed with 1 min annealing at 100 °C. 25 μL of Spiro-OMeTAD solution prepared by mixing 85.8 mg spiro-MeOTAD, 33.8 μl 4-tert-butylpyridine, 19.3 μl Li-TFSI (520 $mg \cdot mL^{-1}$ in acetonitrile) solution and 17.9 μl FK 209 Co(III) TFSI salt (375 $mg \cdot mL^{-1}$ in acetonitrile) in 1 mL CB was spin-coated at 3000 rpm on the perovskite surface. After aging in dry air overnight, 120 nm gold was then evaporated to form the metal electrodes.

10.3. Results and Discussion

10.3.1. In-situ photoluminescence studies performed by the Yang group

For the in-situ photoluminescence (PL) measurements during perovskite growth, a 532 nm laser diode, coupled with a visible-range spectrometer, were mounted in a N_2 glove box. As shown in Figure 10.1A, the acquisition of PL signals lasted for approximately 1 min during the spin-

coating, followed by 5 mins of annealing at 65 ˚C. Figure 10.1B and C depict the evolution of PL spectra during the formation of mixed-halide FAMACsPb($I_{0.8}Br_{0.2}$)$_3$ and pure-iodide FAMACsPbI_3 (10 mol% of Cs was doped in both conditions unless otherwise mentioned; Br% ratio was controlled by partially substituting FAPbI_3 with MAPbBr_3); data displayed on the left initiates from antisolvent dripping during spin coating.

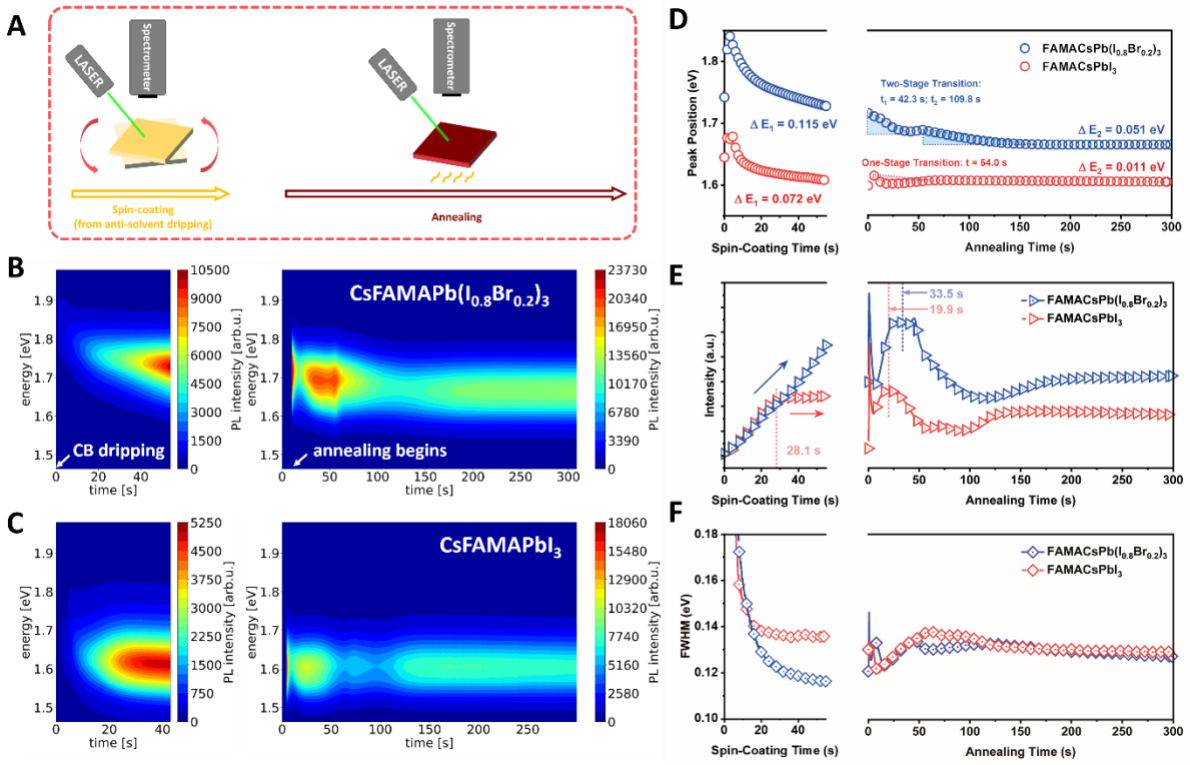

Figure 10.1. In-situ photoluminescence measurements monitoring the formation kinetics of perovskite films. (A) Illustration of the in-situ PL measurement during spin-coating and annealing stage of perovskite formation. The contour plot of the captured PL spectra during the growth of (B) CsFAMAPb($I_{0.8}Br_{0.2}$)$_3$ and (C) CsFAMAPbI_3 films during spin-coating (left) and annealing (right). The extracted values of emission peak position (D), PL intensity (E), and FWHM (F) from the in-situ PL measurements.

It was observed that for both formulations, PL signals initiated at much higher energy levels (1.88 eV for FAMACsPb($I_{0.8}Br_{0.2}$)$_3$ and 1.67 eV for FAMACsPbI_3) compared with the final

bandgap of perovskite films (approximately 1.67 eV and 1.57 eV based on PL peak, respectively). For $FAMACsPb(I_{0.8}Br_{0.2})_3$, the energy shifted by 0.115 eV during spin-coating stage (ΔE_1) and 0.051 eV upon annealing (ΔE_2). The corresponding values were 0.072 eV and 0.011 eV for $FAMACsPbI_3$, much less than the mixed-halide composition. We speculate that the emission peak shifting during the perovskite formation could be attributed to a combination of two effects: 1. The quantum confinement of the nano-grains during the early growth period, in which case larger initial crystal size would show smaller energy shifting; 2. A change in the concentration of the Br%, which causes a compositional evolution during perovskite formation.[39-41] It is also interesting that the $FAMACsPbI_3$ film took only ~54 s to reach its stable peak position upon annealing, while for $FAMACsPb(I_{0.8}Br_{0.2})_3$ the shifting lasted for over 150 s. This indicates that the growth of pure-iodide perovskite was much faster than that of the mixed-halide one. It is worth mentioning that for $FAMACsPb(I_{0.8}Br_{0.2})_3$, the emission peak transition during annealing underwent two separate stages (denoted as t_1 beginning at 42.3 s and t_2 beginning at 109.8 s) before its stabilization. The PL intensity (Figure 10.1E) observed during perovskite growth was also a combination of two effects, namely the formation of increasing amounts of highly illuminating perovskite-phase crystals and an increase in the self-absorption, especially close to the band edge. The intensity of $FAMACsPbI_3$ quickly saturated after 28.1 s upon casting an anti-solvent, while the intensity of $FAMACsPb(I_{0.8}Br_{0.2})_3$ continued to increase during spin-coating. At the annealing stage, these two compositions reached their maximum intensities at 33.5 s and 19.9 s, respectively, which indicates that the pure-iodide perovskite potentially has a higher growth rate. Analyzing the full width at half maximum (FWHM, Figure 10.1F), $FAMACsPb(I_{0.8}Br_{0.2})_3$'s signal achieved a much sharper peak during spin-coating and stabilized significantly slower than that of the $FAMACsPbI_3$. Similar but more apparent difference between pure-iodide and mixed-halide perovskite was observed

when A-site was changed to $FA_{0.8}Cs_{0.2}$ in order to ensure that the effect was independent of MA%, in which we used $MAPbBr_3$ as the Br source. Compared with pure-iodide perovskites, those with high Br% exhibited much larger peak position shifting (ΔE) during the growth, multi-stage transitions in peak position shifting, and slow peak position/FWHM stabilization and reaching of peak intensity maxima.

These compelling in-situ PL results demonstrate that adjustment of Br% not only affords the bandgap tunability of halide perovskites, but also indicate more fundamental changes that commence in their formation kinetics: adding bromine suppressed the perovskite formation rate (from the delayed evolution of PL intensity of mixed-halide perovskites), thus, potentially formed smaller nuclei upon crystallization that led to a larger ΔE. However, quantum-confinement is very unlikely to be the only reason behind the peak shifting due to multi-stage transitioning of mixed-halide perovskites. We speculate that for WBG mixed-halide perovskites, possibly, the initial crystal nuclei are very Br-rich (Br% higher than the chemical stoichiometry of the precursor) and only subsequently, more iodine would be incorporated. This formation kinetics led to the excess growth stage (t_2) in Figure 10.1D, where the Br-richness played a significant role in the PL during the early growth and were very distinctive with the tri-iodide perovskites.

10.3.2. Absorption and crystallinity studies performed by the Yang group

As it has been observed both in absorption spectra (Figure 10.2A) and in digital photographs (Figure 10.2B) of $FAMACsPbX_3$ perovskites, the as-cast pure-iodide film absorbed stronger near the band edge and appeared visually darker, which were consistent with our conclusion of their faster formation rate from the in-situ PL measurement. Besides the fully annealed films, the as-cast films (without thermal annealing) were also tested under X-ray

diffraction (XRD) but were sealed in a DMF-containing N_2 atmosphere before measuring. Interestingly, most peaks exhibited similar intensities for as-cast films in both $FAMACsPbI_3$ and $FAMACsPb(I_{0.8}Br_{0.2})_3$ (Figure 10.2C). However, by zooming in the patterns for (001) peak, the $FAMACsPb(I_{0.8}Br_{0.2})_3$ film had much larger shift in 2θ, indicating the as-cast film exhibited a smaller lattice constant which can be attributed to the early Br-rich phase. For the fully annealed films, PbI_2 peaks were observed in both compositions. However, $FAMACsPbI_3$ exhibited only minor peaks of PbI_2 and the signal from the α-phase was much stronger. Considering that 150°C was a relatively high temperature, especially for the WBG perovskites (most literatures annealed at ~100-120 °C)[5,42,43], it is likely that the incorporation of high Br% caused the organic A-site cation (FA^+ in this case) to be less stable and easier to dissociate.

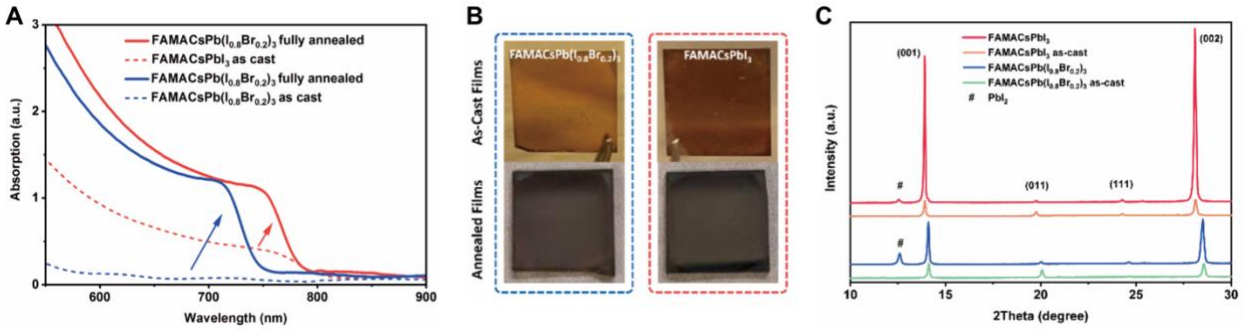

Figure 10.2. Absorption and XRD patterns of perovskite thin films. (A) Absorption spectra of $FAMACsPbX_3$ films before(as-cast)/after fully annealed. (B) Photographs of the as-cast (top) and fully annealed (bottom) perovskite films with the stoichiometries of $CsFAMAPb(I_{0.8}Br_{0.2})_3$ (left) and $CsFAMAPbI_3$ (right). (C) The XRD patterns of the as-cast and fully annealed perovskite films.

10.3.3. Computational insights into formation mechanism

Probing deeper into how increasing Br% could modulate the perovskite formation and cause the excess Br-rich growth stage, we used density functional theory (DFT) to first calculate the interaction energies of PbXX' (X and X' denote for either I or Br) species with the coordinating solvent DMSO. During spin-coating, DMSO is believed to be partially removed by the anti-

solvent, while the residual would form adduct phase with PbXX' and FAX to assist with the formation of α-phase perovskite.[18,44] As it is shown in Figure 10.3A, our calculations revealed that DMSO had the strongest interaction with PbI_2 (0.84 eV), followed by the ones with PbIBr (0.79 eV) and with $PbBr_2$ (0.77 eV), indicating Br-rich species have lower solubility in DMSO, consistent with other reports related to their solubility limits (see Figure 10.4 for optimized configurations and bond distances).[12] The formation energies of PbXX':DMSO adduct crystals were also calculated (for optimized crystal structures, see Figure 10.5). The formation energy decreased as I was gradually replaced by Br (-0.18 eV for PbI_2:DMSO, -1.10 eV for PbIBr:DMSO and -1.32 eV for $PbBr_2$:DMSO), which suggests that the formation of Br%-rich intermediate phase is more favorable. The surface energies between tri-iodide perovskites with varying A-site cation were also calculated to be much higher than that of the tri-bromide perovskites regardless of which A-site cation was incorporated (either PbX_2 or X-site termination, Figure 10.3B). As forming new surfaces impede nucleation from happening, Br-rich perovskite could be more likely to form during the early part of the formation. By putting together the experimental and computational results, we postulate that Br%-rich species reach supersaturation during solvent removal more rapidly during nucleation for the WBG mixed-halide perovskites, more likely to advance to the intermediate adduct phase (PbX_6:DMSO intermediates),[45-46] and preferential in converting into the perovskite phase, which was the origin of the excess Br-rich growth stage observed in in-situ PL. However, even though this Br-rich phase was observed in the early growth stage for WBG mixed-halide perovskites, they still reached the target bandgap when the growth was completed.

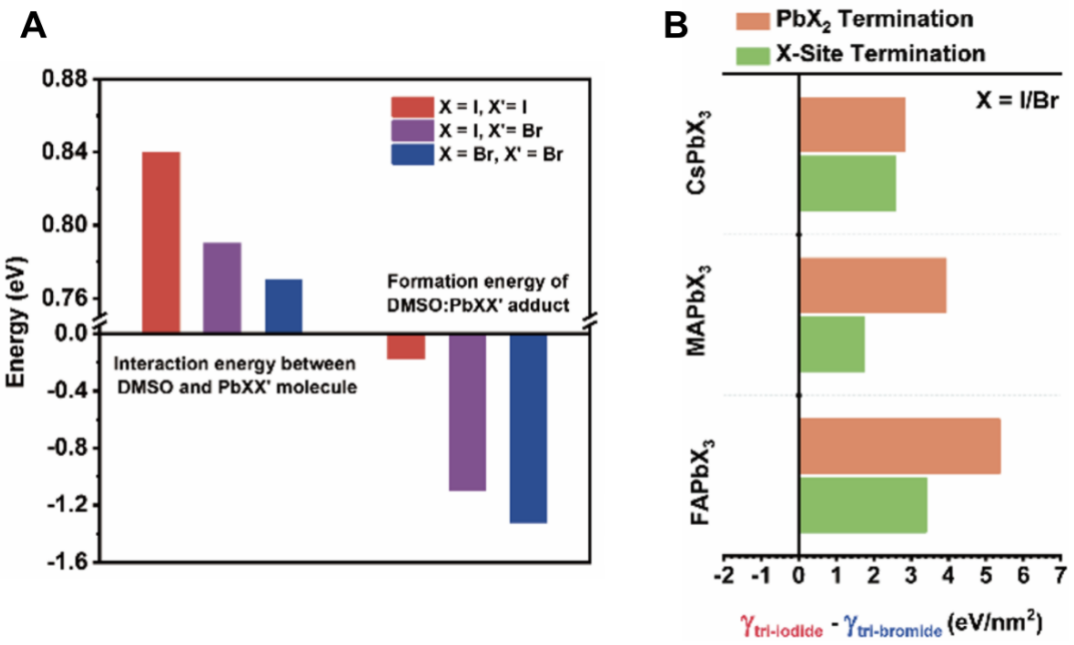

Figure 10.3. Computed interaction, formation and surface energies. (A) Interaction energy between DMSO and PbXX' molecule and formation energy of DMSO:PbXX' adduct phase. (B) The calculated results of surface energy difference in tri-iodide perovskites and tri-bromide perovskites with cations to be Cs, MA, or FA.

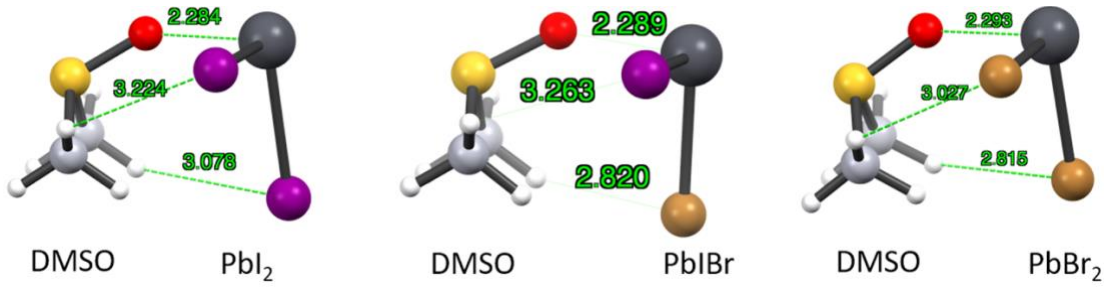

Figure 10.4. Optimized molecular structures and intermolecular interaction distances between coordinating solvent, DMSO, and PbXX' molecules.

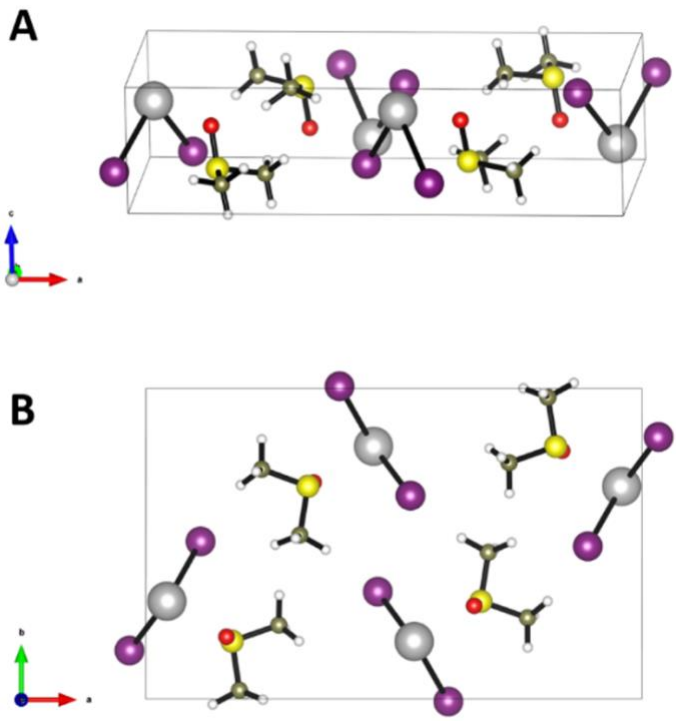

Figure 10.6. Side (A) and top (B) views of the optimized supercell of DMSO:PbXX' adduct. X sites were assumed to be I in the structure.

10.3.4. Solar-cell performance studies performed by the Yang group

Finally, solar cell devices based on both mixed-halide and tri-iodide perovskites were fabricated as well to combine insights gained from in-situ measurements and thin film characterizations with device performance. As shown in Figure 10.7, devices with both perovskites exhibited >79% FF, while the J_{SC} of $FAMACsPb(I_{0.8}Br_{0.2})_3$ (23.1 mA/cm^2) was distinctly lower than that of $FAMACsPbI_3$ (25.1 mA/cm^2) due to the increased bandgap. The *Voc* gain of $FAMACsPb(I_{0.8}Br_{0.2})_3$ over $FAMACsPbI_3$, however, was minor with V_{OC} values of 1.16 V and 1.19 V, ($V_{OC,SQ}$ - V_{OC} of 0.13 V and 0.20 V, qE_g -V_{OC} of 0.40 V and 0.48V) respectively. The solar cell performance results demonstrated a consistent trend coinciding with the thin film characterizations, where non-radiative recombination became more probable in mixed-halide perovskite and endured more performance losses. It could explain that although the tri-iodide

perovskites have the bandgap that should only merely out-perform the one of the mixed-halide WBG based on the theoretical limit, the record efficiency experience such a boost after the development of stable α-$FAPbI_3$ based perovskites.

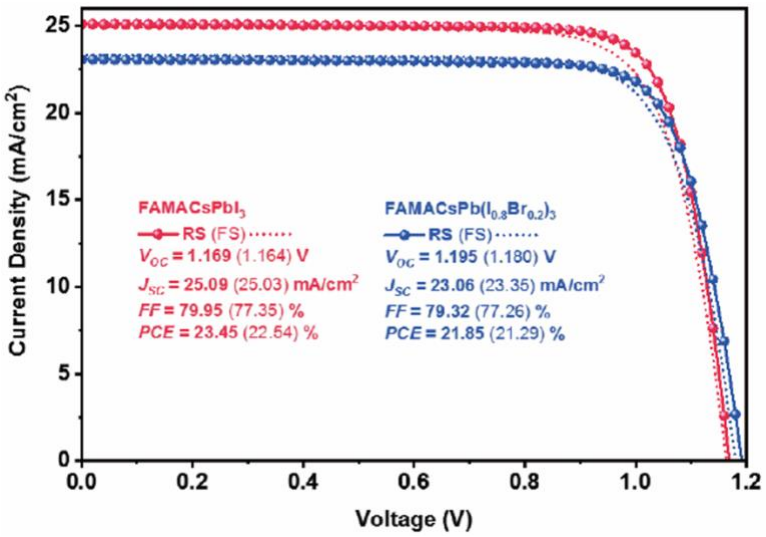

Figure 10.7. *J-V* characteristics of perovskite solar cell devices based on $CsFAMAPb(I_{0.8}Br_{0.2})_3$ and $CsFAMAPbI_3$.

10.3.5. Resulting overall model of the formation kinetics and defect physics

To this point, a hypothetic physical model shown in Figure 10.8 could be established for WBG mixed-halide perovskites in an attempt to link formation kinetics and defect physics. As in-situ PL measurement suggested, the excess Br-rich growth state of mixed-halide perovskites with higher energy emission could be attributed to the initial crystal nuclei that had higher Br% than the stoichiometry of the precursor solution. To finally achieve halide homogeneity upon annealing, an ion-exchange-like process associated with iodide diffusing inwards the nucleus and bromide diffusing outwards, or even halide migration across the interfaces would be necessary. Different from direct phase transition from hexagonal phases to perovskite phase (either cubic or tetragonal) with only local atomic displacements, these diffusion processes potentially increased the risk of

increasing the lattice distortion, and forming multiple intrinsic defects including vacancies, interstitials, or anti-sites (among which X_i, FA_{Pb}, V_{Pb}, V_{FA} and X_{FA} were neutral/negatively charged) compared with the tri-iodide perovskite where this halide homogenization-diffusion process was absent. Combining our results and the latest discovery of the top-to-bottom downwards growth of perovskite films,[47] this could rationalize the higher total defect densities of the mixed-halide film, especially at the surface region. Meanwhile, if the formation of these preferential defects did associate with the homogenization and halide diffusion kinetics, the prediction of their formation by DFT calculations, which rely on local equilibrium, would be highly challenging.

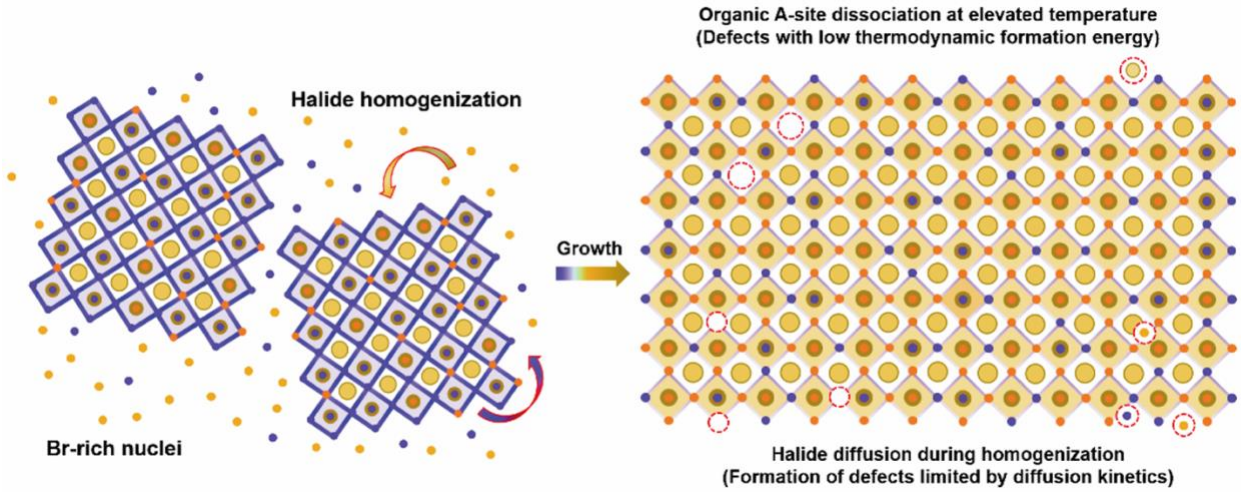

Figure 10.8. A hypothetical physical model of formation kinetics in mixed-halide perovskite with high Br% (left) and their potential role with defect physics (right). Several but not all possible point defects were illustrated at the surface or in the bulk. For simplification purpose, only the halides were specified for Br as purple dots and I as yellow dots.

On the other hand, XRD results of mixed-halide and tri-iodide perovskites suggested the crystallinity was clearly affected by increasing bromine, and the organic A-site became less stable at elevated temperature and formed more PbX_2 binaries when there was high Br% incorporation. These features could also promote the formation of intrinsic defects related to the organic A-site.

Even though this issue could be optimized by lowering the annealing temperature, it served as an indirect proof that WBG mixed-halide perovskite were less resistant in preventing A-site decomposition or dissociation. In fact, as is shown in Figure 10.9, both formation energies of V_{FA} and FA_i (calculated under a Pb-rich condition) were lower for 20%Br compared with 0%Br (especially for FA_i). Further increasing Br% to 100% suggested that Br% dramatically increased the likelihood of FA_i formation. Considering that the photoluminescence tests and device performances also showed good consistency with each other, it was reasonable to draw a very strong correlation that the high Br% concentration itself (~20% for an ideal front cell) could modulate the growth kinetics. It promoted the formation of excess defects, and also caused intrinsic performance penalties including the non-radiative recombination, not to mention that these flaws were also believed to further accelerate halide-segregation and degradation in long-term operation.[11,22]

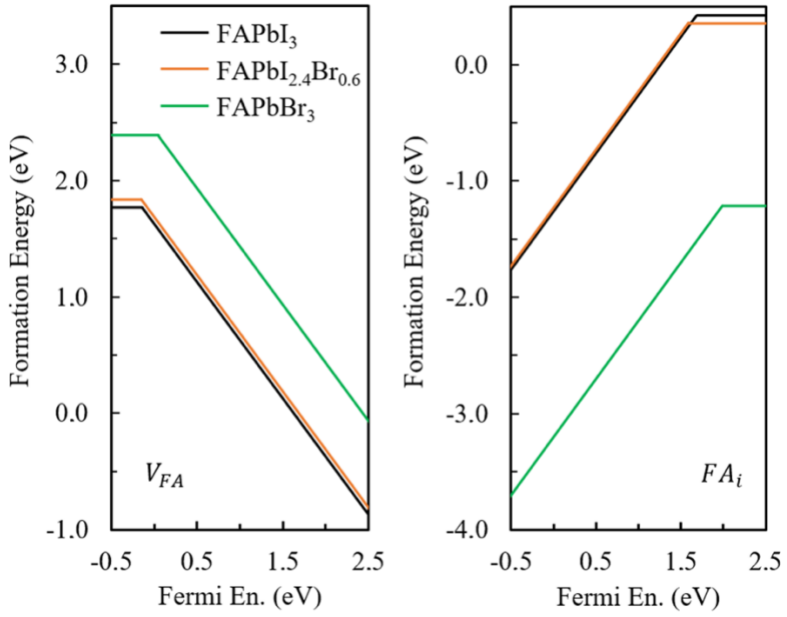

Figure 10.9. Fermi energy (E_F) dependence of the defect formation energies: (left) FA vacancy and (right) FA interstitial point defects in $FAPbI_3$ (orange line), $FAPb(I_{0.8}Br_{0.2})_3$ (black line) and $FAPbBr_3$ (green line). E_F = 0 was set at valence band minimum.

10.4. Conclusion

The formation kinetics of mixed-halide perovskites are systematically investigated to understand their significant distinction from the tri-iodide perovskites: adding bromide will slow down the growth rate, introduce an excess growth stage during annealing to form the target stoichiometry from initially Br-rich crystal nuclei, and increase the defect densities in the film. We present a unique perspective from a formation kinetics viewpoint, which explains that even though WBG perovskites show acceptable solar cell performance after passivation, halide segregation could be further minimized using a certain stoichiometry. Although the interfacial losses had been gradually minimized by the introduction of new transporting materials, this study shows that WBG mixed-halide perovskites were not yet as close to the theoretical limit compared with tri-iodide perovskites.

10.5. References

(1) Green, M.; Dunlop, E.; Hohl-Ebinger, J.; Yoshita, M.; Kopidakis, N.; Hao, X. *Prog. Photovoltaics Res. Appl.* **2021**, *29*, 3–15.

(2) McMeekin, D. P.; Sadoughi, G.; Rehman, W.; Eperon, G. E.; Saliba, M.; Hörantner, M. T.; Haghighirad, A.; Sakai, N.; Korte, L.; Rech, B.; Johnston, M. B.; Herz, L. M.; Snaith, H. J. *Science* **2016**, *351*, 151–155.

(3) B. R.-C. E. Chart, *https://www.nrel.gov/pv/cell-efficiency.html* **2021**.

(4) Jeong, M.; Choi, I. W.; Go, E. M.; Cho, Y.; Kim, M.; Lee, B.; Jeong, S.; Jo, Y.; Choi, H. W.; Lee, J.; Bae, J.-H.; Kwak, S. K.; Kim, D. S.; Yang, C. *Science* **2020**, *369*, 1615–1620.

(5) Al-Ashouri, A.; Köhnen, E.; Li, B.; Magomedov, A.; Hempel, H.; Caprioglio, P.; Márquez, J. A.; Morales Vilches, A. B.; Kasparavicius, E.; Smith, J. A.; Phung, N.; Menzel, D.; Grischek, M.; Kegelmann, L.; Skroblin, D.; Gollwitzer, C.; Malinauskas, T.; Jošt, M.; Matič, G.; Rech, B.; Schlatmann, R.; Topič, M.; Korte, L.; Abate, A.; Stannowski, B.; Neher, D.; Stolterfoht, M.; Unold, T.; Getautis, V.; Albrecht, S. *Science* **2020**, *370*, 1300–1309.

(6) Kim, G.-W.; Petrozza, A. *Adv. Energy Mater.* **2020**, *10*, 2001959.

(7) Steirer, K. X.; Schulz, P.; Teeter, G.; Stevanovic, V.; Yang, M.; Zhu, K.; Berry, J. J. *ACS Energy Lett.* **2016**, *1*, 360–366.

(8) Ni, Z.; Bao, C.; Liu, Y.; Jiang, Q.; Wu, W.-Q.; Chen, S.; Dai, X.; Chen, B.; Hartweg, B.; Yu, Z.; Holman, Z.; Huang, J. *Science* **2020**, *367*, 1352–1358.

(9) Wang, R.; Xue, J.; Wang, K.-L.; Wang, Z.-K.; Luo, Y.; Fenning, D.; Xu, G.; Nuryyeva, S.; Huang, T.; Zhao, Y.; Yang, J. L.; Zhu, J.; Wang, M.; Tan, S.; Yavuz, I.; Houk, K. N.; Yang, Y. *Science* **2019**, *366*, 1509–1513.

(10) Tan, S.; Yavuz, I.; Weber, M. H.; Huang, T.; Chen, C.-H.; Wang, R.; Wang, H.-C.; Ko, J. H.; Nuryyeva, S.; Xue, J.; Zhao, Y.; Wei, K.-H.; Lee, J.-W.; Yang, Y. *Joule* **2020**, *4*, 2426–2442.

(11) Barker, A. J.; Sadhanala, A.; Deschler, F.; Gandini, M.; Senanayak, S. P.; Pearce, P. M.; Mosconi, E.; Pearson, A. J.; Wu, Y.; Srimath Kandada, A. R.; Leijtens, T.; De Angelis, F.; Dutton, S. E.; Petrozza, A.; Friend, R. H. *ACS Energy Lett.* **2017**, *2*, 1416–1424.

(12) Chen, L.; Tan, Y.-Y.; Chen, Z.-X.; Wang, T.; Hu, S.; Nan, Z.-A.; Xie, L.-Q.; Hui, Y.; Huang, J.-X.; Zhan, C.; Wang, S.-H.; Zhou, J.-Z.; Yan, J.-W.; Mao, B.-W.; Tian, Z.-Q. *J. Am. Chem. Soc.* **2019**, *141*, 1665–1671.

(13) Xie, L.-Q.; Chen, L.; Nan, Z.-A.; Lin, H.-X.; Wang, T.; Zhan, D.-P.; Yan, J.-W.; Mao, B.-W.; Tian, Z.-Q. *J. Am. Chem. Soc.* **2017**, *139* (9), 3320–3323.

(14) Kim, M.; Kim, G.-H.; Lee, T. K.; Choi, I. W.; Choi, H. W.; Jo, Y.; Yoon, Y. J.; Kim, J. W.; Lee, J.; Huh, D.; Lee, H.; Kwak, S. K.; Kim, J. Y.; Kim, D. S. *Joule* **2019**, *3*, 2179–2192.

(15) Min, H.; Kim, M.; Lee, S.-U.; Kim, H.; Kim, G.; Choi, K.; Lee, J. H.; Seok, S. II. *Science* **2019**, *366*, 749–753.

(16) Kim, G.; Min, H.; Lee, K. S.; Lee, D. Y.; Yoon, S. M.; Seok, S. II. *Science* **2020**, *370*, 108–112.

(17) Leijtens, T.; Bush, K. A.; Prasanna, R.; McGehee, M. D. *Nat. Energy* **2018**, *3* (10), 828–838.

(18) Ahn, N.; Son, D.-Y.; Jang, I.-H.; Kang, S. M.; Choi, M.; Park, N.-G. *J. Am. Chem. Soc.* **2015**, *137*, 8696–8699.

(19) Dang, H. X.; Wang, K.; Ghasemi, M.; Tang, M.-C.; De Bastiani, M.; Aydin, E.; Dauzon, E.; Barrit, D.; Peng, J.; Smilgies, D.-M.; De Wolf, S.; Amassian, A. *Joule* **2019**, *3*, 1746–1764.

(20) Qin, M.; Tse, K.; Lau, T.-K.; Li, Y.; Su, C.-J.; Yang, G.; Chen, J.; Zhu, J.; Jeng, U.-S.; Li, G.; Chen, H.; Lu, X. *Adv. Mater.* **2019**, *31*, 1901284.

(21) Correa-Baena, J.-P.; Luo, Y.; Brenner, T. M.; Snaider, J.; Sun, S.; Li, X.; Jensen, M. A.; Hartono, N. T. P.; Nienhaus, L.; Wieghold, S.; Poindexter, J. R.; Wang, S.; Meng, Y. S.; Wang, T.; Lai, B.; Holt, M. V; Cai, Z.; Bawendi, M. G.; Huang, L.; Buonassisi, T.; Fenning, D. P. *Science* **2019**, *363*, 627–631.

(22) Mahesh, S.; Ball, J. M.; Oliver, R. D. J.; McMeekin, D. P.; Nayak, P. K.; Johnston, M. B.; Snaith, H. J. *Energy Environ. Sci.* **2020**, *13*, 258–267.

(23) Beal, R. E.; Hagström, N. Z.; Barrier, J.; Gold-Parker, A.; Prasanna, R.; Bush, K. A.; Passarello, D.; Schelhas, L. T.; Brüning, K.; Tassone, C. J.; Steinrück, H.-G.; McGehee, M. D.; Toney, M. F.; Nogueira, A. F. *Matter* **2020**, *2*, 207–219.

(24) *Gaussian 16*, Revision A.03, Frisch, M. J.; Trucks, G. W.; Schlegel, H. B.; Scuseria, G. E.; Robb, M. A.; Cheeseman, J. R.; Scalmani, G.; Barone, V.; Petersson, G. A.; Nakatsuji, H.; Li, X.; Caricato, M.; Marenich, A. V.; Bloino, J.; Janesko, B. G.; Gomperts, R.; Mennucci, B.; Hratchian, H. P.; Ortiz, J. V.; Izmaylov, A. F.; Sonnenberg, J. L.; Williams-Young, D.; Ding, F.; Lipparini, F.; Egidi, F.; Goings, J.; Peng, B.; Petrone, A.; Henderson, T.; Ranasinghe, D.; Zakrzewski, V. G.; Gao, J.; Rega, N.; Zheng, G.; Liang, W.; Hada, M.; Ehara, M.; Toyota, K.; Fukuda, R.; Hasegawa, J.; Ishida, M.; Nakajima, T.; Honda, Y.; Kitao, O.; Nakai, H.; Vreven, T.; Throssell, K.; Montgomery, J. A., Jr.; Peralta, J. E.; Ogliaro, F.; Bearpark, M. J.; Heyd, J. J.; Brothers, E. N.; Kudin, K. N.; Staroverov, V. N.; Keith, T. A.; Kobayashi, R.; Normand, J.; Raghavachari, K.; Rendell, A. P.; Burant, J. C.; Iyengar, S. S.; Tomasi, J.; Cossi, M.; Millam, J. M.; Klene, M.; Adamo, C.; Cammi, R.; Ochterski, J. W.;

Martin, R. L.; Morokuma, K.; Farkas, O.; Foresman, J. B.; Fox, D. J. Gaussian, Inc., Wallingford CT, **2016**.

(25) Macrae, C. F.; Sovago, I.; Cottrell, S. J.; Galek, P. T. A.; McCabe, P.; Pidcock, E.; Platings, M.; Shields, G. P.; Stevens, J. S.; Towler, M.; Wood, P. A. *J. Appl. Crystallogr.* **2020**, *53*, 226–235.

(26) Macrae, C. F.; Edgington, P. R.; McCabe, P.; Pidcock, E.; Shields, G. P.; Taylor, R.; Towler, M.; van de Streek, J. *J. Appl. Crystallogr.* **2006**, *39*, 453–457.

(27) Bruno, I. J.; Cole, J. C.; Edgington, P. R.; Kessler, M.; Macrae, C. F.; McCabe, P.; Pearson, J.; Taylor, R. *Acta Crystallogr. Sect. B* **2002**, *58*, 389–397.

(28) Kresse, G.; Furthmüller, J. *Comput. Mater. Sci.* **1996**, *6*, 15–50.

(29) Kresse, G.; Furthmüller, J. *Phys. Rev. B* **1996**, *54*, 11169.

(30) Perdew, J. P.; Burke, K.; Ernzerhof, M. *Phys. Rev. Lett.* **1996**, *77*, 3865.

(31) Perdew, J. P.; Ruzsinszky, A.; Csonka, G. I.; Vydrov, O. A.; Scuseria, G. E.; Constantin, L. A.; Zhou, X.; Burke, K. *Phys. Rev. Lett.* **2008**, *100*, 136406.

(32) Grimme, S.; Antony, J.; Ehrlich, S.; Krieg, H. *J. Chem. Phys.* **2010**, *132* (15), 154104.

(33) Grimme, S. *J. Comput. Chem.* **2006**, *27*, 1787–1799.

(34) Blöchl, P. E. *Phys. Rev. B* **1994**, *50*, 17953.

(35) Csonka, G. I.; Perdew, J. P.; Ruzsinszky, A.; Philipsen, P. H. T.; Lebègue, S.; Paier, J.; Vydrov, O. A.; Ángyán, J. G. *Phys. Rev. B* **2009**, *79*, 155107.

(36) Freysoldt, C.; Neugebauer, J.; Van de Walle, C. G. *Phys. Rev. Lett.* **2009**, *102*, 16402.

(37) Naik, M. H.; Jain, M. *Comput. Phys. Commun.* **2018**, *226*, 114–126.

(38) Yin, W.-J.; Shi, T.; Yan, Y. *Appl. Phys. Lett.* **2014**, *104*, 63903.

(39) Parrott, E. S.; Patel, J. B.; Haghighirad, A.-A.; Snaith, H. J.; Johnston, M. B.; Herz, L. M. *Nanoscale* **2019**, *11*, 14276–14284.

(40) Song, T.-B.; Yuan, Z.; Babbe, F.; Nenon, D. P.; Aydin, E.; De Wolf, S.; Sutter-Fella, C. M. *ACS Appl. Energy Mater.* **2020**, *3*, 2386–2393.

(41) Song, T.-B.; Yuan, Z.; Mori, M.; Motiwala, F.; Segev, G.; Masquelier, E.; Stan, C. V; Slack, J. L.; Tamura, N.; Sutter-Fella, C. M. *Adv. Funct. Mater.* **2020**, *30*, 1908337.

(42) Kim, D.; Jung, H. J.; Park, I. J.; Larson, B. W.; Dunfield, S. P.; Xiao, C.; Kim, J.; Tong, J.; Boonmongkolras, P.; Ji, S. G.; Zhang, F.; Pae, S. R.; Kim, M.; Kang, S. B.; Dravid, V.; Berry, J. J.; Kim, J. Y.; Zhu, K.; Kim, D. H.; Shin, B. *Science* **2020**, *368*, 155–160.

(43) Lin, R.; Xiao, K.; Qin, Z.; Han, Q.; Zhang, C.; Wei, M.; Saidaminov, M. I.; Gao, Y.; Xu, J.; Xiao, M.; Li, A.; Zhu, J.; Sargent, E. H.; Tan, H. *Nat. Energy* **2019**, *4*, 864–873.

(44) Lee, J.-W.; Dai, Z.; Lee, C.; Lee, H. M.; Han, T.-H.; De Marco, N.; Lin, O.; Choi, C. S.; Dunn, B.; Koh, J.; Di Carlo, D.; Ko, J. H.; Maynard, H. D.; Yang, Y. *J. Am. Chem. Soc.* **2018**, *140*, 6317–6324.

(45) Cao, J.; Jing, X.; Yan, J.; Hu, C.; Chen, R.; Yin, J.; Li, J.; Zheng, N. *J. Am. Chem. Soc.* **2016**, *138*, 9919–9926.

(46) Huang, X.; Chen, R.; Deng, G.; Han, F.; Ruan, P.; Cheng, F.; Yin, J.; Wu, B.; Zheng, N. *J. Am. Chem. Soc.* **2020**, *142*, 6149–6157.

(47) Chen, S.; Xiao, X.; Chen, B.; Kelly, L. L.; Zhao, J.; Lin, Y.; Toney, M. F.; Huang, J. *Sci. Adv.* **2021**, *7*, eabb2412.